

University of Kentucky

UKnowledge

---

Theses and Dissertations--Chemical and  
Materials Engineering

Chemical and Materials Engineering

---

2016

# **PEPTIDE-FUNCTIONALIZED MAGNETIC NANOPARTICLES FOR CANCER THERAPY APPLICATIONS**

Anastasia K. Hauser

*University of Kentucky*, amkrus2@g.uky.edu

Digital Object Identifier: <http://dx.doi.org/10.13023/ETD.2016.157>

[Right click to open a feedback form in a new tab to let us know how this document benefits you.](#)

## **Recommended Citation**

Hauser, Anastasia K., "PEPTIDE-FUNCTIONALIZED MAGNETIC NANOPARTICLES FOR CANCER THERAPY APPLICATIONS" (2016). *Theses and Dissertations--Chemical and Materials Engineering*. 59.  
[https://uknowledge.uky.edu/cme\\_etds/59](https://uknowledge.uky.edu/cme_etds/59)

This Doctoral Dissertation is brought to you for free and open access by the Chemical and Materials Engineering at UKnowledge. It has been accepted for inclusion in Theses and Dissertations--Chemical and Materials Engineering by an authorized administrator of UKnowledge. For more information, please contact [UKnowledge@lsv.uky.edu](mailto:UKnowledge@lsv.uky.edu).

## **STUDENT AGREEMENT:**

I represent that my thesis or dissertation and abstract are my original work. Proper attribution has been given to all outside sources. I understand that I am solely responsible for obtaining any needed copyright permissions. I have obtained needed written permission statement(s) from the owner(s) of each third-party copyrighted matter to be included in my work, allowing electronic distribution (if such use is not permitted by the fair use doctrine) which will be submitted to UKnowledge as Additional File.

I hereby grant to The University of Kentucky and its agents the irrevocable, non-exclusive, and royalty-free license to archive and make accessible my work in whole or in part in all forms of media, now or hereafter known. I agree that the document mentioned above may be made available immediately for worldwide access unless an embargo applies.

I retain all other ownership rights to the copyright of my work. I also retain the right to use in future works (such as articles or books) all or part of my work. I understand that I am free to register the copyright to my work.

## **REVIEW, APPROVAL AND ACCEPTANCE**

The document mentioned above has been reviewed and accepted by the student's advisor, on behalf of the advisory committee, and by the Director of Graduate Studies (DGS), on behalf of the program; we verify that this is the final, approved version of the student's thesis including all changes required by the advisory committee. The undersigned agree to abide by the statements above.

Anastasia K. Hauser, Student

Dr. J. Zach Hilt, Major Professor

Dr. Thomas Dziubla, Director of Graduate Studies

PEPTIDE-FUNCTIONALIZED MAGNETIC NANOPARTICLES FOR CANCER  
THERAPY APPLICATIONS

---

DISSERTATION

---

A dissertation submitted in partial fulfillment of the  
requirements for the degree of Doctor of Philosophy in the  
College of Engineering  
at the University of Kentucky

By  
Anastasia Kruse Hauser

Lexington, Kentucky

Co-directors: Dr. J. Zach Hilt, Professor of Chemical and Materials Engineering  
and Dr. Kimberly W. Anderson, Professor of Chemical and Materials Engineering

Lexington, Kentucky

2016

Copyright © Anastasia Kruse Hauser 2016

## ABSTRACT OF DISSERTATION

### PEPTIDE-FUNCTIONALIZED MAGNETIC NANOPARTICLES FOR CANCER THERAPY APPLICATIONS

Lung cancer is one of the leading causes of cancer deaths in the United States. Radiation and chemotherapy are conventional treatments, but they result in serious side effects and the probability of tumor recurrence remains high. Therefore, there is an increasing need to enhance the efficacy of conventional treatments. Magnetic nanoparticles have been previously studied for a variety of applications such as magnetic resonance imaging contrast agents, anemia treatment, magnetic cell sorting and magnetically mediated hyperthermia (MMH). In this work, dextran coated iron oxide nanoparticles were developed and functionalized with peptides to target the nanoparticles to either the extracellular matrix (ECM) of tumor tissue or to localize the nanoparticles in subcellular regions after cell uptake.

The magnetic nanoparticles were utilized for a variety of applications. First, heating properties of the nanoparticles were utilized to administer hyperthermia treatments combined with chemotherapy. The nanoparticles were functionalized with peptides to target fibrinogen in the ECM and extensively characterized for their physicochemical properties, and MMH combined with chemotherapy was able to enhance the toxicity of chemotherapy.

The second application of the nanoparticles was magnetically mediated energy delivery. This treatment does not result in a bulk temperature rise upon actuation of the nanoparticles by an alternating magnetic field (AMF) but rather results in intracellular damage via friction from Brownian rotation or nanoscale heating effects from Néel relaxations. The nanoparticles were functionalized with a cell penetrating peptide to facilitate cell uptake and lysosomal escape. The intracellular effects of the internalized nanoparticles alone and with activation by an AMF were evaluated.

Iron concentrations *in vivo* are highly regulated as excess iron can catalyze the formation of the hydroxyl radical through Fenton chemistry. Although often a concern of using iron oxide nanoparticles for therapeutic applications, these inherent toxicities were harnessed and utilized to enhance radiation therapy. Therefore, the third application of magnetic nanoparticles was their ability to catalyze reactive oxygen species formation and increase efficacy of radiation. Overall, iron oxide nanoparticles have a variety of cancer therapy applications and are a promising class of materials for increasing efficacy and reducing the side effects of conventional cancer treatments.

KEYWORDS: iron oxide nanoparticles, peptides, magnetically mediated hyperthermia, magnetically mediated energy delivery, reactive oxygen species

Anastasia Kruse Hauser  
Student's Signature

March 23, 2016  
Date

PEPTIDE-FUNCTIONALIZED MAGNETIC NANOPARTICLES FOR CANCER  
THERAPY APPLICATIONS

By

Anastasia Kruse Hauser

Dr. J. Zach Hilt

Co-Director of Dissertation

Dr. Kimberly W Anderson

Co-Director of Dissertation

Dr. Thomas Dziubla

Director of Graduate Studies

---

## ACKNOWLEDGEMENTS

There are several people who have made this dissertation possible through their support and encouragement during my time at the University of Kentucky. First, I would like to sincerely thank my advisors, Dr. J. Zach Hilt and Dr. Kimberly W. Anderson. Their guidance throughout this process has proved invaluable and I would not be where I am today without them. A huge thank you to Dr. Hilt for reaching out and inviting me to participate in undergraduate research and to Dr. Anderson for suggesting I apply to the REU program. Without that undergraduate research experience I would have not considered graduate school. During my time working with both Dr. Hilt and Dr. Anderson, I have learned the importance of character, integrity, and professionalism as well as how to be an effective mentor.

I would also like to thank Dr. Thomas Dziubla, a committee member and mentor, for his help troubleshooting and brainstorming new ideas. Additionally, I would like to thank him for the support he has given the Materials and Chemical Engineering (MACE) Graduate Student Association. Dr. Ronald McGarry has also played a vital role in my dissertation and graduate education. I am grateful for the time he has been able to spare from the clinic to provide a unique perspective to this project. Dr. Bradley Anderson, the outside examiner, has also had a large influence on my education at UK, both during my undergraduate studies in the Biopharmaceutical track and in graduate school through the Cancer and Nanotechnology Training Center (CNTC). Dr. Anderson has always pushed me to be a better scientist and I greatly appreciate all of his advice over the years.

This research has been funded and supported by several agencies and grants, and without this funding the work presented here would not have been possible. These include the National Science Foundation Graduate Research Fellowship Program, National Science Foundation Integrative Graduate Education and Research Traineeship, and the National Institute of Health Cancer and

Nanotechnology Training Center. The P.E.O. Scholar Award, while not directly funding the research, helped provide financial support during my graduate education.

I would like to extend a thank you to all of my fellow graduate students, past and present: Dr. Samantha Meenach, Dr. Nathanael Stocke, Dr. Daniel Schlipf, Dr. Andrew Lakes, Kaitlyn Wooten, Jacob Lilly, Jennifer Fischer, Rachel Essex, Angela Gutierrez, Shuo Tang, Trang Ma, and Dr. Rohit Bhandari. Specifically, I would like to thank Dr. Robert Wydra for all of his help and for being a great mentor during my undergraduate research experience. And to Carolyn Jordan, thanks for always being up for coffee breaks and willing to listen. I have also had the pleasure of working with several exceptional undergraduates: Kendall (Huddleston) Murphy, Michelle Pressley, Alex Tsoras, Sarah Patterson, Jonathan Coburn, Ronita Mathias, and Emily Daley. Mentoring undergraduates was one of my favorite parts of graduate school and I thank you for all of your hard work!

Lastly, I would like to thank my family and friends for their love and encouragement. Thank you to one of my best friends, Tess Simon, for forcing me to eat a “real meal” once a week and for always being there to listen and give advice. A very special thank you to my parents for always believing in me and instilling in me the importance of faith and family. Even though I will not be what you consider to be a “real doctor”, I hope to contribute to making the world a better place for your grandchildren. Thank you to my brother, John, and sister, Alyssa, for always being able to make me laugh (even if it’s at my own expense). Most importantly, I would like to thank my husband, Paul, for his continual love and encouragement, even while living 149 miles apart. Thank you for pushing me to pursue my dreams even if it made things a bit more difficult. Amidst all the technical knowledge I have gained in graduate school, I have also learned that distance truly does make the heart grow fonder.



## Table of Contents

ACKNOWLEDGEMENTS.....	iii
Table of Contents.....	v
List of Tables.....	ix
List of Figures.....	x
Chapter 1 Introduction.....	1
1.1 Objectives.....	3
Chapter 2 Active targeting strategies of iron oxide magnetic nanoparticles.....	5
2.1 Introduction.....	5
2.2 Active Targeting.....	8
2.2.1 Antibodies.....	10
2.2.2 Aptamers.....	14
2.2.3 Peptides.....	17
2.2.4 Small Molecules.....	25
2.3 Conclusions and Future Perspectives.....	31
Chapter 3 Magnetic nanoparticles and nanocomposites for remote controlled therapies.....	33
3.1 Introduction.....	33
3.2 Remote controlled energy release.....	36
3.2.1 Thermal therapy.....	36
3.2.2 Nanoscale Energy Delivery.....	42
3.3 Combination therapy.....	47
3.4 Conclusions.....	53
Chapter 4 Synthesis and characterization of CREKA-conjugated iron oxide nanoparticles for hyperthermia applications.....	55
4.0 Abstract.....	55
4.1 Introduction.....	56
4.2 Materials and Methods.....	59
4.2.1 Materials.....	59
4.2.2 Crosslinked dextran coated iron oxide nanoparticle synthesis.....	60
4.2.3 CREKA conjugation of iron oxide nanoparticles.....	60
4.2.4 Particle characterization.....	62
4.2.5 Cytotoxicity analysis of particle systems.....	64
4.2.6 CREKA and CREKA IONP binding affinity to fibrinogen clots.....	64

4.2.7 In vitro magnetically mediated hyperthermia and cisplatin combined treatment .....	65
4.2.8 Statistical analysis .....	66
4.3 Results and Discussion .....	66
4.3.1 Particle characterization .....	66
4.3.2 Remote controlled heating of iron oxide magnetic nanoparticles via AMF .....	69
4.3.3 Cytotoxicity analysis of particles .....	70
4.3.4 Fibrinogen binding affinity .....	71
4.3.5 Magnetically-mediated hyperthermia .....	72
4.4 Conclusion .....	76
Chapter 5 The effects of synthesis method on the physical and chemical properties of dextran coated iron oxide nanoparticles .....	78
5.0 Abstract .....	78
5.1 Introduction .....	79
5.2 Materials and Methods .....	83
5.2.1 Materials .....	83
5.2.2 Dextran coated iron oxide nanoparticle synthesis via two-step method .....	84
5.2.3 Dextran coated iron oxide nanoparticle synthesis via semi-two-step method .....	84
5.2.4 Dextran coated iron oxide nanoparticle synthesis via simultaneous semi-two-step method .....	85
5.2.5 Dextran coated iron oxide nanoparticle synthesis via one-step method .....	85
5.2.6 Epichlorohydrin crosslinking of dextran coated iron oxide nanoparticles .....	85
5.2.7 Particle characterization .....	86
5.3 Results and Discussion .....	88
5.4 Conclusions .....	99
Chapter 6 Peptide conjugated magnetic nanoparticles for magnetically mediated energy delivery .....	101
6.0 Abstract .....	101
6.1 Introduction .....	102
6.2 Materials and Methods .....	107
6.2.1 Materials .....	107
6.2.2 Synthesis of uncoated iron oxide nanoparticles .....	107
6.2.3 Synthesis of dextran coated iron oxide nanoparticles (Fe <sub>3</sub> O <sub>4</sub> + Dx) .....	108
6.2.4 Epichlorohydrin (ECH) crosslinking of dextran coated iron oxide nanoparticles (Fe <sub>3</sub> O <sub>4</sub> + Dx-ECH) .....	108
6.2.5 Amine functionalization of crosslinked dextran coated iron oxide nanoparticles (Fe <sub>3</sub> O <sub>4</sub> + Dx-ECH-Amine) .....	108

6.2.6 TAT peptide conjugation to iron oxide nanoparticles ( $\text{Fe}_3\text{O}_4 + \text{TAT}$ ).....	109
6.2.7 Iron concentration assay .....	109
6.2.8 Iron oxide nanoparticle characterization.....	109
6.2.9 Cell Culture.....	110
6.2.10 Iron oxide nanoparticle uptake.....	110
6.2.11 Reactive Oxygen Species (ROS) Generation.....	111
6.2.12 Acridine orange lysosomal permeabilization experiments .....	111
6.2.13 Mitochondrial membrane depolarization studies (JC-1).....	112
6.2.14 Caspase 3/7 apoptosis studies .....	112
6.2.15 Viability studies .....	112
6.3 Results and Discussion .....	113
6.3.1 Iron oxide nanoparticle characterization.....	113
6.3.2 Cellular uptake of iron oxide nanoparticles .....	116
6.3.3 Intracellular reactive oxygen species formation .....	117
6.4 Conclusions.....	125
Chapter 7 Targeted iron oxide nanoparticles for the enhancement of radiation therapy .....	127
7.0 Abstract.....	127
7.1 Introduction.....	128
7.2 Materials and Methods.....	133
7.2.1 Materials .....	133
7.2.2 Synthesis of uncoated iron oxide nanoparticles (uncoated $\text{Fe}_3\text{O}_4$ ).....	133
7.2.3 Synthesis of dextran coated iron oxide nanoparticles ( $\text{Fe}_3\text{O}_4 + \text{Dx}$ ) .....	134
7.2.4 Epichlorohydrin (ECH) crosslinking of dextran coated iron oxide nanoparticles ( $\text{Fe}_3\text{O}_4 + \text{Dx-ECH}$ ).....	134
7.2.5 Amine functionalization of crosslinked dextran coated iron oxide nanoparticles ( $\text{Fe}_3\text{O}_4 + \text{Dx-ECH-Amine}$ ).....	134
7.2.6 TAT peptide conjugation to iron oxide nanoparticles ( $\text{Fe}_3\text{O}_4 + \text{TAT}$ ).....	135
7.2.7 Iron Concentration Assay.....	135
7.2.8 Cell Culture.....	135
7.2.9 Transmission electron microscopy.....	135
7.2.10 Acridine orange lysosomal permeabilization experiments .....	136
7.2.11 Mitochondrial stress test .....	136
7.2.12 Reactive Oxygen Species (ROS) Generation.....	138
7.2.13 Viability studies .....	138
7.3 Results and Discussion .....	138

7.4 Conclusions.....	149
Chapter 8 Conclusions .....	151
8.1 Significant Findings .....	152
Appendix A Combination treatment of multi-cellular tumor spheroids .....	154
A. 1 Introduction.....	154
A.2 Materials and Methods.....	158
A.2.1 Materials.....	158
A.2.2 Cell culture .....	159
A.2.3 MCTS formation .....	159
A.2.4 MCTS dissociation.....	160
A.2.5 Acid phosphatase assay.....	160
A.2.6 Resazurin assay .....	160
A.2.7 Calcein AM/Ethidium homodimer-1 (live/dead) assay .....	161
A.2.8 Assay validation studies.....	161
A.2.9 Incubator-induced hyperthermia with CDDP .....	162
A.2.10 Incubator induced hyperthermia with radiation .....	163
A.3 Results and discussion .....	163
A.3.1 MCTS assay validation .....	163
A.3.2 Cisplatin combined with hyperthermia on MCTS .....	168
A.3.3 Radiation combined with hyperthermia on MCTS .....	169
A.4 Conclusions.....	173
References.....	175
Vita.....	202

## List of Tables

Table 4.1 Nanoparticle systems synthesized and characterized, their size as analyzed via DLS, and SAR values from AMF heating. Size of Fe <sub>3</sub> O <sub>4</sub> +Dx-ECH-Amine-CREKA via DLS could not be completed due to the fluorescent tag but minimal difference from the other systems is expected. ....	67
Table 4.2 Bound-to-free fluorescence for each system to fibrin clots represented by average ± standard error (n = 4). The * indicates a significant difference from the FITC-IONP bound-to-free fluorescence ratio (p<0.05). ....	72
Table 4.3 Magnetically mediated hyperthermia treatments and controls. ....	73
Table 5.1 Size analysis via dynamic light scattering of iron oxide nanoparticles synthesized by the various methods represented by average ± standard deviation (three independent batches and three samples from each batch).....	89
Table 5.2 Dextran weight percentage via thermogravimetric analysis of iron oxide nanoparticles synthesized by the various methods (n=3).....	91
Table 5.3 Iron oxide crystal size estimated using XRD spectra and the Scherrer equation and TEM images of iron oxide nanoparticles synthesized by the various methods (mean ± st. dev. n=3 for XRD and n=150 for TEM).....	97
Table 5.4 Specific absorption rates (W/g) of iron oxide nanoparticles (3 mg/mL Fe <sub>3</sub> O <sub>4</sub> ) heating in an alternating magnetic field (58 kA/m, 292 kHz) of iron oxide nanoparticles synthesized by the various methods (n=3). ....	99
Table 6.1. Iron oxide nanoparticle size from dynamic light scattering in DI water and cell culture media and zeta potential represented as average ± standard deviation (n=3). ....	115
Table 7.1 Equations developed by Babincova et al. for analysis of combinational treatments. ...	148
Table 7.2 Calculations to analyze the effects of combined Fe <sub>3</sub> O <sub>4</sub> + TAT nanoparticles and radiation treatments. Values represent viability average ± standard error (n=12) on days 3, 5 and 7 post treatment. * (p<0.05) and ** (p<0.01) indicate a significant difference from the [Fe <sub>3</sub> O <sub>4</sub> + TAT]x[Radiation]/100 group on the same day. ....	149

## List of Figures

Figure 2.1 Targeting methods for magnetic nanoparticles include A) passive targeting and B) active targeting. Active targeting includes targeting the i) extracellular matrix, ii) cell surface receptors and/or iii) utilizing cell penetrating peptides to target specific intracellular organelles. ....	7
Figure 3.1 This section highlights the uses of MNPs for controlled release therapies. A) Thermal therapy can be remotely controlled for i) local applications or ii) nanoscale heating applications. B) Thermal therapy is often administered in combination with a secondary treatment such as i) a therapeutic or ii) radiation.....	36
Figure 4.1 Iron oxide nanoparticle synthesis process for the (a) dextran coating, (b) epichlorohydrin crosslinking, (c) amine conjugation, and (d) conjugation with an AMAS linker, connecting the FAM-labeled CREKA to the primary amine. ....	62
Figure 4.2 TEM images of (a) dextran coated iron oxide nanoparticles ( $\text{Fe}_3\text{O}_4+\text{Dx}$ ) and (b) dextran-epichlorohydrin crosslinked iron oxide nanoparticles ( $\text{Fe}_3\text{O}_4+\text{Dx-ECH}$ ). ....	66
Figure 4.3 Normalized absorbance (at 540 nm) of the iron oxide nanoparticle systems in (a) PBS and (b) DMEM with 10% v/v FBS over 12 hours using UV-visible spectroscopy. ....	68
Figure 4.4 Normalized mass loss of each nanoparticle system in the synthesis process via TGA. ....	69
Figure 4.5 Heating profiles of each nanoparticle system in the synthesis process (5 mg/mL $\text{Fe}_3\text{O}_4$ ) in the presence of an alternating magnetic field at 58 kA/m and 292 kHz (n = 3). The gray box indicates the target hyperthermia range. ....	70
Figure 4.6 Normalized viability of each nanoparticle system in the synthesis process on A549 lung cancer cells after (a) 24 hours of exposure and (b) 48 hours of exposure. Error bars represent standard error (n = 4) and * indicates a significant difference (p < 0.05) using a 1-way ANOVA test. ....	71
Figure 4.7 Relative viability of A549 lung cancer cells 48 hours post magnetically mediated hyperthermia treatment. Error bars represent standard error (n = 12) and ** indicates a significant difference (p < 0.01). Representative images of A549 cells stained with calcein AM after 48 hours for: (a) Control, (b) IONP, (c)MMH, (d) CDDP, (e) CDDP+IONP, and (f) CDDP+MMH. ....	75
Figure 4.8 Relative viability of A549 lung cancer cells 72 hours post magnetically mediated hyperthermia treatment. Error bars represent standard error with n = 12 and ** indicates a significant difference (p < 0.01). Representative images of A549 cells stained with calcein AM after 72 hours for: (a) Control, (b) IONP, (c) MMH, (d) CDDP, (e) CDDP+IONP, and (f) CDDP+MMH. ....	76
Figure 5.1 Schematic of iron oxide nanoparticle synthesis methods. The co-precipitation reaction for each of the methods is completed at 85 °C for one hour after the addition of the reducing agent (ammonium hydroxide). ....	83
Figure 5.2 FTIR spectra of dextran coated iron oxide nanoparticles synthesized by the various methods. ....	91
Figure 5.3 Mass loss and d%/dT with increasing temperature of dextran coated and epichlorohydrin crosslinked iron oxide nanoparticles synthesized via the (a) two-step method, (b) semi-two-step method, (c) simultaneous semi-two-step method, (d) one-step method with 5 grams dextran, and (e) one-step method with 1 gram dextran. ....	92

Figure 5.4 Stability of dextran coated and epichlorohydrin crosslinked iron oxide nanoparticles synthesized via the (a) two-step method, (b) semi-two-step method, (c) simultaneous semi-two-step method, (d) one-step method with 5 grams dextran, and (e) one-step method with 1 gram dextran in PBS over 12 hours analyzed by UV-visible spectroscopy ( $\lambda=540$ ).....	93
Figure 5.5 XRD patters of dextran coated iron oxide nanoparticles synthesized via the (a) two-step method, (b) semi-two-step method, (c) simultaneous semi-two-step method, (d) one-step method with 5 grams dextran, (e) one-step method with 1 gram dextran and (f) dextran only.....	96
Figure 5.6 TEM images of dextran coated iron oxide nanoparticles synthesized via the (a) two-step method, (b) semi-two-step method, (c) simultaneous semi-two-step method, (d) one-step method with 5 grams dextran, and (e) one-step method with 1 gram dextran.....	97
Figure 6.1 TAT-conjugated iron oxide nanoparticles are internalized by cancer cells and permeabilize endosomal/lysosomal membranes due to the positive charge of the peptide. Upon exposure to an AMF, the nanoparticles generate the hydroxyl radical via Fenton chemistry, friction from Brownian rotaion and nanoscale heat effects by Neél relaxation.....	106
Figure 6.2. Iron oxide nanoparticle synthesis and functionalization of the TAT peptide.....	115
Figure 6.3 Nanoparticle characterization. a. FTIR spectra of amine functionalized and TAT conjugated iron oxide nanoparticles. b. TEM images of dextran coated iron oxide nanoparticles to confirm Fe <sub>3</sub> O <sub>4</sub> crystalline structure. c. X-ray diffraction pattern of dextran coated iron oxide nanoparticles.....	116
Figure 6.4 Uptake of Fe <sub>3</sub> O <sub>4</sub> nanoparticles into a.) A549 and b.) H358 lung cancer cells. Error bars represent standard error (n=3) and significant differences are indicated by * (p<0.05) and ** (p<0.01) via a one-way ANOVA.....	117
Figure 6.5 Normalized carboxy-DCF fluorescence of a.) A549 and b.) H358 lung cancer cells after treatment with Fe <sub>3</sub> O <sub>4</sub> nanoparticles with and without 30 minutes or 1 hour AMF exposure. Error bars represent standard error (n=3) and significant difference is indicated by * (p<0.05) via a two-way ANOVA.....	119
Figure 6.6 Average fluorescence of A549 and H358 cells after 2 hours of exposure to 50 $\mu$ M carboxy-DCF. Error bars represent standard error (n=5) and * indicates a significant difference (p<0.05) via a t-test.....	120
Figure 6.7 Relative acridine orange (AO) fluorescence of a.) A549 and b.) H358 lung cancer cells after treatment with Fe <sub>3</sub> O <sub>4</sub> nanoparticles with and without 1 hour AMF exposure. Error bars represent standard error (n=3) and significant difference from the control is indicated by * (p<0.05) via a two-way ANOVA.....	121
Figure 6.8 Percentage of a.) A549 and b.) H358 cells with depolarized mitochondrial membranes as indicated by a decrease in the ratio between FL3/FL1 (JC1 ratio). Error bars represent standard error (n=3) and * indicates a significant difference (p<0.05) compared to the control as determined via a two-way ANOVA.....	122
Figure 6.9 Percentage apoptosis of a.) A549 and b.) H358 lung cancer cells 12 and 24 hours after treatment with Fe <sub>3</sub> O <sub>4</sub> nanoparticles with and without 1 hour AMF. Error bars represent standard error (n=3) and significant difference from the control is indicated by * (p<0.05) via a two-way ANOVA.....	124

Figure 6.10 Relative viability of a.) A549 and b.) H358 lung cancer cells 48 hours after treatment with Fe<sub>3</sub>O<sub>4</sub> nanoparticles with and without 1 hour AMF. Error bars represent standard error (n=3) and significant difference from the control is indicated by \* (p<0.05) via a two-way ANOVA. 125

Figure 7.1 TAT-conjugated iron oxide nanoparticles are internalized into the cell, followed by lysosomal membrane permeabilization. This results in release of proteolytic enzymes as well as the nanoparticles into the cytoplasm where they can interact with organelles such as the nucleus and mitochondria and catalyze the formation of the hydroxyl radical. .... 132

Figure 7.2 Bioenergetic profile of control A549 cells over time. Error bars represent standard error (n=12)..... 137

Figure 7.3 Internalization of Uncoated or TAT-conjugated iron oxide nanoparticles by A549 lung carcinoma, with and without radiation treatment. Scale bars represent 200 nm..... 139

Figure 7.4 Normalized acridine orange (AO) fluorescence of A549 lung carcinoma after 2 hour treatment with Fe<sub>3</sub>O<sub>4</sub> nanoparticle systems with and without radiation. Error bars represent standard error (n=3) and \*\* indicates a significant difference from the control (p<0.01) via a two-way ANOVA. .... 141

Figure 7.5 Basal oxygen consumption rates of A549 lung carcinoma cells after Fe<sub>3</sub>O<sub>4</sub> nanoparticle treatment with and without radiation. Error bars represent standard error (n=12). \* indicates a significant difference between the no radiation and radiation treatments within a nanoparticle system (p<0.05), † indicates a significant difference compared to the control without radiation (p<0.05) and ‡ indicates a significant difference from the control with radiation (p<0.05), via a two-way ANOVA with an interaction term. .... 143

Figure 7.6 Maximal oxygen consumption rates of A549 lung carcinoma cells after Fe<sub>3</sub>O<sub>4</sub> nanoparticle treatment with and without radiation. Error bars represent standard error (n=12). \* indicates a significant difference between the no radiation and radiation treatments within a nanoparticle system (p<0.05), † indicates a significant difference compared to the control without radiation (p<0.05) and ‡ indicates a significant difference from the control with radiation (p<0.05), via a two-way ANOVA with an interaction term. .... 144

Figure 7.7 Oxygen consumption rate vs. extracellular acidification rate of A549 lung carcinoma after exposure to Fe<sub>3</sub>O<sub>4</sub> nanoparticle systems with and without radiation and FCCP stimulation. Error bars represent standard error (n=12) and \*\* indicates a significant difference in both OCR and ECAR from no-radiation Fe<sub>3</sub>O<sub>4</sub> nanoparticle. .... 145

Figure 7.8 Relative carboxy-DCF fluorescence in A549 lung carcinoma following 24 hour treatment with Fe<sub>3</sub>O<sub>4</sub> nanoparticle systems with and without 5 Gy radiation treatment. Error bars represent standard error (n=12) and \* indicates a significant difference compared to radiation alone and † indicates a significant difference compared to 500 µg/mL uncoated and 500 µg/mL amine functionalized Fe<sub>3</sub>O<sub>4</sub> nanoparticles. .... 146

Figure 7.9 Relative viability of A549 lung carcinoma 3, 5 or 7 days following a) uncoated b) Dx-ECH c) amine functionalized or d) TAT-conjugated Fe<sub>3</sub>O<sub>4</sub> nanoparticle treatment with and without 5 Gy radiation. Error bars represent standard error (n=12) and \* indicates a significant difference (p<0.05) via a one-way ANOVA..... 148



## Chapter 1 Introduction

Cancer is the second leading cause of death in the United States. Survival rates of lung cancer are especially low with the 1- and 5-year relative survival rates at 44% and 17%, respectively. These low survival rates are partially due to more than half (57%) of patients not being diagnosed until the cancer has progressed to an advanced stage. In addition, current treatments (e.g., chemotherapy and radiation) result in severe side-effects. Therefore, there is a clear need to improve current cancer therapies in order to prolong survival and reduce the toxic side-effects of treatments.

Treatment of lung cancer via hyperthermia, the heating of tissue to 42-45 °C, in conjunction with radiation and chemotherapy has resulted in synergistic effects in regard to efficacy of the conventional treatment and has the potential to decrease the prevalence of toxic side effects (Genet, Fujii et al. 2013). Current hyperthermia methods include whole body and regional hyperthermia. Whole body hyperthermia is relatively invasive and results in greater toxic side-effects than regional hyperthermia, but both have several disadvantages, including the burning of healthy tissue, limited penetration of heat into the body, under-dosage of heat, and complications such as increased heart rate and increased cardiac output (Zwischenberger, Vertrees et al. 2004, Issels 2008, Kumar and Mohammad 2011). Magnetically-mediated hyperthermia (MMH), the heating of tissue using heat generated by magnetic nanoparticles in the presence of an alternating magnetic field (AMF), shows great promise in overcoming the limitations of current hyperthermia treatments due to the ability of nanoparticles to deliver heat directly to the tumor site. Iron oxide nanoparticles are a class of magnetic nanoparticles which have been previously studied due to their inherent biocompatibility, magnetic properties, and lack of protein adsorption after proper coating (Laurent, Dutz et al. 2011). Iron oxide nanoparticles have the ability to passively and/or actively target tumors and, upon activation by an external alternating magnetic field, generate heat via multiple possible

loss mechanisms: hysteresis, Néel paramagnetic switching, and friction from Brownian rotation (Dennis, Jackson et al. 2009).

One of the main limitations to MMH is the difficulty in achieving a high magnetic nanoparticle concentration within tumor tissue following intravenous injection of the nanoparticles. Properly masking the nanoparticles with a biocompatible coating to improve stability, biocompatibility, and circulation time has been used to improved tumor concentrations via passive targeting and utilization of the enhanced permeation and retention (EPR) effect (Veiseh, Gunn et al. 2010, Wu, Wu et al. 2015). Additionally, functionalizing the nanoparticle surface with active targeting ligands has been shown to improve tumor targeting and retention of the magnetic nanoparticles (Turcheniuk, Tarasevych et al. 2013, Singh and Sahoo 2014, Hola, Markova et al. 2015).

Despite extensive research, MMH treatment has yet to make its clinical debut. A recent focus for magnetic nanoparticle research has been in magnetically mediated energy delivery (MagMED). In this approach, cells internalize magnetic nanoparticles and when exposed to an AMF, the nanoparticles locally delivery energy in the form of local heat dissipation, mechanical effects, and/or surface reactivity without a measurable temperature rise (Kozissnik, Bohorquez et al. 2013). MagMED treatment has been shown to elicit cellular responses such as lysosomal permeabilization, increased mitochondrial reactive oxygen species (ROS) generation, opening of ion channels, and apoptosis (Domenech, Marrero-Berrios et al. 2013, Sanchez, Diab et al. 2014, Connord, Clerc et al. 2015).

The main focus of magnetic nanoparticles in biomedical research has been their ability to deliver energy to increase the regional temperature in response to an AMF, but recent focus has shifted to understanding the mechanisms of MagMED toxicity, such as the generation of ROS. Iron oxide nanoparticles can catalyze the Haber-Weiss reaction through Fenton chemistry, producing the highly reactive hydroxyl radical. Cancer cells are more susceptible to oxidative insults compared to normal cells due to fast cell proliferation and metabolism so additional ROS stress

induced by exogenous agents can overwhelm the relatively low antioxidant capacity and disrupt the redox homeostasis inside cancer cells leading to selective tumor cell toxicity (Huang, Chen et al. 2013).

This dissertation provides an investigation into applications of peptide-functionalized iron oxide magnetic nanoparticles for cancer therapy. Peptides were chosen as the targeting ligands for the studies completed as part of this dissertation, and chapter 2 reviews various targeting modalities utilized to effectively target magnetic nanoparticles to tumor tissues. Chapter 3 then reviews magnetic nanoparticles for remote controlled therapies such as thermal therapy, nanoscale energy delivery, and combinational therapies.

## **1.1 Objectives**

The overall objective of this dissertation was to develop peptide-functionalized iron oxide magnetic nanoparticles for cancer therapy applications such as magnetically mediated hyperthermia, magnetically mediated energy delivery, and reactive oxygen species generation in order to enhance the efficacy of conventional cancer treatments. The overall objective was accomplished through the following four projects:

1. Synthesis and characterization of CREKA-conjugated iron oxide nanoparticles for hyperthermia treatment of cancer
2. Effect of synthesis method on the physical and chemical properties of dextran-coated iron oxide nanoparticles
3. Peptide conjugated magnetic nanoparticles for magnetically mediated energy delivery to A549 lung carcinoma and H358 bronchi alveolar
4. Peptide conjugated iron oxide nanoparticles for the enhancement of radiation therapy

Chapter 4, entitled “Synthesis and characterization of CREKA-conjugated iron oxide nanoparticles for hyperthermia treatment of cancer” presents a peptide-conjugated iron oxide magnetic nanoparticle system for targeted magnetically mediated hyperthermia treatment in

combination with chemotherapy. This chapter analyzes the physicochemical characteristics of the nanoparticle system and provides a proof-of-concept study with magnetically mediated hyperthermia and cisplatin, a common chemotherapeutic. Although iron oxide nanoparticle synthesis has been extensively studied, researchers are continually searching for methods to improve size, stability, and heating capabilities of the nanoparticles. The iron oxide nanoparticles developed in chapter 4 had optimal size and stability but low heating capabilities compared to other systems in literature. Chapter 5 entitled “Effect of synthesis method on the physical and chemical properties of dextran-coated iron oxide nanoparticles” aimed to improve the properties of dextran-coated iron oxide nanoparticles synthesized by the co-precipitation method. This chapter also solidified the process by which dextran-coated iron oxide nanoparticles are synthesized in our lab.

Chapter 6, “Peptide conjugated magnetic nanoparticles for magnetically mediated energy delivery to A549 lung carcinoma and H358 bronchi alveolar”, utilizes iron oxide nanoparticles conjugated to a cell penetrating peptide in the presence of an AMF to elicit intracellular changes through MagMED. The physicochemical properties of the nanoparticle system are characterized and a variety of assays are completed in hopes of improving our understanding of the intracellular effects of this treatment. Chapter 7, “Peptide conjugated iron oxide nanoparticles for the enhancement of radiation therapy” utilizes the iron oxide nanoparticles developed in chapter 6 to catalyze intracellular ROS generation and permeabilize lysosomal structures which sensitizes the cancer cells to subsequent radiation treatment. Finally, chapter 8 reports the conclusions of this dissertation and potential future directions for peptide-functionalized iron oxide nanoparticles.

## Chapter 2 Active targeting strategies of iron oxide magnetic nanoparticles

### 2.1 Introduction

Magnetic nanoparticles have been utilized in a variety of biological applications due to their flexible design and low toxicity, including contrast agents in magnetic resonance imaging (MRI), magnetic separation, magnetically mediated hyperthermia (MMH), and magnetically mediated energy delivery (MagMED). Although a multitude of magnetic nanoparticles exist, iron oxide is a class of magnetic nanoparticles that has received particular interest due to ease of preparation, ease of modification, and superparamagnetic properties. Maghemite ( $\text{Fe}_2\text{O}_3$ ) and magnetite ( $\text{Fe}_3\text{O}_4$ ) iron oxide crystals usually fall below the superparamagnetic size threshold of approximately 15 nm, making them the most common form of iron oxide studied for biological applications (Tucek, Zboril et al. 2006, Pankhurst, Thanh et al. 2009, Laurent, Dutz et al. 2011). In addition, iron oxide nanoparticles are biocompatible at low doses and biodegradable, which increases their potential for biological applications.

Coating of magnetic nanoparticles with a biocompatible compound is required prior to biological use. The magnetic nanoparticle coating can serve to decrease nanoparticle aggregation by suppressing particle-particle interactions, prevent degradation of the core iron oxide in biological environments, and provide functional groups for conjugation of targeting agents, drugs, or other biological compounds (Gupta and Gupta 2005). Coating the magnetic nanoparticles can also mask the nanoparticles from recognition by the immune system, prolonging circulation time and ultimately leading to increased uptake.

There are a wide variety of organic and inorganic coatings for magnetic nanoparticles that protect and stabilize the nanoparticles for biological use. There are several recent reviews that examine these coatings and their applications (Gupta, Naregalkar et al. 2007, Veisoh, Gunn et al. 2010, Xie, Liu et al. 2011, Jiang, Win et al. 2013, Jin, Lin et al. 2014, Chu, Yu et al. 2015, Wu, Wu et al. 2015). Organic coating materials include small molecules, surfactants, polymers, and

biomolecules. Magnetic nanoparticles coated with these materials are commonly used for MRI, drug targeting, and magnetic separation. Citric acid and silanes are examples of small molecules which can be used to synthesize water-soluble iron oxide nanoparticles directly (Wydra, Kruse et al. 2013) and to functionalize compounds to bare iron oxide nanoparticles. Small molecules allow the magnetic nanoparticles to retain their saturation magnetization values after coating due to the low mass fraction of the total particle (Wu, Wu et al. 2015). Polymers are a class of organic coatings that pose several advantages over small molecules such as multifunctional groups and ability to provide more colloidal stability (Pierrat, Zins et al. 2007). Several polymers, both natural and synthetic, have been studied for functionalizing magnetic nanoparticles. Dextran is widely used due to its biocompatibility and stability following crosslinking, but other polymers commonly studied include poly (ethylene glycol), chitosan, poly (D,L-lactide) (PLA), and poly (acrylic acid) (Chu, Yu et al. 2015). Biomolecules have continued to gain interest as coating materials for magnetic nanoparticles, and a variety of biomolecules have been successfully conjugated to the surface of iron oxide nanoparticles including enzymes, antibodies, proteins, and polypeptides (Glickson, Lund-Katz et al. 2009, Hajshafiei, Fatahian et al. 2014, Zaloga, Janko et al. 2014, Wu, Wu et al. 2015, Xie and Zang 2016).

Inorganic coatings can also be used to coat magnetic nanoparticles for biological applications, and these are also used for improving semiconductor efficiency and information storage. Silica is by far the most explored inorganic coating for biological magnetic nanoparticles. Silica coatings enhance nanoparticle dispersion by screening the magnetic dipolar attraction between the nanoparticles while providing protection from acidic environments (Tarn, Ashley et al. 2013). Other inorganic coatings include metals (gold, silver, copper, etc.), metal oxides, and sulfoxides.

Prolonging circulation time of magnetic nanoparticles by coating with a biocompatible agent is often insufficient to accumulate the nanoparticles at a specific tissue site. For example, researchers have taken advantage of the underdeveloped, leaky vasculature of cancer tissue to

passively target cancer tissue by the enhanced permeation and retention (EPR) effect (Bertrand, Wu et al. 2014). As nanoparticles circulate throughout the body, they passively accumulate within cancerous tissue and are retained due to the inability of the tissue to properly remove waste. While this method has been shown to increase magnetic nanoparticle concentrations within tumor tissues, the concentration is often insufficient to induce a therapeutic effect or significantly influence MRI contrast. Therefore, active targeting is regularly utilized to increase magnetic nanoparticle concentration within the tissue of interest and more specifically target the tissue based on selective recognition as shown in Figure 2.1.

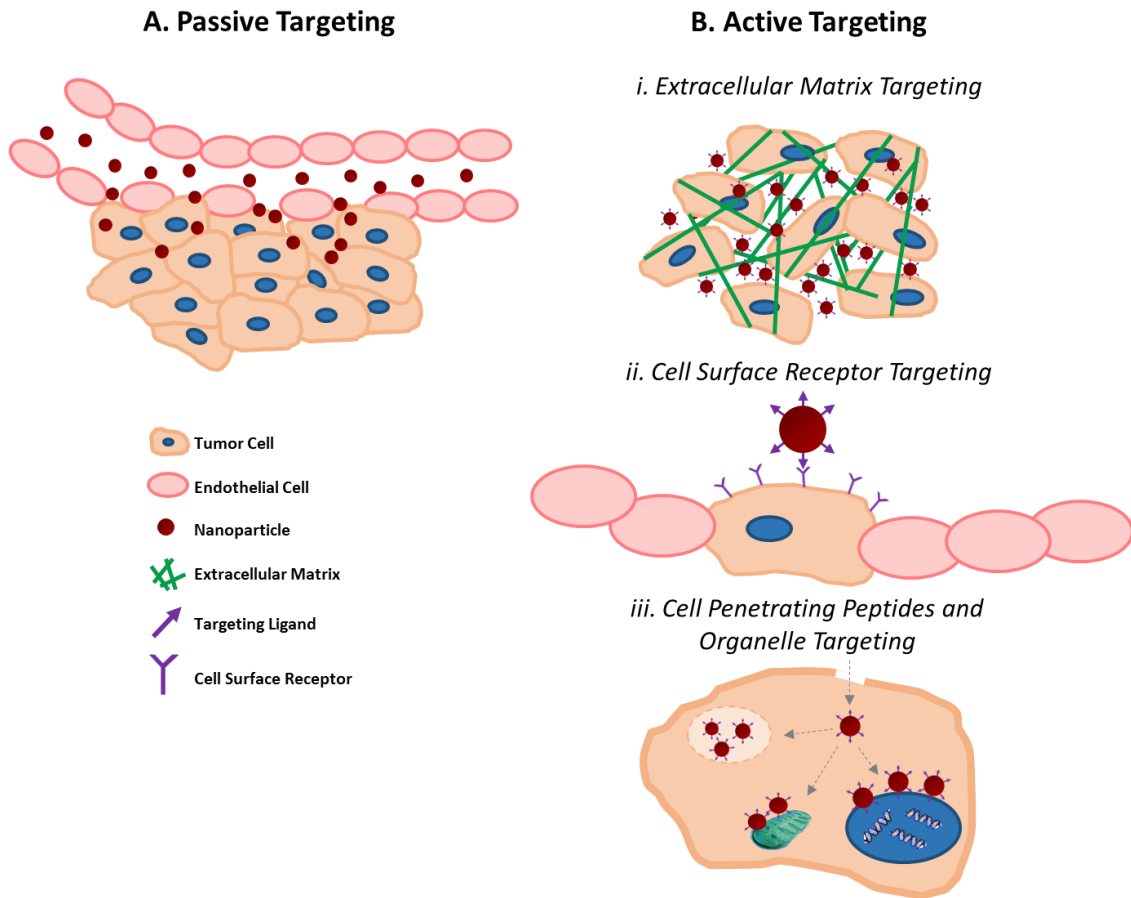


Figure 2.1 Targeting methods for magnetic nanoparticles include A) passive targeting and B) active targeting. Active targeting includes targeting the i) extracellular matrix, ii) cell surface receptors and/or iii) utilizing cell penetrating peptides to target specific intracellular organelles.

## 2.2 Active Targeting

Active targeting of magnetic nanoparticles involves functionalizing the nanoparticle surface with a specific moiety in order to direct the magnetic nanoparticle towards a specific binding site of interest. The targeting method can help detect, characterize, and treat diseases based on accumulation and aims to avoid off-target toxicities. This targeting method is often more effective than relying solely on passive accumulation. Targeting functionalities for magnetic nanoparticles include peptides, antibodies, and small molecules leading to a variety of biological targets such as cell surface receptors, enzymes, proteins, and integrins.

Although there are a variety of methods for conjugating ligands to the surface of magnetic nanoparticles, amines or carboxylic acids on the nanoparticle surface are commonly used for further functionalization. These primary functional groups are usually present on the nanoparticle surface via adsorption of polymers or small molecules (Hola, Markova et al. 2015). Amine functionalized nanoparticles are easily modified with ligands containing carboxylic acids through the use of 1-ethyl-3-(3-dimethylaminopropyl) carbodiimide (EDC) and N-hydroxosuccinimide (NHS) crosslinking. Ligands with sulfhydryl groups such as those present on peptides and antibodies can be functionalized to the surface using heterobifunctional linkers such as N-Succinimidyl 3-[2-pyridyldithio]-propionate (SPDP) or N- $\alpha$ -maleimidoacet-oxysuccinimide ester (AMAS) (McCarthy and Weissleder 2008). However, it has been suggested that EDC/NHS chemistry leads to randomly oriented antibodies on the nanoparticle surface which could result in a loss of bioactivity of the conjugated antibody. Therefore, a more sophisticated method is to react amine groups on the nanoparticle surface with heterobifunctional linkers to introduce maleimide, pyridyl disulfide or iodoacetyl groups (Gruettner, Mueller et al. 2013). A comparison of antibody binding after magnetic nanoparticle conjugation using EDC/NHS chemistry or maleimide and SPDP based reactions demonstrated advantages of the latter. The bioactivity of the antibody was 88% after



maleimide and SPDP reactions, and 35% for the EDC/NHS chemistry (Gruettner, Mueller et al. 2007).

Nanoparticles with carboxylic acid functionalized surfaces can also be modified with targeting ligands but through a more tedious reaction which requires activation of the carboxylic acids. Amine and carboxylic acid groups on the surface of nanoparticles are also interchangeable as reaction of amine groups with succinic anhydride or glutaric anhydride converts the surface to carboxylates, whereas the activation of carboxylic acid functionalized particles with EDC and NHS followed by reaction with diamine results in amine functionalized nanoparticles.

There are a wide variety of moieties used to functionalize magnetic nanoparticles for active targeting. Determining the appropriate ligand for functionalization depends upon the biological target and the ultimate goal. Smaller peptides and nucleic acid based aptamers can be engineered to have only one active molecular handle per molecule which ensures consistent linking to the nanoparticle surface and no loss of binding activity. Small organic molecules can also be engineered to assemble at high densities but may require longer linker molecules to ensure that the nanoparticle coating does not obscure the active region (Veiseh, Gunn et al. 2010). Peptides and aptamers can also be chemically synthesized and have been shown to be non-immunogenic unlike many antibodies and proteins. Relatively bulky proteins and antibodies can be difficult to assemble onto a nanoparticle surface due to lack of consistent covalent bonding orientation due to these ligands having multiple active functional groups per molecule and non-specific physical interactions between the molecule and the nanoparticle. However, due to the ease of conjugation and specificity of these molecules they continue to gain interest for nanoparticle targeting. This section provides an overview of recent advances in active targeting of magnetic nanoparticles via antibody, aptamer, peptide, and small molecule functionalization.

### 2.2.1 Antibodies

Antibodies are one of the most used biomolecules to provide specificity and bioactivity to nanoparticles due to their high specificity and large diversity. It is feasible to obtain or engineer specific antibodies against virtually any substance in high amounts so it is possible to find antibodies that recognize a large number of antigens ranging from large pathogens (viruses, bacteria, etc.) to small molecules (drugs, hormones, bacterial toxins, allergenic peptides, etc.). Antibodies have high binding affinities and retain their specificity for target molecules even in complex environments or low target concentrations (Montenegro, Grazu et al. 2013). Antibodies have continued to gain interest for their cancer targeting abilities due to cancer cells having different surface expression than healthy cells however, other applications include cell separation (Bloemen, Denis et al. 2015) and targeting of atherosclerotic plaques (Jacobin-Valat, Laroche-Traineau et al. 2015).

Anti-human epidermal growth factor receptor 2 (HER/neu) monoclonal antibodies are commonly used for breast cancer targeting as about 25% of breast cancer patients show overexpression of HER2/neu, making it a target of interest for enhancing drug delivery. There are a variety of anti-HER2 moieties that have been studied for nanoparticle targeting. Kanazaki et al. synthesized iron oxide nanoparticles conjugated to one of three anti-HER2 moieties: Trastuzumab, anti-HER single chain fragment variable (scFv) and anti-HER2 peptide (Kanazaki, Sano et al. 2015). Iron oxide nanoparticles conjugated with the anti-Her2 scFv showed higher tumor accumulation and tumor-to-background ratios than the other targeting moieties. Recently, Mu et al. functionalized PEG coated iron oxide magnetic nanoparticles with the anti-HER2/neu peptide and carboxymethylated-B-cyclodextrin to allow hydrophobic loading of paclitaxel (PTX) (Mu, Kievit et al. 2015). SK-BR-3 (HER2/neu positive) and MDA MB 231 (HER2/neu negative) cells were used for uptake studies and uptake was significantly greater in the SK-BR-3 cells indicating that uptake was dependent upon the presence of HER2/neu. Cytotoxicity results showed that the iron

oxide nanoparticle system was non-cytotoxic, and PTX treatment was nearly the same for both cell lines but the nanoparticle formulation loaded with PTX was more effective on SK-BR-3 cells. *In vivo* targeting of the nanoparticles to a SK-BR-3 xenograft tumor mouse model showed enhanced accumulation of the targeted nanoparticles compared to non-targeted. The radiant efficacy ratio (tumor/whole body) was increased by 2.5 fold in the targeted system.

Another recent study which utilized the Herceptin monoclonal antibody (Trastuzumab) was completed by Choi et al. In this study, chitosan conjugated, pluronic-based nano-carriers loaded with iron oxide nanoparticles and doxorubicin were developed (Choi, Lee et al. 2015). The Cy5.5 fluorophore was conjugated to the nanoparticle along with Herceptin monoclonal antibody. Cytotoxicity of the multifunctional nanoparticles was greater than DOX alone when tested on SK-BR-3 cells likely due to the Herceptin antibody. Tumor bearing mice were established by subcutaneous inoculation of SK-BR-3 cells into the right rear flank. After injection of the targeted or non-targeted nanoparticle systems, the fluorescence intensity was monitored over time. Accumulation at the tumor site of the targeted multifunctional NPs increased up to 24 hours post injection and although the non-targeted system still accumulated at the tumor site, there was significantly greater fluorescence in the mice receiving the targeted system compared to the non-targeted. Tumor growth suppression was monitored, and as expected, the targeted multifunctional nanoparticles (day 20: 885 mm<sup>3</sup>) showed a stronger tumor suppression than the non-targeted nanoparticles (day 20: 1314 mm<sup>3</sup>), DOX alone (day 20: 2873 mm<sup>3</sup>), or saline (day 20: 3340 mm<sup>3</sup>). Animal weight was monitored during the experiment to confirm the absence of additional toxicities due to the nanoparticle treatment.

Another common target in breast cancer cells is MUC1. Shanehsazzadeh et al. developed dextran crosslinked iron oxide nanoparticles that were conjugated with C595 monoclonal antibody to target MUC1 (Shanehsazzadeh, Gruettner et al. 2015). Uptake of the targeted nanoparticles into MUC1 positive cells was more than 9 times higher than the uptake into MUC1 negative cells. *In*

*in vitro* MRI signal enhancements in MDA MB 231 and MCF 7 were -75 and -70%, respectively, indicating that nanoparticle systems uptake was sufficient to enhance contrast in MR imaging in both cell lines.

The varying expressions of protein, ligands, and receptors on cancer cell surfaces are what allows for selective targeting of nanoparticles. Prostate specific membrane antigen (PSMA) is expressed at high levels in prostate cancer cells but minimally in healthy tissue, allowing for selective targeting. PSMA contains a unique sequence which mediates internalization and endosomal recycling, leading to high intracellular retention. The J591 antibody has high specificity for PSMA and was selected by Tse et al. for conjugation to iron oxide nanoparticles to enhance MRI contrast of preclinical prostate cancer (Tse, Cowin et al. 2015). Conjugation of J591 to the iron oxide nanoparticles did not affect its binding ability to PSMA but rather increased the iron concentration in cells positive for PSMA compared to cells lacking PSMA expression. In an *in vivo* study with orthotopic LNCaP-luc tumor bearing mice, intravenous injection of the J591-conjugated iron oxide nanoparticles led to significant reduction in MRI intensity compared to non-targeted nanoparticles. Prussian blue staining also indicated significant accumulation of iron within the tumor when the mice were treated with the targeted nanoparticles.

Epidermal growth factor receptor (EGFR) is commonly expressed on glioblastoma (GBM) and is the target for the recombinant monoclonal antibody cetuximab. Cetuximab is a 152 kDa chimeric monoclonal antibody which binds to the extracellular domain of the human EGFR, and has been used to treat GBM. Kaluzova et al. conjugated cetuximab to amphiphilic triblock copolymer coated iron oxide nanoparticles in order to investigate the therapeutic targeting effect of the cetuximab-iron oxide nanoparticles against EGFR and EGFRvIII expressing GBM stem-like cells, as these cells are responsible for tumor initiation, progression, and re-growth after chemoradiation (Kaluzova, Bouras et al. 2015). GBM neurospheres were utilized for testing the nanoparticle system as neurospheres are pathologically relevant models that maintain genomic changes of the primary

tumor, exhibit stem-like properties, and display the invasive characteristics of GBM. Cetuximab-iron oxide nanoparticles significantly decreased cell survival in all neurospheres tested, especially after 72 hours of treatment. Cetuximab alone had a modest effect and due to non-specific uptake of free iron oxide nanoparticles, viability of N08-74 neurospheres was also compromised, but less effectively. Mice were implanted with GBM neurospheres and the mice which received the cetuximab-iron oxide nanoparticles lived significantly longer (164 days) compared to the control (146 days) or the cetuximab only (147 days) groups. In follow-up work, a similar cetuximab conjugated iron oxide nanoparticle system was used in combination with fractional radiotherapy to increase the radiosensitivity of glioblastoma in a rodent model (Bouras, Kaluzova et al. 2015). Primary *in vitro* work found that exposure of human GBM cells to cetuximab-iron oxide nanoparticles for 24 hours followed by fractionated radiation resulted in a significant decrease in GBM survival compared to control cells with radiation, cetuximab with radiation, or iron oxide nanoparticles with radiation. Elevated levels of cleaved caspase 3 and apoptosis were found in the cetuximab-iron oxide nanoparticle and radiation combined treatment as well. *In vivo* studies were completed with athymic mice inoculated with GBM cells. Mice were treated with cetuximab-iron oxide nanoparticles, cetuximab or PBS followed by fractionated radiation and the median survival for the three groups was 60, 24, and 15 days, respectively, indicating that the tumor cells were sensitized to subsequent radiation treatment by the cetuximab-iron oxide nanoparticles.

Another growth factor which is of particular interest for targeting cancer is the vascular endothelial growth factor (VEGF). Many tumor types have extensive areas of hypoxia and necrosis leading to up-regulation of angiogenesis which includes secretion of pro-angiogenic factors such as VEGF, making VEGF a promising target for tumor tissue. Abakumov et al. synthesized bovine serum albumin (BSA) coated iron oxide nanoparticles that were further functionalized with the monoclonal antibody against VEGF (mAb VEGF) (Abakumov, Nukolova et al. 2015). *In vitro* targeting of the nanoparticles to their receptor was evaluated on C6 glioma cells expressing

membrane bound VEGF. The immunofluorescence assay suggested that the targeted nanoparticles bound to glioma C6 cells but negative control IgG conjugated nanoparticles did not. Confocal imaging showed that the nanoparticles were located within lysosomes following cell uptake. *In vivo* MRI was completed on rats bearing glioma C6 tumors but there was no difference between the MR image contrast in rats receiving IgG functionalized or mAb VEGF functionalized nanoparticles five minutes and two hours following IV injection. However, after 24 hours, there was significant contrast in the targeted group compared to the control indicating that the residence time of the nanoparticles at the tumor is increased by functionalizing with mAb VEGF.

### 2.2.2 Aptamers

Aptamers are single stranded oligonucleotides, DNA or RNA, with the ability to bind with high affinity and specificity to a broad range of targets such as peptides, proteins, drugs, organic and inorganic molecules, or even whole cells and viruses based on their specific binding pockets or the target molecule (Delaviz, Gill et al. 2015). Aptamer-based nanoparticle formulations have merits comparable to those of natural receptors such as antibodies and enzymes. Aptamers have the ability to be amplified by polymerase chain reaction, they are flexible yet fold into well-defined 3D structures upon binding to the target, and they can be easily modified or labeled with dyes or functional groups (Kim, Raston et al. 2016). Although aptamer technology is still in its infancy compared to that for antibodies, interest and applications continue to grow. While aptamers are used for nanoparticle targeting to specific tissues for imaging or theranostic applications, recent advances in aptamer targeting have focused on detection and separation of target molecules (Ilkhani, Sarparast et al. 2015, Zhang, Ma et al. 2015, Sun, Lu et al. 2016, Wang, Qian et al. 2016). The opportunity for magnetic separation of a target molecule is afforded by attaching aptamers to magnetic nanoparticles. For example, Delaviz et al. developed a method for selectively capturing hepatitis C virus (HCV) particles from human plasma samples using aptamer-conjugated magnetic nanoparticles (Delaviz, Gill et al. 2015). The aptamer used was specific for binding to E1E2

glycoprotein of HCV. *In vitro* results indicated that after exposure to the aptamer functionalized magnetic nanoparticles, the viral load in a solution was significantly reduced. At the highest concentration of aptamer-conjugated magnetic nanoparticles used, viral particle removal was more than 91%. A similar concept was utilized by Xi et al. who tethered selected aptamers against the hepatitis B surface antigen (HBsAg) to the surface of carboxylated magnetic nanoparticles (Xi, Huang et al. 2015). After binding of HBsAg to the nanoparticles, they were magnetically decanted and treated with a primary and secondary antibody system which catalyzed the chemiluminescence of AMPPD, allowing for quantification of the HBsAg concentration. The nanoparticle system resulted in a linear relationship between concentration of HBsAg and chemiluminescence intensity in the range of 0.1-200 ng/mL using aptamer H01. The detection limit of 0.1 ng/mL was below the detection limit of the ELISA assay used in the hospital and this technique is more time efficient than ELISA assays.

Another unique detection method developed by Hu et al. utilized a simple optical aptasensor based on gold nanoparticles and magnetic beads for the detection of AGR2 proteins (Hu, Li et al. 2015). The system is a sandwich-type, where the magnetic beads are functionalized with the anti-AGR2 aptamer and the gold nanoparticles are functionalized with the partially complementary DNA probe of the aptamer. As the concentration of AGR2 increased in solution, the sandwich structure disassembled so the magnetic beads bound to the proteins and the gold nanoparticles remained in suspension. After separation of the magnetic beads containing the AGR2, the gold nanoparticles were detected by a spectrometer to determine the concentration. Analyses of spiked human serum samples for AGR2 protein concentration revealed a recovery range of 93.5-103.8%.

An interesting proof of concept study was completed by Park et al. for the optical detection of *Salmonella Typhimurium* (Park, Jeong et al. 2015). Magnetic nanoparticles were functionalized with aptamers that specifically interact with outer membrane proteins on the surface of *Salmonella Typhimurium*. The surface reactivity of the magnetic nanoparticles is reduced via DNA-mediated

shielding of catalytic activity. In the presence of hydrogen peroxide, uncoated magnetic nanoparticles promote the oxidation of 3,3',5,5'-tetramethylbenzidine (TMB) (a colorimetric substrate) by peroxidase-like activity. The blue-colored product can be detected by the naked eye. In the presence of *Salmonella Typhimurium* the aptamers detach from the nanoparticle surface and the nanoparticles can react with the hydrogen peroxide and TMB to generate a blue-colored substrate. However, this reaction is limited when the aptamers remain attached to the nanoparticle due to lack of *Salmonella Typhimurium*. This study showed a decrease in colorimetric absorbance of TMB following DNA (aptamer) attachment to the nanoparticles and then an increase in colorimetric absorbance when *Salmonella Typhimurium* was added, causing the aptamers to detach and expose the nanoparticles.

As previously mentioned, aptamers have also been conjugated to magnetic nanoparticles for imaging and targeted drug delivery applications as they are cheaper than antibodies yet have similar binding affinities. Meng et al. developed a multifunctional nanoprobe for contrast enhanced bimodal cellular imaging and targeted therapy (Meng, Lu et al. 2015). This mesoporous silica nanoparticle based system was loaded with doxorubicin and chlorin e<sub>6</sub> and coated with MnO<sub>2</sub> sheets and aptamer sgc8 for targeting PTK7 expressing cells. In the binding and cell uptake studies, there was a significant increase in fluorescence of CEM (positive) cells compared to Ramos (negative) cells after treatment with the nanoprobe. A control aptamer sequence was also tested as a targeting modality and in both cell lines a weak signal was observed. A second recent study that utilized aptamer targeted nanoparticles for drug delivery was completed by Roy et al. The anticancer bio-drug bovine lactoferrin (bLf) was conjugated to iron oxide nanoparticles encapsulated with chitosan coated calcium phosphate (Roy, Kanwar et al. 2015). The nanoparticles were targeted with the locked nucleic acid (LNA) modified aptamer against the epithelial cell adhesion molecule (EpCAM) and nucleolin molecules. The nanoformulation was fed orally to mice injected with triple positive (EpCAM, CD133, CD44) sorted colon cancer stem cells in a xenograft cancer stem cell



mouse model. Complete regression of the tumor was observed in 70% of mice fed the non-targeted nanocomposites, with 30% of the mice showing recurrence after 30 days. Only 10% of the mice fed the targeted system showed tumor recurrence indicating a higher survival rate after treatment with the targeted nanoparticles.

### *2.2.3 Peptides*

Peptides are short, single strand amino acid sequences that target receptors on cell surfaces or components of the extracellular matrix of tissues. Peptides can often rival the binding affinity of much larger molecules such as antibodies, but due to their smaller size, multiple peptides can be functionalized to the surface of a single nanoparticle resulting in nanoparticles that contain multiple binding sites. A variety of peptides have been synthesized for specific biological targets, and this section reviews the most recent advances in peptide conjugated magnetic nanoparticles.

#### *2.2.3.1 Targeting the extracellular matrix*

CREKA is a linear, five amino acid peptide, which was found to bind to fibrin(ogen) complexes within the extracellular matrix of tumors. Fibrin(ogen) is upregulated within the ECM of tumor tissue compared to healthy tissue, making it a potential target for nanoparticle accumulation. In 2010, Agemy et al. developed a self-amplifying nanoparticle delivery system by conjugating CREKA to the surface of iron oxide nanoworms through a Michael addition reaction between the thiol on the cysteine in the peptide sequence and the maleimide on the functionalized nanoparticles (Agemy, Sugahara et al. 2010). CREKA nanoworms accumulated in the vessels of orthotopic 22Rv1 human prostate cancer xenograft tumors and caused clotting in them, as evidenced by the presence of fibrin(ogen)-containing deposits in the vessel lumens. After methylation of the CREKA peptide to increase stability, a 70% reduction in blood flow to the tumor was observed as well as a strong reduction in tumor size and extended survival of the animals. Based upon this CREKA-conjugated nanoworm system, Kruse et al. developed CREKA-conjugated iron oxide nanoparticles for magnetically mediated hyperthermia treatment of lung cancer (see Chapter 4) (Kruse, Meenach

et al. 2014). CREKA conjugated iron oxide nanoparticles bound to fibrin clots to a greater extent than non-functionalized nanoparticles and had sufficient heating capabilities to induce hyperthermia conditions upon exposure to an alternating magnetic field (AMF) (292 kHz, 56 kA/m). A combination proof of concept study was then completed to prove that magnetically mediated hyperthermia can increase the efficacy of a common chemotherapeutic, cisplatin, in A549 lung carcinoma.

The CREKA peptide has also been used to target fibrin(ogen) complexes in adhered blood clots, or thrombi. Song et al. developed a similar CREKA-conjugated iron oxide nanoparticle system, which was also conjugated with fluorescein, as a multimodal imaging agent of microthrombi (Song, Huang et al. 2014). The CREKA functionalized nanoparticles tested *in vitro* were shown to bind to fibrin clots to a greater extent than non-targeted nanoparticles. Microthrombus was induced in microcirculation of a rat model with acute myocardial ischemia reperfusion. CREKA-conjugated iron oxide nanoparticles were found to preferentially accumulate within microthrombi and generated a 1.95 fold greater fluorescence ratio as compared to the non-targeted nanoparticles. CREKA-conjugated iron oxide nanoparticles also resulted in signal loss on MR T2 images *in vivo* whereas no significant change resulted after PBS or non-targeted nanoparticle treatment.

#### 2.2.3.2 Targeting cell surface ligands

Other peptides have been developed to target specific cell surface ligands that are overexpressed on cancer cells but have low or no expression on healthy cells. Chlorotoxin (CTX) is a tumor targeting peptide that has been shown to preferentially bind to a variety of cancer cells such as prostate, intestinal, sarcomas, and glioblastoma by binding to metalloproteinase-2 (MMP2) on the cell surface. Previous work by the Zhang group with chlorotoxin for magnetic nanoparticle targeting for MRI (Sun, Du et al. 2010) and siRNA delivery (Veiseh, Kievit et al. 2010) led to the development of their multifunctional nanocomposite system (Stephen, Kievit et al. 2014). This

multifunctional nanocomposite was developed to deliver O<sup>6</sup>-benzylguanine (BG) glioblastoma multiforme (GBM). BG, an inhibitor of DNA repair by serving as a pseudo-substrate for DNA methyltransferase (MGMT), irreversibly inactivates the DNA repair protein. Therefore, when BG is combined with a DNA methylating agent, temozolomide (TMZ), resistance of GBM to TMZ is reduced. The nanocomposite was comprised of a redox responsive biopolymer shell of PEG and chitosan that was conjugated to chlorotoxin and loaded with BG and iron oxide nanoparticles. BG is known to induce bone marrow toxicity so while free BG and TMZ significantly reduce white blood cell counts and platelet levels indicating toxicity, the BG nanoparticle formulation with TMZ resulted in significantly reduced degree of WBC and platelet suppression. Animal survival increased from 4 days to 9 days when treated with TMZ combined with the BG nanoparticle formulation, compared to TMZ with the unloaded nanocomposite. The magnetic nanoparticles also allowed for MR T<sub>2</sub> imaging contrast enhancement. Overall, this nanocomposite is promising for targeted combination treatment of GBM.

A peptide recently used for conjugation to magnetic nanoparticles is bombesin (BBN) or its human counterpart gastrin releasing peptide (GRP). This peptide has been shown to play an important role in cancer growth as gastrin releasing peptide receptors are overexpressed in many cancers but have low expression levels in normal tissues. In this study, a bombesin analogue was conjugated to dextran coated iron oxide nanoparticles as a new targeting MRI contrast agent for breast cancer detection (Jafari, Salouti et al. 2015). There was no significant decrease in cell viability of T47D cells after 24 hours of incubation with bombesin-conjugated iron oxide nanoparticles up to a concentration of 30 µg/mL. In addition, no difference in cell viability between bombesin targeted and non-targeted nanoparticles was observed. T47D cell surfaces were highly labeled with bombesin-conjugated iron oxide nanoparticles due to specific binding of bombesin to the overexpressed GRP receptor on the surface. Non-targeted iron oxide nanoparticles were not associated with T47D cell surfaces and Bombesin-conjugated iron oxide nanoparticles did not bind

to 5637 cells, which do not express GRP. An *in vivo* proof of concept study for bombesin-conjugated iron oxide nanoparticles for MR imaging contrast was also completed successfully.

A more common biological target is the  $\alpha_v\beta_3$  integrin, an adhesion integrin overexpressed on the surfaces of endothelial cells of neo-angiogenic vessels involved in the angiogenic process (Schleich, Po et al. 2014). Angiogenesis, or the process by which new blood vessels are formed, is the ultimate cause of tumor growth and metastasis. Therefore, researchers have continued to utilize the  $\alpha_v\beta_3$  integrin as a target for enhanced nanoparticle delivery. The arginine-glycine-aspartic acid (RGD) peptide has been shown to preferentially bind to the  $\alpha_v\beta_3$  integrin and has therefore been functionalized to a variety of magnetic nanoparticles to improve accumulation at the tumor site and enhance MR imaging or drug delivery.

Several recent studies have shown RGD-functionalized magnetic nanoparticles to enhance the negative contrast of T<sub>2</sub> MR imaging (Zhang, Jugold et al. 2007, Kumar, Yigit et al. 2010, Xie, Chen et al. 2010, Xie, Liu et al. 2011, Yang, Zhuang et al. 2011, Chen, Tao et al. 2012, Jarzyna, Deddens et al. 2012, Lin, Dayananda et al. 2012, Rosen, Chan et al. 2012, Zhao, Huang et al. 2012, Menichetti, Manzoni et al. 2013, Passemard, Staedler et al. 2013). For example, Melemenidis et al. utilized a cyclic variant of RGD (cRGD) conjugated to iron oxide nanoparticles and analyzed binding to the  $\alpha_v\beta_3$  integrin. HUVECs were stimulated with S-nitroso-N-acetylpenicillamine (SNAP) to upregulate the  $\alpha_v\beta_3$  integrin, and binding of the cRGD-targeted nanoparticles increased by 14-fold compared to binding in non-stimulated cells (Melemenidis, Jefferson et al. 2015). Additionally, under nanoparticle exposure via flow conditions of 1 dyne/cm<sup>2</sup>, SNAP stimulated HUVECs retained cRGD-targeted nanoparticles 44 times more than non-stimulated cells. Intravenous (IV) administration of cRGD iron oxide nanoparticles to mice bearing melanoma or colorectal subcutaneous tumors resulted in enhanced negative contrast within the tumor on T<sub>2</sub> weighted images compared to pre-contrast images.

Other groups have worked to develop RGD-targeted dual-modality imaging probes. Wang et al. also used a cyclic form of RGD conjugated to liposomes encapsulating 2,3-dimercaptosuccinic acid (DMSA) coated iron oxide nanoparticles and CdSe quantum dots into the interior vesicle and phospholipid bilayer, respectively (Wang, Li et al. 2015). The average fluorescence of RM-1 cells after exposure to targeted liposomes was about 2.5 times stronger than after exposure to non-targeted liposomes due to interaction of cRGD with the  $\alpha_v\beta_3$  integrins on the cell surface. An *in vivo* bone metastasis model of prostate cancer was used to examine MR imaging capabilities. Four hours after administration of the targeted liposomes there was a relative signal decrease in  $T_2$  indicating accumulation of the magnetic-fluorescent liposomes. Deng et al. developed dual modality RGD-targeted magnetic nanoparticles radiolabeled with  $^{125}\text{I}$  for SPECT and MR imaging (Deng, Zhang et al. 2015). Twenty-four hours post nanoparticle injection, the Bcap37 tumor-to-contralateral site ratio was 10.61 in SPECT imaging, and a significant signal reduction in MR imaging was observed. Xue et al. also combined SPECT and MR imaging modalities into a single RGD-targeted nanoparticle system using  $^{99\text{m}}\text{Tc}$  radiolabeling and ultra-small iron oxide nanoparticles for MRI contrast. Using free RGD as a competitive binding agent the authors proved that accumulation of the nanoparticles at the tumor site was due to RGD binding to the  $\alpha_v\beta_3$  integrins, since a decrease in both SPECT and MRI contrast was observed under the competitive conditions.

RGD-targeted magnetic nanoparticles are commonly used for negative contrast enhancement in  $T_2$  MR imaging. However, recent studies have developed targeted magnetic nanoparticles for  $T_1$  MRI contrast (Luo, Yang et al. 2015) or both  $T_1$  and  $T_2$  contrast (Xue, Zhang et al. 2015). Luo et al. developed RGD-targeted ultra-small iron oxide nanoparticles (<5 nm) for  $T_1$  MRI contrast since the magnetic moment of the nanoparticles sharply decreases as their size decreases due to reduction of their volume magnetic anisotropy and spin disorders on the surface (Luo, Yang et al. 2015). A xenografted U87MG tumor model was used to show  $T_1$  enhancement via the targeted, ultra-small

nanoparticle system. Both targeted and non-targeted nanoparticles increased the signal to noise ratio of T1 MR images but the effect over three hours was significantly greater for the RGD targeted nanoparticles.

RGD conjugation to magnetic nanoparticles also provides the opportunity for dual targeting for drug delivery: magnetic and active targeting. Lin et al. recently developed RGD-functionalized poly[(N-isopropylacrylamide-r-acrylamine)-b-L-lactic acid] (PNAL) coated iron oxide nanoparticles loaded with paclitaxel for the treatment of HeLa cells (Lin, Kang et al. 2015). *In vitro* studies confirmed the cytotoxicity enhancement of the nanoparticle system in the presence of a magnetic field, which was further enhanced by functionalization with RGD. *In vivo* studies completed by Schleich et al. with paclitaxel and iron oxide nanoparticle-loaded PEGylated PLGA nanoparticles showed that by combining RGD-functionalization to the nanoparticle surface with magnetic targeting, survival of CT26 tumor bearing mice was significantly increased to 21.5 days from 14.7 or 15 days for active or magnetic targeting, respectively (Schleich, Po et al. 2014). Additionally, tumor growth was significantly reduced when the combination targeting modalities were compared to either alone.

A variety of other peptides have been used as specific biological targets but they are not as common as some of the previously discussed peptides. The EPPT (Glu-Pro-Pro-Thr) peptide, which targets under-glycosylated MUC-1 tumor antigen found on more than 90% of breast cancers, has not been used since 2010 for magnetic nanoparticle delivery (Medarova, Rashkovetsky et al. 2009, Kumar, Medarova et al. 2010). A different magnetic nanoparticle system developed by Sungsuwan et al. induced the production of MUC-1 specific antibodies that recognized MUC-1-positive tumor cells, killing them through complement-mediated cytotoxicity. Rather than being functionalized with EPPT as in the previous example, the magnetic nanoparticles were functionalized with amphiphilic lipo(glycol)peptides leading to antigen presentation to the immune system. Another tumor targeting peptide is WSG (Try-Ser-Gly), which was used to coat iron oxide

nanoparticles without the aid of another coating material. The WSG coated nanoparticles more easily assembled into cancers compared to non-targeted nanoparticles, indicating the tumor targeting properties of WSG (Wei, Yin et al. 2013).

#### 2.2.3.3 Cell penetrating peptides

Another peptide category that has been of particular interest recently is that of cell penetrating peptides (CPPs). Also known as membrane translocation sequences, Trojan peptides, or protein transduction domains, these small, cationic and/or amphipathic peptides have the ability to enter cells and mediate uptake of a wide range of macromolecular cargoes (Farkhani, Valizadeh et al. 2014). The cellular uptake mechanism depends upon the attached cargo as CPPs attached to small cargoes can enter the cell via direct translocation whereas large molecules attached to CPPs tend to be up taken via micropinocytosis in an energy dependent manner (Ma, Shi et al. 2011). A few recent reviews give additional details on the uptake mechanisms of CPPs and their conjugation to a wide array of nanoparticle systems (Chou, Ming et al. 2011, Cleal, He et al. 2013, Farkhani, Valizadeh et al. 2014, Amin, Joo et al. 2015, Jafari, Dizaj et al. 2015). Thus, this section will focus on very recent advances in CPP conjugation to magnetic nanoparticles.

The first CPP to be discovered was the HIV-1 encoded TAT peptide which mediates interaction with anionic motifs on the cell surface in a non-receptor mediated manner (Bolhassani 2011, Koren and Torchilin 2012). The TAT peptide carries both a transmembrane and nuclear localizing signal within its sequence, making it an even more attractive targeting modality for nuclear delivery. In a study by Wang et al., the TAT peptide and FITC fluorophore were functionalized to PEG600-b-PGA, which was then self-assembled with iron oxide nanoparticles (Wang, Qiao et al. 2012). The TAT functionalized nanoparticles quickly entered Caco-2 cells, and the fluorescence following 4 hours of incubation was much greater in cells exposed to the targeted nanoparticles compared to non-targeted nanoparticles. The targeted magnetic nanoparticles were found to internalize into the cells and penetrate the nuclear membrane while the non-targeted control nanoparticles were located

at the cell membrane. Another study by Nair et al. focused on the intracellular location and trafficking of TAT-conjugated iron oxide nanoparticles using 3D electron tomography (Nair, Fukuda et al. 2012). TAT-conjugated PEG coated iron oxide nanoparticles were exposed to human glioblastoma, and it was shown that some of the nanoparticles had accumulated in a vacuole then moved out into the cytoplasm. In unpublished work by Hauser et al., TAT-conjugated dextran coated iron oxide nanoparticles were developed to enhance radiation therapy in A549 lung carcinoma (see Chapter 7). Radiation treatment increases mitochondrial formation of hydrogen peroxide. The presence of excess iron ions catalyzes the formation of highly reactive hydroxyl radicals. Therefore, the more intracellular iron oxide present, the greater the damage by the hydroxyl radical. TAT peptide functionalization to iron oxide nanoparticles increased the intracellular iron concentration and increased reactive oxygen species (ROS) formation in the presence of radiation compared to radiation alone. The TAT-conjugated nanoparticles were found to destabilize lysosomal membranes and interact with the mitochondria, sensitizing the cells to radiation treatment. In subsequent work by Hauser et al. the TAT-conjugated dextran coated nanoparticles were utilized for magnetically mediated energy delivery (MagMED) (see Chapter 6). The nanoparticles were internalized by A549 or H358 lung cancer cells and induced cellular damage upon exposure to an AMF. An increase in ROS generation was observed upon exposure to an AMF, and a slight increase in cell apoptosis was observed. Although the iron oxide nanoparticles were too large to permeate the nuclear membrane, the TAT peptide promoted lysosomal destabilization and escape of the nanoparticles into the cytosol, allowing for enhanced effects of the nanoparticles. The TAT peptide has also been shown to be toxic due to destabilization of organelle membranes. Cavalli et al. conjugated a  $\gamma$ -amino-proline derived peptide to dextran coated iron oxide nanoparticles and compared their toxicity with TAT-functionalized nanoparticles (Cavalli, Carbajo et al. 2012). While the  $\gamma$ -amino-proline derived peptide conjugated iron oxide nanoparticles exhibited lower internalization than the TAT peptide, they were determined to be less toxic and



stable towards protease degradation. These nanoparticles were also able to reduce  $T_2$  intensity without showing HeLa cell cytotoxicity.

Another magnetic nanoparticle system that utilizes CPPs was developed by Chen et al. They utilized a peptide and a polymer to enhance nanoparticle penetration of the blood-brain barrier (BBB). PF127, a pluronic polymer that enhances BBB penetration via inhibiting the P-glycoprotein efflux pump, and angiopep-2 (ANG), a peptide with high capability for BBB penetration via receptor mediated endocytosis, were both conjugated to polyacrylic acid coated iron oxide nanoparticles (Chen, Su et al. 2014). The effects of PF127 and ANG were analyzed separately and both were found to enhance intracellular concentrations of iron oxide in U87 cells. The combined targeting system was analyzed in an *ex vivo* BBB model and found to increase the amount permeated from 4.9  $\mu\text{g/mL}$  for PF127 targeted only to 7.6  $\mu\text{g/mL}$ . The dual targeted nanoparticles also had increased transversal relaxation rates (167.54/mM/second) compared to conventional iron oxide nanoparticle products.

#### 2.2.4 Small Molecules

Small molecules, such as glucose and folic acid, have also gained interest as targeting agents of magnetic nanoparticles due to the ability to functionalize the nanoparticle surface with an increased number of targeting groups with limited steric constraints (McCarthy and Weissleder 2008). The more targeting ligands, the more likely there will be a multivalent effect between the particle and its target.

Glucose functionalization to magnetic nanoparticles was recently investigated for targeting colon cancer metastasis in the liver due to increased metabolic activity of cancer cells requiring excess glucose, leading to a targeting method for glucose functionalized magnetic nanoparticles. Wydra et al. functionalized glucose to the surface of citric acid stabilized iron oxide nanoparticles via amine-carboxyl coupling of d-glucosamine and citric acid (Wydra, Rychahou et al. 2015). Glucose functionalization to the nanoparticle surface increased internalization by CT26 cells

compared to citric acid coated or uncoated nanoparticles. Cells with internalized magnetic nanoparticles were exposed to an AMF for 30 minutes and the generation of reactive oxygen species was analyzed. Although there was a slight increase in ROS generation due to the presence of uncoated and glucose coated iron oxide nanoparticles, only the citric acid coated iron oxide nanoparticles resulted in significant ROS generation. All the nanoparticle systems combined with AMF exposure significantly increased apoptosis in CT26 cells compared to no AMF exposure when the percent apoptosis was measured 24 hours post treatment. Therefore, it appears as though the increase in ROS generation after exposure of CT26 cells containing internalized magnetic nanoparticles to an AMF can trigger apoptotic pathways and result in increased apoptosis compared to IONP exposure alone.

Glucose functionalization of the surface of magnetic nanoparticles to target cancer cells due to their enhanced metabolic activity has been studied by other groups as well (Xiong, Zhu et al. 2012, Herea, Chiriac et al. 2015). Maharramov et al. coated iron oxide nanoparticles with 2-deoxy-D-glucose, which is a glucose analogue in which the hydroxyl group bound to the second carbon is replaced by a hydrogen atom (Maharramov, Ramazanov et al. 2014). The goal of using the glucose analogue was to target the nanoparticles to the cancer cells due to metabolic needs, but block the glycolytic pathway. A proof of concept study on the growth inhibitory effects of 2-deoxy-D-glucose functionalized magnetic nanoparticles was completed on HCT116, HT29, and RKO colorectal cells. Although 2-deoxy-D-glucose was more toxic alone, the nanoparticle formulations significantly reduced the viability compared to control cells. Future use for the nanoparticle system would include MR imaging.

Other groups have developed glucose functionalized magnetic nanoparticles for cancer cell targeting via the glucose transporter protein (Shan, Hu et al. 2012, Barbaro, Di Bari et al. 2015). Barbaro et al. developed a small D-glucose coated iron oxide nanoparticle using metal vapor synthesis to target pancreatic cancer cells that express glucose transporter (GLUT-1) in the cell

membrane (Barbaro, Di Bari et al. 2015). Glucose coated iron oxide nanoparticles were taken up at greater concentrations into BxPC3 cells expressing GLUT-1 compared to polyvinylpyrrolidone (PVP) iron oxide nanoparticles. Additionally, pre-treatment with antiGLUT1 reduced cellular accumulation of glucose functionalized nanoparticles by 41% but did not affect PVP functionalized nanoparticles.

Folic acid is another small molecule that is of particular interest for tumor targeting of magnetic nanoparticles due to its high binding affinity to the folate receptor (FR), low cost, ease of conjugation, compatibility with both organic and aqueous solvents, and a lack of immunogenicity (Low, Henne et al. 2008). The FR is overexpressed on the surface of several cancers including breast, kidney, lung, brain and ovary (Parker, Turk et al. 2005) and due to the limited expression of FR on normal tissues, folate may be an appropriate choice for targeting tumor cells in NP based cancer therapies. Folate can bind to FR and facilitate the transfer of folate-targeted nanoparticles through receptor mediated endocytosis. Folic acid is an essential nutrient needed by all cells for biosynthesis of nucleotides and the normal action of some metabolic pathways that mediate uptake via a non-destructive endosomal pathway (Parker, Turk et al. 2005, Murthy 2007, Mansoori, Brandenburg et al. 2010).

Bahrami et al. in 2015 reviewed folate conjugated nanoparticles as a therapeutic approach for cancer therapy with a section devoted to magnetic nanoparticles (Bahrami, Mohammadnia-Afrouzi et al. 2015). For additional information or studies prior to 2015, readers are directed to this review. Therefore, this section will summarize recent advances in folate-conjugated magnetic nanoparticles. Several investigations have developed strategies to conjugate folate derivatives to magnetic nanoparticles and characterize their physicochemical properties (Dolores, Raquel et al. 2015, Karamipour, Sadjadi et al. 2015, Socaci, Magerusan et al. 2015) while others have proven the targeting ability and receptor-mediated endocytosis associated with folate functionalized nanoparticles (Li, Yang et al. 2015, Razjouyan, Zolata et al. 2015). FR targeted core-shell magnetic

nanoparticles have been of particular interest for thermal therapy (Sadhasivam, Savitha et al. 2015), drug delivery (Li, Dong et al. 2015, Tudisco, Cambria et al. 2015) and imaging (Chen, Zheng et al. 2015, Ma, Liu et al. 2015, Yin, Hong et al. 2015) of cancer. Carbon encapsulated iron oxide nanoparticles were surface engineered with PEG-folic acid by Sadhasivam et al. to induce selective hyperthermia in FR overexpressed cancer cells (Sadhasivam, Savitha et al. 2015). The nanoparticle system was non-toxic to human fibroblasts (low FR expression) both with and without AMF exposure as determined by the LDH assay. However, in HeLa cells (high FR expression), significant cytotoxicity was induced upon treatment with the targeted nanoparticles and AMF compared to the targeted nanoparticles alone. This is a result of enhanced uptake by the HeLa cells as non-targeted nanoparticles resulted in a relative iron uptake of 0.105 mg/mL while the targeted nanoparticles resulted in a relative iron uptake of 0.316 mg/mL.

Li et al. encapsulated iron oxide nanoparticles and sorafenib (SRF) into folate-conjugated PLGA nanoparticles (Li, Dong et al. 2015). Cell uptake potential of SFR, non-targeted magnetic nanoparticles and targeted magnetic nanoparticles were investigated in FR over-expressing BEL7402 hepatocellular carcinoma. Uptake was time dependent in all systems, but significantly greater for targeted nanoparticles. The 24 hour IC<sub>50</sub> values in BEL7402 cells for SRF, non-targeted magnetic nanoparticles and targeted magnetic nanoparticles were 2.35 µg/mL, 2.48 µg/mL, and 0.84 µg/mL respectively, suggesting that folic acid-targeted nanoparticles were more effective at inducing cell toxicity.

Another application of folic acid targeted nanoparticles to enhance the intracellular transport of N-methylated drugs was evaluated by Tudisco et al. (Tudisco, Cambria et al. 2015). PEG, folic acid, and carboxy-X-rhodamine were conjugated to magnetic nanoparticles along with tetraphosphonate cavitand (Tiiii) that has molecular recognition properties towards N-methylated guests. The most significant finding of this study was that the nanoparticles were able to facilitate intracellular transport of PCZ, an N-methylated molecule, when PCZ and the nanoparticles were

introduced to LoVo cells simultaneously. The decrease in cell viability following dual, simultaneous treatment compared to PCZ alone indicated that the nanoparticles interact with PCZ, and are then internalized via folate receptors.

As previously mentioned, folate receptor targeted magnetic nanoparticles are often used as MRI contrast agents. Ma et al. developed magnetic-lanthanide-doped fluoride nanoparticles which were targeted with folic acid to be used as bimodal probes for cellular fluorescence and magnetic resonance imaging of HeLa cells overexpressing FR (Ma, Liu et al. 2015). *In vitro* fluorescence imaging after exposure to targeted and non-targeted nanoparticles was evaluated using HeLa cells overexpressing FR. HeLa cells treated with folic acid-conjugated nanoparticles displayed a strong green fluorescence. In contrast, HeLa cells treated with non-targeted nanoparticles and MCF-7 cells (lower FR expression) treated with targeted nanoparticles had a weak fluorescence signal. The targeted nanoparticles were also used to increase T2 contrast in HeLa cells *in vitro*. Yin et al. were also interested in magnetic nanoparticles for dual imaging modalities (Yin, Hong et al. 2015). Amphiphiles were embedded with oligo(*p*-phenyleneethynylene) (OPE) via covalent linkages and this OPE based structure was further functionalized with folic acid to serve as the targeting ligand. These amphiphilic OPE molecules were used to encapsulate fluorescent magnetic nanoparticles so the final magnetic nanoparticles could be used for fluorescence and magnetic resonance imaging. HeLa cells were incubated with the targeted and non-targeted nanoparticle formulations at different concentrations (with and without folic acid) for three hours. A decrease in MRI signal intensity was observed as nanoparticle concentration increased. However, cells incubated with the targeted nanoparticles exhibited a greater signal decrease than those incubated with non-targeted nanoparticles at concentrations greater than 0.042 mg/mL. The dual imaging capability of this nanoparticle system was analyzed *in vivo* as well. Tumor bearing mice were injected with the targeted or non-targeted nanoparticle system. MR imaging four hours after injection indicated a T2 signal reduction within the tumor compared to pre-injection images for both nanoparticle systems.

However, the signal reduction was greater in the targeted nanoparticle groups due to increased intra-tumor iron concentration as confirmed by Prussian blue staining. Two-photon optical imaging of tumor biopsies showed similar results to the MRI analyses. Tumor slices excised from mice treated with targeted nanoparticles showed intense fluorescence with high resolution and sensitivity. However, weak fluorescence was observed in tumors of mice that received the non-targeted nanoparticle formulation.

While the majority of FR targeted nanoparticles are used for cancer therapy or imaging applications, Dai et al. coated superparamagnetic iron oxide nanoparticles with glucose and dextran then functionalized the nanoparticles with folic acid due to its specific binding to the recruited and activated macrophages of synovium in rheumatoid arthritis (RA) that overexpress folic acid receptors. RA was induced in rat paws using Freund's complete adjuvant injection, and 14 days after the injection, degeneration or necrosis in the epithelium as well as infiltration of inflammatory cells were observed. Functionalized nanoparticles were injected and the rat ankles were imaged via MRI 24 hours later. The folic acid functionalized nanoparticles resulted in significant negative contrast enhancement while non-targeted nanoparticles only marginally reduced the signal intensity. Another non-cancer application of folate receptor targeted magnetic nanoparticles was investigated by Li et al. who developed a small magnetite antiretroviral therapy (SMART) nanoparticle platform to assess antiretroviral drug tissue biodistribution and PK using MRI scans (Li, Gendelman et al. 2015). Alendronate (ALN), a bisphosphate drug that is clinically used to treat osteoporosis, was conjugated to polymers for stable magnetite coating. Folic acid was then conjugated to the polymers that were attached to the exterior of magnetite. The nanoparticles were detected by MRI and rapid uptake by mononuclear phagocytes (MP) provided a noninvasive method of detecting regions of disease-associated infection including virus induced inflammation. This platform provided a means to rapidly evaluate the efficiency of targeting strategies for HIV reservoirs.

Additionally, a variety of studies have utilized folate-conjugated micelles (Li, Yan et al. 2015) or liposomes loaded with magnetic nanoparticles for drug delivery and MR imaging contrast. For example, Du et al. synthesized thermosensitive liposomes functionalized with PEG<sub>2000</sub> and folic acid containing C<sub>60</sub>-Fe<sub>3</sub>O<sub>4</sub> nanocomposites and docetaxel (Du, Han et al. 2015). This multifunctional liposome formulation allowed for combined magnetic and folate receptor targeting as well as controlled docetaxel release and thermal ablation via the magnetic nanoparticles in the presence of RF. *In vitro* studies indicated that these multifunctional liposomes resulted in higher inhibition efficiency of MCF-7 (FR positive) cells than docetaxel alone suggesting that the delivery system was able to deliver more drug into the cells. Cellular uptake was analyzed by adding FITC to the multifunctional liposomes, and the uptake of the magnetic liposomes was greater than the nanoparticles with docetaxel having no folate targeting or liposome structure. Upon radio frequency exposure, the C<sub>60</sub> component of the liposome generated heat, destabilizing the liposome structure and releasing docetaxel. *In vivo* studies indicated that dual targeting (FR and magnetic) and RF exposure significantly reduced tumor growth compared to control groups.

### **2.3 Conclusions and Future Perspectives**

Active targeting of magnetic nanoparticles has significantly improved nanoparticle specificity and accumulation compared to passive targeting and utilization of the enhanced permeation and retention effect. Conjugation of ligands to the surface of magnetic nanoparticles has afforded the opportunity to target specific entities within a tissue, whether it be a component of the extracellular matrix, cell surface receptors, or organelles. Active targeting of magnetic nanoparticles has been repeatedly shown to improve nanoparticle uptake into tissues and cells, making magnetically mediated hyperthermia more effective and increasing MRI contrast. As discussed in this review, a variety of targeting ligands can be conjugated to the surface of magnetic nanoparticles. Antibodies, aptamers, peptides, and small molecules have all proven to be effective targeting agents for magnetic nanoparticles, but choosing the appropriate targeting ligand is dependent upon the target

and application of the nanoparticle system. Although antibodies are very specific targeting moieties, they are expensive. Aptamers have increased in popularity as an alternative to antibodies in that the specificity is retained, and their synthesis is less expensive than antibody production. Peptides can be synthesized for a variety of targets with binding specificity rivaling that of larger molecules such as antibodies. They are relatively inexpensive to synthesize and, due to their smaller size, nanoparticles can be functionalized with multiple peptides per particle to increase the binding opportunities. Small molecules have also gained interest as targeting agents as their size allows for multiple molecules per particle and lower steric constraints than other targeting ligands.

Although significant improvements in active targeting of magnetic nanoparticles both *in vitro* and *in vivo* have been realized, there are still shortcomings that should be addressed in order to continue to advance. First, in attempt to translate targeted nanoparticle systems into the clinic and receive FDA approval, a single nanoparticle formulation with the ability to be functionalized with a variety of targeting ligands should be established. This would allow for a versatile system that could be easily altered for different targets and applications. Secondly, subcellular targeting is a relatively new focus in magnetic nanoparticle targeting but poses interesting opportunities. Lysosome sequestration is the normal fate of magnetic nanoparticles taken up by cells through endocytosis leading to degradation and low therapeutic effect. However, if the nanoparticles are appropriately functionalized to target subcellular organelles, their potential for therapeutic efficacy is drastically increased. Finally, *in vivo* testing of targeted magnetic nanoparticles should be scaled to larger animals in order to improve understanding and translation of the targeted nanoparticles to humans.



### **Chapter 3 Magnetic nanoparticles and nanocomposites for remote controlled therapies**

The chapter is taken directly or adapted from work published in Hauser, Wydra, et al. (2015) Copyright 2015 Elsevier B.V. Used with permissions from Anastasia K. Hauser, Robert J. Wydra, Nathanael A. Stocke, Kimberly W. Anderson and J. Zach Hilt, “Magnetic nanoparticles and nanocomposites for remote controlled therapies”, Journal of Controlled Release and Elsevier B.V.

#### **3.1 Introduction**

Magnetic nanoparticles (MNPs) have been extensively studied for a variety of biological applications such as FDA-approved MRI contrast agents (Reimer and Balzer 2003), FDA-approved iron deficiency treatment (Auerbach 2008), thermal therapy, and drug delivery. MNPs are often coated with or embedded in a polymer or organic matrix in order to: increase colloid stability and extend circulation time in biological environments, provide a means for functionalization with targeting agents or fluorescent markers, or afford the opportunity for drug loading and conjugation (Berry and Curtis 2003, Gupta and Gupta 2005, Duguet, Vasseur et al. 2006, Berry 2009, Shubayev, Pisanic et al. 2009, Frimpong and Hilt 2010, Amstad, Textor et al. 2011, Ho, Sun et al. 2011). MNPs are able to convert energy from an alternating magnetic field (AMF) to heat primarily through Neel and Brownian relaxations, with Neel relaxation being the internal dipole rotation and Brownian referring to the physical rotation of the nanoparticle. The heat generated by the MNPs in the presence of an AMF can be utilized for a variety of therapies, including controlled release of a drug, local thermal therapy, magnetically mediated energy delivery (MagMED), and combinational treatments. Additionally, MNPs respond to static magnetic field gradients and low frequency AMFs where the heating effect is negligible or non-existent, allowing for other controlled drug delivery strategies, including external guiding/targeting of magnetic nanoparticles and mechanical deformations/disruptions for triggered release.

The unique capability of MNPs and their composites to be remotely controlled has been utilized for various applications (Brazel 2009, Liu, Hu et al. 2009, Satarkar, Biswal et al. 2010, Kumar and

Mohammad 2011, Bonini, Berti et al. 2013, Li, Huang et al. 2013, Thevenot, Oliveira et al. 2013, Jhaveri, Deshpande et al. 2014, Ridi, Bonini et al. 2014, Schleich, Danhier et al. 2015). When applied in drug delivery, the remote control of the MNPs enables for controlled drug delivery (temporal and/or spatial). For temporal control, the remote actuation is often based on the AMF heating of MNPs to cause a temperature-responsive change in the delivery system release properties. In other cases of temporal control, the remote actuation is based on static or low frequency magnetic fields where the mechanical forces induced by the magnetic field result in modulation of the release behavior. For spatial control, the applied magnetic field can remotely control the accumulation of a delivery system within the body. In many cases, enhanced therapeutic delivery and associated outcomes have been reported as a result of the remote control over the temporal and/or spatial release of a drug.

Magnetically mediated hyperthermia (MMH) treatment, also referred to as magnetic fluid hyperthermia (MFH), is another important application of MNPs. MMH is the heating of tissue to hyperthermia temperatures of approximately 41-45°C by activation of the MNPs in the presence of an AMF. This inherently localized heating therapy has been studied extensively for cancer therapy both in isolation or combination with a conventional cancer therapy such as chemotherapy or radiation (Pankhurst, Connolly et al. 2003, Tartaj, Morales et al. 2003, Mornet, Vasseur et al. 2004, Goya, Grazu et al. 2008, Corchero and Villaverde 2009, Pankhurst, Thanh et al. 2009, Kumar and Mohammad 2011). Localized thermal therapy via MMH has been shown to be more effective than other forms of hyperthermia delivery.

MMH has also been shown to enhance the efficacy of traditional cancer therapies such as chemotherapy, radiation, surgical resection, and gene therapy. A variety of chemotherapeutics are more effective when administered in the hyperthermia range due to increased rate constants of alkylation, increased drug uptake, and inhibition of repair of drug-induced lethal or sub-lethal damage (Issels 2008). Chemotherapeutics have also been chemically or physically bound to

magnetic nanoparticles for controlled drug release upon exposure to an external stimuli such as an AMF or change in pH, and upon further exposure to AMF, simultaneous thermal therapy can be administered (Gautier, Allard-Vannier et al. , Jhaveri, Deshpande et al. 2014, Rejinold, Jayakumar et al. 2015). Additionally, hyperthermia has been shown to increase blood supply to the tumor, which increases local oxygen levels. Since the efficacy of radiation therapy is tied to the formation of free radicals more than direct DNA damage, MMH can enhance the effectiveness of radiation by increasing free radical formation. Overall, thermal therapy via MNPs is a promising treatment method when combined with traditional therapies due to localized tumor heating and sensitization of the tumor tissue to additional modalities.

One of the major translational hurdles of MMH is that a large concentration of nanoparticles is required to achieve the necessary increase in temperature *in vitro* and especially *in vivo*, and this limitation, to date, has limited the application of MMH to direct injection into solid tumors for *in vivo* application (Johannsen, Jordan et al. 2004, Jordan, Scholz et al. 2006). Therefore, researchers have recently focused more on MagMED for nanoscale energy therapy (Kozissnik, Bohorquez et al. 2013). This form of therapy utilizing AMF-activated MNPs relies on intracellular effects of MNPs and results in a therapeutic effect without a measurable temperature rise, with the exact mechanism of toxicity still under investigation. Intracellular concentrations of MNPs can be increased by cellular targeting with ligands and antibodies, which has been shown to further enhance the effectiveness of MagMED as a treatment modality (Berry and Curtis 2003, Gupta and Gupta 2005, Shubayev, Pisanic et al. 2009, Creixell, Bohorquez et al. 2011, Kievit, Stephen et al. 2012). Therapeutic approaches based on MagMED have led many researchers to focus on determining intracellular targets and understanding intracellular mechanisms.

This chapter summarizes recent advances in applications of MNPs and magnetic nanocomposites for remote controlled thermal therapy, nano-scale energy delivery, and combinational therapy (Figure 3.1).

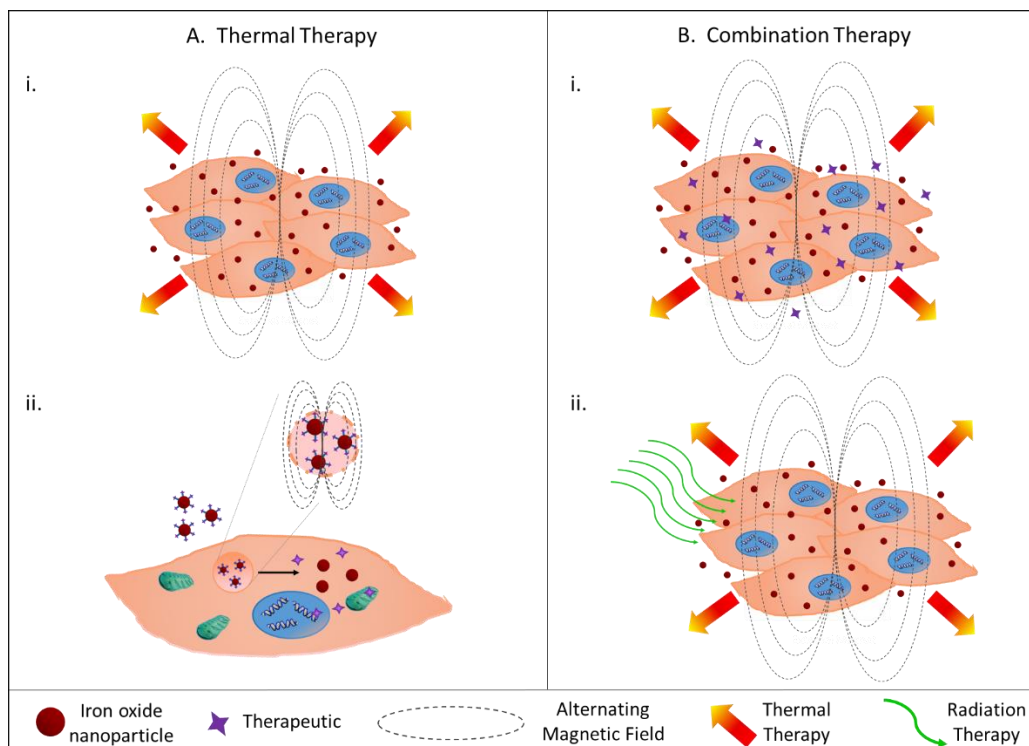


Figure 3.1 This section highlights the uses of MNPs for controlled release therapies. A) Thermal therapy can be remotely controlled for i) local applications or ii) nanoscale heating applications. B) Thermal therapy is often administered in combination with a secondary treatment such as i) a therapeutic or ii) radiation.

### 3.2 Remote controlled energy release

#### 3.2.1 Thermal therapy

Magnetic nanoparticles have been extensively studied for thermal therapy applications due to their ability to convert energy from an AMF into thermal energy. This controlled release of thermal energy from MNPs can be used for hyperthermia treatment, which is defined as the heating of tissue to 41-45°C (Hildebrandt, Wust et al. 2002) and has been shown to be an effective treatment of various types of cancer. Some have suggested that the efficacy of hyperthermia is likely due to tumor tissue being more susceptible to heat insults than healthy tissue (Jordan, Scholz et al. 1999, Moroz, Jones et al. 2002). Magnetically mediated hyperthermia (MMH), which is also known as

magnetic fluid hyperthermia (MFH), is where MNPs or larger magnetic particles are localized within the tumor environment and then exposed to an AMF, resulting in heat generation. For cancer therapy, MMH has several advantages over other delivery routes of thermal therapy in that it is localized to only the tumor tissue through selectively targeting (e.g., active or passive targeting, direct injection, etc.) and provides even temperature distribution throughout the tumor tissue. By comparison, regional and whole body hyperthermia are used to heat larger regions such as a limb or cavity, or to treat metastatic disease, but often lead to undesirable damage of healthy tissue. Beyond delivering thermal energy, MNPs have additional physical properties that make them advantageous for thermal delivery such as physical rotation of the nanoparticle in the presence of an AMF (Zhang, Kircher et al. 2014), elevated nanoparticle surface temperatures (Polo-Corrales and Rinaldi 2012) and nanoscale heating effects (Xu, Karmakar et al. 2010, Creixell, Bohorquez et al. 2011). These are all potential explanations to the improvement of MMH over other hyperthermia treatments.

This improvement was demonstrated by Rodriguez-Luccioni et al. when they addressed the effects of MMH using MNPs functionalized with carboxymethyl dextran compared to hot water hyperthermia (HWH) on MCF-7 and Caco-2 cells (Rodriguez-Luccioni, Latorre-Esteves et al. 2011). MMH resulted in a greater decrease in cell viability for both cell lines compared to HWH. A thorough review of MMH using iron oxide nanoparticles and the mechanisms of heat dissipation was written by Laurent et al. in 2011 (Laurent, Dutz et al. 2011), and others have addressed the advances, challenges, promises, and perils of MNPs for hyperthermia applications (Kozissnik, Bohorquez et al. 2013, Singh, McMillan et al. 2014). Therefore, this section focuses on recent studies that utilize controlled delivery of thermal energy from MNPs and the therapeutic and immunotherapeutic effects of the treatment.

Several research groups have studied the efficacy of magnetically mediated thermal therapy as a treatment modality for cancer both *in vitro* and *in vivo* (Le, Shinkai et al. 2001, Johannsen, Jordan

et al. 2004, Ivkov, DeNardo et al. 2005, Johannsen, Thiesen et al. 2005, Kettering, Winter et al. 2007, Kallumadil, Tada et al. 2009, Suto, Hirota et al. 2009, Lee, Jang et al. 2011, Bae, Park et al. 2012, Kut, Zhang et al. 2012, Lartigue, Hugounenq et al. 2012, Mustafa, Zhang et al. 2013, Rivet, Yuan et al. 2014, Soni, Tyagi et al. 2014). Thermoablation is another form of thermal therapy induced by raising the bulk solution temperature above 45°C. A recent review highlights the use of various nanomaterials, including MNPs, for thermoablative treatment, imaging, and diagnostics (Sawdon, Weydemeyer et al. 2014). The temperature at which the thermal therapy is performed dictates cellular response, with apoptosis being linked to hyperthermia temperatures and necrosis being associated with thermoablation. Both of these thermal therapy treatments can be administered via MNPs in the presence of an AMF, but it is important to understand the properties of magnetic nanoparticles in cellular environments in order to synthesize magnetic nanoparticle systems with the potential for maximum energy delivery. Di Corato et al. analyzed energy delivery by magnetic nanoparticles in a cellular environment and compared it to nanoparticles in suspension (Di Corato, Espinosa et al. 2014). In all systems, there was a systematic decrease in the heating efficiency for nanomaterials associated with tumor cells, which was likely due to inhibition of the Brownian relaxation in cellular conditions. The magnitude of this decrease was associated with the type of nanoparticle, but in general, it was determined that nanoparticles in the superparamagnetic domain are minimally affected by the cellular environment.

Various superparamagnetic nanoparticle systems have been developed to improve the efficacy of thermal therapy as a treatment of cancer. Wydra et al. developed an iron oxide nanoparticle system coated with citric acid or poly(ethylene glycol) (400) dimethacrylate (PEG400DMA) via atomic transfer radical polymerization (ATRP) (Wydra, Kruse et al. 2013). A549 lung carcinoma were exposed to 10 mg/mL Fe<sub>3</sub>O<sub>4</sub> and exposed to an AMF (301 kHz, 27.9 kA/m) for 10 minutes resulting in a bulk solution temperature of 55°C in the center of the dish where the magnetic field

amplitude was greatest. Minimal cell death occurred in the periphery indicating that temperatures in the thermal ablation range were sufficient at inducing cell death, most likely through necrosis.

Other studies have looked to address the differences between thermal therapies in the hyperthermia and thermoablation temperature ranges (Hu, Ma et al. 2011, Wang, Dong et al. 2012). In a study completed by Wang et al., the efficacy of high end hyperthermia treatment (47°C) was compared to thermoablation treatment at 51°C on subcutaneous MPC-83 tumors in female mice (Wang, Dong et al. 2012). Thermal therapy was administered at temperatures of 47 or 51°C for 30 minutes (300 kHz, 100 G) after the tumors had grown to 10 mm in diameter. After hyperthermia treatment at either temperature, the tumors in the 20 mice disappeared within 14 days. However, subcutaneous nodules of 3 mice in the 47°C group and 2 mice in the 51°C group began to relapse within 2 months after hyperthermia. Additionally, 7/10 mice in the 47°C group and 8/10 in the 51°C group were alive 140 days after hyperthermia treatment. This is a significant increase in survival of the hyperthermia groups compared to the control. In another study by Hu et al., A549 xenograft mice were injected with three different doses of iron oxide MNPs, which resulted in varying tumor temperatures of 41.3, 44.5, and 46.8°C (Hu, Ma et al. 2011). Tumor temperatures from 42-46°C resulted in disruption of the enzymatic system and structure of the tumor, therefore inducing apoptosis. Above 46°C, numerous large necrotic areas were observed within the tumors, and the nanoparticles were either distributed in the interstitial matrix of tumors or phagocytized by tumor cells.

In addition to cellular death, thermal therapy has a variety of consequences on the tumor microenvironment (Kolosnjaj-Tabi, Di Corato et al. 2014) and tumor growth factor expression (Wang, Xu et al. 2014). In a study completed by Kolosnjaj-Tabi et al. in 2014, PEG-coated iron oxide nanocubes were injected intratumorally into epidermoid carcinoma xenograft mice and treated for three days with 30 minutes of AMF exposure (111 kHz, 23.8 kA/m), which resulted in a temperature rise of  $7.8 \pm 2.2^\circ\text{C}$  (Kolosnjaj-Tabi, Di Corato et al. 2014). This hyperthermia

treatment resulted in the slackening of generally compact collagen fibers, which in turn increased nanocube penetration into the cell-rich tumor core. After MMH treatment, the intra-fibrillar space of the collagen matrix was shown to increase from  $101 \pm 17$  nm to  $133 \pm 32$  nm due to a phase transition of the collagen network. Thermal therapy via magnetic nanoparticles has also been shown to down regulate vascular endothelial growth factor (VEGF) in rats with Walker 265 breast carcinoma (Wang, Xu et al. 2014). Thermal treatment in the range of 50-55°C was administered 1, 2 or 3 times for 30 minutes via AMF exposure (180 kHz, 55 G) resulting in tumor growth inhibition and promoting the survival of tumor bearing rats. Gene expression of VEGF and its receptors in the tumor were decreased, thereby inhibiting tumor angiogenesis.

Thermal therapy using MNPs in an AMF has also been utilized as an immunotherapeutic treatment with promising results (Yanase, Shinkai et al. 1998, Shinkai, Yanase et al. 1999, Suzuki, Shinkai et al. 2003, Toraya-Brown, Sheen et al. 2014). Magnetic cationic liposomes (MCLs) were used for hyperthermia treatment in three of these studies due to their higher affinity for tumor cells than neutrally charged magnetoliposomes. In one of the first immunotherapy treatment studies via thermal therapy, T-9 rat glioma tumors were formed in the left flank of female rats, and MCLs were injected into half the tumors followed by exposure to an AMF (118 kHz, 384 Oe) for 30 minutes (3 times at 24 hour intervals) (Yanase, Shinkai et al. 1998). 89% of the rats treated with hyperthermia had complete regression. Three months later, cured rats or naïve rats were challenged with T-9 or malignant fibrous histiocytoma cells in the right flank. All right flank tumors (T-9 or malignant fibrous histiocytoma) formed in the mice not initially treated with hyperthermia. Conversely, T-9 right flank tumors did not form in mice treated with hyperthermia in the T-9 left flank tumors. However, malignant fibrous histiocytoma cell injection into the right flank resulted in tumor formation. Therefore, the immune response was found to be specific for the original T9 cells. Additionally, CD3+, CD4+, CD8+, and NK immunocytes were detected in the left and right tumors of mice treated with hyperthermia, but no immunocytes were found in the control group.



A subsequent study was completed on B16 melanoma subcutaneous tumors (Suzuki, Shinkai et al. 2003) and showed that 9 out of the 10 mice had complete tumor disappearance 120 days after two 30 minute hyperthermia treatments with MCLs in an AMF (118 kHz). Spleen cells were obtained from the cured mice, and in an *in vitro* study, these cells were shown to have increased cytotoxic activity against B16 cells compared to spleen cells from naïve mice. An *in vivo* immunotherapy study was also completed wherein mice were challenged with B16 melanoma cells 120 days after treatment. In the naïve mice, tumors formed 6 days post inoculation. However, 66% of the cured mice rejected the melanoma cells resulting in no nodule formation. The extended time between hyperthermia treatment and secondary inoculation suggests that MMH has the potential to decrease metastatic potential of B16 melanoma cells.

A more recent study on the immunotherapeutic effects of MMH was completed by Toraya-Brown et al. in 2014 and showed that local hyperthermia treatment induced CD8+ T cell-mediated resistance against distal and secondary tumors (Toraya-Brown, Sheen et al. 2014). B16 tumors were established in both the left and right flanks simultaneously, but only the left flank tumor was treated with MMH (43°C) for 30 minutes. Right flank tumors of the left flank heated group were found to grow significantly slower than the non-heated group. Another experiment examined secondary tumor formation in the right and left flanks after a right flank tumor was treated with hyperthermia and then excised three days post treatment. Secondary tumor growth was inhibited on both the primary tumor side and the contralateral side in the heated group compared to the non-heated group. This study also revealed that the timing of secondary tumor inoculation plays a role in tumor formation. One day after hyperthermia treatment resulted in no resistance to secondary tumor formation while inoculation 30 days after treatment inhibited tumor growth on the primary side but not the contralateral side. Additionally, it was found that local hyperthermia increases CD8+ T cells – required for inducing resistance against secondary tumors – as the effects of heating

the primary tumor were completely abrogated by treating with CD8+ antibodies to deplete CD8+ formation.

In addition to the *in vitro* and *in vivo* studies completed using magnetically mediated thermal therapy, there have also been a few clinical trials investigating quality of life and feasibility of thermotherapy using magnetic nanoparticles (Johannsen, Gneueckow et al. 2007, Johannsen, Gneueckow et al. 2007). Maximum temperatures of 55°C were obtained in the prostate using only 25% of the available magnetic field amplitude, and mean intra tumor temperatures were kept between 42 and 46°C for 60 minutes (once per week for 6 weeks). It was determined that this treatment was not enough to kill the cancerous cells but is applicable as a combination treatment (Johannsen, Gneueckow et al. 2007). A quality of life assessment was also completed on this clinical trial, and it was found that quality of life was only temporarily impaired by MNP thermotherapy with urinary symptoms which appeared almost exclusively during the first three weeks of treatment (Johannsen, Gneueckow et al. 2007).

### 3.2.2 Nanoscale Energy Delivery

As discussed above, thermal therapy has been studied for decades, with various successes in MMH and related treatments, but this approach has yet to gain widespread clinical recognition either as an independent treatment or in conjunction with traditional therapies. This section explores the most recent advances in the promising area of MagMED therapy, wherein MNPs are engineered for the selective destruction of cells and/or intracellular structures without a macroscopic temperature rise (Kozissnik, Bohorquez et al. 2013).

Instead of relying on a bulk temperature rise to induce hyperthermia conditions, it was suggested by Gordon, *et al.* in 1979 that intracellular hyperthermia would be more advantageous due to insulation by the cell membrane and lack of convection from blood flow which dissipates heat away from the tumor tissue which is especially problematic in small metastatic tumors (Gordon, Hines et al. 1979). Although there was a growing body of evidence suggesting that local

heating and energy delivery could be used to kill cancer cells, theoretical calculations by Rabin *et al.* indicated that the heat dissipation from the nanoparticle surface through conduction is greater than the heat being generated by the nanoparticles (Rabin 2002). At the single nanoparticle level, Rabin's calculations suggest the nanoparticle temperature difference at steady state to be no greater than  $10^{-5}$  °C, indicating that a single nanoparticle cannot cause any thermal damage. On the macro-scale, Rabin's most conservative calculation indicated that the region occupied by a cluster of magnetic nanoparticles within a cell must be at least 1.1 mm in diameter (two orders of magnitude larger than the typical cancer cell) in order to induce a temperature rise of 6 °C, suggesting that a larger target region is required in order to achieve hyperthermia temperatures. These calculations were completed without taking into account the effects of blood perfusion and potentially higher thermal conductivity values that would both require an even larger heated region in order to reach the same hyperthermia levels.

Despite the theoretical calculations by Rabin in 2002, nanoscale heating effects of MNPs were continually studied, and in 2011, an especially interesting study by Creixell *et al.* showed the ability of internalized iron oxide MNPs in the presence of an AMF to induce significant cellular toxicities without a measureable temperature rise. Iron oxide MNPs were targeted to the epidermal growth factor receptor (EGFR) overexpressed on MDA MB 468 cells by conjugation of epidermal growth factor (EGF) (Creixell, Bohorquez *et al.* 2011). The targeted MNPs were internalized by MDA MB 468 breast cancer cells and in the presence of an AMF induced a significant decrease in cell viability without a measureable temperature rise. Additionally, the cell survival fraction significantly decreased with increasing field amplitude. After these ground-breaking results, the phrase magnetically mediated energy delivery (MagMED) was coined to describe the conversion of magnetic field energy to other forms such as heat or rotational work but without significantly increasing the bulk temperature (Kozissnik, Bohorquez *et al.* 2013).

The theoretical calculations were further disputed when Huang, *et al.* utilized iron oxide nanoparticles targeted to proteins on the membrane of cells expressing TRPV1 to locally deliver heat and open cation channels (Huang, Delikanli et al. 2010). Within 15 seconds of applying the AMF, the cytosolic calcium concentration increased from 100 nM to 1.6  $\mu$ M due to increased calcium influx through the thermally activated TRPV1 channel. Nanoparticle heating at the surface was confirmed using a tethered thermoresponsive fluorophore (DyLight549) which decreased in fluorescence almost immediately upon AMF exposure, indicating heating of more than 15 °C within 15 seconds. Golgi-targeted green fluorescence protein was used to monitor bulk cell temperatures, and remained virtually unchanged during AMF exposure. In a similar study by Polo-Corrales and Rinaldi in 2012, surface temperature of magnetic nanoparticles in the presence of an AMF was monitored using thermoresponsive fluorescent polymers (Polo-Corrales and Rinaldi 2012). Iron oxide MNPs were functionalized with a polymer consisting of poly(N-isopropylacrylamide) copolymerized with a fluorescent modified acrylamide. As temperature increased above 35 °C, the polymer coating changed from hydrophilic to hydrophobic, resulting in an increase in fluorescence intensity. In the presence of an AMF, fluorescence intensity of the polymer coating increased although there was negligible bulk temperature rise, suggesting that the nanoparticle surface temperature was above 35 °C and further contradicting the theoretical calculations provided by Rabin in 2002.

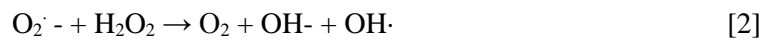
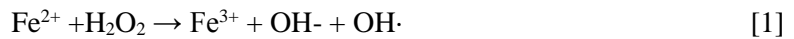
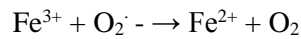
Localized MNP heating has also been studied as a mechanism for timed drug release from liposomes. Amstad *et al.* fabricated liposomes containing iron oxide MNPs within their lipid bilayer with a  $T_m$  well above body temperature (Amstad, Kohlbrecher et al. 2011). Upon actuation of the MNPs by an AMF, the liposome permeability increased due to local temperature increases above  $T_m$ . However, the liposomal structure remained intact suggesting that the bulk temperature did not rise above  $T_m$  and allowed for repeated release from the liposomes.

In addition to the effects of surface heating of magnetic nanoparticles in an AMF, rotational work has also been studied as an explanation to the experimental effects of MagMED. For example, mechanical forces have been used to induce lysosomal permeabilization, leading to the release of proteolytic enzymes such as cathepsins which initiate apoptotic pathways (Linder, Erdal et al. 2005, Kirkegaard and Jaattela 2009, Johansson, Appelqvist et al. 2010). This technique has also been shown to stimulate apoptosis in apoptosis-resistant cell lines (Jaattela 2004). For example, Sanchez *et al.* functionalized a ligand of a G-protein coupled receptor which is over expressed in several malignant cancers to iron oxide MNPs and showed that the internalized nanoparticles decreased cell survival through a lysosomal pathway upon nanoparticle activation by a low power AMF (275 kHz, 40/52 mT) (Sanchez, Diab et al. 2014). Similarly, Domenech *et al.* induced lysosomal permeabilization using EGFR-targeted MNPs in the presence of an AMF (233 kHz, 42 kA/m) (Domenech, Marrero-Berrios et al. 2013). In EGFR positive cells (MDA MB 231), lysosomal disruption was linked to increased cytoplasmic cathepsin B concentrations and increased ROS generation, which led to a significant decrease in viability compared to cells treated with the nanoparticles and no AMF. Connord et al. developed a miniaturized electromagnet to fit under a confocal microscope allowing for real-time analysis of MMP and AMF (53 mT) treatment (Connord, Clerc et al. 2015). Iron oxide MNPs coated with PEG-Amine and functionalized with gastrin, which specifically binds to cholecystokinin-2 receptor, were used in this study. Confocal images taken prior to AMF exposure indicate co-localization of LysoTracker and the MNPs. However, after 30 minutes of AMF treatment, the lysosomes had been permeabilized and co-localization decreased. Another interesting but not fully understood observation was lysosomal alignment with the magnetic field. These results indicate the importance of real-time imaging in order to better understand the intracellular effects of MagMED.

Zhang *et al.* developed a dynamic magnetic field generator to induce nanoparticle rotations about their axis to confirm whether physical nanoparticle rotations can disrupt lysosomal

membranes and induce apoptosis (Zhang, Kircher et al. 2014). By functionalizing the nanoparticles with lysosomal-associated membrane protein-1 (LAMP1), it was found that the shear forces generated by oscillating torques were enough to damage the lysosomal membranes, proving that Brownian rotation of magnetic nanoparticles also plays an important role in MagMED treatment.

In addition to the thermal and mechanical effects described above, the production of reactive oxygen species (ROS) via iron oxide nanoparticles is a potential chemical effect of MagMED. Several studies have correlated the production of ROS to the inherent cytotoxicity of iron oxide MNPs (Mahmoudi, Simchi et al. 2009, Khan, Mohammad et al. 2012, Ahamed, Alhadlaq et al. 2013, Ahamed, Alhadlaq et al. 2013, Koenczoel, Weiss et al. 2013, Luo, Li et al. 2015). Iron oxide MNPs catalyze the Haber-Weiss reaction which makes use of Fenton chemistry (Kehrer 2000). The Fenton chemistry reaction set is shown as Equation 1 and the Haber-Weiss reaction (net reaction) is shown as Equation 2.



When iron oxide nanoparticles enter a cell, they can stimulate the generation of ROS via one of two pathways: (1) the release of ions into the cytosol resulting in the iron ions participating in the Haber-Weiss cycle or (2) the surface of the nanoparticle may act as a catalyst (Klein, Sommer et al. 2012). Although this reaction can proceed without the addition of an AMF, recent work by Wydra *et al.* demonstrated that the reaction is further catalyzed by iron oxide nanoparticles in the presence of an AMF (Wydra, Oliver et al. 2015). This study used the degradation of methylene blue by magnetite nanoparticles, and hydrogen peroxide was used to measure the reactivity of uncoated iron oxide MNPs in an AMF. Temperature is a driving factor of the Fenton reaction up to 40 °C, so by increasing the surface temperature of the MNPs, hydroxyl radical formation was

catalyzed, degrading methylene blue. At low nanoparticle concentrations, where the bulk temperature remained constant upon exposure to an AMF, local nanoscale heating effects were more pronounced, leading to an enhancement in methylene blue degradation compared to the Arrhenius prediction.

### **3.3 Combination therapy**

Thermal therapy is often used in combination with conventional cancer therapies such as chemotherapy, radiation, surgical resection, and gene therapy to enhance the efficacy of these treatments. A variety of chemotherapeutics are more effective when administered in the hyperthermia range due to increased rate constants of alkylation, enhanced drug uptake, and inhibition of repair of drug-induced lethal or sub-lethal damage (Issels 2008, Hervault and Thanh 2014). When selecting a chemotherapeutic combination therapy, an important consideration is the mechanism of action to make sure that it will complement the hyperthermia modality. When utilizing MMH, chemotherapeutics can either be administered in bulk or bound to the MNPs and released upon exposure to an AMF. Cisplatin (CDDP) (Lee, Rodriguez-Luccioni et al. 2011, Alvarez-Berrios, Castillo et al. 2013, Petryk, Giustini et al. 2013, Kruse, Meenach et al. 2014), bortezomib (BZ) (Alvarez-Berrios, Castillo et al. 2014, Alvarez-Berrios, Castillo et al. 2015), and melphalan (Brusentsov, Brusentsova et al. 2007) are common chemotherapeutics that have been studied for bulk combination treatments with MMH.

Cisplatin binds to DNA, resulting, ultimately, in inter- or intra-strand crosslinking that prevents DNA transcription, blocks cell replication, and finally results in apoptosis. Cisplatin has been previously shown to be more effective when administered in the hyperthermia temperature range (Halamikova, Vrana et al. 2007, Issels 2008, Itoh, Yamada et al. 2010). Lee et al. reported the effects of treatment sequence and heating technique (MMH or HWH) on Caco-2 cells (Lee, Rodriguez-Luccioni et al. 2011). The highest cytotoxicity was observed when CDDP and MMH were applied at the same time with an additional drug exposure period, but MMH was more

effective than HWH independent of treatment sequence. The mechanism of cell death after combined treatment is likely to be a form of programmed cell death, such as apoptosis rather than necrosis. In a subsequent study (Alvarez-Berrios, Castillo et al. 2013), the enhancement of cisplatin in Caco-2 cells by MMH was correlated with an increase in cell membrane fluidity. The presence of copper inhibited CDDP uptake in control cells by hindering copper transporter-mediated active transport, but this same inhibition was not seen in HWH or MMH. Platinum concentration inside cells after MMH was significantly greater than after HWH, which corresponded to the increase in membrane fluidity observed after MMH. Another study by Kruse et al. used crosslinked dextran coated iron oxide MNPs in the presence of an AMF to administer hyperthermia treatment to A549 lung carcinoma in combination with CDDP (Kruse, Meenach et al. 2014) (see Chapter 4). Hyperthermia treatment was administered for 30 minutes simultaneously with CDDP and resulted in an additive effect of the combined treatment when analyzed 72 hours post treatment.

An *in vivo* study of MMH (60 minutes at 43°C) combined with CDDP on murine mammary adenocarcinoma model showed that MMH combined with CDDP was 1.7 times more effective than MMH alone and 1.4 times more effective than CDDP alone (Petryk, Giustini et al. 2013). Tumor growth was monitored over time and the control took 14 days to grow three times its original size whereas MMH alone resulted in a delay to 21 days, CDDP alone took 25 days and the combined treatment took 36 days.

Bortezomib (BZ), an inhibitor of the chymotrypsin-like activity of the 26S proteasome in mammalian cells, is another chemotherapeutic that has been studied in combination with MMH (Alvarez-Berrios, Castillo et al. 2014, Alvarez-Berrios, Castillo et al. 2015). Alvarez-Berrios et al. showed that MMH enhances the cytotoxicity of BZ in both BZ sensitive (MDA MB 468 and caco-2) and resistant (A2780) cancer cell lines (Alvarez-Berrios, Castillo et al. 2014). Carboxymethyl coated iron oxide MNPs (3.8 mg/mL) in the presence of an AMF (233 kHz) at 29.39 or 34.73 kA/m resulted in hyperthermia treatment at 43°C or 45°C, respectively. A different concentration of BZ



for each cell line was used in order to produce approximately the same level of proteasome inhibition after a pre-exposure time of 3 hours. Although BZ sensitive cells and BZ resistant cells showed similar levels of proteasome inhibition, thermal sensitization induced by MMH in combination with BZ in cells resistant to BZ resulted in significant cell death potentially due to an increase in cell membrane fluidity.

BZ is a drug that increases the toxicity of proteotoxic stress in cancer cells because such cells produce significant amounts of misfolded and non-functional proteins, such that alternative mechanisms of cell protection against proteomic stress can be overwhelmed (Alvarez-Berrios, Castillo et al. 2015). Additionally, it has been shown that the combination of cellular effects induced by MMH, such as microtubule disruption and protein damage, results in progressive enhanced proteotoxic stress, which can lead to programmed cell death. MCF-7 cells treated with MMH or MMH and BZ at 43 °C (30 minute recovery time) showed more protein aggregation surrounding the nucleus compared to HWH or BZ with HWH, respectively. After 2.5 hours of recovery time, MMH had induced significant microtubule damage (43°C). It was speculated that the combination of microtubule damage and increased protein aggregation caused by MMH induces progressive enhanced proteotoxic stress, which produces significant cell death.

As previously mentioned, chemotherapeutics can be combined with MMH by functionalizing the magnetic nanoparticle with a chemotherapeutic of interest – by tethering with a responsive linker or encapsulation within a coating matrix – resulting in controlled drug release upon exposure to an external stimuli such as an AMF (as discussed in greater detail in section 2.1 above) or change in pH. Huang et al. recently synthesized pH sensitive cisplatin-loaded magnetite hydroxyapatite nanoparticles (Huang, Chen et al. 2015). In a low pH environment, 20% of the CDDP was released compared to 5% at a pH of 7. After treatment with the nanoparticles at 300 µg/mL for 48 hours, A549 viability was significantly decreased, and further decreased in the presence of an AMF for 30 minutes resulting in a temperature increase to 43°C. Additionally, in an *in vivo* subcutaneous rat

model, tumor growth was completely inhibited in the group treated with the nanoparticle system combined with AMF treatment. In another study by Babincova et al., iron oxide nanoparticles were coated with a hydrophilic starch polymer coupled with phosphate functional groups (Babincova, Altanerova et al. 2008). The negative coating charge allowed for ionic binding of positively charged species such as cisplatin. A 20 minute hyperthermia treatment was induced using an AMF (3 MHz, 1.5 mT), and during this time, almost all of the drug was released from the nanoparticle. The combined MMH and CDDP treatment from the drug loaded iron oxide nanoparticle resulted in a relative viability of  $23.6 \pm 8.6\%$ . This is significantly less than either the hyperthermia treatment ( $85.2 \pm 7.5\%$ ) or the equivalent CDDP treatment ( $73.8 \pm 5.6\%$ ) alone, indicating a synergistic toxicity of CDDP and MMH.

5-fluorouracil (5-FU) has also been conjugated to iron oxide nanoparticles for combination therapy. Li et al. functionalized a magnetite core with PMSA followed by covalent modification with poly-A15 (Li, Huang et al. 2013). The nanoparticles were then functionalized with 5-FU and tagged with a HER2 antibody. A subcutaneous model with a bladder cancer cell line (MBT-2) was used to evaluate the efficacy of combined 5-FU and 15 minute thermal therapy treatment. For small tumors, hyperthermia treatment alone was able to significantly reduce the tumor volume. However, for larger tumors, only the combined treatment of using 5-FU functionalized nanoparticles for MMH resulted in a decrease in tumor volume. A complementary result was seen when the targeted, drug functionalized nanoparticles were injected through the tail vein followed by AMF exposure. The nanoparticles without AMF treatment did not inhibit tumor growth (likely due to no 5-FU release) nor did treatment with an equivalent dose of 5-FU. The drug loaded nanoparticles with AMF exposure led to complete tumor regression two days after the last treatment. In another study, 5-FU and curcumin were functionalized to magnetic nanoparticles, and when exposed to an AMF, the dual drug release combined with thermal therapy led to an enhanced efficacy compared to either drug treatment alone (Balasubramanian, Girija et al. 2014). This is thought to be due to increased

efficiency of drug diffusion from the nanoparticles or to the fact that injured cells could not recuperate from the impairment induced by thermal treatment owing to the combined treatment of 5-FU and curcumin.

Heat shock protein (HSP) inhibitors are of particular interest due to up regulation of heat shock proteins during hyperthermia treatment. Geldanamycin, a HSP 90 inhibitor, was conjugated to iron oxide nanoparticles via a thermally cleavable linker for controlled release upon exposure to an AMF (Yoo, Jeong et al. 2013). An *in vitro* study on MDA MB 231 cells showed geldanamycin functionalized iron oxide MNPs negated the increased HSP 90 expression seen with MMH alone, and an *in vivo* study resulted in complete tumor regression 8 days after treatment when the geldanamycin functionalized MNPs were used for MMH.

Additional studies have been completed using methotrexate (Gao, Yan et al. 2012), doxorubicin (Xu, Karmakar et al. 2012), and erlotinib (Xu, Karmakar et al. 2012) functionalized magnetic nanoparticles for combination therapy. These studies also indicate that drug combined with hyperthermia via MNPs in an AMF is more effective than either treatment alone. Methotrexate combined with MMH resulted in a synergistic treatment of MCF-7 cells *in vitro* (Gao, Yan et al. 2012) while doxorubicin efficacy was significantly increased when combined with MMH (Xu, Karmakar et al. 2012).

MMH can also be combined with radiation and gene therapy for enhanced efficacy. There are several studies that address hyperthermia combined with radiation (Horsman and Overgaard 2007, Hurwitz, Hansen et al. 2011, Neshasteh-Riz, Rahdani et al. 2014), but minimal studies that utilize MMH with radiation therapy. Hyperthermia has been shown to increase blood supply to the tumor, which increases the local oxygen levels and the efficacy of radiation therapy is tied to the formation of free radicals more so than DNA damage. In an orthotopic tumor model of R3327 Dunning tumor cell line, MNPs with an aminosilane shell were used for two rounds of MMH for 30 minutes each combined with 20 Gy, 40 Gy or 60 Gy total radiation therapy (Johannsen, Thiesen et al. 2006).

Thermal therapy viability inhibition alone was 44.1-51.7% whereas the combined treatment (20 Gy radiation total with hyperthermia) had an inhibition of 87.5-89.2% compared to the control. A clinical trial was also completed in which 59 patients with recurrent glioblastoma received a direct injection of iron oxide MNPs followed by 30 minutes of heating (43°C) in an AMF (100 kHz, 2-15 kA/m) (Maier-Hauff, Ulrich et al. 2011). A median radiation dose of 30 Gy was given to the patients immediately before or following hyperthermia treatment. The combined therapy resulted in an extension of the median overall survival after primary tumor diagnosis from 14.6 to 23.2 months. There was also a gain of 7.2 months for survival following tumor recurrence. Although there are differences between the treatments of the patients, the increase in survival time can be attributed to the combination of thermo-radiotherapy.

Thermal therapy via magnetic nanoparticles combined with gene therapy is a recently developed area in this field. A review of heat responsive gene expression utilizing thermal therapy via other methods than MNPs was published in 2009 (Walther and Stein 2009). More recently in 2014, Shah et al. evaluated the efficacy of pro-apoptotic amphipathic tail-anchoring peptide (ATAP) delivery by MNPs. MMH was used to increase pro-apoptotic proteins in glioblastoma multiforme cells and metastatic breast cancer cells, while the ATAP peptide selectively targeted mitochondria and induced cytochrome c release through disruption of the mitochondrial membrane. The result of gene therapy treatment combined with MMH resulted in enhanced toxicity compared to ATAP therapy alone, which is likely due to an increase in peptide solubility upon conjugation to the nanoparticles. In another study completed by Yin et al. in the same group, lethal-7a miRNA was conjugated to MNPs, as lethal-7a is a known tumor suppressor that inhibits malignant growth by targeting factors such as the BRCA family, RAS, IGF1R and c-Myc, which all overlap with downstream regulation of heat shock proteins (Yin, Shah et al. 2014). Combined thermal therapy via MMH and gene therapy with lethal-7a showed an additive effect, resulting in significantly more apoptosis in brain cancer cells than either treatment alone. Overall, gene therapy combined with

MMH is a promising avenue for combination therapy and can potentially result in more personalized treatment of cancer.

### 3.4 Conclusions

Thermal therapy using MNPs has been shown to decrease cancer cell growth both *in vivo* and *in vitro* to a greater extent than thermal therapy administered by external methods such as HWH. In addition, immunotherapeutic effects of thermal therapy have been observed and show promise for future development. However, due to the bulk concentration of nanoparticles required to heat tissue into the hyperthermia range, translation to clinical trials has been minimal. Additionally, applications of MMH as a viable treatment modality is limited by tumor size due to heat transfer from small tumors (i.e. metastases) to the surrounding tissue. In order to improve thermal therapy via MNPs, *in vivo* heating properties need to be improved and specific strategies for targeting to tumor tissue to decrease non-specific accumulation need to be developed.

Energy delivery on the nanoscale provides another avenue of thermal therapy where only intracellular nanoparticles are actuated by an AMF, resulting in subcellular heating effects without a macroscopic temperature rise. Energy delivery on the nanoscale has been shown to result in destabilization of lysosomal membranes and toxic effects to other organelles. Previously, the focus of MNP development was improving the heating capabilities to overcome the thermal delivery limitations, but in addition to this need for other therapy strategies, many researchers are now exploring intracellular targets for nanoscale thermal therapy applications. Further studies need to be performed to gain a better fundamental understanding of the mechanisms at play. However, an exciting prospectus is to combine the knowledge gained through combined chemotherapy with this new therapy strategy. Novel nanoparticle architectures should be synthesized to deliver therapeutics intracellularly, relying on nanoscale thermal effects to improve efficacy.

Thermal therapy as a single treatment is often insufficient to induce irreparable cellular damage, but when combined with a secondary treatment, the combination therapy is often found to

be more effective than either treatment alone. A variety of chemotherapeutics are more effective when administered at elevated temperatures due to increased rate constants of alkylation, increased drug uptake, and repair inhibition of drug-induced lethal or sub-lethal damage. Thermal therapy also increases oxygen content within tissue, making radiation more effective. Therefore, as a combination treatment, thermal therapy via MNP activation in an AMF has greater application. However, the same limitations such as concentration dependence, heating properties, and AMF parameters still remain. As the field progresses, it will be important to develop targeted MNPs with excellent heating properties in order to overcome some of these limitations and, as previously mentioned, explore nanoscale thermal therapy in combination with conventional treatments.

In the last several years, there have been many exciting developments in the use of MNPs and their composites for remote controlled therapies. These include novel remote controlled drug delivery systems at various scales for modulated release and magnetic field guidance, controlled energy release for thermal therapy and nanoscale energy therapy, and thermal therapy in combination with other treatments such as chemotherapy or radiation. With numerous *in vivo* demonstrations of efficacy, these remote controlled therapies are starting to progress to the clinic, and they are expected to greatly impact the treatment of various diseases in the future.

## **Chapter 4 Synthesis and characterization of CREKA-conjugated iron oxide nanoparticles for hyperthermia applications**

The dextran-coated iron oxide nanoparticle system were synthesized via a one-step co-precipitation reaction. The dextran surface was then crosslinked and functionalized with the CREKA peptide. The physicochemical properties of the nanoparticles were characterized at each step of the synthesis process. The goal of this work was to analyze the physicochemical properties of the nanoparticle system and to complete a proof-of-concept magnetically mediated hyperthermia study. The chapter is taken directly or adapted from work **published in Kruse, Meenach, et al. (2014)** Copyright 2014 Elsevier B.V. Used with permissions from Anastasia M. Kruse, Samantha A. Meenach, Kimberly W. Anderson and J. Zach Hilt, “Synthesis and characterization of CREKA-conjugated iron oxide nanoparticles for hyperthermia applications”, Acta Biomaterialia and Elsevier B.V.

### **4.0 Abstract**

One of the current challenges in the systemic delivery of nanoparticles in cancer therapy applications is the lack of effective tumor localization. Iron oxide nanoparticles coated with crosslinked dextran were functionalized with the tumor homing peptide CREKA, which binds to fibrinogen complexes in the extracellular matrix of tumors. This allows for the homing of these nanoparticles to tumor tissue. The iron oxide nanoparticle core allows for particle heating upon exposure to an alternating magnetic field (AMF) while the dextran coating stabilizes the particles in suspension and decreases the cytotoxicity of the system. Magnetically mediated hyperthermia (MMH) allows for the heating of tumor tissue to increase the efficacy of traditional cancer treatments using the iron oxide nanoparticles. While MMH provides the opportunity for localized heating, this method is currently limited by the lack of particle penetration into tumor tissue, even after effective targeted delivery to the tumor site. The CREKA-conjugated nanoparticles presented were characterized for their size, stability, heating capabilities and biocompatibility. The particles had a hydrated diameter of 52 nm, were stable in PBS and media with 10% v/v FBS over at least

twelve hours, and generated enough heat to raise solution temperatures well into the hyperthermia range (41 – 45 °C) when exposed to an AMF due to an average specific absorption rate (SAR) of 83.5 W/g. Cytotoxicity studies demonstrated that the particles have low cytotoxicity over long exposure times at low concentrations. A fibrinogen clotting assay was used to determine the binding affinity of CREKA-conjugated particles, which was significantly greater than the binding affinity of dextran, only coated iron oxide nanoparticles demonstrating the potential for this particle system to effectively home to a variety of tumor locations. Finally, it was shown that *in vitro* MMH increased the effects of cisplatin compared to cisplatin or MMH treatments alone.

#### **4.1 Introduction**

Non-small cell lung cancer (NSCLC) is the leading cause of cancer-related deaths in the United States each year (ACS 2013). Survival without treatment for stage IV NSCLC is 6 months if left untreated and only 9 to 12 months with treatment. Hyperthermia, the heating of tissue to 41-45 °C, has been shown to be effective in treating lung cancer when used in conjunction with radiation or chemotherapy (Vertrees, Das et al. 2005, Itoh, Yamada et al. 2010, Lee, Rodriguez-Luccioni et al. 2011). Current hyperthermia treatments (e.g., whole body and regional hyperthermia) have several disadvantages, including damaging healthy tissue, limited penetration of heat into the body, under-dosage of heat, and complications such as increased heart rate and increased cardiac output (Zwischenberger, Vertrees et al. 2004, Issels 2008, Kumar and Mohammad 2011). Hyperthermia treatments are further challenged by deep seated tumors and lack the ability to penetrate surrounding tissues to raise the tumor tissue into the hyperthermia range (Dennis, Jackson et al. 2009). Although various limitations exist, treatment of cancer via hyperthermia in conjunction with cisplatin was shown to have synergistic effects (Babincova, Altanerova et al. 2008) and sensitization of cisplatin-resistant cell lines (Hettinga, Lemstra et al. 1995). Cisplatin (20 µg/mL or 200 µg/mL) combined with mild incubator-induced hyperthermia at 41 °C was shown to significantly decrease the surviving fraction of T24 bladder cancer cells *in vitro* (Itoh, Yamada et



al. 2010). In another study completed by Hettinga and coworkers, murine tumor cells were mutated *in vitro* for cisplatin resistance (Hettinga, Lemstra et al. 1995). The cisplatin-resistant cell line was exposed to cisplatin (0 - 10  $\mu\text{g/mL}$ ) for 45 minutes at either 37 °C or 44 °C. Hyperthermia with cisplatin exposure resulted in a significant decrease in the percentage of cell survival of the cisplatin-resistant cells. A second experiment demonstrated that the cisplatin-resistant cells were sensitized by hyperthermia by pre-heating the cells at 44 °C for 10 minutes prior to 45 minutes of cisplatin exposure at 37 °C. This treatment sequence further decreased the cell survival of the cisplatin-resistant cells (Hettinga, Lemstra et al. 1995).

In the presence of an alternating magnetic field (AMF), iron oxide magnetic nanoparticles generate heat and can induce hyperthermia. Magnetically-mediated hyperthermia, which is the heating of tissue using heat generated by magnetic nanoparticles in the presence of an AMF, shows great promise in overcoming the limitations of current hyperthermia treatments due to the ability of nanoparticles to deliver heat directly to the tumor site, therefore limiting the heat exposure to surrounding tissues. Iron oxide nanoparticles (IONPs) have the ability to passively or actively target tumors, and in the presence of an external AMF, can generate heat via multiple possible loss mechanisms including Néel paramagnetic switching, friction losses from Brownian rotation, and hysteresis (Dennis, Jackson et al. 2009). IONPs have been studied as imaging agents, drug delivery systems, and therapeutic enhancers due to their inherent biocompatibility, magnetic properties, and lack of protein adsorption after proper coating (Laurent, Dutz et al. 2011). In cancer therapy applications of IONPs, the main limitation to treating solid tumors is the limitations of particle localization. Vascularization and the enhanced permeation and retention (EPR) effect allow for passive targeted delivery of nanoparticles to the periphery of solid tumors. However, active targeting through peptides or ligands can result in higher local concentrations of nanoparticles and lower systemic concentrations, which is required for more effective treatment (Ruoslahti, Bhatia et al. 2010).

CREKA, a tumor homing peptide, recognizes fibrin-associated plasma proteins, which are overexpressed in cancerous tissue but not in normal, healthy tissue. The walls of tumor vessels and the interstitial space within tumors contain these fibrin-fibronectin complexes due to protein seepage from the leaky vasculature of the tumor (Ruoslahti, Bhatia et al. 2010). It was shown that CREKA can specifically target fibrin-fibronectin complexes as demonstrated by the lack of the peptide targeting to syngeneic B16F1 melanoma tumors grown in mice null of fibrinogen or lacking plasma fibronectin but significant homing to syngeneic B16F1 melanoma tumors in wild-type mice of the same litter (Simberg, Duza et al. 2007). CREKA is a small, linear peptide of five amino acids, which makes it attractive to use for conjugation with nanoparticles since multiple peptides can be conjugated to a single nanoparticle (Simberg, Duza et al. 2007). IONPs do not require internalization into cancer cells to be effective at heating the tumor tissue. Internalization of IONPs has been shown to enhance the anti-cancer effects of thermal energy dissipation compared to bulk hyperthermia methods (Creixell, Bohorquez et al. 2011). Intracellular hyperthermia does not result in a bulk temperature rise but rather relies on the ability of individual nanoparticles to raise the temperature of their immediate surroundings (Krpetic, Nativo et al. 2010). Although targeting promoted uptake of IONPs can enhance their intracellular concentration, the targeting peptides, such as EGFR, are still cell line specific. Therefore, CREKA conjugation to IONPs is advantageous over other peptides in that it binds to complexes within the tumor vasculature rather than specific integrins on the surface of cells (Ruoslahti, Bhatia et al. 2010).

In this study, peptide-conjugated dextran-coated IONPs for enhanced tumor homing have been developed and characterized. Physicochemical characterization and *in vitro* biocompatibility studies are imperative for rationally developing and understanding a nanoparticle system. Prior to *in vivo* studies, the properties of this nanoparticle system such as size, stability, heating profiles, toxicity, and fibrinogen binding affinity need to be optimized. The desired size range for our nanoparticles is around 50 nm, which is expected to allow for tumor penetration and initial

accumulation to tumor tissue via the EPR effect. Stability in media is an important property for systemically delivered nanoparticles, and the heating properties must be sufficient to induce hyperthermia conditions upon exposure to an AMF with substantial SAR values. Nanoparticle systems used for biological applications such as these must be screened for toxicity at low concentrations over long time frames, and for this specific peptide-conjugated IONP system, the binding affinity of the particles to fibrinogen complexes was important to verify since fibrinogen complexes within the tumor vasculature are the target of this system. A proof-of-concept study was then completed to show that this nanoparticle system could be used to enhance the effectiveness of cisplatin through magnetically mediated hyperthermia. This peptide-conjugated IONP has optimal physical characteristics, such as size (Fox, Szoka et al. 2009, Phillips, Gran et al. 2010) and stability, for tumor homing via fibrin-fibronectin complexes and heating capabilities, which can be utilized for the hyperthermia treatment of lung cancer, in combination with chemotherapy. Although this study focuses on CREKA-conjugated IONPs for the treatment of lung cancer, this nanoparticle system has the ability to treat a multitude of cancerous tumors since it recognizes fibrinogen complexes rather than specific surface integrins, which are often cell line dependent.

## **4.2 Materials and Methods**

### *4.2.1 Materials*

Iron (III) chloride hexahydrate ( $\text{FeCl}_3 \cdot 6\text{H}_2\text{O}$ ), iron (II) chloride ( $\text{FeCl}_2 \cdot 4\text{H}_2\text{O}$ ), 9 – 11 kDa dextran, epichlorohydrin (ECH), cisplatin (CDDP), fibrinogen, di-methyl sulfoxide (DMSO), and thrombin were obtained from Sigma Aldrich (St. Louis, MO). Ammonium hydroxide ( $\text{NH}_4\text{OH}$ ) was purchased from EMD Chemicals (Gibbstown, NJ). N- $\alpha$ -maleimidoacet-oxysuccinimide ester (AMAS) linker was obtained from Thermo Scientific (Rochester, NY). CREKA peptide conjugated with 5-fluorescein isothiocyanate-aminohexanoic acid (FITC-CREKA) was custom ordered through Biomatik (Cambridge, Ontario). Fetal bovine serum (FBS) was purchased from Fisher Scientific (Florence, KY). Dulbecco's Modified Eagle Medium (DMEM), pen-strep, L-glutamine,

Fungizone®, and sodium pyruvate were all purchased from Invitrogen (Grand Island, NY), and trypsin was purchased from American Type Culture Collection (ATCC, Manassas, VA). 190 proof ethanol was purchased from Pharmco-Aaper (Shelbyville, KY) and phosphate buffered saline solution (PBS) (10X) was purchased from EMD Millipore (Billerica, MA). All materials were used as received.

#### *4.2.2 Crosslinked dextran coated iron oxide nanoparticle synthesis*

A modified one-pot co-precipitation method (Frimpong, Dou et al. 2010) was used to prepare dextran coated IONPs.  $\text{FeCl}_3 \cdot 6\text{H}_2\text{O}$  and  $\text{FeCl}_2 \cdot 4\text{H}_2\text{O}$  were combined in a 2:1 molar ratio (2.2 grams and 0.8 grams, respectively) and dissolved in 25 mL deionized (DI) water and sealed in a three-neck flask under vigorous stirring and an inert nitrogen environment. 11 grams of dextran was solubilized in 50 mL of DI water and added to the three-neck flask. The solution was heated to 85 °C at which 5 ml of  $\text{NH}_4\text{OH}$  was injected into the vessel. The reaction was carried out for 1 hour at 85 °C. The particles were centrifuged at 1000 rpm for 10 minutes to remove large agglomerates. The remaining particles were then dialyzed against DI water for 24 hours. Dextran coated IONPs were crosslinked using ECH for increased stability (Stephen Palmacci 1993). The particle colloid (9 mL, 1 mmol Fe) was added to 9 mL 5M NaOH and 2 mL ECH. The reaction was carried out for 24 hours at room temperature under continuous agitation. The particles were then dialyzed against DI water for 24 hours to remove excess ECH. Crosslinked IONPs were then aminated to allow for peptide conjugation. This was accomplished by reacting 0.2 mL of 30% ammonium hydroxide with the particles (5 mL, 0.2 mmol Fe) for 24 hours at room temperature under continuous agitation. The particles were then dialyzed against DI water for 24 hours.

#### *4.2.3 CREKA conjugation of iron oxide nanoparticles*

Amine conjugated IONPs were further conjugated with AMAS linker. The primary amines on the nanoparticles react with the N-hydroxysuccinimide of the linker, and CREKA can then be conjugated to the particle surface by reacting the sulfhydryl group on the cysteine with the

maleimide group of the linker. Particles were re-suspended at a concentration of 1 mg Fe/mL in PBS, and 2.5 mg AMAS per 2 mg Fe were dissolved in DMSO prior to addition to the nanoparticle suspension (Simberg, Duza et al. 2007). After the AMAS addition under vortexing, the reaction was carried out for 40 minutes at room temperature. Particles were then washed three times with PBS on 100,000 MWCO cellulose Millipore filtration columns. FAM-CREKA was then added to the particle suspension at 25 mg per 4 mg Fe (Simberg, Duza et al. 2007). Particles were incubated overnight at 4°C and then washed again with PBS. To serve as a control for the CREKA-conjugated IONPs, fluorescein isothiocyanate (FITC) was conjugated to amine groups on crosslinked dextran IONPs. FITC was added in a 1:10 molar ratio to iron oxide (0.434 mmol Fe<sub>3</sub>O<sub>4</sub> and 0.0434 mmol FITC) and dissolved in 5 mL ethanol. The reaction was carried out for six hours at room temperature. The particles were then washed with DI water and concentrated using ultrafiltration columns. A summary of the systems investigated is included in Table 4.1, and a schematic of the systems synthesized is included in Figure 4.1.

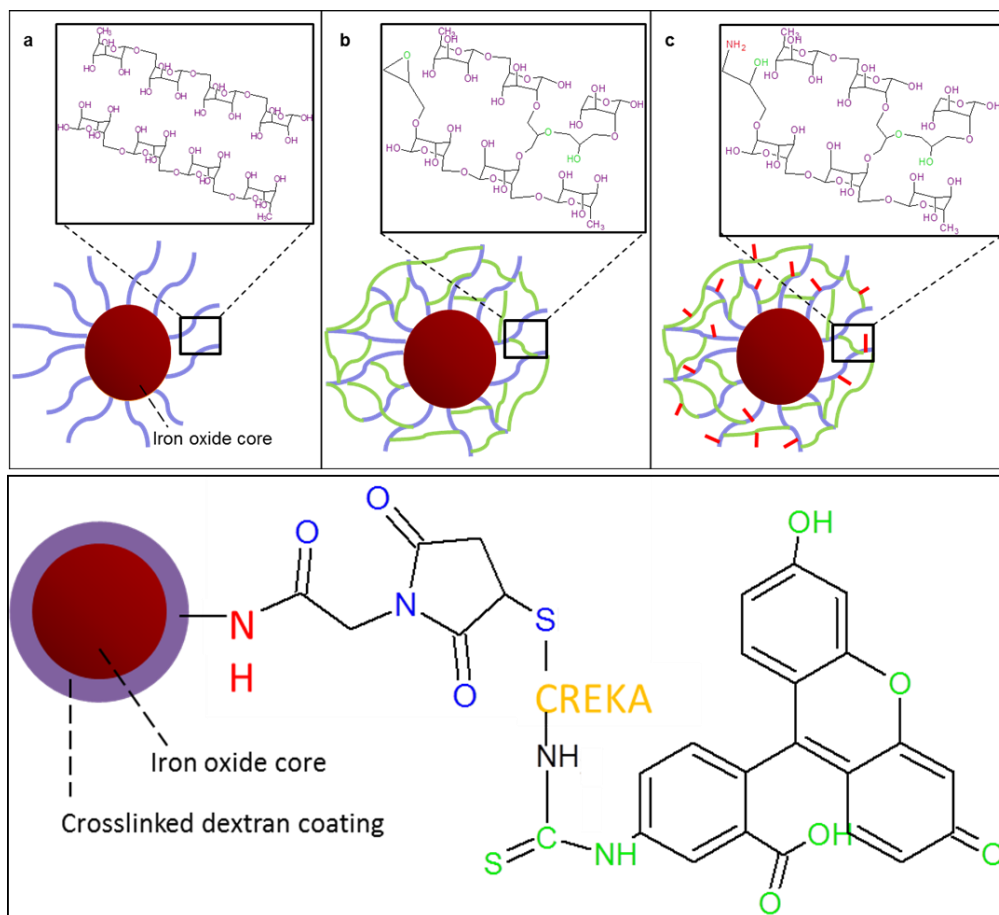


Figure 4.1 Iron oxide nanoparticle synthesis process for the (a) dextran coating, (b) epichlorohydrin crosslinking, (c) amine conjugation, and (d) conjugation with an AMAS linker, connecting the FAM-labeled CREKA to the primary amine.

#### 4.2.4 Particle characterization

*Transmission electron microscopy (TEM).* TEM was completed using a JEOL 2010F system operating at 200 KeV. Iron oxide nanoparticles were diluted to 200  $\mu\text{g/mL}$  Fe in DI water and then dried on carbon TEM grids prior to analysis.

*Ultraviolet (UV)-Visible spectroscopy.* The stability of the nanoparticles was analyzed using a CaryWin 50 probe UV-visible spectrophotometer. IONPs were diluted to 200  $\mu\text{g/mL}$  Fe in PBS or DMEM with 10% FBS. Sample absorbance was read at 540 nm over 12 hours.

*Thermogravimetric analysis (TGA).* TGA was used to quantify the mass percent of the iron oxide core in the particle systems using a Netzsch Instruments STA 449A system. Approximately 5 mg of particle sample was heated at a rate of 5 °/minute. At 100 °C, the sample was held isothermally for 20 minutes to vaporize residual water. The samples were heated at 5 °/minute until reaching 500 °C where they were held isothermally for an additional 20 minutes. The reported mass loss reported was the actual mass loss normalized to the initial sample mass after isothermal heating at 100 °C.

*Dynamic light scattering (DLS).* DLS measurements were obtained using a Beckman Coulter Delsa Nano C particle analyzer. Nanoparticle solutions were diluted to 200 µg/mL and were sonicated in a water bath prior to size analysis.

*Alternating magnetic field (AMF) heating.* The nanoparticle heating profiles were obtained using a custom made Taylor Winfield magnetic induction source, and the temperature was measured with a fiber optic temperature sensor (Luxtron FOT Lab Kit from LumaSense). Nanoparticle suspensions were diluted in DI water to a concentration of 5 mg/ml iron oxide. One milliliter of suspension in a 2 ml microcentrifuge tube was placed in the center of the AMF induction coil. The suspension was heated at a field amplitude of 58 kA/m and frequency of 292 kHz until the temperature of the suspension reached steady-state. The specific absorption rate (SAR) values of the nanoparticle suspensions were then calculated using the following equation:

$$SAR = \frac{C_{p,Fe}m_{Fe} + C_{p,H2O}m_{H2O}}{m_{Fe}} \frac{dT}{dt} \quad [4.1]$$

where  $C_{p,Fe}$  is the heat capacity of iron,  $m_{Fe}$  the mass of iron,  $C_{p,H2O}$  the heat capacity of water,  $m_{H2O}$  the mass of water, and  $dT/dt$  the initial slope of the heating profile.

#### *4.2.5 Cytotoxicity analysis of particle systems*

A549 lung carcinoma cells obtained from ATCC were cultured from passages 5 - 10 in DMEM supplemented with 10% FBS, 10  $\mu\text{g/ml}$  Fungizone®, 2  $\mu\text{g/ml}$  penicillin-streptomycin, and 4mM L-glutamine. Cells were seeded into 96-well plates at 4,000 cells/well and incubated for 24 hours. The cells were then exposed to nanoparticles in complete cell media at concentrations of 50, 100, 350, and 500  $\mu\text{g Fe/ml}$ . Cytotoxicity was determined using a calcein red fluorescent stain (1  $\mu\text{M}$ ,  $\lambda_{\text{ex}}=540\text{nm}$  and  $\lambda_{\text{em}}=590\text{nm}$ ) after 24 and 48 hours. Cell viability was analyzed using a Biotek SynergyMx microplate reader and the fluorescence of the cells exposed to the nanoparticle solutions was normalized to the fluorescence of the control cells.

#### *4.2.6 CREKA and CREKA IONP binding affinity to fibrinogen clots*

To synthesize fibrinogen clots, 75  $\mu\text{L}$  of fibrinogen solution (2 mg/mL) in 0.9% NaCl was added to a 96-well plate. 30  $\mu\text{L}$  of a 2.5 U/mL thrombin solution in 0.9% NaCl was subsequently added to the same 96-well plates. The plates were placed in an incubator shaker at 37°C for 5 minutes, and then gels were formed after four hours incubation at 37°C. Binding affinity of fluorescently labeled CREKA conjugated IONPs (CREKA-IONP) was compared to the binding affinity of unconjugated CREKA (CREKA only) and FITC conjugated iron oxide nanoparticles without CREKA (FITC-IONP). CREKA-IONP and FITC-IONP systems were diluted by taking 5, 10, 25, and 50  $\mu\text{L}$  of nanoparticle solution and diluting to a total volume of 50  $\mu\text{L}$  with DI water. The exact nanoparticle concentration was not necessary as taking the fluorescence ratio of the bound to free particles was determined at the same concentration. CREKA was diluted to 50, 100, 250 and 500  $\mu\text{M}$ . 50  $\mu\text{L}$  of solution (particle or CREKA only) was added to each clot. After one hour, half of the samples were washed twice with 120  $\mu\text{L}$  of DI water to remove any CREKA or IONPs not bound to the fibrinogen clots, and the fluorescence of the plate was read on the microplate reader ( $\lambda_{\text{ex}}=488\text{ nm}$  and  $\lambda_{\text{em}}=520\text{ nm}$ ). The bound CREKA or FITC fluorescence (washed gels) was normalized to the corresponding free (unwashed gels) solution for each sample.



#### 4.2.7 *In vitro magnetically mediated hyperthermia and cisplatin combined treatment*

One mL of A549 lung carcinoma cells (passage 15) was suspended in complete cell culture media in a 1.5 ml microcentrifuge tube at a concentration of 300,000 cells. The vials were then centrifuged at 800 x g for 5 minutes to pellet the cells. The media supernatant was removed and the cells were resuspended in 1 mL of the respective treatment solutions. The six treatments are outlined in Table 4.3. Cisplatin treatments were administered at 100  $\mu$ M, IONP were administered at a concentration of 3 mg/mL, and hyperthermia was induced by the presence of an alternating magnetic field (51-58 kA/m). Treatments lasted 30 minutes, and all controls were also exposed to experimental conditions (i.e. room temperature) for 30 minutes. After treatment, the vials were centrifuged at 800 x g for 5 minutes, the treatment solution was removed, and replaced with fresh media. A second centrifugation cycle was completed to further wash the cells of the treatment solutions. The treated cells were then seeded into 48-well plates at 30,000 cells/mL (250  $\mu$ L/well). The viability of the cells was analyzed 48 and 72 hours post-treatment using a calcein AM assay (2  $\mu$ M,  $\lambda_{ex}$ =494 nm and  $\lambda_{em}$ =517 nm) analyzed by a microplate reader. The fluorescence of the cells exposed to the various treatments was normalized to the fluorescence of the control cells at each time point. Additional analyses were completed to determine the type of effect MMH and cisplatin had on A549 cells after 72 hours using the following equations (Babincova, Altanerova et al. 2008): synergistic,  $[MMH + CDDP] < [MMH] \times [CDDP]/100$ ; additive,  $[MMH + CDDP] = [MMH] \times [CDDP]/100$ ; sub-additive,  $[MMH] \times [CDDP]/100 < [MMH + CDDP] < [MMH]$ ; if  $[MMH] < [CDDP]$ ; interference,  $[MMH] < [MMH + CDDP] < [CDDP]$ , if  $[MMH] < [CDDP]$ ; and antagonistic,  $[CDDP] < [MMH + CDDP]$ , if  $[MMH] < [CDDP]$ , where  $[MMH]$  represents the cell viability percentage exposed to magnetically mediated hyperthermia alone,  $[CDDP]$  represents the cell viability percentage exposed to cisplatin alone, and  $[MMH+CDDP]$  represents the cell viability percentage exposed to combined magnetically mediated hyperthermia and cisplatin.

#### 4.2.8 Statistical analysis

Statistical analysis was completed using Daniel's XL Toolbox in Microsoft Excel. A 1-way ANOVA test was used to determine the statistical differences of the cytotoxicity analysis and magnetically mediated hyperthermia study. A Student's t-test was used to determine the statistical differences of the fibrinogen binding study.

### 4.3 Results and Discussion

#### 4.3.1 Particle characterization

The iron oxide nanoparticles exhibited diameters of 5 – 13 nm as shown by the TEM images in Figure 4.2. The clustering of the iron oxide suggests that multiple cores are encapsulated by the dextran coating for each nanoparticle. Due to the low density (i.e., low contrast) of the dextran coating, no differences were observed between the TEM images of the  $\text{Fe}_3\text{O}_4+\text{Dx}$  and  $\text{Fe}_3\text{O}_4+\text{Dx}$ -ECH nanoparticles. As seen in Table 4.1, size analysis indicated that the number average hydrated diameters of the nanoparticle systems were approximately 52 nm. All polydispersity indexes were below 0.2 indicating uniform nanoparticle sizes.

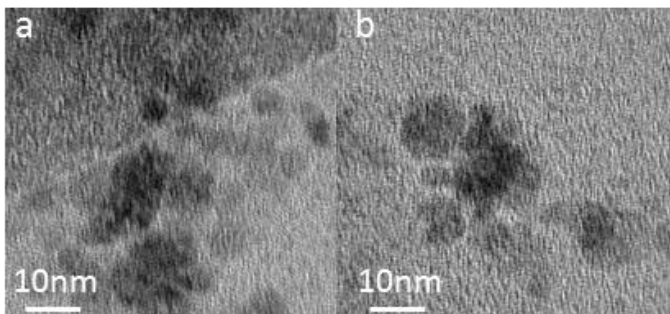


Figure 4.2 TEM images of (a) dextran coated iron oxide nanoparticles ( $\text{Fe}_3\text{O}_4+\text{Dx}$ ) and (b) dextran-epichlorohydrin crosslinked iron oxide nanoparticles ( $\text{Fe}_3\text{O}_4+\text{Dx}$ -ECH).

Table 4.1 Nanoparticle systems synthesized and characterized, their size as analyzed via DLS, and SAR values from AMF heating. Size of Fe<sub>3</sub>O<sub>4</sub>+Dx-ECH-Amine-CREKA via DLS could not be completed due to the fluorescent tag but minimal difference from the other systems is expected.

<b>Nanoparticle System</b>	<b>Size (nm)</b>	<b>SAR (W/g)</b>
Fe <sub>3</sub> O <sub>4</sub> +Dx	52 ± 16	81 ± 19
Fe <sub>3</sub> O <sub>4</sub> +Dx-ECH	56 ± 11	98 ± 16
Fe <sub>3</sub> O <sub>4</sub> +Dx-ECH-Amine	52 ± 8	89 ± 9
Fe <sub>3</sub> O <sub>4</sub> +Dx-ECH-Amine-CREKA	---	66 ± 18

Particles of this size have been shown to extravasate into tumor tissue and have been used in passive tumor targeting by taking advantage of the leaky vasculature of the tumor and the enhanced permeation and retention effect (Fox, Szoka et al. 2009, Phillips, Gran et al. 2010).

Ensuring the stability of nanoparticles in various types of solutions over time is very important, especially for the systemic delivery of therapeutics. Particle-particle interactions can induce aggregation and particle settling which can adversely affect the properties of the nanoparticles, such as heating capabilities and tumor targeting. Particle aggregates greater than 200 nm not only settle out of solution, but also attract opsonin proteins *in vivo* which label the particles for removal through the mononuclear phagocyte system (MPS)/reticuloendothelial system (RES) (Fox, Szoka et al. 2009). Using UV-visible spectroscopy, it was shown that the nanoparticles were stable in both PBS and DMEM supplemented with 10% v/v FBS for each stage of particle synthesis over a time period of 12 hours (Figure 4.3), with the normalized absorbance indicating minimal to no particle settling in solution. Overall, these results indicate the high stability of the evaluated particle systems in multiple solutions.

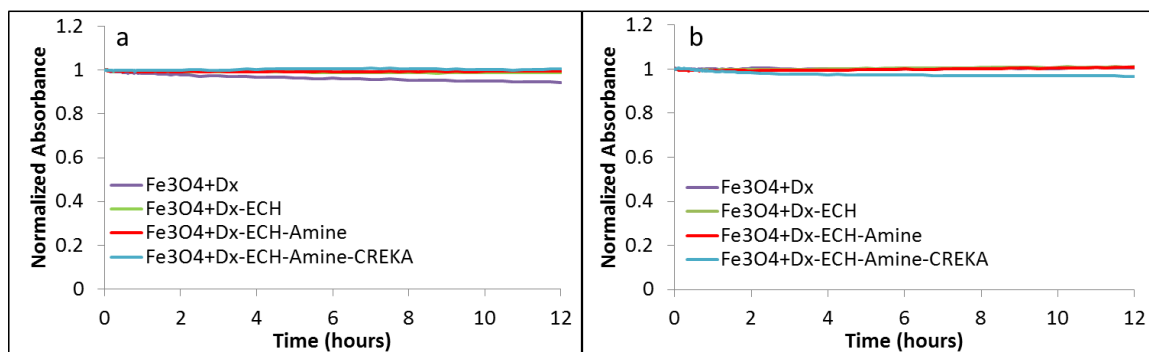


Figure 4.3 Normalized absorbance (at 540 nm) of the iron oxide nanoparticle systems in (a) PBS and (b) DMEM with 10% v/v FBS over 12 hours using UV-visible spectroscopy.

Thermogravimetric analysis was used to confirm the presence of the dextran coating on the iron oxide nanoparticles. This showed that the coating accounted for 59 - 64% of the nanoparticle mass prior to CREKA conjugation. The coating weight percentage was calculated by subtracting the final mass fraction from the initial normalized mass. As depicted in Figure 4.4, crosslinking of the dextran coating with ECH was confirmed by the shift of the mass loss profile to the right where an increase in the temperature at which the greatest mass loss occurred shifted from 285 °C ( $\text{Fe}_3\text{O}_4+\text{Dx}$ ) to 306 °C, ( $\text{Fe}_3\text{O}_4+\text{Dx-ECH}$  and  $\text{Fe}_3\text{O}_4+\text{Dx-ECH-Amine}$ ), indicating a greater thermal stability of the coating. The observed single drop in particle mass with increasing temperature confirms a single dextran layer on the surface of the particles, as this abrupt change in weight has been previously associated with a monolayer of dextran (Bautista, Bomati-Miguel et al. 2005) . The dextran coating of the final CREKA-IONP only accounted for 30% of the nanoparticle mass due to the dissolution of free dextran and AMAS linker in DMSO during the final CREKA conjugation process. Dextran has a very high affinity for DMSO resulting in any free or weakly bound dextran solubilizing in the DMSO and being washed from the nanoparticle system during the washing process. As indicated by UV-visible spectroscopy, the CREKA-IONP remained stable in PBS and DMEM indicating that dextran was still present on the surface of the particles.

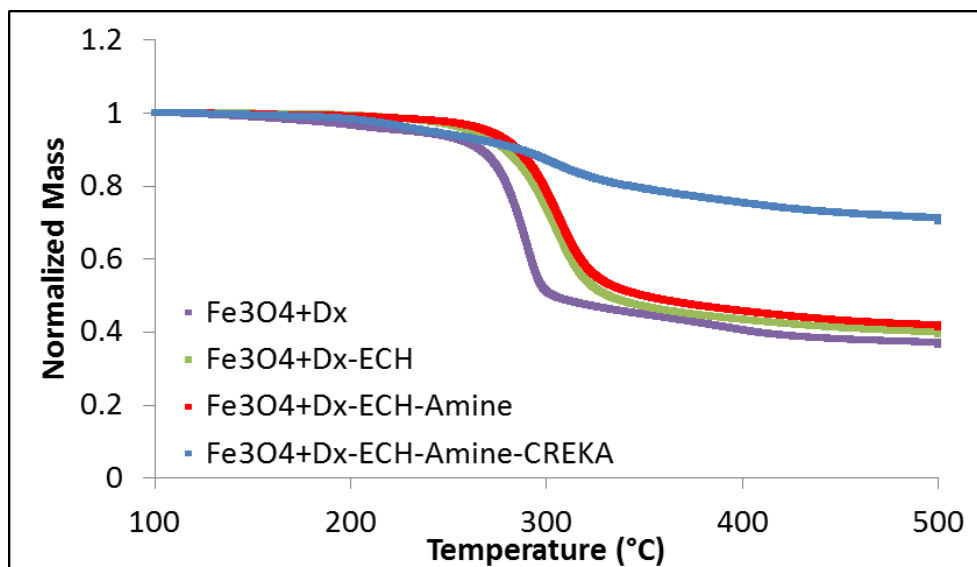


Figure 4.4 Normalized mass loss of each nanoparticle system in the synthesis process via TGA.

#### 4.3.2 Remote controlled heating of iron oxide magnetic nanoparticles via AMF

In the presence of an AMF (58 kA/m, 292 kHz), the iron oxide nanoparticle systems (5 mg/mL Fe<sub>3</sub>O<sub>4</sub>) heated the bulk solution into or above the hyperthermia range (41 - 45 °C) as seen in Figure 4.5. Fe<sub>3</sub>O<sub>4</sub>+Dx, Fe<sub>3</sub>O<sub>4</sub>+Dx-ECH, and Fe<sub>3</sub>O<sub>4</sub>+Dx-ECH-Amine particles heated to 41 °C within 300 seconds. The final CREKA-IONP system took longer to reach the hyperthermia range and heated to a lower final temperature than the other systems. The iron concentration of the nanoparticles was determined using an iron assay prior to dilution for heating in the AMF except for the CREKA-IONP system. The exact iron concentration of the CREKA-IONP could not be determined due to low volume of particles so the initial iron concentration used in the synthesis of the CREKA-IONP was used. Therefore, if any iron oxide nanoparticles were lost in the ultracentrifugation washing steps post CREKA conjugation, the actual iron concentration of the AMF heating samples would be lower than calculated, accounting for the lower final temperature and decreased initial slope of the heating profile. The SAR values are reported in Table 4.1 and indicate the energy being produced per gram of iron oxide. The lower SAR value for the CREKA-IONP is rationalized by the previous explanation of the concentration discrepancy. The AMF amplitude and frequency

correspond to a field frequency product of  $1.7 \times 10^{10} \text{A}/(\text{m}\cdot\text{s})$  which is significantly greater than the often quoted limit for use in humans (Atkinson, Brezovich et al. 1984). The high field frequency product may be an issue for future use in humans, but, the cited value is only an estimation. There is a need for further studies to determine the effects of alternating magnetic fields on healthy tissues in order to more accurately determine the limitations of AMF exposure (Kozissnik, Bohorquez et al. 2013).

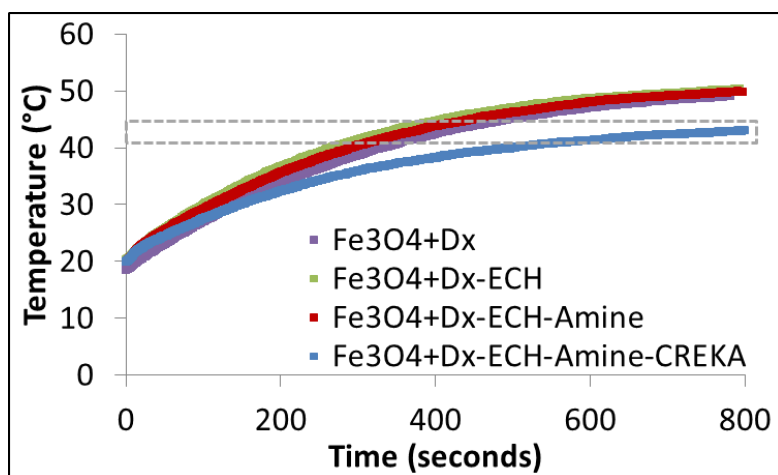


Figure 4.5 Heating profiles of each nanoparticle system in the synthesis process (5 mg/mL Fe<sub>3</sub>O<sub>4</sub>) in the presence of an alternating magnetic field at 58 kA/m and 292 kHz (n = 3). The gray box indicates the target hyperthermia range.

#### 4.3.3 Cytotoxicity analysis of particles

The cytotoxicity of the particles produced in each step in the particle synthesis was evaluated using A549 lung carcinoma cells. A549 cells were exposed to low doses of iron oxide nanoparticles for 24 and 48 hours, and the viability of the cells was analyzed using a calcein AM stain. As depicted in Figure 4.6, the particles exhibited no toxicity (at least 100% viability) after 24 hours. Dextran is a hydrophilic, water-soluble polymer which is inert in biological systems, therefore decreasing protein adsorption to the nanoparticle surface which would lead to toxicity (Imren, Gumusderelioglu et al. 2006). After 48 hours, the particles were still mostly non-toxic at these concentrations, but there was a significant difference between the control and the CREKA-IONP

at 100, 350, and 500  $\mu\text{g Fe/mL}$  as determined via a 1-way ANOVA test. However, the viability of the A549 cells after exposure to these concentrations for 48 hours is still above 80%, indicating that the particles are minimally toxic even though the difference from the control is significant.

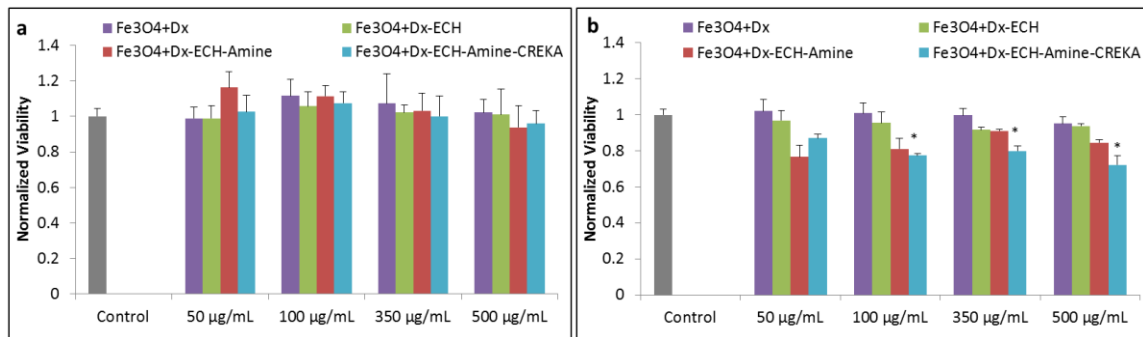


Figure 4.6 Normalized viability of each nanoparticle system in the synthesis process on A549 lung cancer cells after (a) 24 hours of exposure and (b) 48 hours of exposure. Error bars represent standard error ( $n = 4$ ) and \* indicates a significant difference ( $p < 0.05$ ) using a 1-way ANOVA test.

#### 4.3.4 Fibrinogen binding affinity

CREKA-IONPs were shown to bind to fibrin clots with a significantly greater bound-to-free fluorescence ratio than fluorescently tagged iron oxide nanoparticles (FITC-IONP) (Table 4.2). The bound-to-free fluorescence ratios of free CREKA and CREKA-IONPs were not significantly different, indicating that conjugation to the nanoparticle surface does not inhibit the binding properties of CREKA. The sulfhydryl group on the cysteine of CREKA is not required for binding to fibrinogen clots. Therefore, conjugation to the nanoparticle surface through a Michael addition reaction with an AMAS linker does not influence the fibrinogen binding properties of CREKA. These results indicate that CREKA can be functionalized to the IONP in order to localize the nanoparticles at the tumor site through binding with fibrinogen complexes in the extracellular matrix. CREKA-IONPs do not bind to specific integrins on the cell surface providing the opportunity to target a wider range of cancers. Additionally, CREKA-IONPs have resulted in amplified homing by inducing localized tumor clotting *in vivo* (Simberg, Duza et al. 2007). These

clots then attract more CREKA-IONPs, and the cycle continues. This amplified homing of CREKA to the fibrin complexes within the tumor make it attractive for localizing high concentrations of IONPs at the tumor site for magnetically mediated hyperthermia.

Table 4.2 Bound-to-free fluorescence for each system to fibrin clots represented by average  $\pm$  standard error (n = 4). The \* indicates a significant difference from the FITC-IONP bound-to-free fluorescence ratio (p<0.05).

<b>System</b>	<b>Bound-to-free fluorescence</b>
CREKA only	0.69* $\pm$ 0.03
CREKA-IONP	0.62* $\pm$ 0.03
FITC-IONP	0.42 $\pm$ 0.04

#### 4.3.5 Magnetically-mediated hyperthermia

The heating properties of the magnetic iron oxide nanoparticles were utilized to induce *in vitro* hyperthermia conditions on A549 lung carcinoma, and the effects of combined MMH and cisplatin treatments were evaluated since MMH is known to increase cisplatin efficacy at elevated temperatures (Lee, Rodriguez-Luccioni et al. 2011, Alvarez-Berrios, Castillo et al. 2013). Five treatments plus a control were evaluated as seen in Table 4.3 and cell viability 48 and 72 hours post-treatment was determined to allow time for cellular response to the treatments. After 48 hours (Figure 4.7), there was no significant difference between MMH treatment alone and combined cisplatin and MMH treatment (CDDP+MMH). However, at this time point there was also no difference between the viability of cells exposed to cisplatin and the control, indicating that the cells had not responded to the cisplatin treatment. As seen in Figure 4.8, after 72 hours there was a significant difference (p < 0.01) between the viability of cells exposed to MMH treatment alone and combined cisplatin and MMH treatment (CDDP+MMH). At this time point, the cells had responded to the cisplatin treatment, as shown by the significantly decreased viability of cells exposed to cisplatin compared to the control. Additionally, cell morphology dramatically changed when the cells were treated with cisplatin combined with MMH compared to either treatment alone.



Images in Figures 4.7 and 4.8, show the cell with blebs, or localized decoupling of the cytoskeleton from the cell membrane, which is an indicator of apoptosis, or programmed cell death (Charras, Coughlin et al. 2008). Therefore, cisplatin combined with MMH had a significantly greater effect on cell viability than either treatment alone.

Table 4.3 Magnetically mediated hyperthermia treatments and controls.

<b>Treatment</b>	<b>Description</b>
Control	Media only
IONP	3 mg/mL Fe <sub>3</sub> O <sub>4</sub> (Fe <sub>3</sub> O <sub>4</sub> +Dx-ECH)
MMH	3 mg/mL Fe <sub>3</sub> O <sub>4</sub> plus 30 minutes AMF exposure
CDDP	100 μM cisplatin
CDDP+IONP	100 μM cisplatin plus 3 mg/mL Fe <sub>3</sub> O <sub>4</sub>
CDDP+MMH	100 μM cisplatin plus 3 mg/mL Fe <sub>3</sub> O <sub>4</sub> and 30 minutes AMF exposure

The type of effect induced by the combined MMH and CDDP treatment was analyzed using the equations outlined in section 4.2.7. Seventy-two hours after treatment, the percent viability of the combined treatment was  $23.7 \pm 2.9$  and  $[\text{MMH}] \times [\text{CDDP}]/100$  equaled  $26.2 \pm 2.1$ , where the error represents standard error ( $n = 12$ ). Therefore, the combined treatment of hyperthermia and cisplatin was determined to be additive since these values are not significantly different, as indicated by a Student's t-test. This analysis was not completed on the 48 hour post-treatment data due to the cell viability of cisplatin only treatment not being different from the control.

There are several theories as to how the effects of cisplatin are enhanced by hyperthermia. Cisplatin operates by binding to DNA forming inter- or intra-strand crosslinks and interfering with the transcription DNA for protein synthesis, therefore preventing cell division and ultimately leading to cell death (Butour, Alvinerie et al. 1991). *In vitro* studies have shown that hyperthermia increases the intracellular concentration of cisplatin (Ohno, Siddik et al. 1994, Takahashi, Emi et al. 2002) due to increased permeability of the cell membrane (Alvarez-Berrios, Castillo et al. 2013).

Therefore, the number of DNA-cisplatin crosslinks is also increased (Meyn, Corry et al. 1980). Additionally, inhibition of cellular resistance to cisplatin has been observed when combined with hyperthermia (Hettinga, Lemstra et al. 1997). *In vivo*, hyperthermia results in increased blood flow and vascular permeability allowing for greater drug uptake and improved oxygenation of the tumor tissue (Issels 2008). Hyperthermia has been shown to promote cell death by increasing the fluidity of membranes causing adverse intracellular and surface events, inactivating microtubule processes and by enhancing cellular antigen expression or antigen antibody complexation (Hetzl and Dunn 1984). The efficacy of hyperthermia alone is not enough to replace any of the current chemotherapy standards, but its effects are sufficient to enhance the toxic effects of many chemotherapeutics. Therefore, by combining magnetically mediated hyperthermia and cisplatin, the effective dosage of cisplatin can be decreased, and thereby potentially decreasing the toxic side effects of the chemotherapeutic.

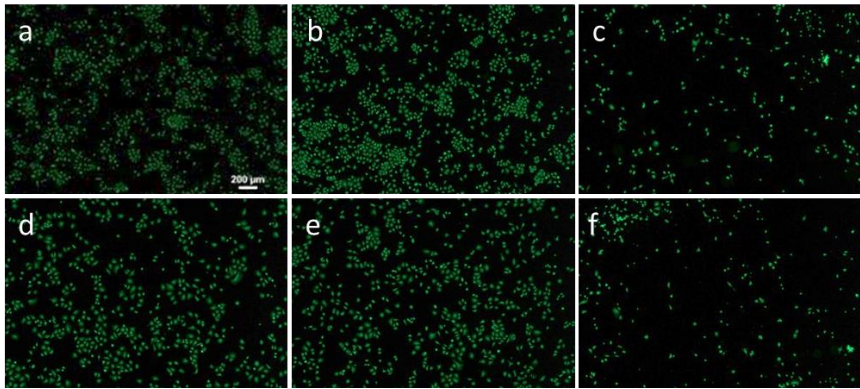
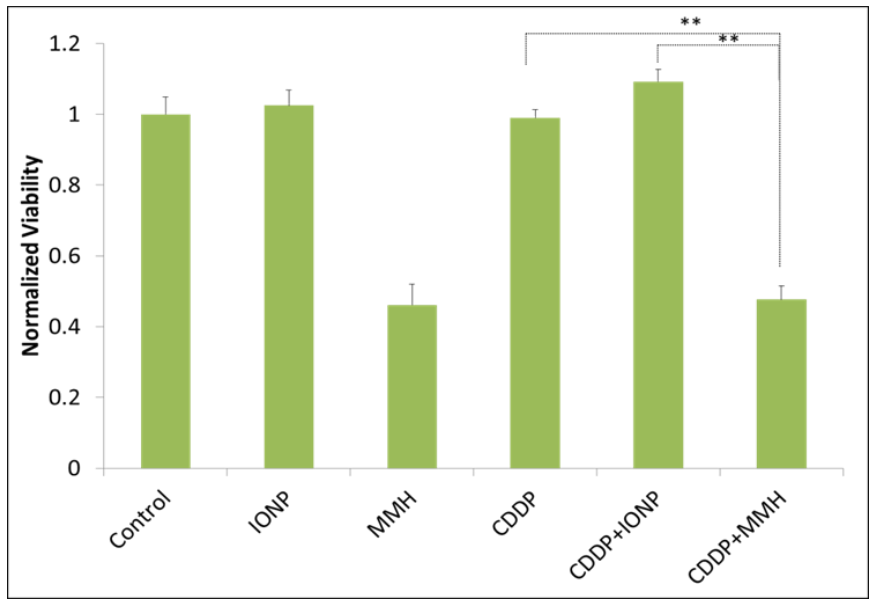


Figure 4.7 Relative viability of A549 lung cancer cells 48 hours post magnetically mediated hyperthermia treatment. Error bars represent standard error (n = 12) and \*\* indicates a significant difference ( $p < 0.01$ ). Representative images of A549 cells stained with calcein AM after 48 hours for: (a) Control, (b) IONP, (c)MMH, (d) CDDP, (e) CDDP+IONP, and (f) CDDP+MMH.

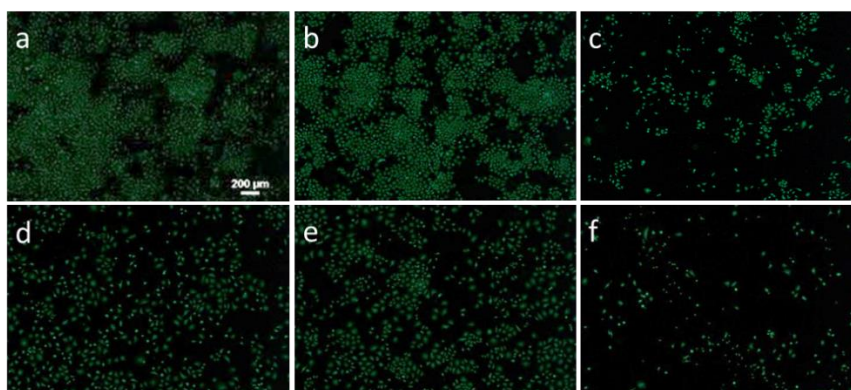
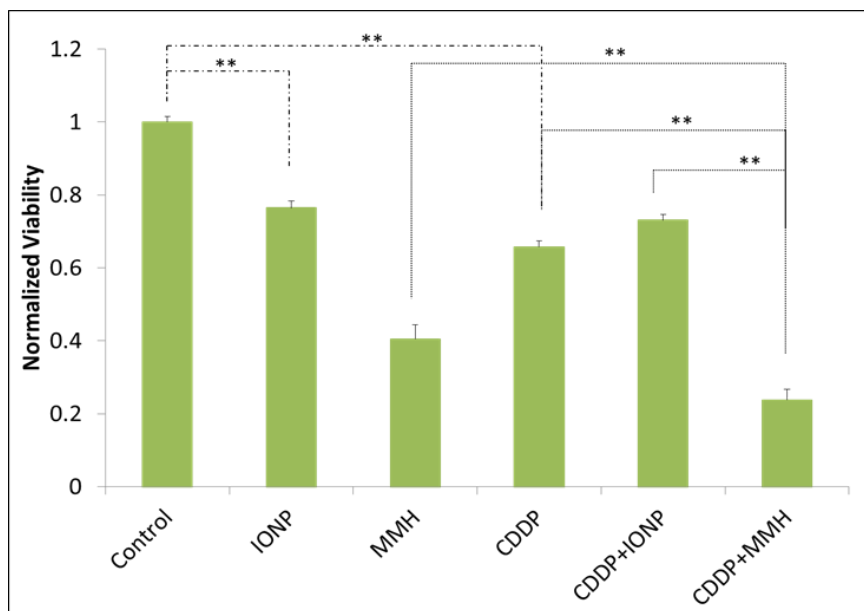


Figure 4.8 Relative viability of A549 lung cancer cells 72 hours post magnetically mediated hyperthermia treatment. Error bars represent standard error with  $n = 12$  and \*\* indicates a significant difference ( $p < 0.01$ ). Representative images of A549 cells stained with calcein AM after 72 hours for: (a) Control, (b) IONP, (c) MMH, (d) CDDP, (e) CDDP+IONP, and (f) CDDP+MMH.

#### 4.4 Conclusion

CREKA-conjugated dextran coated iron oxide nanoparticles were successfully developed and characterized for their use in targeted hyperthermia applications. The nanoparticles have properties suitable for systemic tumor targeting through the enhanced permeation and retention effect such as

stability in cell culture media and a size of approximately 50 nm (Fox, Szoka et al. 2009, Phillips, Gran et al. 2010). In the presence of an alternating magnetic field, the particles generated sufficient heat to increase the bulk solution temperature into the hyperthermia range. CREKA-conjugated nanoparticles were shown to bind to fibrinogen clots with a higher affinity than FITC-conjugated iron oxide nanoparticles, suggesting that the nanoparticles can be effective at targeting fibrinogen overexpressed in tumor tissues. The binding affinity of CREKA was not inhibited by conjugation to the iron oxide nanoparticles as shown by similar bound-to-free ratios of fluorescence. Low concentrations of the nanoparticle systems were non-toxic over long periods of time, indicating that the particles can be used for biological applications. When magnetically mediated hyperthermia was administered in conjunction with cisplatin, an enhanced cytotoxic effect was observed compared to cisplatin or hyperthermia alone. This peptide-conjugated nanoparticle system can be further studied to assess its ability to localize at tumor sites at sufficient concentrations to induce hyperthermia conditions upon exposure to an external alternating magnetic field.

## **Chapter 5 The effects of synthesis method on the physical and chemical properties of dextran coated iron oxide nanoparticles**

The heating properties of the dextran-coated iron oxide nanoparticles synthesized in Chapter 4 were inferior compared to other nanoparticle systems synthesized by the co-precipitation method. This was thought to be due to dextran increasing the solution viscosity and preventing crystal growth after nucleation. Therefore, the goal of this chapter was to analyze how the timing of dextran addition into the co-precipitation reaction affected the physicochemical properties of the nanoparticles. The chapter is taken directly or adapted from work **published in Hauser, Mathias, et al. (2015)** Copyright 2015 Elsevier B.V. Used with permissions from Anastasia K. Hauser, Ronita Mathias, Kimberly W. Anderson and J. Zach Hilt, “The effects of synthesis method on the physical and chemical properties of dextran coated iron oxide nanoparticles”, Materials Chemistry and Physics and Elsevier B.V.

### **5.0 Abstract**

Iron oxide nanoparticles coated with dextran were synthesized via four variations on the co-precipitation method. The methods ranged from *in situ* formation of the nanoparticles within the dextran solution to the adsorption of dextran to the nanoparticle surface following nucleation and extensive washing. The timing of the addition of dextran into the reaction mixture was found to greatly influence the physical and chemical properties of the magnetic nanoparticles. Batches of dextran coated iron oxide nanoparticles were synthesized by each method in triplicate, and the nanoparticles were further crosslinked with epichlorohydrin. The properties of the nanoparticles such as size, percentage of dextran coating, stability in solution, crystallinity, and magnetic properties were evaluated. The simultaneous semi-two-step method injected the reducing agent and the dextran solution into the reaction vessel at the same time. This method resulted in the greatest batch-to-batch reproducibility of nanoparticle properties and the least variation in nanoparticles synthesized in the same batch. The two-step method resulted in the greatest variation of the characteristics examined between batches. The one-step method was used with both five grams and

one gram of dextran to investigate the effects of solution viscosity on the resulting nanoparticle characteristics. The one-step method with five grams of dextran resulted in nanoparticles with significantly smaller crystal sizes ( $5.4 \pm 1.9$  nm) and lower specific adsorption rate (SAR) values ( $138.4 \pm 13.6$  W/g) in an alternating magnetic field (58 kA/m, 292 kHz). However, this method resulted in nanoparticles that were very stable in PBS over 12 hours, which is most likely due to the greater dextran coating ( $60.0 \pm 2.7$  weight percent). For comparison, the simultaneous semi-two-step method generated nanoparticles  $179.2 \pm 18.3$  nm in diameter (crystal size  $12.1 \pm 0.2$  nm) containing  $18.3 \pm 1.2$  weight percent dextran with a SAR value of  $321.1 \pm 137.3$  W/g.

## **5.1 Introduction**

Nanoparticle research has been driven by the need for new technological applications in data storage, biomedical sciences, drug delivery, and therapeutics. Iron oxide nanoparticles represent a class of materials with such applications and are very promising due to their potential biocompatibility and magnetic properties which can be used for magnetic resonance imaging, magnetically mediated hyperthermia, etc. (Andrade, Souza et al. 2010, Frimpong and Hilt 2010). The magnetic differences of iron oxide nanoparticles compared to the bulk material are a consequence of inter and intra particle interactions. Additionally, when the iron oxide nanoparticles are of a single domain, they exhibit superparamagnetism by which they do not retain magnetization in the absence of an externally applied magnetic field (Yoffe, Leshuk et al. 2013).

While the increased surface-to-volume ratio is an attractive property of superparamagnetic iron oxide nanoparticles, it also leads to considerable difficulty as a result of the tendency of nanoparticles to aggregate to reduce their surface energy by forming strong magnetic dipole interactions between the particles (Easo and Mohanan 2013). Monodispersed particles with high magnetic saturation are required for many biological applications, so it is often of interest to functionalize the nanoparticles with a coating layer to prevent agglomeration (Mahmoudi, Simchi et al. 2009). The coating layer can also be designed to increase the circulation time and the

biocompatibility of the nanoparticles for use as MRI contrast agents and magnetically mediated hyperthermia (Laurent, Dutz et al. 2011, Saraswathy, Nazeer et al. 2014). Dextran is a biocompatible long chain hydrophilic polymer composed of glucose with mostly  $\alpha$ -1, 6 glycoside linkages (Sreeja and Joy 2011) that strongly physisorb to magnetite nanoparticles in alkaline solutions via non-covalent interactions of the abundant hydroxyl groups resulting in enmeshed nanoparticle cores (Yoffe, Leshuk et al. 2013). The hydroxyl groups of dextran can then be easily crosslinked and functionalized with primary amines to attach various targeting ligands, peptides, or probes (Simberg, Duza et al. 2007, Park, Von Malzahn et al. 2008, Ayala, Herrera et al. 2013, Kruse, Meenach et al. 2014). Functionalization with primary amines throughout the nanostructure allows for increased loading capacity and the potential for attachment of multiple targeting ligands, imaging agents or therapeutics into one system (Tassa, Shaw et al. 2011).

Iron oxide nanoparticles can be synthesized by various methods including co-precipitation (Massart 1981, Kang, Risbud et al. 1996, Frimpong, Dou et al. 2010), microemulsion (Lee, Lee et al. 2005), thermal decomposition (Park, An et al. 2004, Sun, Zeng et al. 2004, Lee, Woo et al. 2008, Buyukhatipoglu and Clyne 2010, Sharapova, Uimin et al. 2010, Ayala, Herrera et al. 2013), and mechanical synthesis (Janot and Guerard 2002, Arbain, Othman et al. 2011). The co-precipitation method has traditionally been the most common method and is the primary method by which clinically approved iron oxide nanoparticles are synthesized (Qiao, Yang et al. 2009). Co-precipitation requires the reaction to be performed in an inert atmosphere to prevent oxidation of the  $\text{Fe}^{2+}$  ions and oxidation of magnetite nanoparticles to maghemite. The surface of magnetite nanoparticles will oxidize to maghemite in the presence of oxygen which reduces the magnetic saturation of the material (Gupta and Gupta 2005). The process of co-precipitation involves initial nucleation followed by slow growth as the solutes diffuse to the surface of the crystal (Easo and Mohanan 2013). Within the co-precipitation method, there are various procedures that alter parameters of the reaction in order to tune the properties of the iron oxide nanoparticles produced.



Variables such as pH, temperature, reaction time, and iron ion ratios have been examined to determine their effects on the size, stability, and heating properties of the nanoparticles. Vayssieres *et al.* (Vayssieres, Chaneac *et al.* 1998) varied the pH of the reaction solution between 8.5 and 12 and found that the resulting iron oxide nanoparticles became smaller as the solution increased in alkalinity. It was also determined that a minimum pH of 10-11 is required for the nanoparticle size to remain stable over time. Murbe *et al.* (Murbe, Rechtenbach *et al.* 2008) addressed the effect of reaction temperature on the physical and chemical properties of iron oxide nanoparticles showing that as the temperature at which initial nucleation occurred increased from 25 to 70°C, the nanoparticle size also increased from 16 to 39 nm. Additionally, the magnetic saturation of the nanoparticles increased from 76 to 88 emu/g. Frimpong *et al.* (Frimpong, Dou *et al.* 2010) addressed the effects of reaction temperature and staged reactions on the magnetic properties of citrate capped iron oxide nanoparticles, and they also found that as temperature increased, the nanoparticle crystal size also increased. The saturation magnetization was also influenced by the reaction temperature and method as the one-step method resulted in nanoparticles with a lower magnetic saturation value and decreased heating capabilities than the two-step reactions. A significant amount of research has been completed on dextran coated iron oxide nanoparticles, specifically on varying the molecular weight of the dextran. Xu *et al.* (Xu, Shen *et al.* 2005) formed iron oxide nanoparticles in the presence of dextran with a molecular weight of 20 or 40 kDa. The 40 kDa dextran resulted in a viscous reaction solution, so the 20 kDa dextran coated nanoparticles were preferred. However, the magnetic saturation of the nanoparticles was lower than expected due to significant agglomeration of the nanoparticles and a wide range of hydrodynamic radii. Although the effects of reaction temperature, time, pH, and dextran molecular weight have been analyzed, the time and method of dextran addition into the reaction solution have not yet been evaluated. Therefore, this chapter sought to determine the effects of the timely addition of dextran to the

reaction mixture on the physical and chemical properties of the dextran coated iron oxide nanoparticles.

It is important to understand the effects of dextran on the properties of iron oxide nanoparticles in order to develop a synthesis protocol that results in consistent and desirable physicochemical properties. As depicted in Figure 5.1, four co-precipitation methods were developed to synthesize dextran coated iron oxide nanoparticles that were further crosslinked with epichlorohydrin to increase the thermodynamic stability of the dextran on the surface of the nanoparticles (Palmacci and Josephson 1993). The methods varied by the time of dextran addition to the reaction mixture: from *in situ* formation of the iron oxide nanoparticles to formation followed by extensive washing prior to dextran adsorption. Three batches of nanoparticles were synthesized via each method in order to address the variability within a single method as well as the differences between the methods. All other parameters such as pH, reaction temperature, and dextran molecular weight were kept constant among the methods. After synthesis, both the dextran coated and epichlorohydrin crosslinked nanoparticles were characterized for size, dextran weight percent, stability, crystallinity, and heating ability in the presence of an alternating magnetic field. Each of these properties is important to evaluate prior to *in vivo* studies should the nanoparticles be used for biological applications. It is also important to develop protocols for iron oxide nanoparticle synthesis that result in consistent properties of the nanoparticles such as desired size, stability in solution, crystallinity to allow for heating in an AMF as well as image contrast, and dextran coating to increase circulation and biocompatibility. This article addresses the development of a synthesis method that results in consistent and desirable properties of iron oxide nanoparticles.

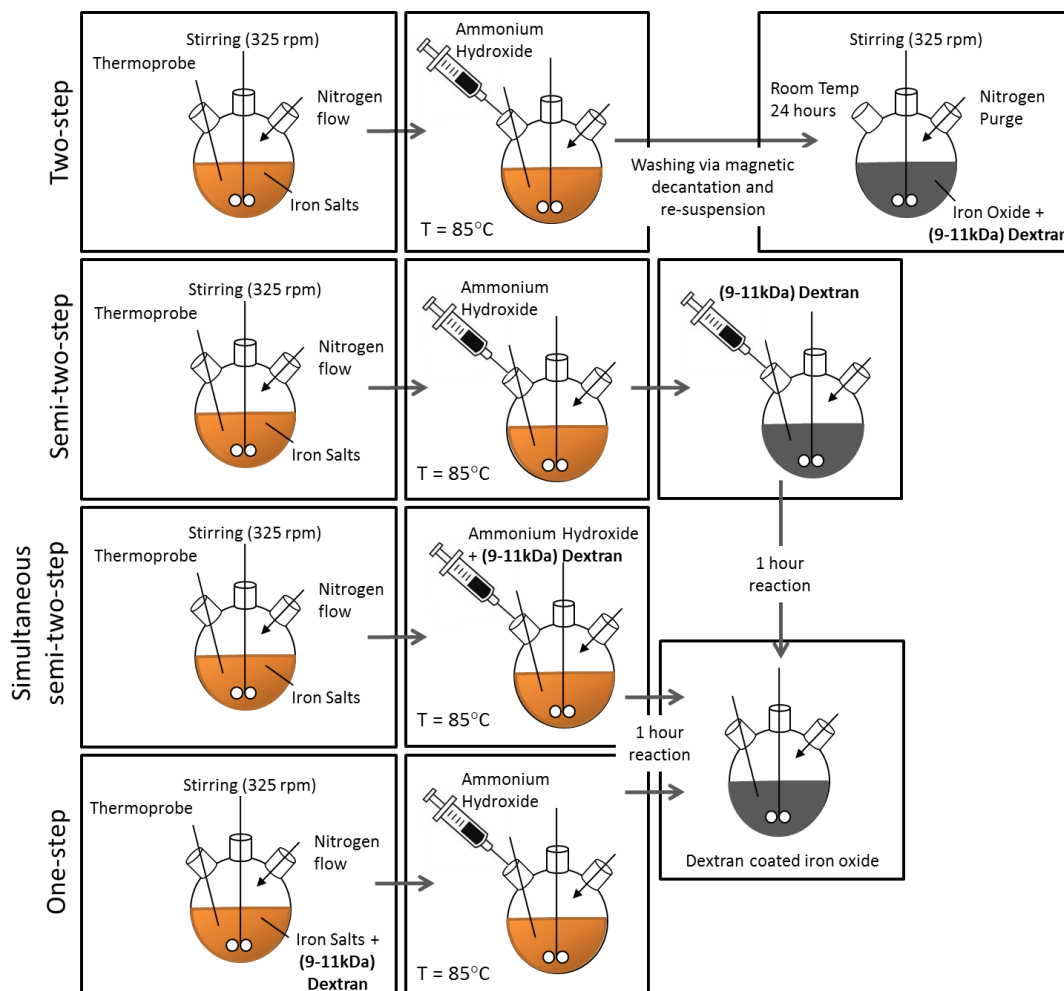


Figure 5.1 Schematic of iron oxide nanoparticle synthesis methods. The co-precipitation reaction for each of the methods is completed at 85 °C for one hour after the addition of the reducing agent (ammonium hydroxide).

## 5.2 Materials and Methods

### 5.2.1 Materials

Iron (III) chloride hexahydrate ( $\text{FeCl}_3 \cdot 6\text{H}_2\text{O}$ ), iron (II) chloride ( $\text{FeCl}_2 \cdot 4\text{H}_2\text{O}$ ), 9 – 11 kDa dextran, epichlorohydrin (ECH) were obtained from Sigma Aldrich (St. Louis, MO). Ammonium hydroxide ( $\text{NH}_4\text{OH}$ ) was purchased from EMD Chemicals (Gibbstown, NJ). Phosphate buffered saline solution (PBS) (10X) was purchased from EMD Millipore (Billerica, MA). All materials were used as received.

### *5.2.2 Dextran coated iron oxide nanoparticle synthesis via two-step method*

A modified one-pot co-precipitation method (Frimpong, Dou et al. 2010) was used to prepare dextran coated IONPs.  $\text{FeCl}_3 \cdot 6\text{H}_2\text{O}$  and  $\text{FeCl}_2 \cdot 4\text{H}_2\text{O}$  were combined in a 2:1 molar ratio (2.2 grams and 0.8 grams, respectively) and dissolved in 40 mL deionized (DI) water and sealed in a three-neck flask under vigorous stirring and an inert nitrogen environment. 5 grams of dextran was solubilized in 20 mL of DI water. The solution was heated to 85 °C at which 5 mL of  $\text{NH}_4\text{OH}$  was added dropwise to the reaction vessel. The reaction was carried out for 1 hour at 85 °C. The particles were magnetically decanted and washed three times with DI water. The nanoparticles were then re-suspended in 45 mL DI water and added to a three neck flask. The dextran solution was added to the reaction vessel and the vessel was purged with nitrogen. The nanoparticles and dextran solution were stirred vigorously at room temperature for 24 hours. After 24 hours, the nanoparticles were magnetically decanted and washed three times with DI water. Finally, the nanoparticles were dialyzed against DI water for 24 hours (100 kDa molecular weight cutoff) then probe sonicated for 10 minutes and centrifuged at 1000 rpm for 5 minutes to remove large agglomerates.

### *5.2.3 Dextran coated iron oxide nanoparticle synthesis via semi-two-step method*

$\text{FeCl}_3 \cdot 6\text{H}_2\text{O}$  and  $\text{FeCl}_2 \cdot 4\text{H}_2\text{O}$  were combined in a 2:1 molar ratio (2.2 grams and 0.8 grams, respectively) and dissolved in 40 mL deionized (DI) water and sealed in a three-neck flask under vigorous stirring and an inert nitrogen environment. 5 grams of dextran was solubilized in 20 mL of DI water. The solution was heated to 85 °C at which 5 ml of  $\text{NH}_4\text{OH}$  was added dropwise to the reaction vessel. The dextran solution was then injected dropwise into the vessel. The reaction was carried out for 1 hour at 85 °C. The particles were magnetically decanted and washed three times with DI water. The nanoparticles were then re-suspended in DI water and dialyzed against DI water for 24 hours (100 kDa molecular weight cutoff). After dialysis, the nanoparticles were probe sonicated for 10 minutes and then centrifuged at 1000 rpm for 5 minutes to remove large agglomerates.

#### *5.2.4 Dextran coated iron oxide nanoparticle synthesis via simultaneous semi-two-step method*

$\text{FeCl}_3 \cdot 6\text{H}_2\text{O}$  and  $\text{FeCl}_2 \cdot 4\text{H}_2\text{O}$  were combined in a 2:1 molar ratio (2.2 grams and 0.8 grams, respectively) and dissolved in 40 mL deionized (DI) water and sealed in a three-neck flask under vigorous stirring and an inert nitrogen environment. 5 grams of dextran was solubilized in 20 mL of DI water. The reaction solution was heated to 85 °C at which 5 ml of  $\text{NH}_4\text{OH}$  was added to the dextran solution and the combined solution was injected dropwise into the vessel. The reaction was carried out for 1 hour at 85 °C. The particles were magnetically decanted and washed three times with DI water. The nanoparticles were then re-suspended in DI water and dialyzed against DI water for 24 hours (100 kDa molecular weight cutoff). After dialysis, the nanoparticles were probe sonicated for 10 minutes and then centrifuged at 1000 rpm for 5 minutes to remove large agglomerates.

#### *5.2.5 Dextran coated iron oxide nanoparticle synthesis via one-step method*

$\text{FeCl}_3 \cdot 6\text{H}_2\text{O}$  and  $\text{FeCl}_2 \cdot 4\text{H}_2\text{O}$  were combined in a 2:1 molar ratio (2.2 grams and 0.8 grams, respectively) and dissolved in 40 mL deionized (DI) water and sealed in a three-neck flask under vigorous stirring and an inert nitrogen environment. Five grams of dextran or one gram of dextran was solubilized in 20 mL of DI water and added to the three-neck flask. The solution was heated to 85 °C at which 5 ml of  $\text{NH}_4\text{OH}$  was injected dropwise into the vessel. The reaction was carried out for 1 hour at 85 °C. The particles were magnetically decanted and washed three times with DI water and then dialyzed against DI water for 24 hours (100 kDa molecular weight cutoff). After dialysis, the nanoparticles were probe sonicated for 10 minutes and then centrifuged at 1000 rpm for 5 minutes to remove large agglomerates.

#### *5.2.6 Epichlorohydrin crosslinking of dextran coated iron oxide nanoparticles*

Dextran coated IONPs were crosslinked using ECH for increased stability (Palmacci and Josephson 1993). The particle colloid (9 mL, 1 mmol Fe) was added to 9 mL 5M NaOH and 1.5 mL ECH. The reaction was carried out for 24 hours at room temperature under continuous agitation. The

particles were then magnetically decanted and dialyzed against DI water (100 kDa molecular weight cutoff) for 24 hours to remove excess ECH.

### 5.2.7 Particle characterization

*Dynamic light scattering (DLS).* DLS measurements were obtained using a Beckman Coulter Delsa Nano C particle analyzer. Nanoparticle solutions were diluted to 200  $\mu\text{g/mL}$  and were sonicated in a water bath prior to size analysis.

*Ultraviolet (UV)-Visible spectroscopy.* The stability of the nanoparticles was analyzed using a CaryWin 50 probe UV-visible spectrophotometer. IONPs were diluted to 200  $\mu\text{g/mL}$  Fe in PBS. Sample absorbance was read at 540 nm over 12 hours.

*Fourier transform infrared (FTIR) spectra.* Attenuated total reflectance FTIR (ATR-FTIR) was used to determine surface functionalization with a Varian Inc. 7000e spectrometer. Dried samples were placed on the diamond ATR crystal and the spectrum was obtained between 700 and 4000  $\text{cm}^{-1}$  for 32 scans.

*Thermogravimetric analysis (TGA).* TGA was used to quantify the mass percent of the iron oxide core in the particle systems using a Netzsch Instruments STA 449A system. Approximately 5 mg of particle sample was heated at a rate of 5  $^{\circ}\text{C}/\text{minute}$ . At 100  $^{\circ}\text{C}$ , the sample was held isothermally for 20 minutes to vaporize residual water. The samples were heated at 5  $^{\circ}\text{C}/\text{minute}$  until reaching 500  $^{\circ}\text{C}$  where they were held isothermally for an additional 20 minutes. The reported mass loss was the actual mass loss normalized to the initial sample mass after isothermal heating at 100  $^{\circ}\text{C}$ .

*Transmission electron microscopy (TEM).* TEM was completed using a JEOL 2010F system operating at 200 keV. IONPs were diluted to 1 mg/ml Fe in DI water and then dried on carbon TEM grids prior to analysis.

*X-ray diffraction (XRD).* XRD patterns were obtained by a Siemens D-500 X-ray spectrometer with a  $\text{CuK}\alpha$  radiation source ( $\lambda = 1.54 \text{ \AA}$ ) at 40 kV and 30 mA scanning from 5 $^{\circ}$  to 65 $^{\circ}$  at a scan rate of 1 $^{\circ}$  per minute. The XRD patterns were used to confirm the magnetite crystal structure of the iron

oxide nanoparticles. The XRD patterns are in coherence with JCPDS card (19-0629). The crystal domain size was estimated using the Scherrer equation [5.1]

$$\tau = \frac{K\lambda}{\beta \cos\theta} \quad [5.1]$$

where  $\tau$  is the mean size of the ordered (crystalline) domains  $K$  is a dimensionless shape factor with a value close to unity (0.8396 for iron oxide)  $\lambda$  is the X-ray wavelength,  $\beta$  is the line broadening at half the maximum intensity (FWHM) after subtracting the instrumental line broadening, in radians and  $\theta$  is the Bragg angle (17.72 °).

*Alternating magnetic field (AMF) heating.* The nanoparticle heating profiles were obtained using a custom made Taylor Winfield magnetic induction source, and the temperature was measured with a fiber optic temperature sensor (Luxtron FOT Lab Kit from LumaSense). Nanoparticle suspensions were diluted in DI water to a concentration of 3 mg/ml iron oxide. One milliliter of suspension in a 2 ml microcentrifuge tube was placed in the center of the AMF induction coil. The suspension was heated at a field amplitude of 58 kA/m and frequency of 292 kHz until the temperature of the suspension reached steady-state. The specific absorption rate (SAR) values of the nanoparticle suspensions were then calculated using the following equation:

$$SAR = \frac{C_{p,Fe}m_{Fe} + C_{p,H_2O}m_{H_2O}}{m_{Fe}} \frac{dT}{dt} \quad [5.2]$$

where  $C_{p,Fe}$  is the heat capacity of iron,  $m_{Fe}$  is the mass of iron,  $C_{p,H_2O}$  is the heat capacity of water,  $m_{H_2O}$  is the mass of water, and  $dT/dt$  is the initial slope of the heating profile. The intrinsic loss power (ILP) of the nanoparticle systems was calculated using the following equation:

$$ILP = \frac{SAR}{H^2 f} \quad [5.3]$$

where  $H$  is the magnetic field strength and  $f$  is the field frequency. This value will allow for the heating properties of these systems to be compared more accurately to other systems in literature.

### 5.3 Results and Discussion

The hydrodynamic diameter of the nanoparticles was analyzed via dynamic light scattering and reported as the z-average while the variability of particle size within the batches was quantified by the polydispersity index (PDI) in Table 5.1. The two-step method resulted in particles with the largest hydrodynamic diameter along with the greatest deviation between batches. The PDI of the nanoparticles synthesized by the two-step method was also the largest of the methods tested. After crosslinking with epichlorohydrin, the hydrodynamic diameter of the nanoparticles decreased significantly. This is likely due to the extra processing during crosslinking resulting in the loss of larger nanoparticle agglomerates. The one-step method with five grams of dextran resulted in the smallest nanoparticles most likely due to the high viscosity of the solution during nucleation inhibiting the transport of the iron ions to the nanoparticle surface. The high viscosity solution helps to prevent agglomeration of the nanoparticles but their formation is hindered due to transport limitations during the nucleation process. Although the one-step nanoparticles were smaller in hydrodynamic diameter which is advantageous for tumor targeting, their other properties such as heating abilities suffered from the high viscosity solution. The one-step method with one gram of dextran resulted in larger nanoparticles than the one-step method with five grams of dextran. Additionally, there was greater variability in the nanoparticle sizes between the batches. The simultaneous semi-two-step method resulted in nanoparticles with the most consistent sizes within a single batch as indicated by the low PDI after crosslinking, as well as the greatest batch to batch reproducibility as indicated by the lowest standard deviation. The batch-to-batch reproducibility is thought to be due to the simultaneous semi-two-step method being the easiest method to control since it involves a single injection of the ammonium hydroxide in a solution of dextran. The viscosity of the solution is also that of water when initial nucleation occurs allowing for iron ions to transport to the nucleation sites more effectively. Previous studies by Xu, et al. (Xu, Shen et al. 2005) found that lower molecular weight dextran (20kDa vs. 40kDa) was advantageous due to



lower solution viscosity leading to more optimal nanoparticle characteristics. It is also important to note that low molecular weight dextran can precipitate acute renal failure so it is important to coat the nanoparticles with enough dextran to increase cytocompatibility and stability but not so much that excess dextran is administered (Feest 1976). In another study by Saraswathy et al. 70kDa dextran was used to coat iron oxide nanoparticles resulting in a 50 nm diameter and 12 nm core size. The high molecular weight dextran was offset by a using a low weight percentage dextran (3%) in water (Saraswathy, Nazeer et al. 2014). By using a high molecular weight dextran, the potential to cause osmotic nephropathy is decreased, but the amount of dextran coating the nanoparticle surface decreases, which could impact nanoparticle stability.

Table 5.1 Size analysis via dynamic light scattering of iron oxide nanoparticles synthesized by the various methods represented by average  $\pm$  standard deviation (three independent batches and three samples from each batch).

<b>Method</b>	<b>Nanoparticle</b>	<b>Size (nm)</b>	<b>PDI</b>
two-step	Fe <sub>3</sub> O <sub>4</sub> +Dx	382.4 $\pm$ 163.2	0.35 $\pm$ 0.14
	Fe <sub>3</sub> O <sub>4</sub> +Dx-ECH	237.8 $\pm$ 28.8	0.16 $\pm$ 0.02
semi-two-step	Fe <sub>3</sub> O <sub>4</sub> +Dx	233.9 $\pm$ 25.2	0.19 $\pm$ 0.03
	Fe <sub>3</sub> O <sub>4</sub> +Dx-ECH	244.1 $\pm$ 54.7	0.20 $\pm$ 0.08
simultaneous semi-two-step	Fe <sub>3</sub> O <sub>4</sub> +Dx	179.2 $\pm$ 18.3	0.18 $\pm$ 0.02
	Fe <sub>3</sub> O <sub>4</sub> +Dx-ECH	185.6 $\pm$ 23.8	0.02 $\pm$ 0.03
one-step (5 grams Dx)	Fe <sub>3</sub> O <sub>4</sub> +Dx	171.4 $\pm$ 30.9	0.22 $\pm$ 0.09
	Fe <sub>3</sub> O <sub>4</sub> +Dx-ECH	121.7 $\pm$ 24.7	0.14 $\pm$ 0.02
one-step (1 gram Dx)	Fe <sub>3</sub> O <sub>4</sub> +Dx	248.0 $\pm$ 69.0	0.20 $\pm$ 0.05
	Fe <sub>3</sub> O <sub>4</sub> +Dx-ECH	244.2 $\pm$ 34.4	0.16 $\pm$ 0.05

Different synthesis methods also have an effect on dextran adsorbed to the surface of the iron oxide nanoparticles. The presence of dextran on the surface of the iron oxide nanoparticles was confirmed via FTIR spectroscopy (Figure 5.2). The synthesis methods resulted in similar spectra with all spectra containing a broad peak between 3500-3200 cm<sup>-1</sup> indicating the structural O-H in the dextran chains. The peak associated with the asymmetrical stretching vibration of C-H in CH<sub>2</sub>

is found at  $2918\text{ cm}^{-1}$ . Peaks at  $1450$ ,  $1350$ , and  $1273\text{ cm}^{-1}$  can be assigned to the deformation vibration of H-C-OH of the dextran chains. Finally, the asymmetrical and symmetrical vibrations of C-O-C can be found at  $1157$  and  $849\text{ cm}^{-1}$ , respectively.

Quantification of the dextran coating was completed using thermogravimetric analysis (TGA) as shown in Table 5.2. The one-step method with 5 grams of dextran resulted in the greatest dextran adsorption to the nanoparticle surface with approximately 60% of the nanoparticle weight being composed of dextran. On the contrary, the one-step method with one gram of dextran resulted in the least dextran adsorption and no significant change after crosslinking with epichlorohydrin as depicted in Figure 5.3e. The two-step method and the semi-two-step method resulted in the most variability between batches in the amount of dextran coating. In the semi-two-step method, this is most likely due to the multiple injections of ammonium hydroxide and dextran and slight variability in timing. Again, the simultaneous semi-two-step resulted in the most consistent dextran adsorption. All of the weight loss profiles displayed a single drop in mass as temperature increased indicating a single layer of dextran or crosslinked dextran on the nanoparticle surface (Figure 5.3). Additionally, after crosslinking, the mass due to the coating decreased or remained the same most likely due to further dialysis after crosslinking. The right shift in the temperature at which the greatest mass loss occurs confirmed that dextran had been crosslinked as more energy was required to break the covalent bonds prior to degrading the coating.

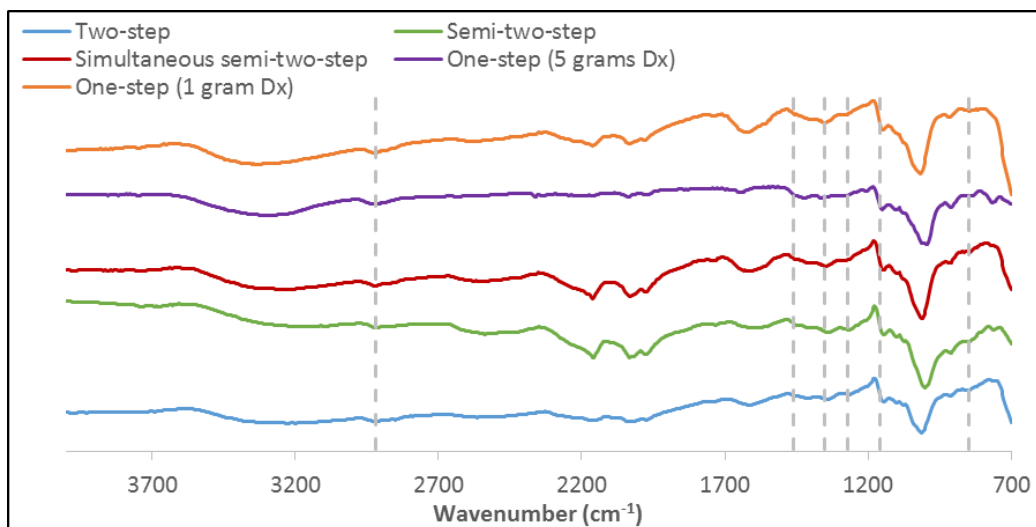


Figure 5.2 FTIR spectra of dextran coated iron oxide nanoparticles synthesized by the various methods.

Table 5.2 Dextran weight percentage via thermogravimetric analysis of iron oxide nanoparticles synthesized by the various methods (n=3).

Synthesis Method	Nanoparticle	Coating Weight%
two-step	Fe <sub>3</sub> O <sub>4</sub> +Dx	23.7 ± 7.8
	Fe <sub>3</sub> O <sub>4</sub> +Dx-ECH	19.0 ± 11.3
semi-two-step	Fe <sub>3</sub> O <sub>4</sub> +Dx	29.3 ± 6.1
	Fe <sub>3</sub> O <sub>4</sub> +Dx-ECH	16.7 ± 9.8
simultaneous semi-two-step	Fe <sub>3</sub> O <sub>4</sub> +Dx	18.3 ± 1.2
	Fe <sub>3</sub> O <sub>4</sub> +Dx-ECH	15.7 ± 5.0
one-step (5 grams Dx)	Fe <sub>3</sub> O <sub>4</sub> +Dx	60.0 ± 2.7
	Fe <sub>3</sub> O <sub>4</sub> +Dx-ECH	58.0 ± 7.2
one-step (1 gram Dx)	Fe <sub>3</sub> O <sub>4</sub> +Dx	12.7 ± 1.7
	Fe <sub>3</sub> O <sub>4</sub> +Dx-ECH	13.0 ± 1.7

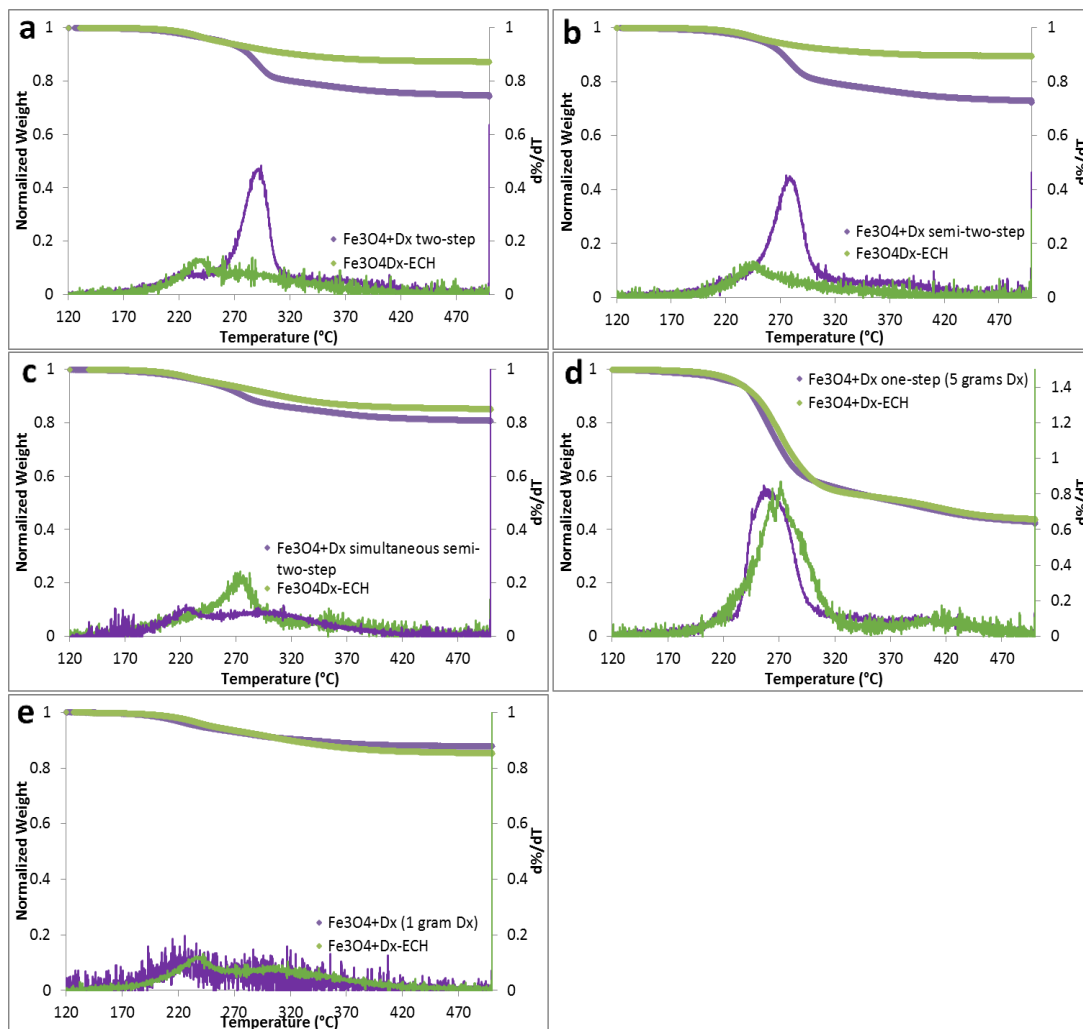


Figure 5.3 Mass loss and  $d\%/dT$  with increasing temperature of dextran coated and epichlorohydrin crosslinked iron oxide nanoparticles synthesized via the (a) two-step method, (b) semi-two-step method, (c) simultaneous semi-two-step method, (d) one-step method with 5 grams dextran, and (e) one-step method with 1 gram dextran.

Stability of the nanoparticles in solution is very important if the nanoparticles are to be used for biological applications as agglomeration could lead to blockage of the circulatory system or lack of targeting ability to the tissue of interest. Therefore, the stability of the nanoparticles in phosphate buffered saline was analyzed over a 12 hour time period for both the dextran coated and crosslinked systems synthesized by each of the methods (Figure 5.4). Dextran coated iron oxide

nanoparticles synthesized by the one-step method with 5 grams of dextran were the most stable both before and after epichlorohydrin crosslinking. This is due to the steric interactions of dextran with the surrounding medium. Since nanoparticles produced by the one-step with 5 grams of dextran had the greatest amount of dextran on the surface, it is expected that these nanoparticles would also be the most stable. However, the two-step, semi-two-step, and the simultaneous semi-two-step methods, resulted in relatively stable nanoparticles in PBS after crosslinking.

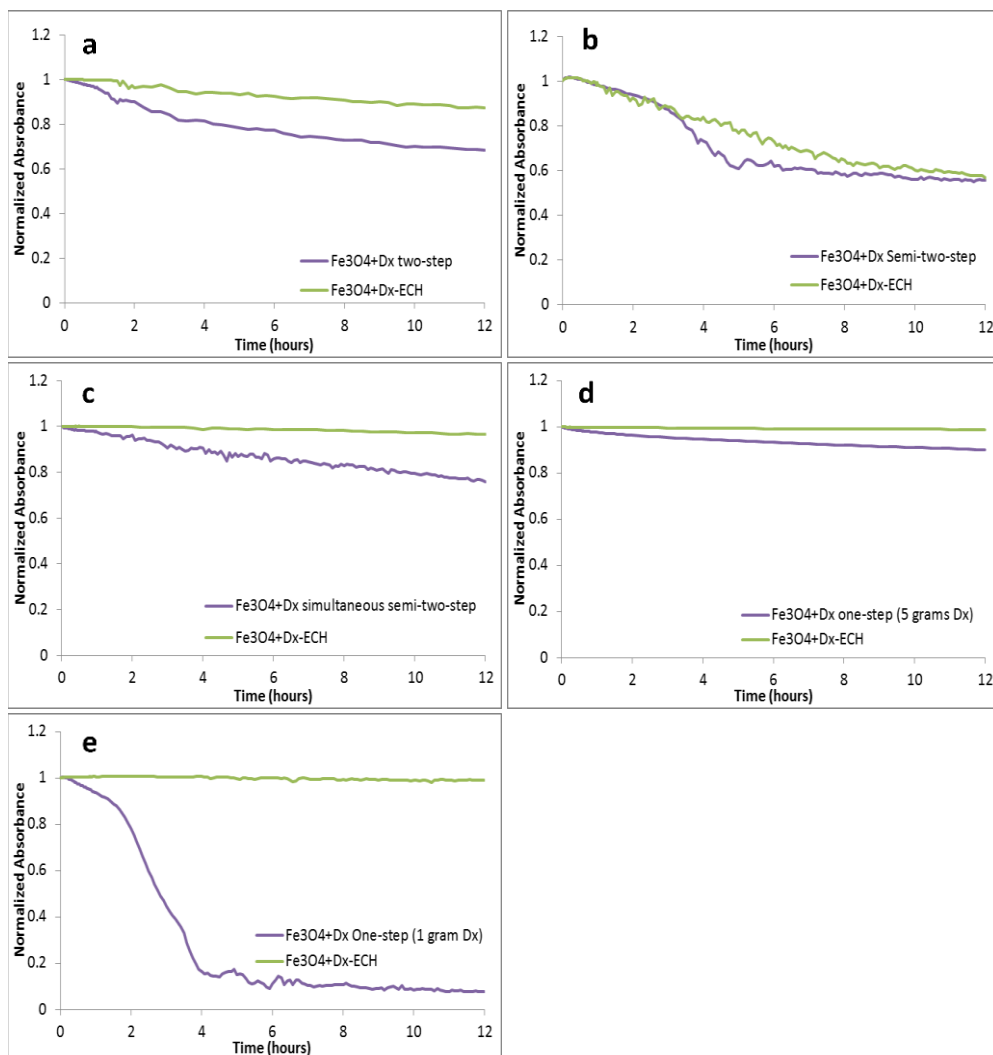


Figure 5.4 Stability of dextran coated and epichlorohydrin crosslinked iron oxide nanoparticles synthesized via the (a) two-step method, (b) semi-two-step method, (c) simultaneous semi-two-step method, (d) one-step method with 5 grams dextran, and (e) one-step method with 1 gram dextran in PBS over 12 hours analyzed by UV-visible spectroscopy ( $\lambda=540$ ).

The XRD patterns (Figure 5.5) of the iron oxide nanoparticles synthesized by each method are in coherence with JCPDS card (19-0629) associated with magnetite. The sharp peaks indicate a highly crystalline structure has been formed by each method. The broad peak at approximately  $2\theta$  equal to  $17^\circ$  is due to the presence of dextran which is confirmed by the XRD pattern of dextran only (Figure 5.5f). This peak has the greatest intensity in the one-step method with five grams of dextran which also has the greatest weight percent of dextran. Slight shoulders are seen in the XRD patterns of the other synthesis methods confirming the presence of dextran, but the lower intensity matches the data obtained via thermogravimetric analysis. The highest intensity peak at  $2\theta$  equal to  $35.44^\circ$  corresponds to the (3 1 1) plane of the iron oxide crystal structure. This peak was used to calculate the crystal size of the nanoparticles using the Scherrer equation and these crystal sizes correspond well with the crystal sizes shown in TEM (Figure 5.6). Table 5.3 displays the calculated crystal sizes from XRD spectra and the Scherrer equation along with the crystal sizes from TEM while Figure 5.5 depicts the XRD patterns. All the crystal sizes of the iron oxide nanoparticles synthesized were much smaller than the reported hydrodynamic diameter. This is due to multiple crystals being encapsulated within the dextran coating. The crystal size of the nanoparticles synthesized via the one-step method with 5 grams of dextran was significantly smaller than the crystal sizes of the nanoparticles synthesized by the other methods as shown by both XRD (Figure 5.5d) and TEM (Figure 5.6d). This is thought to be due to the concentrated dextran during nucleation. TEM images show the crystal size of nanoparticles synthesized via the two-step and semi-two step were larger than the other methods, which is due to dextran addition taking place post nucleation. Previous work has shown that crystal growth is retarded by the chemisorption of poly(vinyl alcohol) to the surface of the particles when synthesized by a one-step method (Mahmoudi, Simchi et al. 2009). Work completed by Pardoe et al. (Pardoe, Chua-anusorn et al. 2001) has shown that iron oxide nanoparticles coated with dextran are significantly smaller than the control uncoated nanoparticles. Additionally, the polymer chosen to coat the nanoparticles

influences the crystal size of the particles. For example, nanoparticles coated with PVA resulted in larger crystals than dextran coated particles but both were smaller than uncoated nanoparticles (Pardoe, Chua-anusorn et al. 2001). A similar effect was observed by Bee *et al.* (Bee, Massart et al. 1995) in which iron oxide nanoparticle formation was prevented by either chelation of citrate ions with metal ions and therefore preventing nucleation or by adsorption of the citrate ions on the nuclei inhibiting growth of the nuclei. Without a high dextran concentration and therefore a lower viscosity reaction solution, the iron oxide crystals had diameters closer to the other synthesis methods. Once again, the two step method resulted in the most variability in crystal size while the simultaneous semi-two-step was the most consistent.

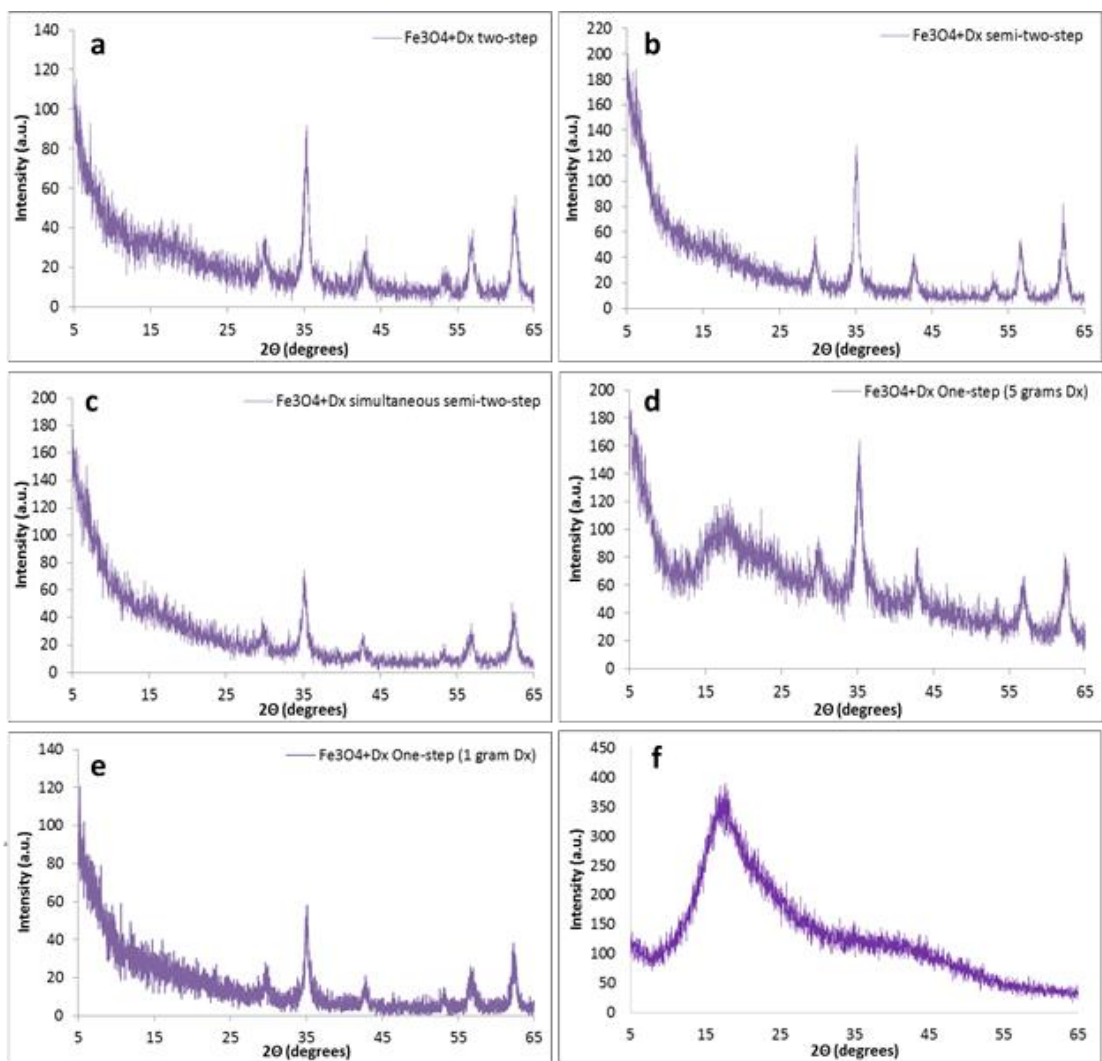


Figure 5.5 XRD patterns of dextran coated iron oxide nanoparticles synthesized via the (a) two-step method, (b) semi-two-step method, (c) simultaneous semi-two-step method, (d) one-step method with 5 grams dextran, (e) one-step method with 1 gram dextran and (f) dextran only.



Table 5.3 Iron oxide crystal size estimated using XRD spectra and the Scherrer equation and TEM images of iron oxide nanoparticles synthesized by the various methods (mean  $\pm$  st. dev. n=3 for XRD and n=150 for TEM).

Synthesis Method	XRD Size (nm)	TEM Size (nm)
two-step	10.0 $\pm$ 2.1	14.5 $\pm$ 4.2
semi-two-step	11.2 $\pm$ 1.0	14.7 $\pm$ 4.6
simultaneous semi-two-step	12.1 $\pm$ 0.2	8.9 $\pm$ 2.2
one-step (5 grams Dx)	5.4 $\pm$ 1.9	6.8 $\pm$ 1.4
one-step (1 gram Dx)	12.4 $\pm$ 1.3	10.1 $\pm$ 3.1

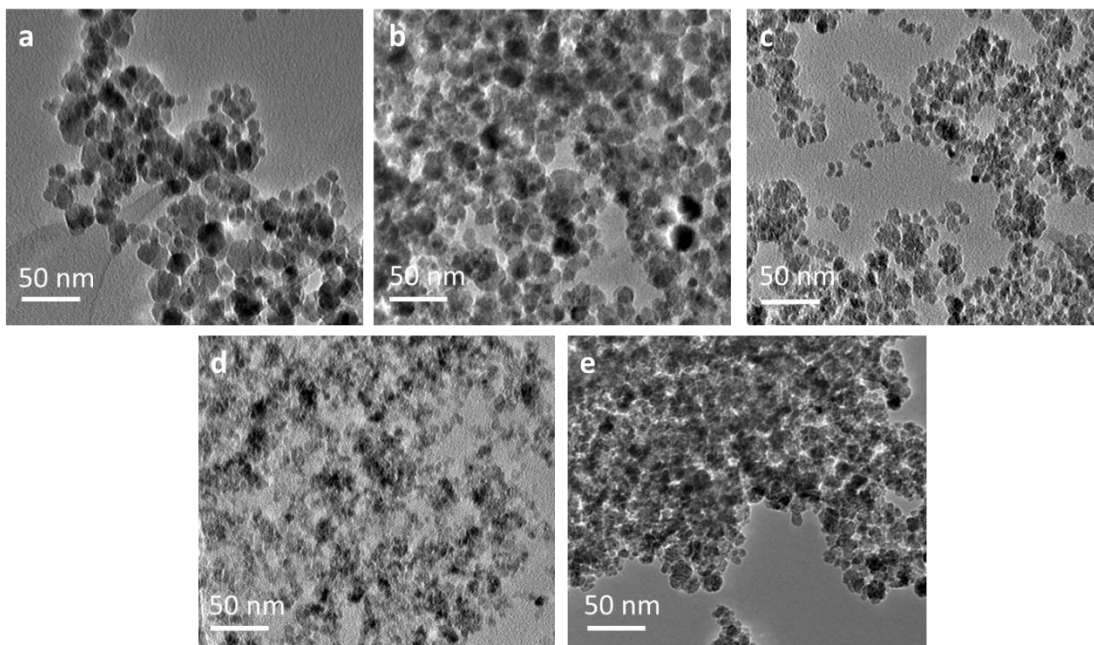


Figure 5.6 TEM images of dextran coated iron oxide nanoparticles synthesized via the (a) two-step method, (b) semi-two-step method, (c) simultaneous semi-two-step method, (d) one-step method with 5 grams dextran, and (e) one-step method with 1 gram dextran.

The crystalline structure of iron oxide nanoparticles enables heating in the presence of an alternating magnetic field via multiple possible loss mechanisms including Néel paramagnetic switching, friction losses from Brownian rotation, and hysteresis (Dennis, Jackson et al. 2009). Table 5.4 summarizes the specific absorption rates of the nanoparticles in the presence of an AMF (58 kA/m, 292 kHz) and the corresponding intrinsic loss power (ILP). The one-step method with five grams of dextran resulted in nanoparticles with the lowest SAR values which are again due to

dextran chemisorption to the surface of the nanoparticles after nucleation (Sreeja and Joy 2011). Nanoparticles produced by other methods had greater SAR values as well as increased variability. The increased SAR value is thought to be due to nanoparticle agglomeration which would allow for ferromagnetic contributions resulting in increased heating. The excess dextran coating on the one-step method with 5 grams of dextran could also form a “dead layer” which would reduce the total effective moment of the nanoparticles (Kodama 1999, Pardoe, Chua-anusorn et al. 2001). Daou *et al.* (Daou, Greneche et al. 2008) established a similar effect by synthesizing magnetite nanoparticles and showing that carboxylate coupling to the nanoparticle surface could induce spin canting at the surface and reduce the saturation magnetization of the nanoparticles. Additionally, this effect has been observed with citrate capped magnetite nanoparticles synthesized via the co-precipitation method in a one or two-step procedure (Frimpong, Dou et al. 2010). The decrease in SAR value after crosslinking with epichlorohydrin is most likely an artifact of the nanoparticles becoming more stable in solution and the additional probe sonication after dialysis. The nanoparticles are not significantly agglomerating and therefore heating via ferromagnetic contributions in addition to Neel paramagnetic switching and Brownian rotation. The ILP of these systems ranged from 0.16 to 0.39 nHm<sup>2</sup>/kg with the one-step (5 grams Dx) being the lowest and the semi-two-step being the highest, but with the most variability. Kallamadil et al. compared the ILP of commercial ferrofluids of various hydrodynamic sizes and found that for hydrodynamic diameters ranging from 100 to 170 nm and crystal sizes of approximately 7 nm, the ILP varied between 0.15 and 0.35 nHm<sup>2</sup>/kg (Kallumadil, Tada et al. 2009). Therefore, these systems have heating properties comparable to those commercially available even though the alternating magnetic field strength may be slightly higher than others have used (Hergt, Hiergeist et al. 2004, Fortin, Wilhelm et al. 2007).

Table 5.4 Specific absorption rates (W/g) of iron oxide nanoparticles (3 mg/mL Fe<sub>3</sub>O<sub>4</sub>) heating in an alternating magnetic field (58 kA/m, 292 kHz) of iron oxide nanoparticles synthesized by the various methods (n=3).

Method	Nanoparticle	SAR (W/g)	ILP (nHm <sup>2</sup> /kg)
two-step	Fe <sub>3</sub> O <sub>4</sub> +Dx	323.6 ± 134.1	0.33 ± 0.14
	Fe <sub>3</sub> O <sub>4</sub> +Dx-ECH	297.6 ± 102.5	0.30 ± 0.10
semi-two-step	Fe <sub>3</sub> O <sub>4</sub> +Dx	384.3 ± 37.6	0.39 ± 0.04
	Fe <sub>3</sub> O <sub>4</sub> +Dx-ECH	313.4 ± 50.9	0.21 ± 0.05
simultaneous semi-two-step	Fe <sub>3</sub> O <sub>4</sub> +Dx	321.1 ± 137.3	0.33 ± 0.14
	Fe <sub>3</sub> O <sub>4</sub> +Dx-ECH	211.0 ± 46.6	0.21 ± 0.05
one-step (5 grams Dx)	Fe <sub>3</sub> O <sub>4</sub> +Dx	138.4 ± 13.6	0.14 ± 0.01
	Fe <sub>3</sub> O <sub>4</sub> +Dx-ECH	158.2 ± 51.1	0.16 ± 0.05
one-step (1 gram Dx)	Fe <sub>3</sub> O <sub>4</sub> +Dx	313.9 ± 42.1	0.32 ± 0.04
	Fe <sub>3</sub> O <sub>4</sub> +Dx-ECH	228.3 ± 32.4	0.23 ± 0.03

## 5.4 Conclusions

Overall, the simultaneous semi-two-step method of synthesizing dextran coated iron oxide nanoparticles was the most consistent method and had the greatest batch-to-batch reproducibility. The nanoparticles synthesized by this method were stable in PBS for 12 hours, had hydrodynamic diameters less than 200 nm, generated sufficient heat in the presence of an AMF, and exhibited crystallinity consistent with magnetite. All of these properties can be tuned to varying degrees by simply altering the timing of dextran addition to the reaction. The amount of dextran also alters the properties of the nanoparticles. The one-step reaction was completed with both one and five grams of dextran to evaluate these effects. It was found that the nanoparticles synthesized with five grams of dextran are more stable, adsorb a greater amount of dextran on their surfaces, and have smaller hydrated diameters than the nanoparticles synthesized with one gram of dextran. However, the poor heating properties and small crystal sizes suggested that the one-step method with 5 grams of dextran may not be the preferred method for synthesizing the nanoparticles.

The one-step method with 1 gram of dextran yielded nanoparticles with improved heating properties and larger crystal sizes but larger and more inconsistent hydrolyzed diameters and decreased stability. The semi-two step and two-step methods resulted in nanoparticles with inconsistent physicochemical properties batch-to-batch. The heating properties were improved compared to the one-step with 5 grams dextran, but the size was larger with greater polydispersity indices. Also, the stability in PBS was decreased. Therefore, the method by which the dextran coated iron oxide nanoparticles are synthesized greatly affects the physical and chemical properties of the nanoparticles and thus, it is critical that the co-precipitation method for the preparation of magnetic nanoparticles is carefully developed and controlled to get desired properties for specific applications.

## **Chapter 6 Peptide conjugated magnetic nanoparticles for magnetically mediated energy delivery**

Limitations of magnetically mediated hyperthermia have led to increased interest in magnetically mediated energy delivery which does not rely on a bulk temperature increase for therapy, but rather on magnetic nanoparticles internalized within cells exerting nanoscale heating or rotational forces intracellularly. The goal of this chapter was to synthesize magnetic nanoparticles functionalized with a cell penetrating peptide and analyze the cellular effects upon internalization and activation via an alternating magnetic field. The chapter is taken directly or adapted from work recently submitted to Future Nanomedicine. Used with permissions from Anastasia K. Hauser, Kimberly W. Anderson and J. Zach Hilt, "Peptide conjugated magnetic nanoparticles for magnetically mediated energy delivery."

### **6.0 Abstract**

Iron oxide nanoparticles have been extensively studied for magnetically mediated hyperthermia applications, although one of the main limitations of this therapy is the high nanoparticle concentration required to increase the tumor tissue temperature into the hyperthermia range (42-45 °C). Therefore, it has been suggested that magnetically mediated energy delivery (MagMED), or the use of magnetic nanoparticles to locally convert alternating magnetic field (AMF) energy into other forms of energy (e.g., heat and rotational work) is a potential alternative strategy. MagMED relies on internalized magnetic nanoparticles and does not require a bulk temperature rise to induce cellular effects. Here, dextran-coated iron oxide nanoparticles functionalized with a cell penetrating peptide (TAT peptide) were synthesized. Uptake of the nanoparticle systems into A549 and H358 lung carcinoma was evaluated along with the intracellular effects of MagMED on the two cell lines such as reactive oxygen species (ROS) generation, lysosomal permeability, mitochondrial membrane depolarization, and initiation of Caspase 3/7 apoptotic pathways. Long term cell viability was also analyzed following MagMED treatment. In both A549 and H358 cells, the novel TAT functionalized nanoparticles and AMF

exposure increased ROS generation compared to the nanoparticle system alone. The TAT functionalized nanoparticles also induced lysosomal membrane permeability and mitochondrial membrane depolarization, but these effects were cell line dependent and were not further enhanced by AMF treatment. Although not statistically significant, there are trends suggesting an increase in apoptosis via the Caspase 3/7 pathways when cells are exposed to TAT functionalized nanoparticles combined with AMF, and although intracellular effects of MagMED treatment were observed, there was no statistical decrease in cell viability 48 hours following treatment.

## 6.1 Introduction

Iron oxide nanoparticles have been studied for a wide variety of biological applications including magnetic resonance imaging (MRI), cell separation techniques, drug delivery, magnetically mediated hyperthermia (MMH), and in the treatment of anemia (Dennis, Jackson et al. 2009, Hu, Ma et al. 2011, Laurent, Dutz et al. 2011, McCormack 2012, Plouffe, Murthy et al. 2015). In magnetically mediated hyperthermia, iron oxide nanoparticles convert energy from an alternating magnetic field (AMF) to heat via Néel relaxation and Brownian rotation (Dennis, Jackson et al. 2009). MMH targets a bulk temperature rise between 42-45 °C which can lead to adverse cellular effects, and although MMH has been extensively studied, its translation into the clinic has been limited. MMH studies completed *in vitro* utilize high nanoparticle concentrations to achieve hyperthermia conditions in monolayer cells or cell suspensions (Laurent, Dutz et al. 2011, Rodriguez-Luccioni, Latorre-Esteves et al. 2011, Wydra, Kruse et al. 2013, Kruse, Meenach et al. 2014) and most *in vivo* experiments directly inject nanoparticles into tumors (usually subcutaneous) due to the need for high local concentrations to generate a bulk temperature rise (Hu, Ma et al. 2011, Wang, Dong et al. 2012). Since direct injection is not suitable for many tumors and metastases, there is a gap between bench scale MMH studies and clinical relevance.

Instead of relying on a bulk temperature rise to induce hyperthermia conditions, it was suggested by Gordon, *et al.* in 1979 that intracellular hyperthermia would be more advantageous

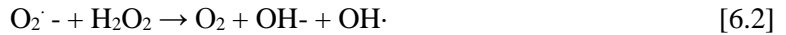
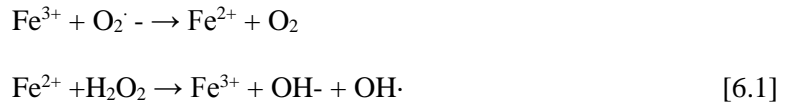
due to insulation by the cell membrane and lack of convection from blood flow which dissipates heat away from the tumor tissue. This is especially problematic in small metastatic tumors (Gordon, Hines et al. 1979). Nanoscale heating effects of the nanoparticles have the ability to induce cellular toxicities as shown by Creixell *et al.* in 2011, where internalized iron oxide nanoparticles in the presence of an AMF induced a significant decrease in cell viability without a measureable temperature rise (Creixell, Bohorquez et al. 2011). Therefore, the phrase magnetically mediated energy delivery (MagMED) was coined to describe the conversion of magnetic field energy to other forms such as heat or rotation work but without significantly increasing the bulk temperature (Kozissnik, Bohorquez et al. 2013).

Although there is a growing body of evidence suggesting that local heating and energy delivery can be used to kill cancer cells, theoretical calculations by Rabin *et al.* indicate that the heat dissipation from the nanoparticle surface through conduction is greater than the heat being generated by the nanoparticles (Rabin 2002). These theoretical calculations were disputed when Huang, *et al.* utilized iron oxide nanoparticles targeted to proteins on the membrane of cells expressing TRPV1 to locally deliver heat and open cation channels (Huang, Delikanli et al. 2010). Nanoparticle heating at the surface was confirmed using a tethered thermoresponsive fluorophore which fluoresced almost immediately upon AMF exposure.

In addition to the effects of surface heating of magnetic nanoparticles in an AMF, rotational work has also been studied as an explanation to the experimental effects of MagMED. For example, mechanical forces have been used to induce lysosomal permeabilization (Sanchez, Diab et al. 2014, Connord, Clerc et al. 2015), leading to the release of proteolytic enzymes such as cathepsins which initiate apoptotic pathways (Linder, Erdal et al. 2005, Kirkegaard and Jaattela 2009, Johansson, Appelqvist et al. 2010). This technique has also been shown to stimulate apoptosis in apoptosis-resistant cell lines (Jaattela 2004). Zhang, *et al.* developed a dynamic magnetic field generator to induce nanoparticle rotations about their axis to examine whether physical nanoparticle rotations

can disrupt lysosomal membranes and induce apoptosis (Zhang, Kircher et al. 2014). By functionalizing the nanoparticles with antibodies for the lysosomal protein marker, it was found that the shear forces generated by oscillating torques were enough to damage the lysosomal membranes, proving that Brownian rotation of magnetic nanoparticles also plays an important role in MagMED treatment.

In addition to the thermal and mechanical effects described above, the production of reactive oxygen species (ROS) via iron oxide nanoparticles is a potential chemical effect of MagMED. Iron oxide nanoparticles catalyze the Haber-Weiss reaction which makes use of Fenton chemistry, and this reaction is considered a major mechanism by which the highly reactive hydroxyl radical is generated in biological systems (Kehrer 2000). The Fenton chemistry reaction set is shown as Equation 6.1 and the Haber-Weiss reaction (net reaction) is shown as Equation 6.2.



When iron oxide nanoparticles enter a cell, they can stimulate the generation of ROS via one of two pathways: (1) the release of ions into the cytosol resulting in the iron ions participating in the Haber-Weiss cycle or (2) the surface of the nanoparticle may act as a catalyst for the Haber-Weiss cycle and the Fenton Reaction (Klein, Sommer et al. 2012). Although this reaction can proceed without the addition of an AMF, recent work by Wydra, *et al.* demonstrated that the reaction is further catalyzed by iron oxide nanoparticles in the presence of an AMF (Wydra, Oliver et al. 2015).

In order to increase intracellular concentrations of iron oxide nanoparticles and therefore increase the efficacy of MagMED, magnetic nanoparticles can be functionalized with ligands, peptides, or antibodies, in order to target and penetrate into the cells. Here, the TAT peptide (sequence: YGRKKRRQRRR) was of particular interest due to its cell penetrating properties and associated ability to avoid receptor mediated endocytosis, as well as its nuclear localizing signal.



The TAT peptide contains a characteristic lysine-arginine sequence, and biomolecules with this tag are known to bind to importin  $\alpha$  and  $\beta$  in the cytoplasm which facilitate active transportation to the nuclear pore complex (NPC) and, if attached to a small enough molecule or particle, through the NPC into the nucleus (Austin, Kang et al. 2011). The positive charge of the NLS peptide also destabilizes the endosome/lysosome membrane leading to nanoparticle and proteolytic enzyme escape from the vesicles, which plays a role in apoptosis initiation. Previous work by Pan *et al.* in 2012 showed that functionalization of doxorubicin (DOX) loaded silica nanoparticles with the TAT peptide facilitated DOX accumulation within the nuclear membrane (Pan, He et al. 2012). Another study by Austin *et al.* proved that TAT-functionalized silver nanospheres were up taken in to HSC-3 cancer cells at significantly greater concentrations than PEG functionalized nanospheres (Austin, Kang et al. 2011). Several studies have utilized the TAT peptide as a cell internalization mechanism (Josephson, Tung et al. 1999, Lewin, Carlesso et al. 2000, Rao, Reddy et al. 2008, Torchilin 2008, Wang, Qiao et al. 2012) as well as a nuclear targeting moiety (Vives, Brodin et al. 1997, de la Fuente and Berry 2005, Oyelere, Chen et al. 2007, Xu, Xie et al. 2008, Yang, Neshatian et al. 2014). Due to the size of the iron oxide nanoparticles being larger than the upper limit of the nuclear pore complex (20—70 nm), it was of interest to use the TAT peptide to escape endosome/lysosomes and facilitate interaction with other organelles such as the mitochondria (Pan, He et al. 2012).

In this study, dextran coated iron oxide nanoparticles were functionalized with a cell penetrating peptide, TAT, and characterized for their physical and chemical properties. Uptake studies into A549 and H358 non-small cell lung carcinoma cells indicated that attachment of the TAT peptide to iron oxide nanoparticles significantly increased cell internalization of the nanoparticles. The effects of internalized iron oxide nanoparticles in combination with AMF exposure on A549 and H358 cells were evaluated. Although A549 and H358 are both non-small cell lung carcinoma cells, this treatment is applicable to a wide variety of cancers, and these cells lines were chosen to assess cell line variability of the treatment. Intracellular generation of ROS, lysosomal membrane

permeability, mitochondrial membrane depolarization, and apoptosis via the Caspase 3/7 pathway were all evaluated. Finally, cell viability was analyzed to determine the toxicity effects of the treatment. Figure 6.1 depicts the three main mechanisms by which MagMED can affect cells. After internalization of the TAT conjugated iron oxide nanoparticles, the lysosomal/endosomal membranes are permeabilized and facilitate nanoparticle escape into the cytosol. Upon actuation by an AMF, nanoparticles dissipate energy through Neel relaxations, frictional energy via Brownian rotation, and catalyze ROS generation. All three of these mechanisms can play a role in the efficacy of MagMED.

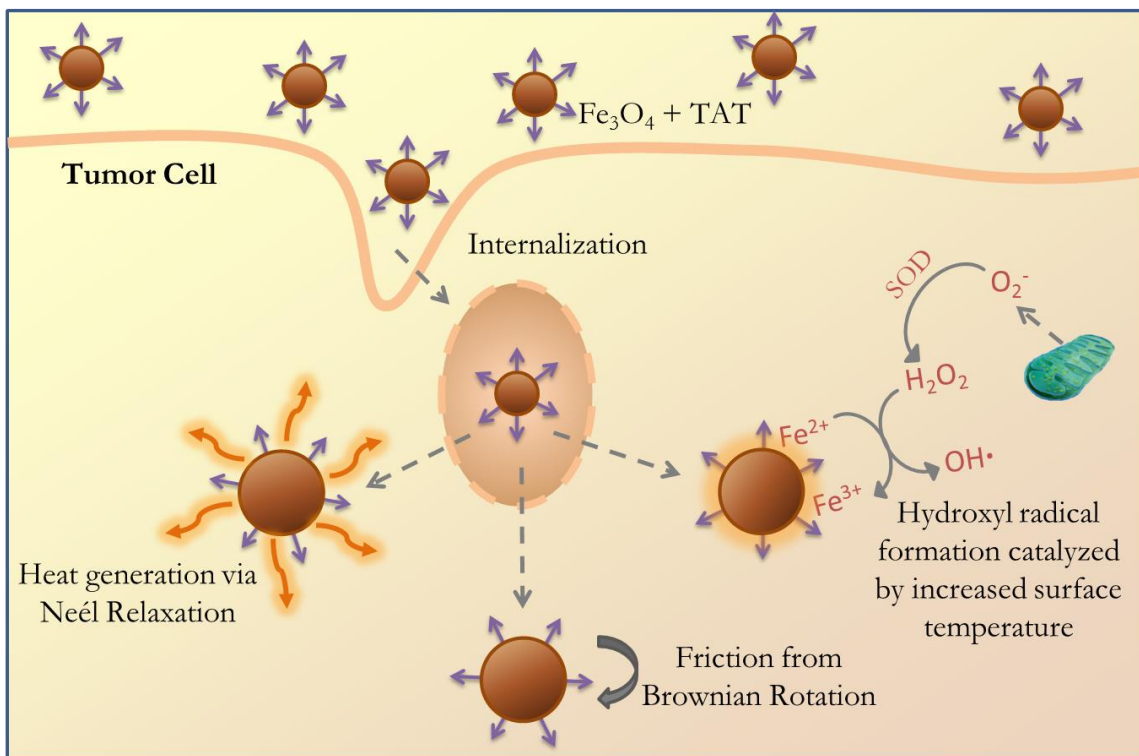


Figure 6.1 TAT-conjugated iron oxide nanoparticles are internalized by cancer cells and permeabilize endosomal/lysosomal membranes due to the positive charge of the peptide. Upon exposure to an AMF, the nanoparticles generate the hydroxyl radical via Fenton chemistry, friction from Brownian rotation and nanoscale heat effects by Neel relaxation.

## 6.2 Materials and Methods

### 6.2.1 Materials

Iron (III) chloride hexahydrate ( $\text{FeCl}_3 \cdot 6\text{H}_2\text{O}$ ), iron (II) chloride ( $\text{FeCl}_2 \cdot 4\text{H}_2\text{O}$ ), 9 – 11 kDa dextran, epichlorohydrin (ECH) were obtained from Sigma Aldrich (St. Louis, MO). Ammonium hydroxide ( $\text{NH}_4\text{OH}$ ) was purchased from EMD Chemicals (Gibbstown, NJ). Phosphate buffered saline solution (PBS) (10X) was purchased from EMD Millipore (Billerica, MA). The activation buffer 2-[N-morpholino] ethane sulfonic acid (MES), *N*-hydroxysulfosuccinimide (sulfo-NHS) and 1-ethyl-3-[3-dimethylaminopropyl] carbodiimide hydrochloride (EDC) were purchased from Thermo scientific (Rockford, IL). The TAT peptide was purchased from Biomatik. Phosphate buffered saline (PBS), Dulbecco's Modified Eagle Medium (DMEM), pen-strep, L-glutamine, Fungizone<sup>®</sup>, sodium pyruvate, CellEvent Caspase 3/7 Assay, JC-1, and calcein AM were obtained from Invitrogen (Frederick, MD). Acridine orange was purchased from Nexcelom Bioscience (Lawrence, MA) and A549 lung carcinoma and trypsin were purchased from American Type Culture Collection (ATCC, Manassas, VA). All materials were used as received.

### 6.2.2 Synthesis of uncoated iron oxide nanoparticles

$\text{FeCl}_3 \cdot 6\text{H}_2\text{O}$  and  $\text{FeCl}_2 \cdot 4\text{H}_2\text{O}$  were combined in a 2:1 molar ratio (2.2 grams and 0.8 grams, respectively) and dissolved in 60 mL deionized (DI) water and sealed in a three-neck flask under vigorous stirring and an inert nitrogen environment. The reaction solution was heated to 85 °C at which 5 ml of  $\text{NH}_4\text{OH}$  was diluted to 40 mL with DI water and the combined solution was injected dropwise into the vessel. The reaction was carried out for 1 hour at 85 °C. The particles were magnetically decanted and washed three times with DI water. The nanoparticles were then re-suspended in DI water and dialyzed against DI water for 24 hours (100 kDa molecular weight cutoff). After dialysis, the nanoparticles were probe sonicated for 10 minutes and then centrifuged at 1000 rpm for 5 minutes to remove large agglomerates.

### *6.2.3 Synthesis of dextran coated iron oxide nanoparticles ( $Fe_3O_4 + Dx$ )*

$FeCl_3 \cdot 6H_2O$  and  $FeCl_2 \cdot 4H_2O$  were combined in a 2:1 molar ratio (2.2 grams and 0.8 grams, respectively) and dissolved in 40 mL deionized (DI) water and sealed in a three-neck flask under vigorous stirring and an inert nitrogen environment. 5 grams of dextran was solubilized in 20 mL of DI water. The reaction solution was heated to 85 °C at which 5 ml of  $NH_4OH$  was added to the dextran solution and the combined solution was injected dropwise into the vessel. The reaction was carried out for 1 hour at 85 °C. The particles were magnetically decanted and washed three times with DI water. The nanoparticles were then re-suspended in DI water and dialyzed against DI water for 24 hours (100 kDa molecular weight cutoff). After dialysis, the nanoparticles were probe sonicated for 10 minutes and then centrifuged at 1000 rpm for 5 minutes to remove large agglomerates.

### *6.2.4 Epichlorohydrin (ECH) crosslinking of dextran coated iron oxide nanoparticles ( $Fe_3O_4 + Dx-ECH$ )*

Dextran coated iron oxide nanoparticles were crosslinked using ECH for increased stability (Palmacci and Josephson 1993). The particle colloid (9 mL, 1 mmol Fe) was added to 9 mL 5M NaOH and 1.5 mL ECH. The reaction was carried out for 24 hours at room temperature under continuous agitation. The particles were then magnetically decanted and dialyzed against DI water (100 kDa molecular weight cutoff) for 24 hours to remove excess ECH.

### *6.2.5 Amine functionalization of crosslinked dextran coated iron oxide nanoparticles ( $Fe_3O_4 + Dx-ECH-Amine$ )*

An equal volume of ammonium hydroxide to mmol iron from  $Fe_3O_4 + Dx-ECH$  were combined and placed on the shaker table for 24 hours. After 24 hours, the nanoparticles were dialyzed against DI  $H_2O$  for an additional 24 hours, with their water changed 3 times during this time period.

#### 6.2.6 TAT peptide conjugation to iron oxide nanoparticles ( $Fe_3O_4 + TAT$ )

10 mg of the TAT-peptide was dissolved in 10 mL MES buffer (2-[N-morpholino] ethane sulfonic acid) and 4 mg EDC and 11 mg sulfo-NHS were also added to the solution. After 15 minutes of continuous agitation, 14  $\mu$ L of 2- mercaptoethanol was added to the reaction in order to quench excess EDC. Amine-functionalized iron oxide nanoparticles were diluted to 1 mg  $Fe_3O_4$ /mL with PBS. The iron oxide suspension was added to the TAT-peptide solution and reacted over night under continuous agitation. After the TAT-iron oxide nanoparticles reaction was complete, the particles were washed with PBS via magnetic decanting until the washing solution was clear. This protocol was adapted from Pan, *et al.* (Pan, He et al. 2012).

#### 6.2.7 Iron concentration assay

Between each step of synthesizing a new system of iron oxide nanoparticles, an iron assay was used to determine the iron concentration of the nanoparticles. 20x, 50x, and 100x dilutions of the iron oxide nanoparticles were made in DI water and 10  $\mu$ L of each dilution was added to 10  $\mu$ L 6M HCl and allowed to sit for 3 hours. After this time, 500  $\mu$ L of 1M acetic acid, 100  $\mu$ L of hydroxylamine hydrochloride, 100  $\mu$ L of 1, 10 phenanthroline, and 280  $\mu$ L of DI water were added to each dilution. Solutions were left overnight. After 24 hours, the absorbance of each solution ( $\lambda = 511$  nm) was used to calculate the iron concentration based on a standard curve.

#### 6.2.8 Iron oxide nanoparticle characterization

*Dynamic light scattering (DLS).* DLS measurements were obtained using a Beckman Coulter Delsa Nano C particle analyzer Nanoparticle solutions were diluted to 200  $\mu$ g/mL in DI water or cell culture media and were sonicated in a water bath for five minutes prior to size analysis. The reported nanoparticle sizes in cell culture media were recorded 10 minutes after bath sonication.

*Zeta Potential.* Zeta potential measurements were obtained using a Beckman Coulter Delsa Nano C particle analyzer. Nanoparticle solutions were diluted to 200  $\mu$ g/mL in 2mM NaCl and were sonicated in a water bath prior to analysis.

*X-ray Diffraction (XRD).* XRD patterns were obtained by a Siemens D-500 X-ray spectrometer with a CuK $\alpha$  radiation source ( $\lambda = 1.54 \text{ \AA}$ ) at 40 kV and 30 mA scanning from 5° to 65° at a scan rate of 1° per minute. The XRD patterns were used to confirm the magnetite crystal structure of the iron oxide nanoparticles. The XRD patterns are in coherence with JDCS card (19-0629). The crystal domain size was estimated using the Scherrer equation [6.3]

$$\tau = \frac{K\lambda}{\beta \cos\theta} \quad [6.3]$$

where  $\tau$  is the mean size of the ordered (crystalline) domains  $K$  is a dimensionless shape factor with a value close to unity (0.8396 for iron oxide),  $\lambda$  is the X-ray wavelength,  $\beta$  is the line broadening at half the maximum intensity (FWHM) in radians after subtracting the instrumental line broadening, and  $\theta$  is the Bragg angle (17.72 °).

*Fourier transform infrared (FTIR) spectra.* Attenuated total reflectance FTIR (ATR-FTIR) was used to determine surface functionalization with a Varian Inc. 7000e spectrometer. Dried samples were placed on the diamond ATR crystal and the spectrum was obtained between 700 and 4000  $\text{cm}^{-1}$  for 32 scans.

### 6.2.9 Cell Culture

A549 and H358 cells were cultured between passages 5-11 in Dulbecco's Modified Eagle Medium (DMEM) supplemented with 10% of Fetal Bovine Serum (FBS), 1mM sodium pyruvate, 4 mM L-glutamine, Pen-Strep (100  $\mu\text{g}$  /mL penicillin and 100  $\mu\text{g}$ /mL streptomycin), and 10  $\mu\text{g}$ /ml of Fungizone. Cells incubated at 37 °C and 5% CO<sub>2</sub>.

### 6.2.10 Iron oxide nanoparticle uptake

A549 and H358 cells were seeded into 6 well plates at a density of 100,000 cells/mL and 2 mL/well. After 24 hours, cells were exposed to the nanoparticle systems (uncoated Fe<sub>3</sub>O<sub>4</sub>, Fe<sub>3</sub>O<sub>4</sub>+Dx-ECH, or Fe<sub>3</sub>O<sub>4</sub>+TAT) at a concentration of 500  $\mu\text{g}$ /mL for 2 hours. After two hours, the nanoparticles were removed and the cells were washed twice with PBS to remove any nanoparticles not internalized within the cells. Cells were then detached from the 6 well plates and counted using a

Nexcelom Cellometer to determine the cell concentration in each well. Cells were then centrifuged and the media supernatant was removed. The cell pellets were dried overnight then dissolved in 6M HCl for 72 hours. After 72 hours, 10  $\mu$ L of the dissolved cell pellet was transferred to a new microcentrifuge tube and the iron concentration assay was completed (*Section 2.7*). The iron concentration was then normalized to the number of cells in the sample.

#### *6.2.11 Reactive Oxygen Species (ROS) Generation*

A549 and H358 cells were seeded at 150,000 cells/mL and 2 mL/well in 6 well plates. After 24 hours of growth, the cells were exposed to various nanoparticle systems (uncoated Fe<sub>3</sub>O<sub>4</sub>, Fe<sub>3</sub>O<sub>4</sub>+Dx-ECH, or Fe<sub>3</sub>O<sub>4</sub>+TAT) at a concentration of 500  $\mu$ g/mL iron oxide for 2 hours. After 2 hours of exposure to the nanoparticles, the nanoparticle solutions were removed and cells were washed 2 times with PBS, prior to trypsinizing and transferring the cells to microcentrifuge tubes. The cells were then centrifuged and re-suspended in 1 mL of 50  $\mu$ M carboxy-DCF solution. The cells were incubated in the carboxy-DCF solution for 30 minutes to facilitate internalization of the dye. Half of the samples were then exposed to an alternating magnetic field (AMF) (292 kHz, 56 kA/m) for 30 minutes or 1 hour with 30 minutes post incubation. Carboxy-DCF fluorescence was measured using an Accuri Flow Cytometer in FL-1.

#### *6.2.12 Acridine orange lysosomal permeabilization experiments*

A549 and H358 cells were seeded at 150,000 cells/mL and 2 mL/well into 6 well plates. Cells were exposed to the nanoparticle systems (uncoated Fe<sub>3</sub>O<sub>4</sub>, Fe<sub>3</sub>O<sub>4</sub>+Dx-ECH, or Fe<sub>3</sub>O<sub>4</sub>+TAT) for two hours at a concentration of 500  $\mu$ g/mL iron oxide then rinsed to remove any nanoparticles not associated with the cells. The cells were trypsinized, the trypsin was neutralized with cell culture media, and then the cells were transferred to 1.5 mL microcentrifuge tubes. Half the cells were exposed to an AMF (292 kHz, 56 kA/m) for one hour, then the cells were stained with acridine orange (10  $\mu$ g/mL) for ten minutes at 37 °C prior to analysis using an Accuri Flow Cytometer (FL-3).

#### *6.2.13 Mitochondrial membrane depolarization studies (JC-1)*

A549 and H358 cells were seeded at 150,000 cells/mL and 2 mL/well into 6 well plates. Cells were exposed to the nanoparticle systems (uncoated Fe<sub>3</sub>O<sub>4</sub>, Fe<sub>3</sub>O<sub>4</sub>+Dx-ECH, or Fe<sub>3</sub>O<sub>4</sub>+TAT) for two hours at a concentration of 500 µg/mL iron oxide then rinsed to remove any nanoparticles not associated with the cells. The cells were trypsinized, the trypsin was neutralized with cell culture media, and then the cells were transferred to 1.5 mL microcentrifuge tubes. Half the cells were exposed to an AMF (292 kHz, 56kA/m) for one hour, then the cells were centrifuged, re-suspended in PBS, and stained with JC-1 (2 µM) for 30 minutes at 37 °C prior to analysis using an Accuri Flow Cytometer (FL-1 and FL-3).

#### *6.2.14 Caspase 3/7 apoptosis studies*

A549 and H358 cells were seeded at 150,000 cells/mL and 2 mL/well into 6 well plates. Cells were exposed to the nanoparticle systems (uncoated Fe<sub>3</sub>O<sub>4</sub>, Fe<sub>3</sub>O<sub>4</sub>+Dx-ECH, or Fe<sub>3</sub>O<sub>4</sub>+TAT) for two hours at a concentration of 500 µg/mL iron oxide then rinsed to remove any nanoparticles not associated with the cells. The cells were trypsinized, the trypsin was neutralized with cell culture media, and then the cells were transferred to 1.5 mL microcentrifuge tubes. Half the cells were exposed to an AMF (292 kHz, 56kA/m) for one hour. At 12 or 24 hours post AMF treatment, the cells were centrifuged, re-suspended in PBS, and stained with CellEvent per manufacturer's instructions (1 µL CellEvent/mL cell solution (500 nM)) for 30 minutes at 37 °C prior to analysis using an Accuri Flow Cytometer (FL-1). Cells were gated into two populations: non-apoptotic and apoptotic, with the apoptotic group being higher in FL-1 fluorescence and decreased in forward scatter as confirmed by a CDDP (100 µM) positive control population.

#### *6.2.15 Viability studies*

A549 and H358 cells were seeded at 150,000 cells/mL and 2 mL/well into 6 well plates. Cells were exposed to the nanoparticle systems (uncoated Fe<sub>3</sub>O<sub>4</sub>, Fe<sub>3</sub>O<sub>4</sub>+Dx-ECH, or Fe<sub>3</sub>O<sub>4</sub>+TAT) for two hours at a concentration of 500 µg/mL iron oxide then rinsed to remove any nanoparticles not



associated with the cells. The cells were trypsinized, the trypsin was neutralized with cell culture media, and then the cells were transferred to 1.5 mL microcentrifuge tubes. Half the cells were exposed to an AMF (292 kHz, 56kA/m) for one hour. The cells were then re-seeded into black walled 96 well plates at 15,000 cells/mL and 100  $\mu$ L/well and allowed to grow for 48 hours prior to staining the cells with 2  $\mu$ M calcein AMF and reading fluorescence on a plate reader (ex/em: 485/528 nm). Fluorescence was normalized to the fluorescence of the control (no nanoparticles and no AMF treatment).

## **6.3 Results and Discussion**

### *6.3.1 Iron oxide nanoparticle characterization*

Iron oxide nanoparticles were synthesized via a one-pot co-precipitation method using a 2:1 molar ratio of iron salts and 30% ammonium hydroxide as the reducing agent. Figure 6.2 depicts the subsequent surface functionalization strategy to conjugate the TAT peptide to the nanoparticle surface via EDC/sulfo-NHS crosslinking. Size and zeta potential measurements are summarized in Table 6.1. The number average hydrated diameter of the nanoparticles ranged from 127 nm for the  $\text{Fe}_3\text{O}_4$  + TAT to 177 nm for the  $\text{Fe}_3\text{O}_4$  + Dx-ECH in water. The crosslinked dextran coating on the nanoparticle surface stabilizes the nanoparticles at physiological pH by introducing steric interactions and a relatively neutral surface charge, as indicated by the zeta potential (Lewin, Carlesso et al. 2000, Ayala, Herrera et al. 2013). The decrease in size between the  $\text{Fe}_3\text{O}_4$  + Dx-ECH and  $\text{Fe}_3\text{O}_4$  + TAT is a result of the additional washing steps required to remove unconjugated TAT peptide after the reaction, which also removes loosely attached dextran which was not crosslinked or removed in previous washing steps. The size of these nanoparticle systems is appropriate for cell internalization while being above the cut-off of renal excretion (Ogawara, Yoshida et al. 1999, Petters, Bulcke et al. 2014). DLS was also completed in cell culture media to gauge nanoparticle sizes during cell culture studies. The nanoparticles were stored suspended in DI water at 4  $^{\circ}$ C, diluted in cell culture media and bath sonicated for five minutes prior to recording

DLS measurements over ten minutes. The larger size associated with uncoated  $\text{Fe}_3\text{O}_4$  and  $\text{Fe}_3\text{O}_4 + \text{Dx-ECH-Amine}$  nanoparticles in cell culture medium is an indication that agglomeration of the nanoparticles during storage is not easily reversible. In addition, protein adsorption to the nanoparticle surface likely caused the nanoparticles to increase in size and agglomerate. There is a slight increase in size of the  $\text{Fe}_3\text{O}_4 + \text{Dx-ECH}$  and  $\text{Fe}_3\text{O}_4 + \text{TAT}$  nanoparticles when suspended in cell culture media compared to DI water likely due to protein adsorption. However, the nanoparticles are stabilized by the dextran crosslinked coating and charge repulsion from the TAT peptide which allows the nanoparticles to be easily re-suspended upon bath sonication. The increase in zeta potential between the  $\text{Fe}_3\text{O}_4 + \text{Dx-ECH-Amine}$  (-7.45 mV) and  $\text{Fe}_3\text{O}_4 + \text{TAT}$  (14.8 mV) indicates successful attachment of the TAT peptide to the surface of the nanoparticle (Rao, Reddy et al. 2008).

FTIR was also completed on the  $\text{Fe}_3\text{O}_4 + \text{Dx-ECH-Amine}$  and  $\text{Fe}_3\text{O}_4 + \text{TAT}$  systems to confirm TAT attachment to the surface (Li, Dong et al. 2014). As shown in Figure 6.3a, there are slight changes in the FTIR spectra, most notably a change in the N-H peak at  $3300 \text{ cm}^{-1}$  indicating a decrease in primary amines in the coating due to conjugation of the TAT peptide using EDC/sulfo-NHS crosslinking. TEM and XRD were used to determine iron oxide crystal size. Example TEM images of the dextran coated iron oxide nanoparticles are shown in Figure 6.3b. The images shown depict multiple nanoparticle crystals of approximately  $8.9 \pm 2 \text{ nm}$  (average  $\pm$  standard deviation as determined by ten images at 60 nanoparticles per image) in size encapsulated within the dextran coating. The crystalline size is not expected to change with further functionalization of the surface. XRD (Figure 6.3c) confirmed the crystalline structure of the nanoparticles to be iron oxide (likely a combination of magnetite and maghemite due to oxidation), and the Scherrer equation (Equation 6.3) and the (311) peak was used to calculate the average crystal length to be approximately  $12.1 \pm 0.2 \text{ nm}$  ( $n=3$  individual batches), which is comparable to the crystal length determined via TEM imaging. Although bulk heating was not the focus of this work, the specific absorption rate (SAR)

is an indication of how the nanoparticles interact with an AMF. Previous characterization of the crosslinked-dextran coated iron oxide nanoparticles indicated a SAR value of  $211.0 \pm 46.6$  W/g (58 kA/m, 292 kHz), confirming the ability of the nanoparticles to respond to an AMF (Hauser, Mathias et al. 2015).

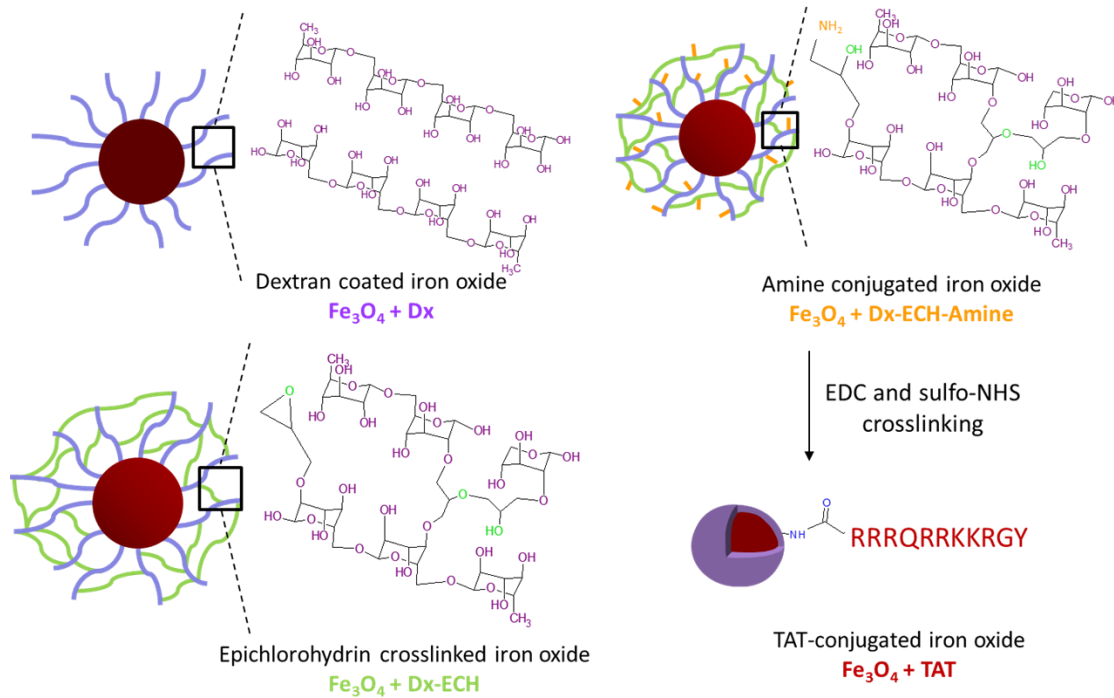


Figure 6.2. Iron oxide nanoparticle synthesis and functionalization of the TAT peptide.

Table 6.1. Iron oxide nanoparticle size from dynamic light scattering in DI water and cell culture media and zeta potential represented as average  $\pm$  standard deviation (n=3).

$\text{Fe}_3\text{O}_4$ Nanoparticle System	DI water		DMEM + 10% FBS		Zeta Potential (mV)
	size (nm)	PDI	size (nm)	PDI	
Uncoated	$136.5 \pm 1.8$	$0.2 \pm 0.02$	$355.1 \pm 23.2$	$0.3 \pm 0.04$	$17.3 \pm 4.1$
Dx-ECH	$177.3 \pm 3.7$	$0.1 \pm 0.03$	$203.4 \pm 4.8$	$0.2 \pm 0.01$	$-5.3 \pm 3.9$
Amine	$173.7 \pm 1.6$	$0.1 \pm 0.02$	$405.7 \pm 29.0$	$0.3 \pm 0.03$	$-7.5 \pm 6.2$
TAT	$126.9 \pm 3.2$	$0.2 \pm 0.02$	$201.5 \pm 15.1$	$0.2 \pm 0.02$	$14.8 \pm 4.7$

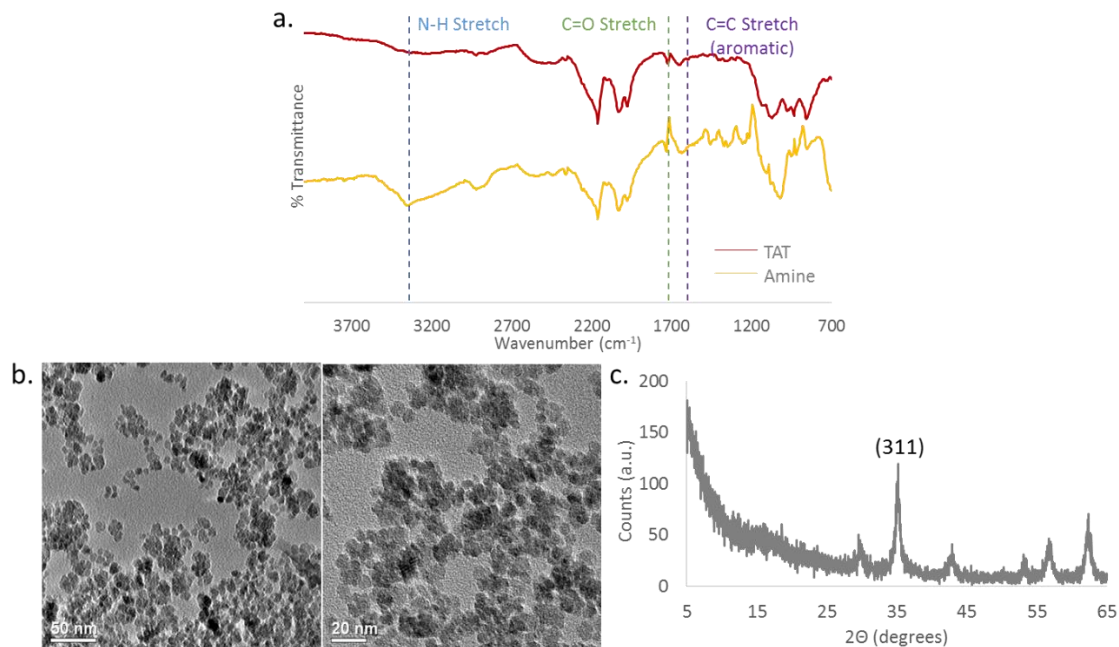


Figure 6.3 Nanoparticle characterization. a. FTIR spectra of amine functionalized and TAT conjugated iron oxide nanoparticles. b. TEM images of dextran coated iron oxide nanoparticles to confirm Fe<sub>3</sub>O<sub>4</sub> crystalline structure. c. X-ray diffraction pattern of dextran coated iron oxide nanoparticles.

### 6.3.2 Cellular uptake of iron oxide nanoparticles

A549 and H358 lung cancer cells were exposed to three nanoparticle systems of interest at a concentration of 500 µg/mL for two hours. This exposure time and concentration were kept constant throughout the studies completed. As shown in Figure 6.4, Fe<sub>3</sub>O<sub>4</sub> + TAT uptake was significantly greater than the other nanoparticle systems in both cell lines due to the TAT peptide being a cell penetrating peptide and positively charged, which enhances internalization of its attached cargo (Thorek and Tsourkas 2008, Torchilin 2008, Villanueva, Canete et al. 2009, Wang, Qiao et al. 2012, Ayala, Herrera et al. 2013). The uncoated Fe<sub>3</sub>O<sub>4</sub> nanoparticles were internalized to a significantly greater extent than Fe<sub>3</sub>O<sub>4</sub> + Dx-ECH in A549 cells and slightly greater in H358 cells. This is likely due to the positive zeta potential associated with uncoated Fe<sub>3</sub>O<sub>4</sub> (Osaka,

Nakanishi et al. 2009). The  $\text{Fe}_3\text{O}_4 + \text{Dx-ECH}$  system did not result in significant uptake, as the iron concentration is not different from that of the control, and this is likely a result of the slightly negative surface charge which limits uptake (Villanueva, Canete et al. 2009). It was expected that the effects of  $\text{Fe}_3\text{O}_4 + \text{TAT}$  nanoparticles in the presence of an AMF will be greater than the other nanoparticle systems studied due to increased intracellular concentrations.

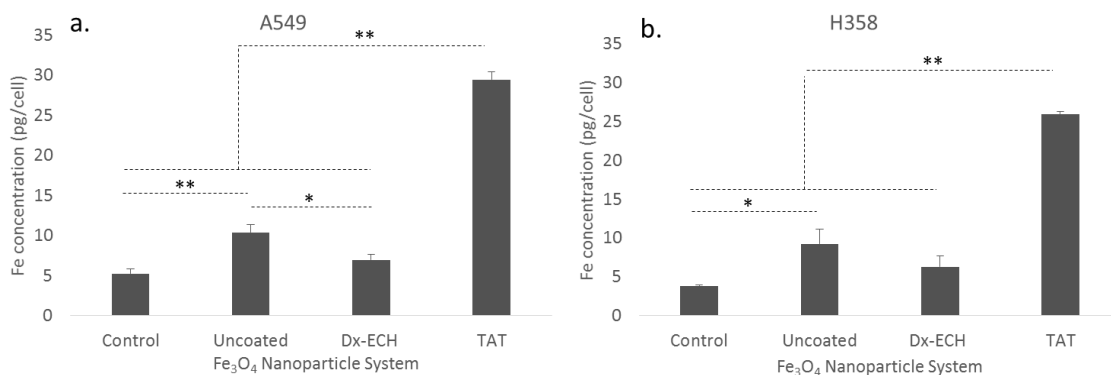


Figure 6.4 Uptake of  $\text{Fe}_3\text{O}_4$  nanoparticles into a.) A549 and b.) H358 lung cancer cells. Error bars represent standard error ( $n=3$ ) and significant differences are indicated by \* ( $p<0.05$ ) and \*\* ( $p<0.01$ ) via a one-way ANOVA.

### 6.3.3 Intracellular reactive oxygen species formation

Iron oxide nanoparticles have the ability to catalyze the formation of the hydroxyl radical via Fenton chemistry. It has been previously shown that hydroxyl radical formation is enhanced in the presence of an AMF due to energy dissipation by Brownian rotation and Néel relaxation resulting in cellular stress (Wydra, Oliver et al. 2015). Figure 6.5a shows carboxy-DCF fluorescence of A549 lung carcinoma exposed to the three nanoparticle systems and a control followed by 30 minutes or one hour AMF treatment, which did not result in a measureable temperature rise. AMF treatment for 30 minutes significantly enhanced ROS production in A549 cells exposed to uncoated  $\text{Fe}_3\text{O}_4$  and  $\text{Fe}_3\text{O}_4 + \text{TAT}$ . The surface of uncoated  $\text{Fe}_3\text{O}_4$  is not shielded and therefore can interact with the cell environment and catalyze hydroxyl radical formation through Fenton chemistry. Enhancement

of ROS generation via uncoated  $\text{Fe}_3\text{O}_4$  in the presence of an AMF was previously shown by Wydra et al., where methylene blue decolorization was enhanced in the presence of uncoated  $\text{Fe}_3\text{O}_4$  and an AMF compared to the theoretical degradation associated with bulk temperature rise (Wydra, Oliver et al. 2015).

$\text{Fe}_3\text{O}_4$  + TAT nanoparticles are potentially inducing local heating effects or frictional effects from Brownian rotation and therefore causing cell stress and increasing ROS production. Only the  $\text{Fe}_3\text{O}_4$  + TAT increased ROS production in A549 lung carcinoma when exposed to an AMF for both 30 minutes and one hour, which is likely due to the increased concentration of intracellular nanoparticles and, therefore, greater local heating and frictional effects. Although not significant, uncoated  $\text{Fe}_3\text{O}_4$  combined with one hour AMF exposure slightly increased intracellular ROS production. The convergence in ROS production between uncoated  $\text{Fe}_3\text{O}_4$  and uncoated  $\text{Fe}_3\text{O}_4$  with one hour AMF can be explained by the inherent ability of the nanoparticle to increase intracellular ROS production through Fenton chemistry at the surface even without local energy dissipation (Wydra, Oliver et al. 2015). The longer AMF exposure time increased the amount of time that the internalized nanoparticles were able to interact intracellularly, which could cause a convergence in ROS generation between the no AMF and one hour AMF treatments for cells exposed to uncoated  $\text{Fe}_3\text{O}_4$ .

It should also be noted that the A549 control cells, which were not exposed to iron oxide nanoparticles, still generate ROS through natural cellular respiration. By increasing AMF exposure time, carboxy-DCF exposure time also increased resulting in increased fluorescence being associated with the longer AMF exposure. By doubling the AMF exposure time, the carboxy-DCF exposure nearly doubled, resulting in a near two-fold increase in fluorescence of control A549 cells. However, this was not observed in H358 cells as shown in Figure 6.5b. Increased H358 incubation time with carboxy-DCF did not show the same increase in fluorescence indicating that the cells were potentially operating at their maximal ROS generation rate. The difference in inherent ROS

production between A549 and H358 cells was determined by incubating the cells with 50  $\mu$ M carboxy-DCF for two hours and then measuring the raw fluorescence of the cells via flow cytometry. As shown in Figure 6.6, H358 cells operated at a higher level of reactive oxygen species than A549 cells. Previous work by Trachootham, *et al.* in 2006 showed that increased oxidative stress in cancer cells is associated with oncogenic transformation by transfecting T72 ovarian cells with the Ras gene (Trachootham, Zhou et al. 2006). Oncogenic transformation resulted in increased oxidative stress as well as increased sensitivity to ROS inducing agents. Therefore, increased oxidative stress results in greater dependence upon antioxidant systems causing the cells to be more sensitive to exogenous agents, which threaten this delicate balance (Trachootham, Zhou et al. 2006, Wang and Yi 2008, Klein, Sommer et al. 2012, Huang, Chen et al. 2013).

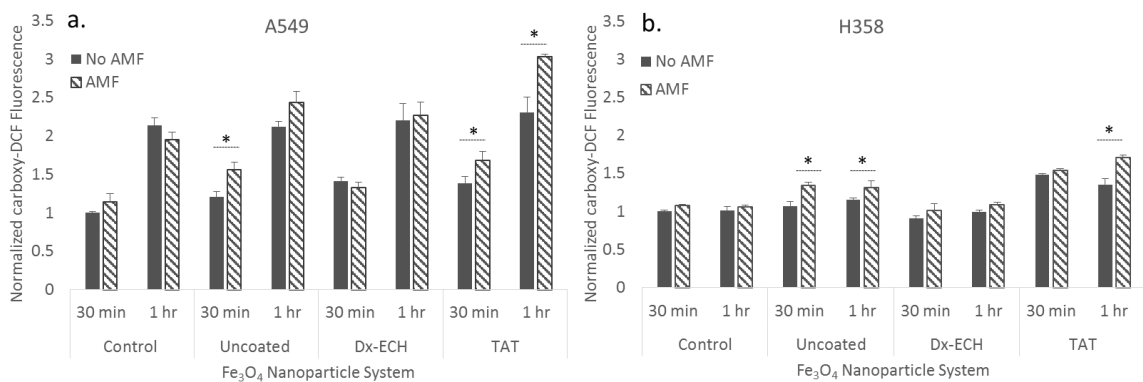


Figure 6.5 Normalized carboxy-DCF fluorescence of a.) A549 and b.) H358 lung cancer cells after treatment with  $\text{Fe}_3\text{O}_4$  nanoparticles with and without 30 minutes or 1 hour AMF exposure. Error bars represent standard error ( $n=3$ ) and significant difference is indicated by \* ( $p<0.05$ ) via a two-way ANOVA.

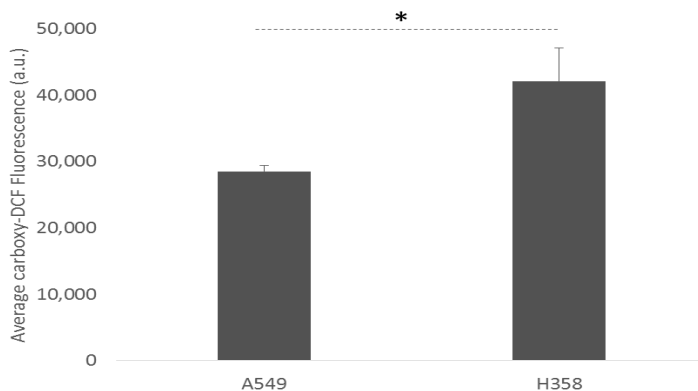


Figure 6.6 Average fluorescence of A549 and H358 cells after 2 hours of exposure to 50  $\mu$ M carboxy-DCF. Error bars represent standard error (n=5) and \* indicates a significant difference (p<0.05) via a t-test.

#### 6.3.4 Intracellular effects of internalized iron oxide nanoparticles and AMF exposure

There are a multitude of intracellular properties and pathways that can be affected by increased ROS production. Therefore, we have evaluated lysosomal permeability, mitochondrial membrane permeability, apoptosis via the Caspase 3/7 pathway, and cell viability of A549 and H358 lung cancer cells after exposure to the nanoparticle systems with and without one hour of AMF exposure. AMF exposure did not result in a measurable temperature rise.

An increase in lysosome permeability is associated with several apoptosis pathways. Destabilization of the lysosomal membranes releases lysosomal contents such as proteolytic enzymes (*e.g.*, cathepsins) into the cytosol, which then induces mitochondrial damage by enhancing the production of superoxide radicals and hydrogen peroxide, further increasing lysosome permeability, resulting in an amplifying feedback loop (Zhao, Antunes et al. 2003). Acridine orange (AO) is a metachromatic fluorophore which gives a distinct red fluorescence at high lysosomal concentrations and a weakly green fluorescence at the low cytosolic concentration and can therefore be used to measure lysosomal membrane permeability, with a decrease in the red fluorescence channel corresponding to an increase in lysosome permeability (Terman, Kurz et al. 2006). AO red



fluorescence was measured for A549 (Figure 6.7a) and H358 (Figure 6.7b) immediately following iron oxide nanoparticle internalization and one hour of AMF exposure, and these fluorescence intensities were then normalized to the control with no AMF exposure. Lysosome permeability increased with Fe<sub>3</sub>O<sub>4</sub> + TAT treatment in both A549 and H358 cells. However, the permeability was not further increased by AMF exposure. This could be a result of saturating the assay as the Fe<sub>3</sub>O<sub>4</sub> + TAT nanoparticles permeabilized the lysosomal membranes to the same extent as the 100 μM hydrogen peroxide positive control (data not shown), and thus, the effects of the AMF could not increase the permeability further. In A549 lung carcinoma, all of the nanoparticles significantly increased lysosome permeability. This could be due to the uncoated Fe<sub>3</sub>O<sub>4</sub> nanoparticles generating ROS within the lysosome, leading to destabilization of the membrane (Terman, Kurz et al. 2006).

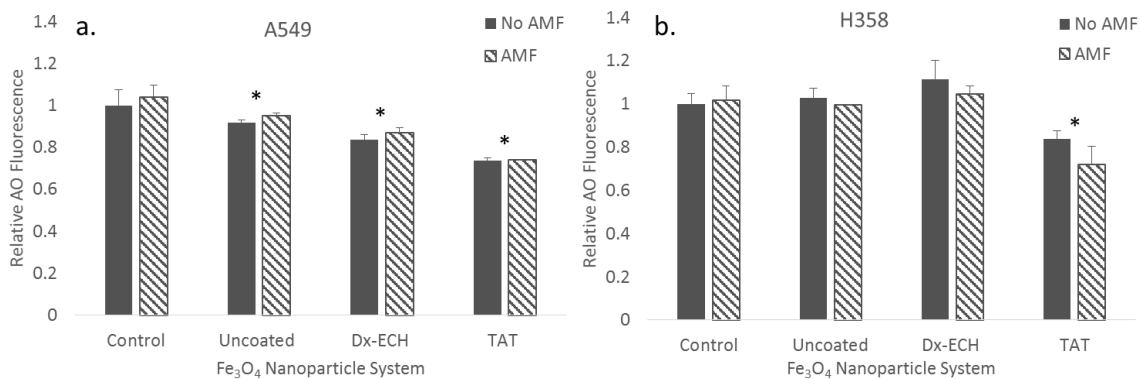


Figure 6.7 Relative acridine orange (AO) fluorescence of a.) A549 and b.) H358 lung cancer cells after treatment with Fe<sub>3</sub>O<sub>4</sub> nanoparticles with and without 1 hour AMF exposure. Error bars represent standard error (n=3) and significant difference from the control is indicated by \* (p<0.05) via a two-way ANOVA.

The JC-1 assay employs a cationic dye that exhibits potential dependent accumulation in mitochondria. At high concentrations, such as those in the mitochondria, the JC-1 dye aggregates to form red-fluorescent J-aggregates. Depolarization of the mitochondrial membrane results in lower JC-1 concentrations and therefore the formation of green-fluorescent monomers.

Mitochondrial membrane potential can be monitored using the JC-1 ratio (red/green fluorescence). A decrease in the red/green fluorescence ratio is the result of mitochondrial membrane depolarization, which occurs in the early stages of apoptosis (Ly, Grubb et al. 2003). Figure 6.8 shows the percentage of cells with mitochondrial membrane depolarization, which resulted in a decreased JC-1 ratio. In A549 lung carcinoma,  $\text{Fe}_3\text{O}_4$  + TAT treatment resulted in a significant increase in the percentage of the cell population with depolarized mitochondrial membranes. However, this was not significantly increased with the addition of AMF treatment. As previously mentioned, mitochondrial integrity can be compromised by increases in lysosomal permeability due to the escape of toxins and proteolytic enzymes into the cytosol. Therefore, it is hypothesized that the  $\text{Fe}_3\text{O}_4$  + TAT nanoparticles permeabilized the lysosomal membranes which then affected the mitochondrial integrity of the A549 lung carcinoma. There is also the possibility that the  $\text{Fe}_3\text{O}_4$  + TAT nanoparticles fully escaped the lysosomes, interacted with the mitochondria, and catalyzed ROS formation at the mitochondria. However, it should be noted that this effect is cell line dependent as the  $\text{Fe}_3\text{O}_4$  + TAT nanoparticles did not disrupt the mitochondrial membrane integrity in H358 lung carcinoma.

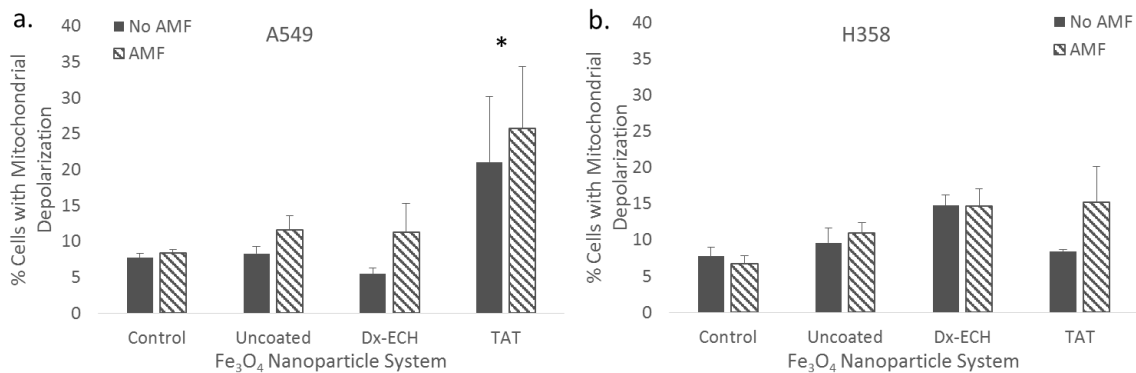


Figure 6.8 Percentage of a.) A549 and b.) H358 cells with depolarized mitochondrial membranes as indicated by a decrease in the ratio between FL3/FL1 (JC1 ratio). Error bars represent standard error (n=3) and \* indicates a significant difference (p<0.05) compared to the control as determined via a two-way ANOVA.

An increase in lysosome membrane permeability and depolarization of the mitochondrial membrane are both found upstream in many apoptotic pathways (Brunk, Neuzil et al. 2001, Ly, Grubb et al. 2003). Therefore, the effects of the iron oxide nanoparticle systems and subsequent AMF exposure on the Caspase 3/7 apoptotic pathway were evaluated. Due to the cells being in different stages of the cell cycle at the time of treatment, the time between treatment and analysis of the apoptotic population was delayed to 12 and 24 hours post treatment. These time points were determined using hydrogen peroxide controls and evaluating the peak times of apoptosis following treatment (data not shown). Although there were no statistically significant differences between the percent of apoptotic cells when comparing the nanoparticle systems to one another and the individual systems with and without AMF treatment, there were trends in the data that are interesting and warrant further exploration of these potential effects. In Figure 6.9, both A549 lung carcinoma and H358 bronchi alveolar appeared to increase in apoptosis when the nanoparticles were combined with AMF, although not significant. Additionally, H358 cells appear to have increased apoptosis compared to A549 in all treatments. This could be a result of the H358 cells being more sensitive to the treatment as well as the processing procedure of the experiment. It also appeared as though uncoated Fe<sub>3</sub>O<sub>4</sub> and Fe<sub>3</sub>O<sub>4</sub> + TAT resulted in greater apoptosis than the Fe<sub>3</sub>O<sub>4</sub> + Dx-ECH in H358 cells which corresponds to the ROS generation data provided previously. The significant error observed in this assay prevents firm conclusions about differences between the treatments. However, as previously mentioned, there were notable trends in the data. In future studies, additional assays, such as Annexin V/Propidium iodide (PI), will be used as the variability in the current assay limit the conclusions that can currently be made. Additionally, prior work by Wydra, *et al.* used the Caspase 3/7 assay to show a significant increase in apoptosis of CT26 colon cancer cells when uncoated, citric acid coated and glucose functionalized iron oxide nanoparticles were combined with AMF (292 kHz, 56 kA/m) exposure for 1 hour compared to the nanoparticle systems alone (Hauser, Wydra et al. , Wydra, Rychahou et al. 2015).The effect was larger in this

case and found to be statistically significant, which further confirms that the efficacy of MagMED treatment is cell line dependent as expected.

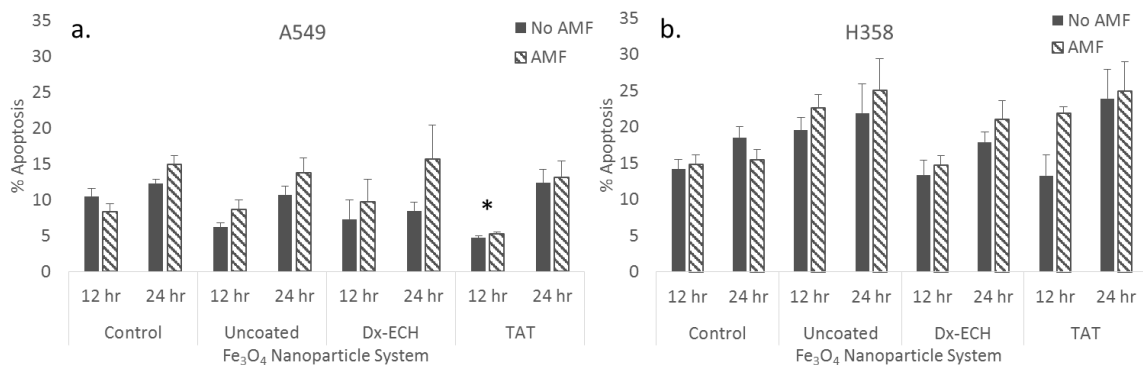


Figure 6.9 Percentage apoptosis of a.) A549 and b.) H358 lung cancer cells 12 and 24 hours after treatment with Fe<sub>3</sub>O<sub>4</sub> nanoparticles with and without 1 hour AMF. Error bars represent standard error (n=3) and significant difference from the control is indicated by \* (p<0.05) via a two-way ANOVA.

A549 and H358 viability 48 hours following treatment with the nanoparticle systems with and without AMF were evaluated and shown in Figure 6.10. In A549 lung carcinoma, there is no significant difference between the nanoparticle systems and the control or within a nanoparticle system with and without AMF treatment. In the H358 cells, only the uncoated Fe<sub>3</sub>O<sub>4</sub> nanoparticles resulted in a decrease in cell viability compared to the control, but there was no additional decrease in viability as a result of AMF treatment. Although intracellular effects of the nanoparticle systems combined with AMF were observed (*e.g.*, especially in intracellular ROS generation), the intracellular effects were not enough to induce a decrease in cell viability. Previous work by Creixell *et al.* showed a significant decrease in cell viability when internalized EGFR targeted iron oxide nanoparticles were combined with an AMF for 2 hours (Creixell, Bohorquez et al. 2011). However, there was significant toxicity of the EGFR targeted nanoparticles alone which could have sensitized the cells to additional treatment with the AMF. Additionally, the AMF treatment time

was two hours instead of the one hour used in these studies. Another study completed by Domenech *et al.* demonstrated that intracellular energy delivery is cell line dependent. MDA-MB 231 and 184-85 cells were incubated with EGF targeted, carboxymethyl dextran coated iron oxide nanoparticles and then exposed to an AMF (233 kHz, 41.75 kA/m) for 1 hour (Domenech, Marrero-Berrios *et al.* 2013). A decrease in viability of MDA-MB-231 cells was observed with the addition of AMF treatment however, while 184-85 cell viability was not affected by AMF treatment. Future work will explore utilizing intracellular energy delivery as a combinational treatment in order to enhance the efficacy of conventional treatments such as chemotherapy and radiation. It is possible that intracellular energy delivery can act as a sensitizer to additional treatments resulting in a synergistic combinational effect.

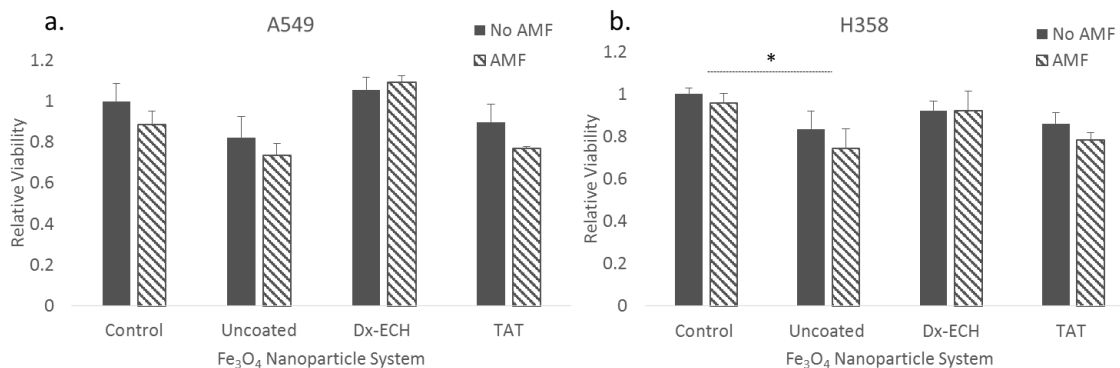


Figure 6.10 Relative viability of a.) A549 and b.) H358 lung cancer cells 48 hours after treatment with  $\text{Fe}_3\text{O}_4$  nanoparticles with and without 1 hour AMF. Error bars represent standard error ( $n=3$ ) and significant difference from the control is indicated by \* ( $p<0.05$ ) via a two-way ANOVA.

## 6.4 Conclusions

Dextran coated iron oxide nanoparticles were successfully functionalized with the TAT peptide and characterized for their physicochemical properties. The nanoparticles ranged in size from approximately 130-180 nm and successful conjugation of the TAT peptide was confirmed by changes in nanoparticle zeta potential and FTIR spectra. TAT functionalization to dextran coated

iron oxide nanoparticles resulted in a novel nanoparticle system in that the nanoparticles were internalized within cells at significantly greater concentrations but were not internalized via receptor-mediated endocytosis. Uncoated  $\text{Fe}_3\text{O}_4$  and  $\text{Fe}_3\text{O}_4 + \text{TAT}$  increased cellular ROS generation in both A549 and H358 cell lines upon exposure to an AMF. Lysosomal permeability was increased in both cell lines following treatment with  $\text{Fe}_3\text{O}_4 + \text{TAT}$  nanoparticles due to the TAT peptide destabilizing the lysosomal membranes. In A549 cells, the mitochondrial integrity was compromised by the  $\text{Fe}_3\text{O}_4 + \text{TAT}$  nanoparticles but this was not enhanced by AMF exposure or observed in H358 cells, indicating a cell dependent response to treatment. Apoptosis response was also cell line dependent, and although not statistically significant, trends were observed that suggested an increase in apoptosis when nanoparticle systems were combined with AMF treatment. However, there was no difference in the treatments when cell viability was analyzed 48 hours post treatment. Future work will aim to increase consistency of apoptosis assays and increase the scope of tested cell lines. Targeting the nanoparticles to specific organelles could also improve the efficacy of MagMED, especially if the particles were targeted to vital organelles such as the mitochondria.

## **Chapter 7 Targeted iron oxide nanoparticles for the enhancement of radiation therapy**

Iron oxide nanoparticles have the ability to catalyze the Fenton reaction to generate reactive oxygen species (ROS). Radiation therapy promotes mitochondrial respiration which leads to increased superoxide anion production. In the presence of iron oxide nanoparticles, the superoxide anion is converted to the highly reactive hydroxyl radical. The goal of this chapter was to evaluate the cellular effects of radiation combined with the peptide functionalized nanoparticles developed in Chapter 6. The chapter is taken directly or adapted from work recently submitted to Biomaterials. Used with permissions from Anastasia K. Hauser, Mihail I. Mitov, Emily F. Daley, Kimberly W. Anderson and J. Zach Hilt, "Targeted iron oxide nanoparticles for the enhancement of radiation therapy."

### **7.0 Abstract**

To increase the efficacy of radiation, iron oxide nanoparticles can be utilized for their ability to produce reactive oxygen species (ROS). Radiation therapy promotes mitochondrial respiration which is often linked to higher cellular energy production and leads to an increase in mitochondrial production of the superoxide anion which is converted to hydrogen peroxide by superoxide dismutase. Iron oxide nanoparticles can then catalyze the reaction from hydrogen peroxide to the highly reactive hydroxyl radical. Therefore, the overall aim of this project was to utilize iron oxide nanoparticles conjugated to a cell penetrating peptide, TAT, to escape lysosomal encapsulation after internalization by cancer cells and catalyze hydroxyl radical formation. It was determined that TAT functionalized iron oxide nanoparticles and uncoated iron oxide nanoparticles resulted in permeabilization of the lysosomal membranes. Additionally, mitochondrial integrity was compromised when A549 cells were treated with both TAT-functionalized nanoparticles and radiation. Pre-treatment with TAT-functionalized nanoparticles also significantly increased the ROS generation associated with radiation. A long term viability study showed that TAT-functionalized iron oxide nanoparticles combined with radiation resulted in a synergistic

combination treatment. This is likely due to the TAT-functionalized nanoparticles sensitizing the cells to subsequent radiation therapy, because the nanoparticles alone did not result in significant toxicities.

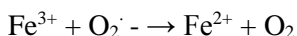
## **7.1 Introduction**

Iron oxide nanoparticles have been previously studied for their multitude of biological applications, magnetic properties, and lack of protein adsorption after proper coating (Laurent, Dutz et al. 2011). Iron oxide nanoparticles have been utilized in magnetically mediated hyperthermia for the treatment of cancer, contrast agents in magnetic resonance imaging, and treatment of anemia (Dennis, Jackson et al. 2009, Hu, Ma et al. 2011, Laurent, Dutz et al. 2011, McCormack 2012). However, recent work suggests that inherent toxicities of the nanoparticles can be utilized to enhance current cancer treatments via the generation of reactive oxygen species (ROS) (Koenczoel, Weiss et al. 2013, Luo, Li et al. 2015).

Cancer cells are more susceptible to oxidative insults compared to normal cells due to fast cell proliferation and metabolism so additional ROS stress induced by exogenous agents can overwhelm the relatively low antioxidant capacity and disrupt the redox homeostasis inside cancer cells leading to selective tumor cell toxicity (Huang, Chen et al. 2013, Luo, Li et al. 2015). Trachootham et al. transfected T72 cells with the Ras gene and showed that oncogenic cells containing the Ras gene operated at increased ROS stress compared to non-transfected cells (Trachootham, Zhou et al. 2006). This increased oxidative stress caused the T72 Ras cells to be more sensitive to PEITC, an exogenous ROS generating agent. ROS have the ability to result in DNA and lipid damage and disturb signal transduction, which can lead to cell death if the damage is severe enough that it cannot be repaired (Kehrer 2000). Therefore, sensitization of cancer cells to radiation by inducing oxidative stress has the potential to synergistically increase treatment efficacy.



The Haber-Weiss reaction results in generation of the highly reactive hydroxyl radical from the reaction between superoxide and hydrogen peroxide. This reaction is thermodynamically unfavorable in biologic systems, and with a second order rate constant of zero in aqueous solution, it was found to require a catalyst to proceed (Kehrer 2000). The iron catalyzed Haber-Weiss reaction, which makes use of Fenton chemistry, is now considered the major mechanism by which the highly reactive radical is generated in biological systems (Kehrer 2000). The Fenton chemistry reaction set is shown as Equation 7.1, and the Haber-Weiss reaction (net reaction) is shown as Equation 7.2.



Under normal conditions, only trace amounts of iron exist outside of physiologic sinks such as transferrin or ferritin. Proteins sequester iron ions so that the ions circulate bound to transferrin and accumulate within cells in the form of ferritin. The absorption of iron is finely regulated to prevent an excess storage and oxidative attack (Emerit, Beaumont et al. 2001). Iron oxide nanoparticles have been previously studied for their multitude of biological applications, and recent work suggests that the uptake of iron oxide nanoparticles can lead to a concentration increase of intracellular unbound iron which may result in cell injury or death (Weissleder, Stark et al. 1989, Klein, Sommer et al. 2012, Alarifi, Ali et al. 2014), especially when combined with additional therapies (Klein, Sommer et al. 2012, Huang, Chen et al. 2013, Klein, Sommer et al. 2014, Luo, Li et al. 2015). When iron oxide nanoparticles are taken up by a cell, they stimulate the generation of ROS via one of two pathways: the release of ions into the cytosol where chelation by citrate or adenosine phosphate takes place resulting in the iron ions participating in the Haber-Weiss cycle or the surface of the iron oxide nanoparticle may act as a catalyst for the Haber-Weiss cycle and the Fenton reaction (Auffan, Achouak et al. 2008, Lewinski, Colvin et al. 2008, Voinov, Pagan et al. 2011, Klein, Sommer et al. 2012). Both pathways result in the formation of the highly reactive

hydroxyl radical. Iron oxide nanoparticles can exist in many forms with two of the most common forms of iron oxide nanoparticles being magnetite ( $\text{Fe}_3\text{O}_4$ ) and maghemite ( $\text{Fe}_2\text{O}_3$ ). It was suggested by Aranda et al. that magnetite nanoparticles would lead to greater ROS formation and oxidative stress due to iron being present as both  $\text{Fe}^{3+}$  and  $\text{Fe}^{2+}$  ions within magnetite while maghemite has mostly ferric iron ions (Aranda, Sequedo et al. 2013). Therefore, these studies focus on magnetite iron oxide nanoparticles for the generation of intracellular ROS.

There are multiple pathways within the cell that naturally generate ROS. The pathway of particular interest is mitochondrial respiration which produces the superoxide anion (Kehrer 2000). The superoxide anion is converted to hydrogen peroxide through natural superoxide dismutase, and in the presence of iron ions, the conversion of hydrogen peroxide to the highly reactive hydroxyl radical is catalyzed (Koenczoel, Weiss et al. 2013). Although the exact mechanism remains unclear, radiation promotes mitochondrial respiration and therefore increases production of the superoxide anion (Kam and Banati 2013). Yamamori et al. showed that A549 lung carcinoma exhibited increased oxygen consumption rates as well as increased rates of mitochondrial ROS production at 6 and 12 hours following 5 Gy radiation (Yamamori, Yasui et al. 2012). If the intracellular concentration of the superoxide anion is increased following radiation and iron oxide nanoparticles are present to catalyze hydroxyl radical formation, it is hypothesized that the hydroxyl radical concentration will subsequently be increased, resulting in increased toxicity.

Iron oxide nanoparticles are usually taken up by cells through endocytosis resulting in the nanoparticles being encapsulated in endosomes/lysosomes. Due to the acidic nature of these subcellular compartments, the nanoparticles can be degraded prior to fulfilling their purpose. However, if a cell penetrating peptide (CPP) is conjugated to the surface of the iron oxide nanoparticle, the nanoparticle can avoid receptor mediated endocytosis (Vives, Brodin et al. 1997). In this work, the CPP of particular interest is the TAT peptide (sequence: YGRKKRRQRRR), which contains a characteristic lysine and arginine sequence. Biomolecules with this tag are known

to bind to importin  $\alpha$  and  $\beta$  in the cytoplasm allowing for active transportation to the nuclear pore complex (NPC) and, if small enough, through the NPC into the nucleus (Austin, Kang et al. 2011). Several studies have utilized the TAT peptide as a cell internalization mechanism (Josephson, Tung et al. 1999, Lewin, Carlesso et al. 2000, Rao, Reddy et al. 2008, Torchilin 2008, Wang, Qiao et al. 2012) as well as a nuclear targeting moiety (Vives, Brodin et al. 1997, de la Fuente and Berry 2005, Oyelere, Chen et al. 2007, Xu, Xie et al. 2008, Yang, Neshatian et al. 2014).

Although lysosomes may eventually uptake TAT-conjugated nanoparticles residing in the cytosol, the TAT peptide is positively charged and can destabilize lysosomal membranes leading to release of lysosomal contents, including proteolytic enzymes and the nanoparticles (Terman, Kurz et al. 2006). An increase in lysosome membrane permeability is an upstream event in many apoptotic pathways, as the proteolytic enzymes lead to mitochondrial damage by enhancing the production of superoxide radicals and hydrogen peroxide, which in turn increases lysosomal membrane permeability, resulting in an amplifying feedback loop (Zhao, Antunes et al. 2003, Kirkegaard and Jaattela 2009). Due to the size of our iron oxide nanoparticles being larger than the upper limit of the nuclear pore complex (20–70 nm), it was of particular interest to escape endosome/lysosomes in order to interact with other organelles such as the mitochondria (Pan, He et al. 2012).

In this study, dextran coated iron oxide nanoparticles were functionalized with the TAT peptide and this nanoparticle system was used to enhance the efficacy of radiation. The TAT peptide increased intracellular concentrations of the nanoparticles compared to uncoated nanoparticles as shown by transmission electron microscopy (TEM). TEM images also indicate that uncoated iron oxide nanoparticles were encapsulated within lysosomes after cell internalization. However, TAT-functionalized nanoparticles were found in the cytoplasm as well as in lysosomes with destabilized membranes. Lysosomal membrane permeability studies confirmed the ability of the TAT peptide to destabilize the lysosomes, and cell respiration studies indicated that TAT-functionalized

nanoparticles combined with radiation resulted in a loss of mitochondrial integrity, causing the cells to operate at lower metabolic levels. When combined with radiation, the TAT-functionalized nanoparticles increased reactive oxygen species generation to a greater extent than radiation alone. The combined treatment also resulted in synergistic cytotoxic effects on A549 lung carcinoma, as shown by a long term viability study. Therefore, it has been concluded that TAT-conjugated iron oxide nanoparticles have the ability to destabilize lysosomal membranes, releasing their toxic contents into the cytosol and causing the cells to be more sensitive to radiation therapy. Additionally, after radiation therapy when the mitochondria have increased respiration levels and are producing greater amounts of the superoxide anion, the iron oxide nanoparticles can catalyze the formation of the highly reactive hydroxyl radical. This hypothesis is depicted in Figure 7.1.

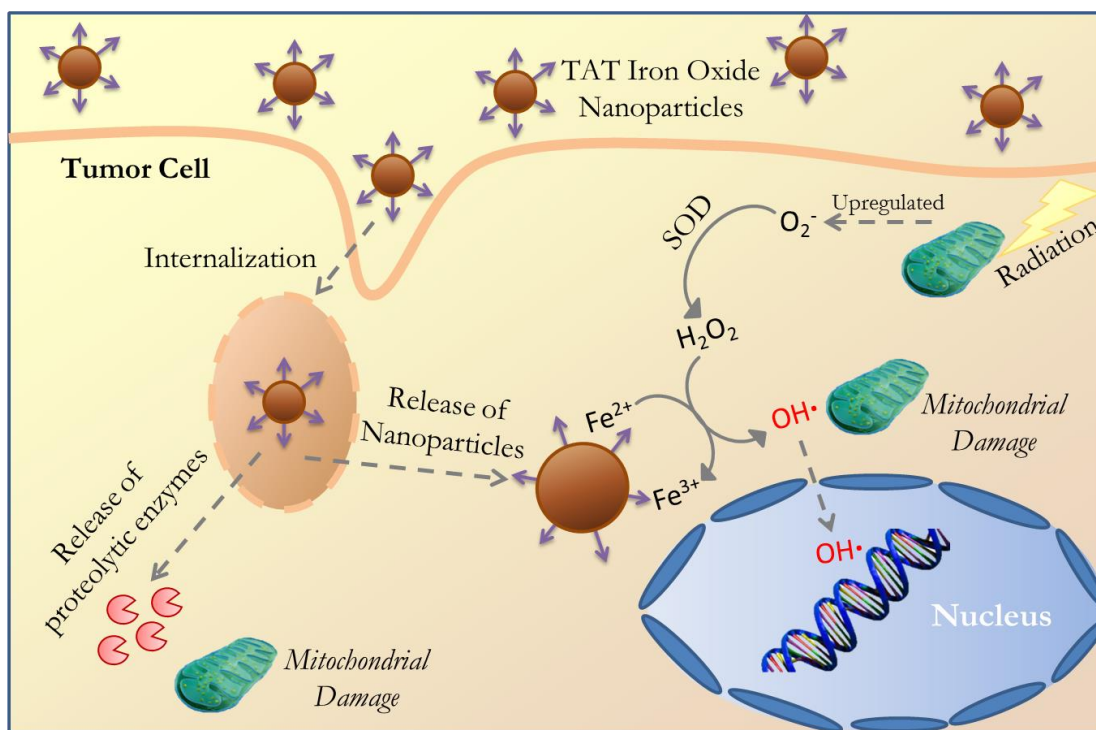


Figure 7.1 TAT-conjugated iron oxide nanoparticles are internalized into the cell, followed by lysosomal membrane permeabilization. This results in release of proteolytic enzymes as well as the nanoparticles into the cytoplasm where they can interact with organelles such as the nucleus and mitochondria and catalyze the formation of the hydroxyl radical.

## 7.2 Materials and Methods

### 7.2.1 Materials

Iron (III) chloride hexahydrate ( $\text{FeCl}_3 \cdot 6\text{H}_2\text{O}$ ), iron (II) chloride ( $\text{FeCl}_2 \cdot 4\text{H}_2\text{O}$ ), 9 – 11 kDa dextran, epichlorohydrin (ECH) were obtained from Sigma Aldrich (St. Louis, MO). Ammonium hydroxide ( $\text{NH}_4\text{OH}$ ) was purchased from EMD Chemicals (Gibbstown, NJ). Phosphate buffered saline solution (PBS) (10X) was purchased from EMD Millipore (Billerica, MA). The activation buffer 2-[N-morpholino] ethane sulfonic acid (MES), *N*-hydroxysulfosuccinimide (sulfo-NHS) and 1-ethyl-3-[3-dimethylaminopropyl] carbodiimide hydrochloride (EDC) were purchased from Thermo scientific (Rockford, IL). The TAT peptide was purchased custom from Biomatik. Phosphate buffered saline (PBS), Dulbecco's Modified Eagle Medium (DMEM), pen-strep, L-glutamine, Fungizone<sup>®</sup>, sodium pyruvate, and calcein AM were obtained from Invitrogen (Frederick, MD). Acridine orange was purchased from Nexcelom Bioscience (Lawrence, MA) and A549 lung carcinoma and trypsin were purchased from American Type Culture Collection (ATCC, Manassas, VA). All materials were used as received.

### 7.2.2 Synthesis of uncoated iron oxide nanoparticles (uncoated $\text{Fe}_3\text{O}_4$ )

$\text{FeCl}_3 \cdot 6\text{H}_2\text{O}$  and  $\text{FeCl}_2 \cdot 4\text{H}_2\text{O}$  were combined in a 2:1 molar ratio (2.2 grams and 0.8 grams, respectively) and dissolved in 60 mL deionized (DI) water and sealed in a three-neck flask under vigorous stirring and an inert nitrogen environment. The reaction solution was heated to 85 °C at which 5 ml of  $\text{NH}_4\text{OH}$  was diluted to 40 mL with DI water and the combined solution was injected dropwise into the vessel. The reaction was carried out for 1 hour at 85 °C. The particles were magnetically decanted and washed three times with DI water. The nanoparticles were then re-suspended in DI water and dialyzed against DI water for 24 hours (100 kDa molecular weight cutoff). After dialysis, the nanoparticles were probe sonicated for 10 minutes and then centrifuged at 1000 rpm for 5 minutes to remove large agglomerates.

### *7.2.3 Synthesis of dextran coated iron oxide nanoparticles ( $Fe_3O_4 + Dx$ )*

$FeCl_3 \cdot 6H_2O$  and  $FeCl_2 \cdot 4H_2O$  were combined in a 2:1 molar ratio (2.2 grams and 0.8 grams, respectively) and dissolved in 40 mL deionized (DI) water and sealed in a three-neck flask under vigorous stirring and an inert nitrogen environment. 5 grams of dextran was solubilized in 20 mL of DI water. The reaction solution was heated to 85 °C at which 5 ml of  $NH_4OH$  was added to the dextran solution and the combined solution was injected dropwise into the vessel. The reaction was carried out for 1 hour at 85 °C. The particles were magnetically decanted and washed three times with DI water. The nanoparticles were then re-suspended in DI water and dialyzed against DI water for 24 hours (100 kDa molecular weight cutoff). After dialysis, the nanoparticles were probe sonicated for 10 minutes and then centrifuged at 1000 rpm for 5 minutes to remove large agglomerates.

### *7.2.4 Epichlorohydrin (ECH) crosslinking of dextran coated iron oxide nanoparticles ( $Fe_3O_4 + Dx-ECH$ )*

Dextran coated iron oxide nanoparticles were crosslinked using ECH for increased stability (Palmacci and Josephson 1993). The particle colloid (9 mL, 1 mmol Fe) was added to 9 mL 5M NaOH and 1.5 mL ECH. The reaction was carried out for 24 hours at room temperature under continuous agitation. The particles were then magnetically decanted and dialyzed against DI water (100 kDa molecular weight cutoff) for 24 hours to remove excess ECH.

### *7.2.5 Amine functionalization of crosslinked dextran coated iron oxide nanoparticles ( $Fe_3O_4 + Dx-ECH-Amine$ )*

An equal volume of ammonium hydroxide to mmol iron from  $Fe_3O_4 + Dx-ECH$  were combined and placed on the shaker table for 24 hours. After 24 hours, the nanoparticles were dialyzed against DI  $H_2O$  for an additional 24 hours, with their water changed 3 times during this time period.

### *7.2.6 TAT peptide conjugation to iron oxide nanoparticles ( $Fe_3O_4$ + TAT)*

10 mg of the TAT-peptide was dissolved in 10 mL MES buffer (2-[N-morpholino] ethane sulfonic acid). 4 mg EDC and 11 mg sulfo-NHS were also added to the solution. Solution was reacted for 15 minutes with continuous agitation after which 14  $\mu$ L of 2- mercaptoethanol was added to the reaction in order to quench excess EDC. Amine-functionalized iron oxide nanoparticles were diluted to 1 mg  $Fe_3O_4$ /mL with PBS. The iron oxide suspension was added to the TAT-peptide solution and reacted over night under continuous agitation. After the TAT-iron oxide nanoparticle reaction was complete, and particles were washed with PBS via magnetic decanting until the washing solution was clear.

### *7.2.7 Iron Concentration Assay*

Between each step of synthesizing a new system of iron oxide nanoparticles, an iron assay was used to determine the iron concentration of the nanoparticles. 20x, 50x, and 100x dilutions of the iron oxide nanoparticles were made in DI water and 10  $\mu$ L of each dilution was added to 10  $\mu$ L 6M HCl and allowed to sit for 3 hours. After this time, 500  $\mu$ L of 1M acetic acid, 100  $\mu$ L of hydroxylamine hydrochloride, 100  $\mu$ L of 1, 10 phenanthroline, and 280  $\mu$ L of DI water were added to each dilution. Solutions were left overnight. After 24 hours, the absorbance of each solution ( $\lambda = 511$  nm) was used to calculate the iron concentration based on a standard curve.

### *7.2.8 Cell Culture*

A549 cells were cultured between passages 5-11 in Dulbecco's Modified Eagle Medium (DMEM) supplemented with 10% of Fetal Bovine Serum (FBS), 1mM sodium pyruvate, 4 mM L-glutamine, Pen-Strep (100  $\mu$ g /mL penicillin and 100  $\mu$ g/mL streptomycin), and 10  $\mu$ g/ml of Fungizone. Cells incubated at 37 °C and 5%  $CO_2$ .

### *7.2.9 Transmission electron microscopy*

A549 cells were seeded into 6 well plates at 13,000 cells/cm<sup>2</sup> and grown for 24 hours. Cells were then exposed to 500  $\mu$ g/mL iron oxide of either uncoated iron oxide nanoparticles or  $Fe_3O_4$  + TAT

for 24 hours. After 24 hours, the nanoparticles suspensions were removed and the cells were rinsed with media to remove non-internalized nanoparticles. Half of the samples were then exposed to 5 Gy radiation. After treatment, the cells were washed with PBS to remove media then fixed in 3.5% glutaraldehyde in 0.1 M Sorenson's buffer for 75 minutes at 4 °C. Cells were then washed 4 times with 0.1 M Sorenson's containing 5% sucrose, post fixed with 1% osmium tetroxide for 45 minutes at 4 °C, then washed again with 0.1 M Sorenson's. Cells were dehydrated in graded ethanols (50-100%) then absolute ethanol twice at 4 °C. Cells were then embedded in Eponate 12 resin and polymerized at 60 °C prior to slicing and mounting for imaging (Philips BioTwin 12 Transmission Electron Microscope).

#### *7.2.10 Acridine orange lysosomal permeabilization experiments*

A549 lung carcinoma cells were seeded at 80,000 cells/mL and 2 mL/well into 6 well plates. Cells were exposed to the nanoparticle systems for three hours at a concentration of 500 µg/mL iron oxide then rinsed to remove any nanoparticles not associated with the cells. Half the cells were exposed to 5 Gy radiation then the cells were stained with acridine orange (10 µg/mL) for ten minutes at 37 °C prior to analysis via flow cytometry (FL-3).

#### *7.2.11 Mitochondrial stress test*

A549 lung carcinoma cells were seeded at densities of 30,000 per well in Seahorse XF96 microplates and allowed to grow overnight. The cells were then exposed to the nanoparticle systems for 3 hours at 500 µg/mL iron oxide then rinsed to remove any nanoparticles not associated with the cells. Half of the samples were then treated with 5 Gy radiation. Mitochondrial stress was then measured using the Seahorse XF 96 Extracellular Flux Analyzer to measure *in vitro* oxygen consumption rate (OCR) and extracellular acidification rate (ECAR). The bioenergetic baseline profiles can be determined by plotting the ECAR vs OCR signal for the last measurement of base line (or just before adding Oligomycin A to the cells as shown in Figure 7.2). To expand, cells were incubated for one hour prior to the start of analysis at 37 °C in XF modified assay medium



containing 25mM Glucose and 1mM Pyruvate. Three baseline OCR and ECAR values were taken over 16 minutes representing the basal respiration rate, which is the total base line OCR minus the non-mitochondrial respiration. The next three measurements were taken for a period over 20 minutes, after the addition of an ATP synthase inhibitor (Oligomycin 1uM) which helps to calculate the amount of oxygen used for ATP turnover. Next, mitochondrial uncoupler, FCCP (0.6  $\mu$ M) was added to force the cells to operate at their maximal respiration rates for 3 measurements over 20 minutes. Finally, antimycin A and rotenone were added to inhibit the electron transport chain of oxidative phosphorylation and therefore disrupt the formation of the proton gradient across the inner membrane, leading to complete cessation of oxygen consumption by the mitochondria, after which three values were taken in 14 minutes. All measurements were normalized to protein using bicinchoninic acid (BCA) assay. Analysis of the effects of Fe<sub>3</sub>O<sub>4</sub> nanoparticle systems combined with radiation on each component of the OCR profile can be found in the supplementary information section.

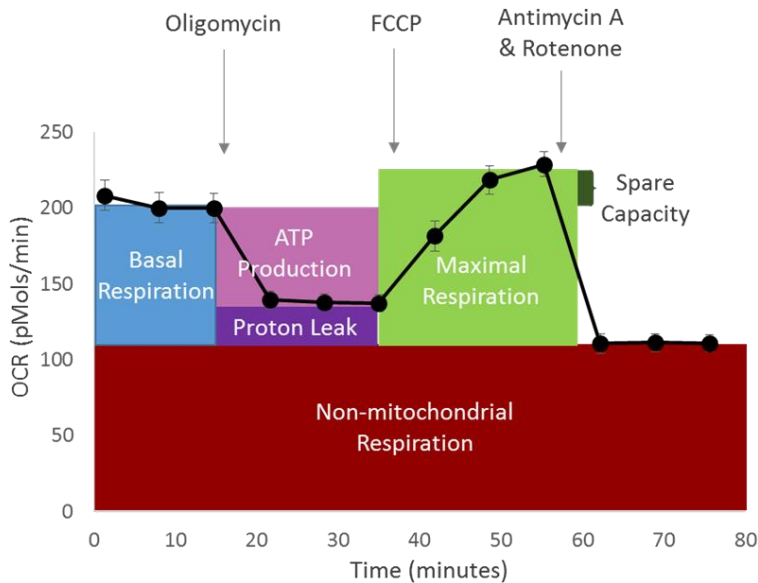


Figure 7.2 Bioenergetic profile of control A549 cells over time. Error bars represent standard error (n=12).

### *7.2.12 Reactive Oxygen Species (ROS) Generation*

A549 human lung carcinoma cells were seeded at 40,000 cells/mL and 100  $\mu$ L/well in black walled 96 well plates. After 24 hours of growth, the cells were exposed to various iron oxide nanoparticle systems (uncoated  $\text{Fe}_3\text{O}_4$ ,  $\text{Fe}_3\text{O}_4$ +Dx-ECH,  $\text{Fe}_3\text{O}_4$ + Dx-ECH-Amine, or  $\text{Fe}_3\text{O}_4$  + TAT) at concentrations of 100  $\mu$ g/mL or 500  $\mu$ g/mL iron oxide for 24 hours. After 24 hours of exposure, the nanoparticle solutions were removed and cells were washed 2 times with media, and 100  $\mu$ L of 50  $\mu$ M carboxy-DCF solution was added to each well followed by 20 minutes of incubation to facilitate internalization of the dye. Half of the samples were then irradiated with 5 Gy radiation. Carboxy-DCF fluorescence was measured using a plate reader (ex/em: 485/528 nm) followed by staining with HOESCHT 33342 nuclear stain to normalize data back to the number of cells present.

### *7.2.13 Viability studies*

A549 human lung carcinoma cells were seeded at 5,000 cells/mL and 100  $\mu$ L/well in black walled 96 well plates. After 24 hours of growth, the cells were exposed to various nanoparticle systems (uncoated,  $\text{Fe}_3\text{O}_4$  + Dx-ECH,  $\text{Fe}_3\text{O}_4$  + Dx-ECH-Amine, or  $\text{Fe}_3\text{O}_4$  + TAT) at a concentration of 500  $\mu$ g/mL iron oxide for 24 hours. After 24 hours of exposure, the nanoparticle solutions were removed and cells were washed 2 times with media and half of the samples were then irradiated with 5 Gy radiation. Cell viability was analyzed 3, 5, and 7 days after treatment using a calcein AM assay. Calcein AM fluorescence was measured on a plate reader and the fluorescence of each treatment was normalized to the fluorescence of the control on that day.

## **7.3 Results and Discussion**

Iron oxide nanoparticle systems were previously synthesized and characterized for physicochemical properties (see Chapter 6). TEM images of A549 lung carcinoma after exposure to uncoated  $\text{Fe}_3\text{O}_4$  or  $\text{Fe}_3\text{O}_4$  + TAT with and without 5 Gy radiation treatment are shown in Figure 7.3. Uncoated  $\text{Fe}_3\text{O}_4$  nanoparticles with and without radiation are localized within lysosomes. No uncoated  $\text{Fe}_3\text{O}_4$  nanoparticles were found to be interacting with the mitochondria or to have

penetrated the nuclear membrane. Uncoated  $\text{Fe}_3\text{O}_4$  nanoparticles are taken up via non-specific endocytosis and do not have the ability to sufficiently destabilize lysosome membranes and escape into the cytosol (Terman, Kurz et al. 2006). Similarly, Könczöl et al. found that uncoated iron oxide nanoparticles were encapsulated in vesicles of A549 lung carcinoma after 24 hours of incubation (Koenczoel, Weiss et al. 2013). There was significantly greater uptake of the  $\text{Fe}_3\text{O}_4$  + TAT nanoparticles into A549 cells as the TAT peptide facilitates cell penetration and escapes receptor mediated endocytosis.  $\text{Fe}_3\text{O}_4$  + TAT nanoparticles could be found both in lysosomes as well as in the cytosol. The nanoparticles appeared to surround the nuclear membrane, but they did not penetrate it due to size restraints of the nuclear pore complex (Pan, He et al. 2012). When combined with radiation, the  $\text{Fe}_3\text{O}_4$  + TAT nanoparticles appeared to destabilize the lysosomal membranes even more and greater interaction with surrounding mitochondria was observed. Similar lysosomal escape into the cytosol by nanoparticles conjugated with a cell penetrating peptide or nuclear localizing signal, such as TAT, has been previously observed (Xu, Xie et al. 2008, Austin, Kang et al. 2011).

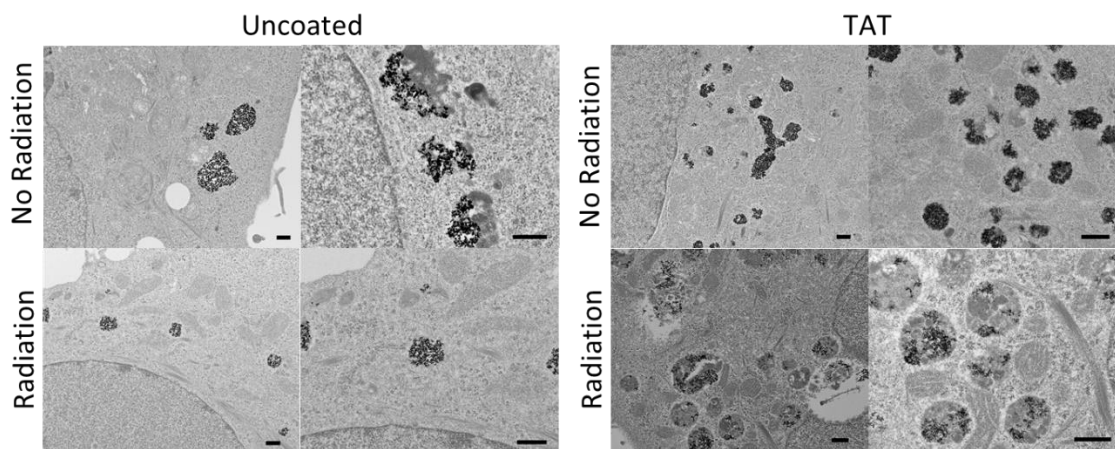


Figure 7.3 Internalization of Uncoated or TAT-conjugated iron oxide nanoparticles by A549 lung carcinoma, with and without radiation treatment. Scale bars represent 200 nm.

Lysosomal membrane permeabilization is an upstream event in many apoptosis pathways as destabilization of the lysosomal membranes releases lysosomal contents such as proteolytic

enzymes (cathepsins, etc.) into the cytosol, which then induce mitochondrial damage by enhancing the production of superoxide radicals and hydrogen peroxide, further increasing lysosome permeability, resulting in an amplifying feedback loop (Zhao, Antunes et al. 2003). Acridine Orange (AO) is a metachromatic fluorophore which gives a distinct red fluorescence at high lysosomal concentrations and a weakly green fluorescence at low cytosolic concentrations and can therefore be used to measure lysosomal membrane permeability, with a decrease in the red fluorescence channel corresponding to an increase in lysosome permeability (Terman, Kurz et al. 2006). This method was used by Domenech et al. to prove that targeted iron oxide nanoparticles have the ability to disrupt lysosomal membranes via mechanical forces actuated by an alternating magnetic field (Domenech, Marrero-Berrios et al. 2013). Therefore, AO was used to quantify lysosomal permeabilization by the  $\text{Fe}_3\text{O}_4$  nanoparticle systems with and without radiation. As shown in Figure 7.4, uncoated  $\text{Fe}_3\text{O}_4$  and  $\text{Fe}_3\text{O}_4 + \text{TAT}$  nanoparticles significantly decreased AO fluorescence compared to the control, but no further decrease was observed with the addition of radiation. Hydrogen peroxide was used as a positive control and there was no difference between hydrogen peroxide treatment and  $\text{Fe}_3\text{O}_4 + \text{TAT}$  nanoparticles indicating lysosomal membrane permeabilization. As previously shown, the TAT peptide on the nanoparticle surface destabilizes lysosomal membranes due to its highly positive charge (Kornhuber, Henkel et al. 2010). Uncoated  $\text{Fe}_3\text{O}_4$  nanoparticles can catalyze the formation of the hydroxyl radical inside the lysosomes leading to lysosome membrane destabilization (Guicciardi, Leist et al. 2004, Kirkegaard and Jaattela 2009, Koenczoel, Weiss et al. 2013). Both  $\text{Fe}_3\text{O}_4 + \text{Dx-ECH}$  and  $\text{Fe}_3\text{O}_4 + \text{Dx-ECH-Amine}$  nanoparticles have protective coatings on their surfaces preventing the formation of ROS by surface reaction, which explains why these systems do not result in lysosomal membrane permeabilization.

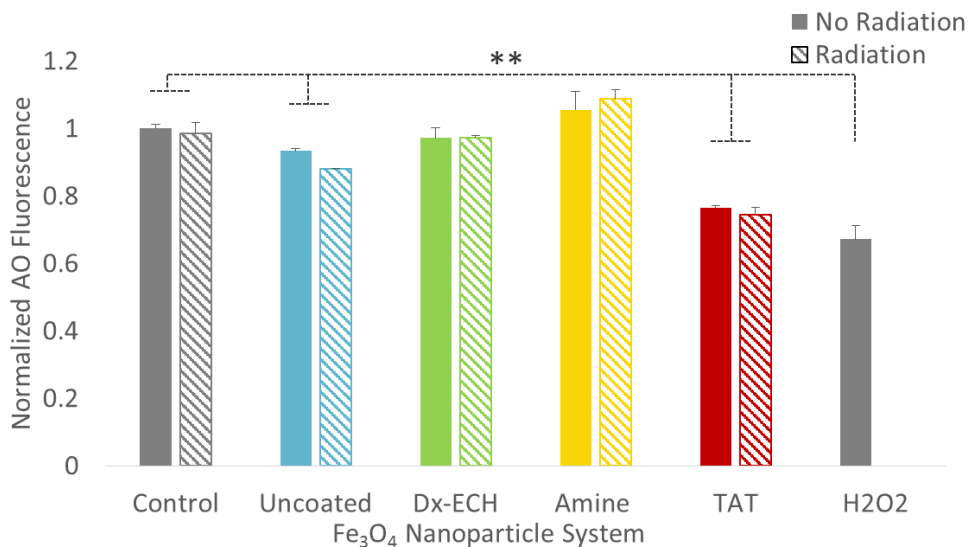


Figure 7.4 Normalized acridine orange (AO) fluorescence of A549 lung carcinoma after 2 hour treatment with Fe<sub>3</sub>O<sub>4</sub> nanoparticle systems with and without radiation. Error bars represent standard error (n=3) and \*\* indicates a significant difference from the control (p<0.01) via a two-way ANOVA.

As previously mentioned, lysosomal permeability and toxicity of iron oxide nanoparticles can lead to toxic mitochondrial effects. The effects of the combined Fe<sub>3</sub>O<sub>4</sub> nanoparticle treatments with radiation on mitochondrial function were analyzed using a XF96 Seahorse instrument, which measures oxygen consumption rate (OCR) and extracellular acidification rate (ECAR) over time. Figure 7.5 represents the basal respiration associated with A549 lung carcinoma cells following Fe<sub>3</sub>O<sub>4</sub> nanoparticle treatment with and without 5 Gy radiation treatment. Control A549 cells, which had not been exposed to Fe<sub>3</sub>O<sub>4</sub> nanoparticles, had significantly increased basal respiration rates after radiation treatment, which is consistent with previous studies (Yamamori, Yasui et al. 2012). Uncoated Fe<sub>3</sub>O<sub>4</sub> and Fe<sub>3</sub>O<sub>4</sub> + TAT nanoparticles significantly decreased basal respiration rates when combined with radiation compared to radiation alone and no increase in respiration was observed following radiation treatment, indicating that mitochondrial integrity was compromised by the presence of the nanoparticles. Figure 7.6 represents the maximal respiration levels associated

with A549 lung carcinoma cells following Fe<sub>3</sub>O<sub>4</sub> nanoparticle treatment with and without radiation. At the maximal respiration levels, there was a significant interaction between the nanoparticle system and radiation, indicating that the effects of the nanoparticle system were dependent on radiation exposure. An increase in respiration rate after radiation treatment was observed in both the control and Fe<sub>3</sub>O<sub>4</sub>+Dx-ECH-Amine nanoparticles. Additionally, the nanoparticle systems decreased the maximal respiration of the cells compared to the control, both with and without radiation treatment, indicating that the nanoparticles compromised the integrity of the mitochondria. Mitochondrial DNA is highly susceptible to damage by ROS and other agents because it is not as well protected by histones as is nuclear DNA (Hervouet, Simonnet et al. 2007). Therefore, additional ROS stress by the uncoated Fe<sub>3</sub>O<sub>4</sub> nanoparticles, or ROS stress induced by release of lysosomal contents, can lead to significant toxicities to the mitochondria.

The overall metabolism of the cells can be depicted by plotting OCR versus ECAR. Figure 7.7 represents the metabolic energy associated with A549 lung carcinoma cells after treatment with Fe<sub>3</sub>O<sub>4</sub> nanoparticle systems with and without radiation and after FCCP stimulation so the cells were operating at their total maximal respiration levels. All cells treated with the Fe<sub>3</sub>O<sub>4</sub> nanoparticle systems only were operating at approximately the same ECAR levels but decreased OCR compared to the control. The initial decrease in OCR associated with Fe<sub>3</sub>O<sub>4</sub> + TAT nanoparticle treatment suggests that these nanoparticles can sensitize the cells to subsequent radiation therapy. The cells treated with both the Fe<sub>3</sub>O<sub>4</sub> + TAT nanoparticles and radiation operated at a significantly lower energy level than cells treated with nanoparticles alone. This is an indication that cells treated with Fe<sub>3</sub>O<sub>4</sub> + TAT nanoparticles and radiation do not have the ability to respond to external stimuli, such as FCCP, indicating a decrease in substrate availability or that mitochondrial mass or integrity has been compromised (Hill, Benavides et al. 2012, Chacko, Kramer et al. 2014). Previous studies have shown that various iron oxide nanoparticle systems can adversely affect mitochondrial integrity. Khan et al. evaluated the effects of iron oxide nanoparticle concentration on the mitochondrial

membrane potential (MMP) of HeLa cells and found that, with increasing nanoparticle concentration, the percentage of cells with loss of MMP increased as well (Khan, Mohammad et al. 2012).

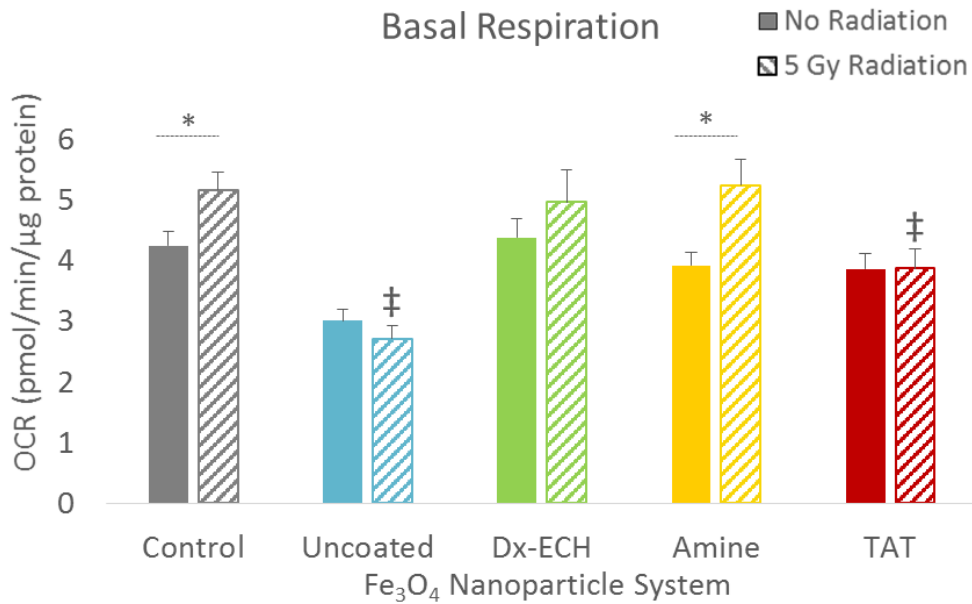


Figure 7.5 Basal oxygen consumption rates of A549 lung carcinoma cells after Fe<sub>3</sub>O<sub>4</sub> nanoparticle treatment with and without radiation. Error bars represent standard error (n=12). \* indicates a significant difference between the no radiation and radiation treatments within a nanoparticle system (p<0.05), † indicates a significant difference compared to the control without radiation (p<0.05) and ‡ indicates a significant difference from the control with radiation (p<0.05), via a two-way ANOVA with an interaction term.

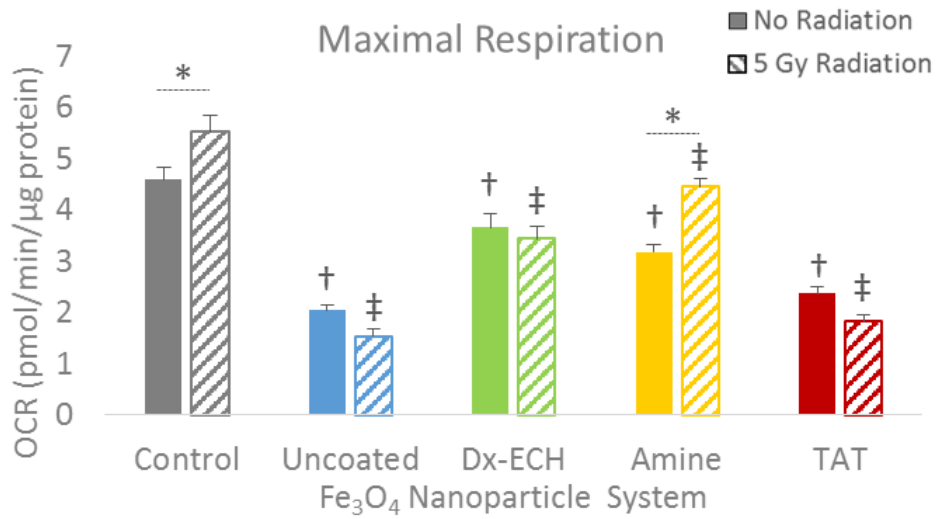


Figure 7.6 Maximal oxygen consumption rates of A549 lung carcinoma cells after Fe<sub>3</sub>O<sub>4</sub> nanoparticle treatment with and without radiation. Error bars represent standard error (n=12). \* indicates a significant difference between the no radiation and radiation treatments within a nanoparticle system (p<0.05), † indicates a significant difference compared to the control without radiation (p<0.05) and ‡ indicates a significant difference from the control with radiation (p<0.05), via a two-way ANOVA with an interaction term.



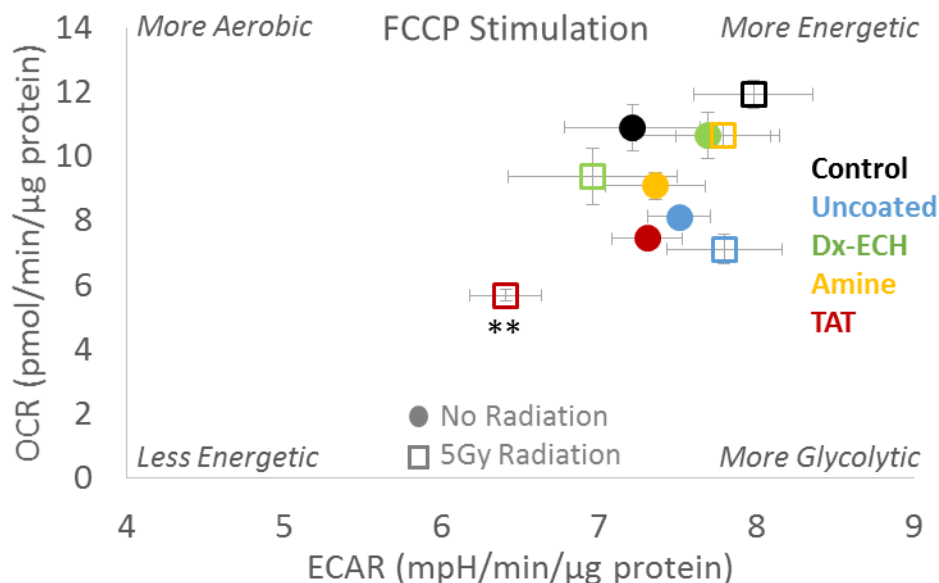


Figure 7.7 Oxygen consumption rate vs. extracellular acidification rate of A549 lung carcinoma after exposure to  $\text{Fe}_3\text{O}_4$  nanoparticle systems with and without radiation and FCCP stimulation. Error bars represent standard error (n=12) and \*\* indicates a significant difference in both OCR and ECAR from no-radiation  $\text{Fe}_3\text{O}_4$  nanoparticle.

Cancer cells are highly sensitive to exogenous ROS inducing agents due to increased inherent ROS production being associated with oncogenic transformation making the cells highly dependent upon their antioxidant systems (Huang, Chen et al. 2013, Luo, Li et al. 2015). Therefore, the ROS production associated with the nanoparticle systems with and without radiation was analyzed. As shown in Figure 7.8, ionizing radiation treatment alone significantly increased ROS production in A549 lung carcinoma, and this was further increased by pre-treatment with uncoated  $\text{Fe}_3\text{O}_4$ ,  $\text{Fe}_3\text{O}_4$  + Dx-ECH-Amine and  $\text{Fe}_3\text{O}_4$  + TAT at a concentration of 500  $\mu\text{g}/\text{mL}$ . Additionally, the  $\text{Fe}_3\text{O}_4$  + TAT increased ROS generation to a significantly greater extent than the other systems. It is hypothesized that uncoated  $\text{Fe}_3\text{O}_4$  nanoparticles increase ROS by surface catalysis of the hydroxyl radical which is the main form of ROS measured by carboxy-DCF (Cohn, Simon et al. 2008, Koenczoel, Weiss et al. 2013). Significant work has been completed to link oxidative stress induced by uncoated iron oxide nanoparticles to nanoparticle toxicity (Ahamed, Alhadlaq et al. 2013,

Cochran, Wattamwar et al. 2013, Alarifi, Ali et al. 2014, Park, Umh et al. 2014, Luo, Li et al. 2015). Ahamed et al. and Khan et al. both showed that uncoated iron oxide nanoparticles induced oxidative stress in A549 lung carcinoma, which increased with increasing concentration and increasing exposure time (Khan, Mohammad et al. 2012, Ahamed, Alhadlaq et al. 2013). The positive charge associated with primary amines functionalized to the nanoparticle surface could slightly increase lysosomal permeability, although this was not observed in the AO studies, resulting in the release of some lysosomal contents and inducing ROS associated toxicities. Fe<sub>3</sub>O<sub>4</sub> + TAT nanoparticles destabilized lysosomal membranes and facilitated release of toxic components, as well as the nanoparticles, which compromised mitochondrial integrity and increased ROS production. Therefore, ROS generation was significantly increased when radiation was combined with the Fe<sub>3</sub>O<sub>4</sub> + TAT nanoparticles.

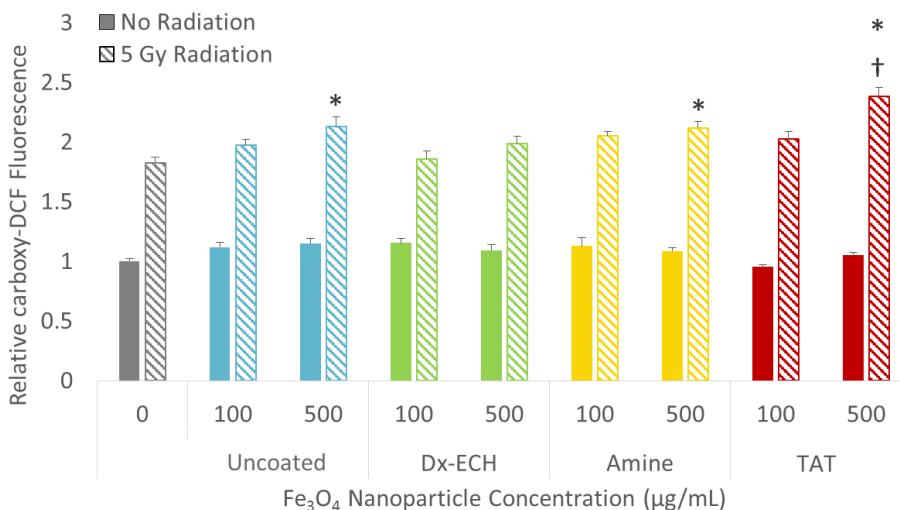


Figure 7.8 Relative carboxy-DCF fluorescence in A549 lung carcinoma following 24 hour treatment with Fe<sub>3</sub>O<sub>4</sub> nanoparticle systems with and without 5 Gy radiation treatment. Error bars represent standard error (n=12) and \* indicates a significant difference compared to radiation alone and † indicates a significant difference compared to 500 µg/mL uncoated and 500 µg/mL amine functionalized Fe<sub>3</sub>O<sub>4</sub> nanoparticles.

To determine whether the nanoparticle systems combined with radiation treatment had an effect on cell viability, a long term viability study was completed. A549 cells were treated for 24 hours with the nanoparticle systems to facilitate uptake, followed by treatment with 5 Gy radiation. Cells were then re-seeded and allowed to grow for 3, 5 or 7 days post treatment. Figure 7.9 displays the relative viability of A549 lung carcinoma 3, 5 and 7 days post treatment with Fe<sub>3</sub>O<sub>4</sub> nanoparticles alone, radiation alone, and the combined treatment. When combined with radiation, uncoated Fe<sub>3</sub>O<sub>4</sub> nanoparticles resulted in a delayed effect, as only at day 7 was the combined treatment significantly different from radiation alone. The uncoated Fe<sub>3</sub>O<sub>4</sub> nanoparticles increased lysosomal permeability and increased intracellular ROS production, but the toxic effects were delayed. The Fe<sub>3</sub>O<sub>4</sub> + Dx-ECH nanoparticles did not significantly enhance the efficacy of radiation treatment. This was expected as this nanoparticle system did not induce lysosomal permeabilization, decrease mitochondrial integrity, nor increase ROS generation. The Fe<sub>3</sub>O<sub>4</sub> + Dx-ECH-Amine nanoparticles did increase the efficacy of radiation treatment in the short term, but the effects did not continue through the analysis times. This could be due to the Fe<sub>3</sub>O<sub>4</sub> + Dx-ECH-Amine nanoparticles having the ability to increase ROS generation upon exposure to radiation, but the nanoparticles did not cause other cellular effects. Therefore, the slight increase in ROS when combined with radiation by the Fe<sub>3</sub>O<sub>4</sub> + Dx-ECH-Amine nanoparticles was enough to induce increased toxicities in short time frames, but as the cells continued to grow for the longer time points, they were able to overcome the toxicities induced by the slight increases in exogenous ROS. Fe<sub>3</sub>O<sub>4</sub> + TAT nanoparticles significantly enhanced the effect of radiation when cell viability was analyzed 3, 5 and 7 days post treatment, indicating that the Fe<sub>3</sub>O<sub>4</sub> + TAT nanoparticles successfully sensitized A549 lung carcinoma cells to radiation therapy. Fe<sub>3</sub>O<sub>4</sub> + TAT nanoparticles increased lysosomal membrane permeabilization, releasing toxic contents into the cytosol, which then compromised mitochondrial integrity and sensitized the cells to radiation treatment. The efficacy of the combined treatment was analyzed using a set of equations established by Babincova et al. (Babincova,

Altanerova et al. 2008). These equations are displayed in Table 7.1, and the calculations for the  $\text{Fe}_3\text{O}_4$  + TAT nanoparticles are shown in Table 7.2. On each day of analysis following treatment, the combined treatment of  $\text{Fe}_3\text{O}_4$  + TAT nanoparticles and radiation therapy on A549 lung carcinoma was significantly greater than the expected outcome of combining the two treatments, indicating that it was a synergistic treatment.

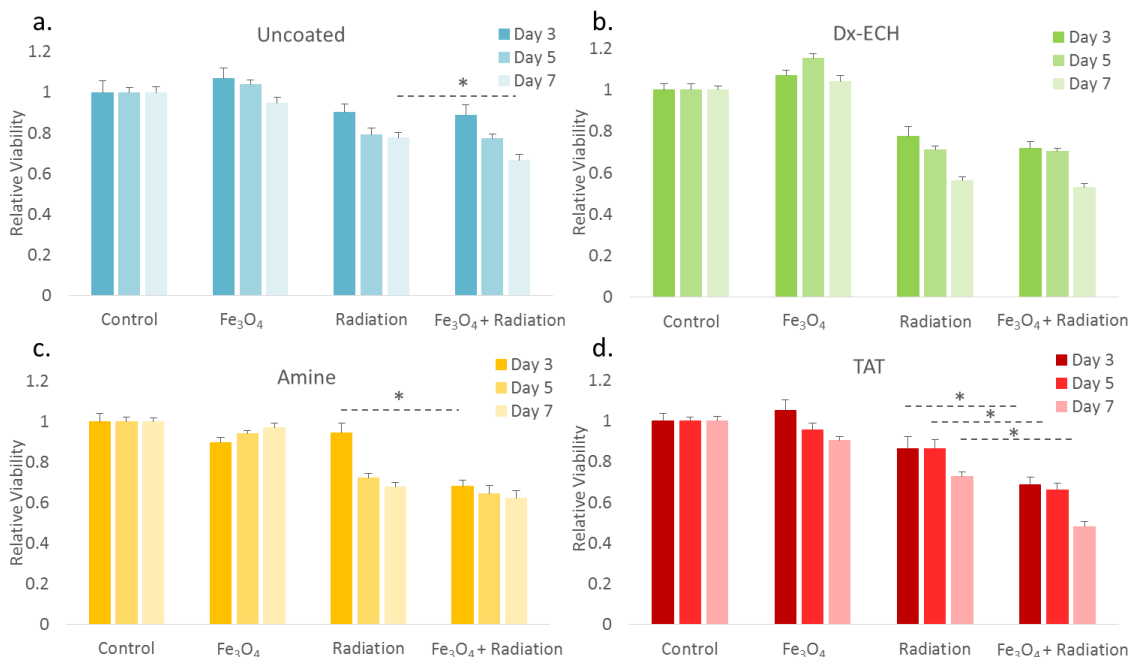


Figure 7.9 Relative viability of A549 lung carcinoma 3, 5 or 7 days following a) uncoated b) Dx-ECH c) amine functionalized or d) TAT-conjugated  $\text{Fe}_3\text{O}_4$  nanoparticle treatment with and without 5 Gy radiation. Error bars represent standard error (n=12) and \* indicates a significant difference ( $p < 0.05$ ) via a one-way ANOVA.

Table 7.1 Equations developed by Babincova et al. for analysis of combinational treatments.

Synergistic:	$[\text{Fe}_3\text{O}_4 + \text{Radiation}] < [\text{Fe}_3\text{O}_4] \times [\text{Radiation}]/100$
Additive:	$[\text{Fe}_3\text{O}_4 + \text{Radiation}] = [\text{Fe}_3\text{O}_4] \times [\text{Radiation}]/100$
Sub-additive:	$[\text{Fe}_3\text{O}_4] \times [\text{Radiation}]/100 < [\text{Fe}_3\text{O}_4 + \text{Radiation}] < [\text{Fe}_3\text{O}_4]$ ; if $[\text{Fe}_3\text{O}_4] < [\text{Radiation}]$
Interference:	$[\text{Fe}_3\text{O}_4] < [\text{Fe}_3\text{O}_4 + \text{Radiation}] < [\text{Radiation}]$ , if $[\text{Fe}_3\text{O}_4] < [\text{Radiation}]$
Antagonistic:	$[\text{Radiation}] < [\text{Fe}_3\text{O}_4 + \text{Radiation}]$ , if $[\text{Fe}_3\text{O}_4] < [\text{Radiation}]$

Table 7.2 Calculations to analyze the effects of combined Fe<sub>3</sub>O<sub>4</sub> + TAT nanoparticles and radiation treatments. Values represent viability average ± standard error (n=12) on days 3, 5 and 7 post treatment. \* (p<0.05) and \*\* (p<0.01) indicate a significant difference from the [Fe<sub>3</sub>O<sub>4</sub> + TAT]x[Radiation]/100 group on the same day.

	<b>Fe<sub>3</sub>O<sub>4</sub> + TAT</b>	<b>Radiation</b>	<b>[Fe<sub>3</sub>O<sub>4</sub> + TAT]x[Radiation]/100</b>	<b>[Radiation + Fe<sub>3</sub>O<sub>4</sub> + TAT]</b>
<b>Day 3</b>	105.4 ± 4.5	86.4 ± 6.1	92.5 ± 9.2	68.7 ± 3.6 *
<b>Day 5</b>	95.6 ± 3.2	86.4 ± 4.6	81.8 ± 3.8	66.2 ± 3.4 **
<b>Day 7</b>	90.4 ± 2.0	72.6 ± 2.6	65.5 ± 2.4	48.0 ± 2.6 **

#### 7.4 Conclusions

The cell penetrating peptide, TAT, was successfully conjugated to dextran-coated iron oxide nanoparticles. Electron microscopy of A549 lung carcinoma after uptake of Fe<sub>3</sub>O<sub>4</sub> + TAT nanoparticles showed the nanoparticles interacting with mitochondria and membrane destabilization of lysosomes containing Fe<sub>3</sub>O<sub>4</sub> + TAT nanoparticles. Lysosomal permeability was confirmed and quantified using the AO assay. Both the uncoated Fe<sub>3</sub>O<sub>4</sub> and Fe<sub>3</sub>O<sub>4</sub> + TAT nanoparticles had the ability to permeabilize lysosomal membranes after cellular uptake due to ROS generation and the positive charge of the TAT peptide, respectively. Fe<sub>3</sub>O<sub>4</sub> + TAT nanoparticles combined with radiation also affected mitochondrial integrity of the cells. When mitochondria were uncoupled with FCCP, cells that had been previously treated with Fe<sub>3</sub>O<sub>4</sub> + TAT nanoparticles combined with radiation showed significantly lower capability to meet ATP demands than the nanoparticle only treatment, indicating a loss of metabolic potential. ROS generation was also predicted to play a role in the additional toxicities associated with radiation when the cells were pre-treated with the nanoparticle systems. When combined with radiation, uncoated Fe<sub>3</sub>O<sub>4</sub>, Fe<sub>3</sub>O<sub>4</sub> + Dx-ECH-Amine, and Fe<sub>3</sub>O<sub>4</sub> + TAT nanoparticles significantly increased ROS production compared to radiation alone in A549 lung carcinoma. Due to this increase in ROS generation, in lysosomal permeability, and the loss of mitochondrial integrity and function, the combined

treatment of  $\text{Fe}_3\text{O}_4$  + TAT nanoparticles and radiation resulted in a synergistic decrease in cell viability.

## Chapter 8 Conclusions

In this dissertation, peptide-conjugated iron oxide magnetic nanoparticles were synthesized, characterized, and evaluated for their cancer therapy applications via magnetically mediated hyperthermia, intra-cellular localized energy delivery, and catalysis of reactive oxygen species. Both magnetically mediated hyperthermia and intra-cellular localized energy delivery rely upon the ability of the magnetic nanoparticles to respond to an alternating magnetic field, while catalysis of reactive oxygen species generation utilizes the capability of the nanoparticles to catalyze the Haber-Weiss reaction via Fenton chemistry. First, an iron oxide nanoparticle system conjugated with a tumor-homing peptide, CREKA, was developed for magnetically mediated hyperthermia treatment of A549 lung carcinoma. The physicochemical properties of the nanoparticle system were fully characterized and revealed their ability to target tumor extracellular matrix components and generate sufficient heat to induce hyperthermia conditions. Additionally, in a proof-of-concept study, magnetically mediated hyperthermia was combined with a chemotherapeutic, cisplatin, and the combined treatment resulted in an additive toxic effect.

Although the heating properties of the previously developed magnetic nanoparticles were sufficient to induce hyperthermia conditions, their specific absorption rate was significantly lower than other magnetic nanoparticle systems reported in literature. Therefore, the method of synthesizing dextran-coated iron oxide magnetic nanoparticles was altered, as it was determined that the time of dextran addition into the synthesis reaction dramatically changed the physicochemical properties of the magnetic nanoparticles. By manipulating the synthesis conditions, it was demonstrated that nanoparticles could be formed with various size, stability, and crystallinity properties for biological applications.

After improving the synthesis method of dextran-coated iron oxide nanoparticles, the magnetic nanoparticles were functionalized with a cell penetrating peptide, TAT, to increase the intracellular concentration of the magnetic nanoparticles. This magnetic nanoparticle system was used to locally

deliver energy upon activation by a magnetic field. It was demonstrated that TAT-functionalization to the magnetic nanoparticles increased cell uptake by A549 and H358 lung cancer cell lines and permeabilized lysosomal membranes, sensitizing the cells to the damaging effects of localized energy delivery upon exposure to an alternating magnetic field. Although not statistically significant, there was an observable trend illustrating increasing apoptosis when lung cancer cells were treated with the TAT-functionalized magnetic nanoparticles and an alternating magnetic field compared to the nanoparticles alone.

The last portion of this dissertation evaluated the intracellular effects of TAT-functionalized iron oxide nanoparticles combined with radiation on lung cancer cells. Studies indicated that the TAT-functionalized nanoparticles sensitized the cells to further treatment with radiation by permeabilizing lysosomal membranes, damaging mitochondrial integrity, and catalyzing production of the highly reactive hydroxyl radical. While the TAT peptide can also serve as a nuclear localizing signal, electron microscopy images indicated that the targeted magnetic nanoparticles were located within destabilized lysosomes or in the cytoplasm, but at significantly greater concentrations than uncoated nanoparticles. Future work in this area should focus on targeting the magnetic nanoparticles to specific organelles such as the mitochondria or the nucleus in an effort to enhance nanoparticle effects and associated therapy.

### **8.1 Significant Findings**

There are several findings in this work that contribute to the scientific community's understanding of peptide-functionalized iron oxide nanoparticles for cancer therapy applications. Research in magnetically mediated hyperthermia for cancer therapy has grown significantly over the past decade with minimal clinical translation. Magnetically mediated energy delivery is a growing alternative to magnetically mediated hyperthermia, so this research directly impacts an important aspect of magnetic nanoparticle research. Although this work was specific to cancer therapy, there are a wide variety of other biological and environmental remediation applications.



- Dextran-coated iron oxide magnetic nanoparticles can be synthesized by a one-pot coprecipitation method and have properties consistent with those required for tumor targeting *in vivo*.
- CREKA-conjugated magnetic nanoparticles can be used for magnetically mediated hyperthermia treatment of lung cancer and combination with cisplatin results in an additive effect.
- Timing of dextran addition to the synthesis reaction of dextran-coated iron oxide nanoparticles significantly affects the physical and chemical properties of the material likely due to the viscosity of the dextran solution retarding crystal growth.
- Functionalization of the cell penetrating TAT peptide to iron oxide nanoparticles increases the intracellular iron concentration within lung cancer cells.
- Internalized, TAT-functionalized iron oxide nanoparticles increase reactive oxygen species production within lung cancer cells upon exposure to an alternating magnetic field and increase lysosomal permeability.
- Although not statistically significant, trends were observed that suggest an increase in cell apoptosis when the TAT-functionalized iron oxide nanoparticle system is combined with alternating magnetic field treatment.
- When combined with radiation, TAT-functionalized iron oxide nanoparticles significantly increase reactive oxygen species production compared to radiation alone in A549 lung carcinoma.
- Treatment with TAT-functionalized iron oxide nanoparticles and radiation significantly reduces the metabolic energy of lung cancer cells indicating compromise of mitochondrial integrity or a decrease in substrate availability.
- Dual treatment with TAT-functionalized iron oxide nanoparticles and radiation results in a synergistic therapy for A549 lung carcinoma.

## **Appendix A Combination treatment of multi-cellular tumor spheroids**

In this study, multicellular tumor spheroids were fabricated and used to analyze the effects of anti-cancer treatments as three-dimensional models more accurately represent avascular tumors *in vivo* compared to traditional monolayer cell cultures. The main limitation of using multicellular tumor spheroids as a screen for treatment efficacy is the difficulty in analyzing spheroid viability via a high throughput assay. Therefore, in this study, three viability assays were screened for accuracy in determining spheroid viability. A single assay was then selected to evaluate the efficacy of radiation and chemotherapy combined with hyperthermia treatment. This work was completed in conjunction with Kendall Huddleston Murphy, Jonathan Colburn, and Sarah Patterson as a part of the NSF Research Experience for Undergraduates at the University of Kentucky.

### **A.1 Introduction**

Monolayer cell cultures have been the traditional form of *in vitro* screening for drugs and novel therapies. However, 2-dimensional (2D) cultures lack many of the physiological properties of cells *in vivo*. *In vivo*, cells reside in a 3-dimensional (3D) matrix complete with an extracellular matrix (ECM) made up of various macromolecules (collagens, proteoglycans, and laminin). 2D cell cultures grown on slides coated with substrata do not form an extra-cellular matrix, leading to several drawbacks of monolayer cultures: 1. lack of molecular gradients which play a vital role in cell differentiation, determination of cell fate, and signal transduction, 2. alterations in gene expression patterns and metabolism, and 3. morphological and phenotypic changes due to altering production of their own ECM proteins (Hutmacher, Horch et al. 2009). 3D cell cultures can be used to better mimic tumor cell growth and responses to drugs and therapies to *in vivo* tumors. Multicellular tumor spheroids (MCTS) 200-500  $\mu\text{m}$  in diameter mimic avascular tumors in that they have diffusion limitations of oxygen and other nutrients resulting in a proliferation gradient: a necrotic core surrounded by a layer of quiescent cells, followed by a viable outer rim (Mueller-

Klieser, Vaupel et al. 1987). Diffusion limitations out of the spheroid result in waste accumulation within the core of the spheroid and contribute to the necrotic core.

Physical properties of MCTS also hinder drug penetration. Nirmalanandhan et al. reported cell-line dependent differences in response to multiple drugs between spheroid and monolayer cell cultures (Nirmalanandhan, Duren et al. 2010). The proximity of cells as well as the presence of an extracellular matrix in MCTS is thought to effect MCTS response to various treatments as well (Minchinton and Tannock 2006). Due to these characteristics and suitability for high throughput studies, MCTS have been applied in various cancer therapy studies. Khoei et al. reported superior hyperthermic resistance of spheroids compared to cell monolayers in DU 145 human prostate carcinoma cells (Khoei, Goliaei et al. 2004) and interestingly enough, Yamauchi et al. demonstrated the opposite result in HT29 colon adenocarcinoma cells with different experimental methods (Yamauchi, Asao et al. 2011). Senavirathna et al. successfully applied a MCTS model to study the effects of proton beam radiotherapy and doxorubicin-loaded temperature-sensitive liposomes (Senavirathna, Fernando et al. 2013).

Coinciding with the increased complexity of MCTS culture, is increased difficulty of analysis. For example, many traditional analysis techniques used in monolayer cell culture studies cannot be applied for MCTS analysis due to assay penetration limitations. Variability in spheroid compactness and shape can also affect results. A popular method of analyzing MCTS is to measure volume over time (Friedrich, Ebner et al. 2007). Other studies dissociate the spheroids and either analyze the dissociated cells directly (Ivascu and Kubbies 2006, Mattix, Olsen et al. 2014), or apply a colony formation assay to analyze the ability of the cells to replicate (Khoei, Goliaei et al. 2004, Yamauchi, Asao et al. 2011). However, the dissociation process is labor-intensive and can cause damage or a decrease in the cell population (Friedrich, Ebner et al. 2007). Neither of these methods provides a basis for determining the viability of intact MCTS. Thus, viability assays appropriate to

MCTS culture must be further developed and validated to increase MCTS use as a translational research method.

Hyperthermia, the heating of tissue to 41 - 45 °C, induces cell apoptosis, or controlled cell death, primarily by denaturing nucleolic, cytoplasmatic, or membrane proteins. *In vitro* tumor cells do not exhibit hyperthermia sensitivity compared to healthy cells however, *in vivo*, tumor tissue is particularly sensitive to hyperthermia treatment due to properties such as hypoxia and low pH levels (Issels 2008). At temperatures above the hyperthermia range, cell death occurs through necrosis with lower selectivity between healthy and tumor tissues (Hildebrandt, Wust et al. 2002). However, high temperatures are difficult to achieve *in vivo* and are generally avoided in clinical application due to the negative effects of necrosis.

Hyperthermia has been previously demonstrated to interact synergistically with radiation and chemotherapy but hyperthermia treatment alone has proved insufficient to result in major effects (Wust, Hildebrandt et al. 2002, Issels 2008). In combination with chemotherapy, hyperthermia is generally most effective when administered simultaneously with drug administration. Mechanisms involved in the interaction between hyperthermia and drugs include increase of blood flow, vascular permeability, and cellular membrane fluidity, all of which enable increased tumor and cellular uptake of drug (Issels 2008). Hyperthermia can also increase the reaction rate of the drug with the cellular target (Halamikova, Vrana et al. 2007) and has been used to overcome drug resistance in some cell lines (Hildebrandt, Wust et al. 2002).

When combined with radiation therapy, hyperthermia has been shown to decrease the repair rate of sub-lethal DNA strand break, and therefore increase the efficacy of radiation. *In vivo*, mild hyperthermia treatment increases tumor oxygenation by increasing blood perfusion to the tumor and therefore increasing reactive oxygen species production upon radiation treatment. On the contrary, studies have indicated that physical clamping or the use of physiological modifiers to reduce blood flow to the tumor can enhance the efficacy of hyperthermia by reducing the

convective cooling effects (Overgaard and Nielsen 1980). The results of radiation combined with hyperthermia studies vary greatly and are also highly dependent on cell line, order of treatment, and tumor size. A study completed by Sapareto et al. showed that timing of irradiation and thermal therapy has dramatic effects on the efficacy of the combined treatment and is also cell line dependent. Irradiating HA-1 cells immediately prior to thermal therapy had the greatest toxic effect, while the opposite was true for EMT6 cells. Therefore, the consensus is that thermal therapy during radiation treatment is most effective (Sapareto, Raaphorst et al. 1979). Larger tumors have been shown to be more sensitive to the combined therapy compared to smaller tumors due to having a higher cell population of radio resistant, yet heat sensitive cells (Vaupel, Kallinowski et al. 1989).

Despite some success in clinical application, hyperthermia therapy faces several key challenges. Due to lack of heat perfusion and the deep location of metastatic tumors, conventional hyperthermia methods such as water baths, microwaves, radiotherapy, and limb perfusion make it difficult to target to tumor tissue without harming healthy tissue. Additionally, hyperthermia temperatures may be difficult to reach and maintain for sufficient time periods (Wust, Hildebrandt et al. 2002). A relatively new hyperthermia treatment, magnetically-mediated hyperthermia (MMH), also known as magnetic fluid hyperthermia, utilizes magnetic nanoparticles in the presence of an alternating magnetic field (AMF) to locally generate heat. Upon activation by an AMF, magnetic nanoparticles convert the field energy into heat through Brownian rotation and Néel paramagnetic switching. Because an AMF can be applied with minimal effect on bodily tissue, MMH is a promising alternative to current hyperthermia treatments (Laurent, Dutz et al. 2011). A clinical trial by Maier-Hauff et al. demonstrated the feasibility of intracranial MMH using aminosilane coated iron oxide nanoparticles and a sophisticated dosing software (Maier-Hauff, Rothe et al. 2007).

There has been significant progress in MMH research (see Chapter 3), but with limited clinical translation due to the lack of consistency between *in vitro* studies, preliminary *in vivo* studies, and

clinical trials. By applying the MCTS model to MMH studies at the *in vitro* screening stage, it should enable a more thorough screening of MMH techniques compared to cell monolayers. First, however, a standard protocol for analysis must be developed in order to use MCTS to try to bridge the gap between *in vitro* and *in vivo* studies. Specifically, an assay is needed that will accurately report spheroid viability in a high throughput manner.

The first objective of this study was to evaluate the efficacy and consistency of selected viability assays on A549 lung carcinoma MCTS. Three viability assays were selected: resazurin, acid phosphatase (APH), and calcein AM/ethidium homodimer-1. Based on experiments by Friedrich et al., it was expected that the APH assay would provide an accurate and consistent method for assaying the A549 lung carcinoma MCTS (Friedrich, Eder et al. 2007). Assays were investigated for accuracy and consistency by varying the number of MCTS analyzed as well as the seeding density of spheroids assayed. The effect of spheroid dissociation was also analyzed for each assay. Secondly, a feasible assay was chosen for a proof of concept study to demonstrate the interaction between cisplatin (CDDP), a common chemotherapeutic, and hyperthermia in the MCTS model. The third objective combined radiation therapy with hyperthermia treatment on MCTS in a proof of concept study.

## **A.2 Materials and Methods**

### *A.2.1 Materials*

Fetal bovine serum (FBS) and Type 1 rat tail collagen were obtained from Fisher Scientific (Florence, KY), and Dulbecco's Modified Eagle Medium (DMEM), pen-strep, L-glutamine, Fungizone<sup>®</sup>, sodium pyruvate, calcein AM, and ethidium homodimer-1 were obtained from Invitrogen (Grand Island, NY). Trypsin (0.25% trypsin/0.53 mM EDTA) and A549 lung cancer cells were purchased from American Type Culture Collection (Manassas, VA). Nunc Sphera 96-well plates and *p*-nitrophenyl phosphate (pNPP), disodium salt, were obtained from Thermo Scientific (Rochester, NY). Sodium acetate trihydrate, resazurin, and cisplatin were purchased

from Sigma Aldrich (St. Louis, MO). Phosphate buffered saline solution (PBS) was obtained from EMD Millipore (Billerica, MA).

### A.2.2 Cell culture

Cell culture media was prepared by adding 10% FBS, 1 mM sodium pyruvate, 4 mM L-glutamine, pen-strep (100 U/mL penicillin and 100 µg/mL streptomycin), and 10 µg/ml Fungizone® to 500 mL DMEM. The media mixture was sterile filtered. A549 lung carcinoma cells were cultured between passages 4 and 24.

### A.2.3 MCTS formation

A549 cells were seeded at 50,000 cells/mL (unless otherwise specified) at 100 µL/well into Nunc Sphera 96-well plates and collagen was added to the cell solution at a concentration of 20 µg/mL to aid spheroid formation. The round bottom 96-well plates were centrifuged at 1250 rpm for 15 min to aggregate the cells. Cells were incubated to allow spheroid compaction and growth at 37 °C and 5% CO<sub>2</sub> for 48 hours. Figure A.1 depicts the MCTS formation process over time.

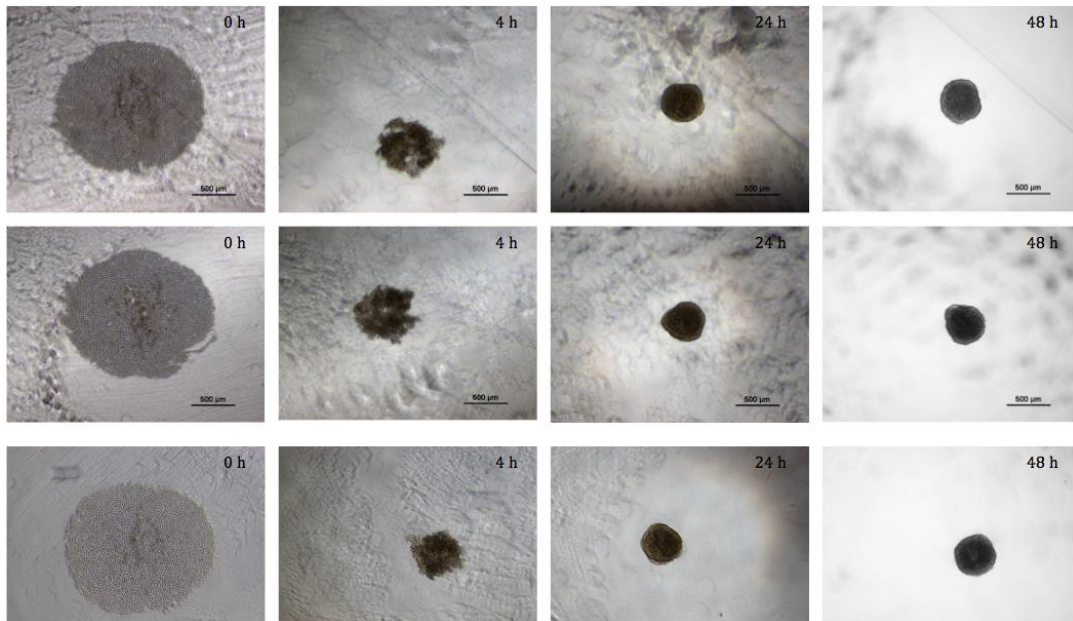


Figure A.1 Chronological images of three different A549 MCTS during formation.

#### *A.2.4 MCTS dissociation*

Plates were centrifuged for 5 min at 1250 rpm, and 140  $\mu$ L per well of supernatant was carefully removed. 0.25% trypsin-EDTA was diluted with PBS to obtain 0.1% trypsin and 160  $\mu$ L was added per well. Plates were again centrifuged and 160  $\mu$ L of supernatant was replaced with 0.1% trypsin. Spheroids were disassociated in wells by rapid pipetting and immediately returned to incubator. Disassociation via shear stress was repeated five times (every 20 min) and if spheroids were not yet dissociated, further shear stress was applied with a 20-gauge needle. Cell suspensions were transferred to a well plate coated for regular cell culture to avoid re-aggregation and the trypsin was neutralized with cell culture media.

#### *A.2.5 Acid phosphatase assay*

Plates were centrifuged and supernatant was replaced with PBS due to potential interference of cell culture media with APH signal (amount of supernatant replaced was adjusted based on corresponding volumes and wells). Plates were centrifuged again, and supernatant was removed to obtain half the desired volume. The desired volume was obtained by adding APH buffer (0.1 M sodium acetate, 0.1% (v/v) Triton X-100, and 8 mg/mL pNPP in deionized water before dilution; use 2 mg/mL pNPP for dissociated cells). Spheroids were incubated with APH buffer (final concentrations of 4 mg/mL and 1 mg/mL for MCTS and dissociated MCTS, respectively) for 6 h and dissociated cells for 90 min. Plates were placed on an incubator shaker for the initial and final 15 min of incubation. After the incubation period, the absorbance of the wells was read at 405 nm by a Biotek SynergyMx microplate reader.

#### *A.2.6 Resazurin assay*

Resazurin (10 mM) was added to each well for a 10% (v/v) solution. Plates were incubated for 6 h at 37 °C to allow resazurin to be metabolized. The plates were placed on an incubator shaker for the initial and final 15 min of this period. The fluorescence of each well was read by a Biotek SynergyMx microplate reader at an excitation of 530 nm and an emission of 590 nm.



### *A.2.7 Calcein AM/Ethidium homodimer-1 (live/dead) assay*

Two spheroids per treatment group were transferred with 200  $\mu\text{L}$  media per spheroid to a 12-well plate. One row was filled with 400  $\mu\text{L}$  of media to obtain background fluorescence. PBS was supplemented with 2  $\mu\text{M}$  calcein AM and 4  $\mu\text{g}/\text{mL}$  ethidium homodimer-1 before addition at 400  $\mu\text{L}/\text{well}$ . Plates were incubated for 1 h. Following incubation, one live and one dead image per spheroid were obtained and combined using a Nikon Eclipse LV 100 microscope. The first control spheroid was used to focus the microscope and to set auto-exposure times, which remained consistent throughout the imaging process. This first spheroid was not included in the data, and all other images were obtained within 5 s to prevent bleaching of fluorescence. Mean intensity values of images were exported for data analysis.

Dissociated spheroids were transferred to a 96-dark-well plate as described in the dissociation procedure; each dissociated spheroid was transferred to a different well. Cells were allowed to attach and to grow for 48 h, at which point media was removed from wells. PBS supplemented with 2  $\mu\text{M}$  calcein was added at 100  $\mu\text{L}$ . After 25 min incubation, mean relative fluorescence values were obtained by a Biotek SynergyMx microplate reader using an area scan (ex: 495/em: 515 nm). After reading fluorescence values, qualitative images were also obtained as described above.

### *A.2.8 Assay validation studies*

The APH and resazurin assays were tested for response to varying numbers of spheroids. Between one and five spheroids were transferred to each well of a 48-well plate and excess media was removed to a final volume of 200  $\mu\text{L}/\text{well}$ . The remainder of the APH assay was completed as described above, with the exception that the spheroids were only incubated for 90 min. For the resazurin assay, between one and five spheroids were transferred to a 48-well plate with 100  $\mu\text{L}$  media/spheroid; additional media was added as necessary to reach a final volume of 500  $\mu\text{L}$  in all wells. Then the resazurin assay was carried out as described above. For all viability assays, the

appropriate background samples were prepared to correct for background absorption and fluorescence.

The APH and resazurin assays were also tested for response to varying seeding density of spheroids. MCTS were seeded at concentrations between 2,500 and 15,000 cells per spheroid and were allowed to grow for 24 h before performing APH and resazurin assays.

All assays were applied to MCTS treated with 0, 20, and 2000  $\mu$ M CDDP dissolved in media for 72 h. These concentrations were chosen because they represent a concentration near and a concentration far greater than the  $IC_{50}$ . Following 72 h of incubation, some spheroids were dissociated, and APH, resazurin, and live/dead assays were performed on intact and dissociated spheroids. All values were normalized to the average value of the controls not treated with CDDP. And for ethidium staining, reported values are one less than the normalized values to give the controls a relative cell death of zero.

#### *A.2.9 Incubator-induced hyperthermia with CDDP*

After 48 h of growth, MCTS were treated with CDDP in media at concentrations between 0 and 2000  $\mu$ M. Immediately following the addition of CDDP, half of the spheroids in each treatment group were returned to an incubator at 37 °C while the remaining spheroids were placed in an incubator set to 43 °C. In order to efficiently raise well temperature, the well plate was placed on a hot pad resting on a hot plate set to 60 °C. When the well temperature reached 43 °C, the well plate was removed from the hot pad and maintained between 42.5 and 43 °C. The well plate remained in the incubator for 30 min after reaching 41.5 °C, which was deemed the effective starting point of hyperthermia treatment. The temperature was continuously monitored through the use of a fiber optic temperature sensor (Luxtron FOT Lab Kit from LumaSense) inserted into a central well through a small hole drilled through a well plate lid. After hyperthermia treatment, the well plate was returned to an incubator at 37 °C.  $IC_{50}$  values and regression curves were obtained using SigmaPlot to fit the data to a four parameter logistic curve.

#### *A.2.10 Incubator induced hyperthermia with radiation*

Following the 48-hour growth period, MCTS were subjected to gamma irradiation. A cesium-137 irradiator was used to administer doses of 0, 2, 4, and 6 Gy at room temperature. Immediately following radiation, a subset of the irradiated spheroids were exposed to hyperthermia. The time delay between treatments could not be reduced to less than 15 minutes due to differing treatment locations. In order to efficiently raise well temperature, the well plate was placed on a hot pad resting on a hot plate set to 60 °C. When the well temperature reached 43 °C, the well plate was removed from the hot pad and maintained between 42.5 and 43 °C. The well plate remained in the incubator for 60 min after reaching 41.5 °C, which was deemed the effective starting point of hyperthermia treatment. The temperature was continuously monitored through the use of a fiber optic temperature sensor (Luxtron FOT Lab Kit from LumaSense) which was inserted into a central well through a small hole drilled through a well plate lid. After hyperthermia treatment, the well plate was returned to an incubator at 37 °C. Viability was analyzed 5 and 7 days post-treatment using the APH assay and live/dead assay as previously described.

### **A.3 Results and discussion**

#### *A.3.1 MCTS assay validation*

Spheroids were analyzed by the APH and resazurin assays and the number of spheroids per well varied from one to five. The response of the assay to this setup can indicate the consistency in signal generation of the assay for a single spheroid as well as its ability to handle increasingly large quantities of cells. Results are portrayed in Figure A.2 and  $R^2$  values are given for each assay based on linear regression of the data. The live/dead assay was not applied in this study due to the difficulty of obtaining images that encompass all the spheroids in a given well. Although neither assay responded linearly, the APH assay displayed a clearer trend compared to the resazurin assay. It could be suggested that the APH assay responded in an exponential manner to increasing number

of spheroids however, this was deemed unlikely as the signal is expected to follow a logarithmic rather than exponential increase in signal at sufficiently high numbers of spheroids.

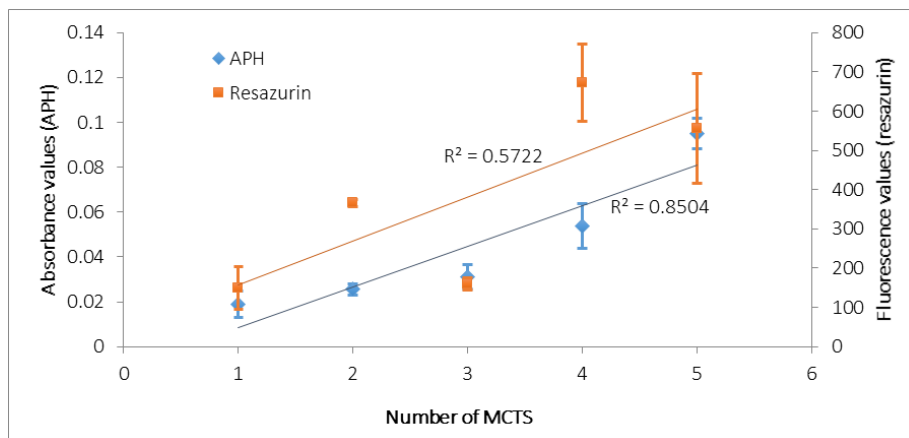


Figure A.2 Results of APH and resazurin assays of wells containing one to five MCTS after 24 hours of formation. Bars represent standard error ( $n \geq 3$ ).

The APH and resazurin assays were further validated by varying MCTS seeding density in order to conclude whether the assay effectively penetrated spheroids and to determine how spheroid size affected assay results. In the case of perfect penetration of an entirely viable spheroid, the assay would respond linearly to an increase in seeding density. If the assay does not penetrate beyond the spheroid surface, the assay response would be expected to resemble a fractional power curve. In reality, the response is likely to lie somewhere in between due to the growth of the spheroids after seeding, death of innermost cells and imperfect penetration of the assay. As demonstrated in Figure A.3, no substantial difference in trend was observed between the APH and resazurin assays. Wells seeded with 2,500 cells per well did not form spheroids but remained largely dispersed throughout the wells. Interestingly, the average fluorescence returned by the resazurin assay of these wells far exceeded all the values for formed spheroids, whereas the average absorbance returned by the APH assay fell below the linear trend. This indicates a much stronger response of resazurin than pNPP to dissociated cells. If this is the case, minor imperfections in spheroid formation could affect the resazurin assay more strongly than the APH assay.

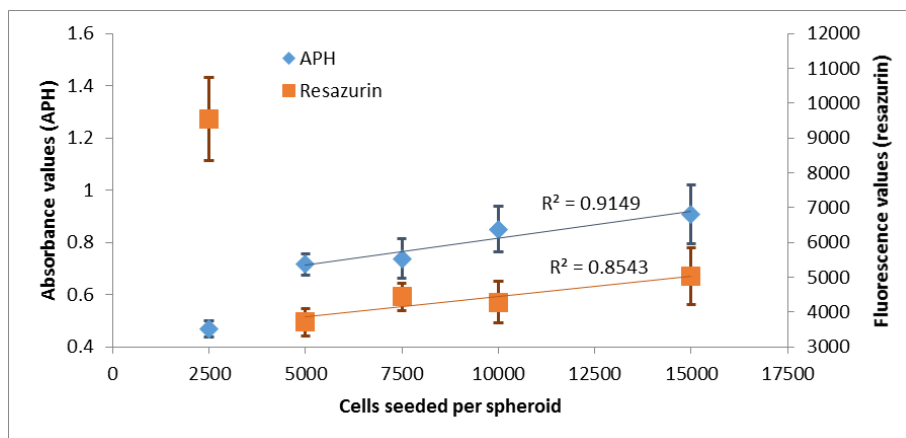


Figure A.3 Results of APH and resazurin assays of spheroids seeded at various densities and grown for 24 hours. Bars represent standard error ( $n \geq 4$ ).

In validation studies with CDDP, there was no accurate standard for determining the response of A549 MCTS to varying concentrations of CDDP. Instead, simply a reasonable decrease in viability due to CDDP treatment was expected. Spheroid dissociation was used to compare response of the assay to tightly packed and dispersed cells, since each assay used is generally accepted as accurate in cell monolayers. Each treatment was normalized to the control to give the relative viability. Results are given in Figure A.4. The APH assay returned consistent relative viability results between intact and dissociated spheroids after exposure to 20 or 2000  $\mu\text{M}$  CDDP. The resazurin assay presented large discrepancies between intact and dissociated spheroids at the same CDDP concentration suggesting that its use for MCTS analysis is limited.

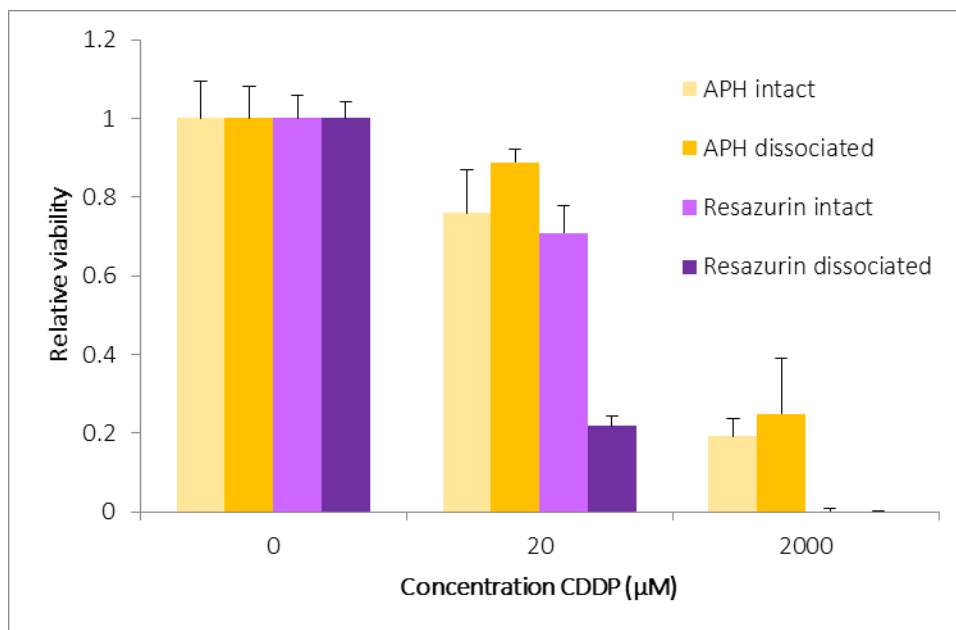


Figure A.4 APH and resazurin assays of intact and dissociated spheroids, and calcein assay of dissociated spheroids. Dissociation and assay were performed following 72 hours of treatment with CDDP. Each group was separately normalized to its own control. Bars represent standard error ( $n \geq 5$ ).

The live/dead assay of intact spheroids was displayed separately in Figure A.5. The calcein AM stain of intact spheroids indicated no trend in viability in response to CDDP, suggesting that it is a poor indicator of spheroid viability. The ethidium stain of intact spheroids demonstrated a reasonable trend however, relative cell death cannot be directly compared with relative viability. As demonstrated by the upper row of Figure A.6, the images associated with the live/dead assay provide a useful means of qualitative analysis of spheroid response to treatment. Besides a general trend in viability, these images suggested that 20 µM CDDP inhibits growth of the spheroid and 2000 µM CDDP was strong enough to begin to disperse cells, causing the spheroid to appear larger than after 20 µM CDDP treatment.

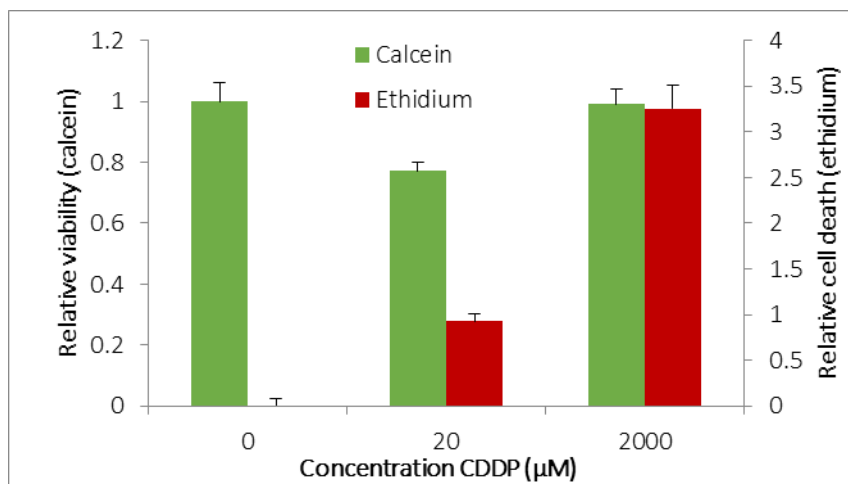


Figure A.5 Live/dead assay of intact spheroids, performed following 72 hours of treatment with CDDP. Each group was separately normalized to its own control. Bars represent standard error ( $n \geq 5$ ).

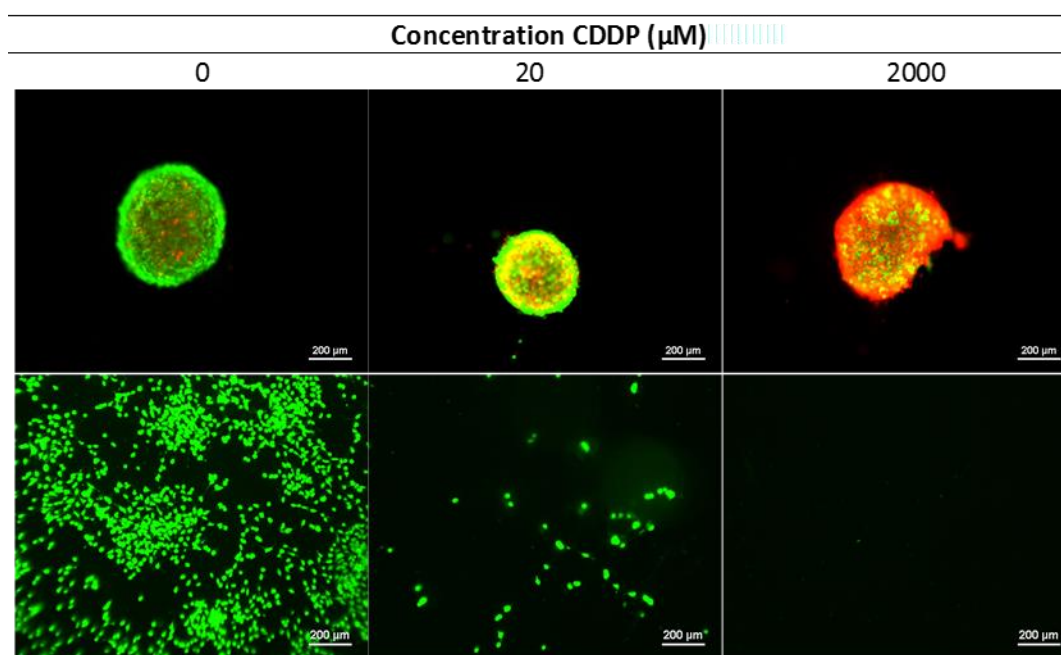


Figure A.6 Representative images of intact spheroids stained with calcein AM and ethidium homodimer-1 (upper), and of dissociated spheroids stained with calcein AM (lower). Staining was performed after 72 hours of treatment with CDDP for intact spheroids and an additional attachment period of 48 hours preceded stain of dissociated spheroids. Scale bars represent 200 μm.

### *A.3.2 Cisplatin combined with hyperthermia on MCTS*

Based on the consistency of the APH assay and on its ease of application, this assay was chosen for a proof of feasibility study investigating the interaction between incubator-induced hyperthermia and CDDP (Figure A.7). CDDP has been previously shown to be more effective when administered at elevated temperatures (Urano, Kuroda et al. 1999) and a sigmoidal response with increasing concentration of CDDP has been previously observed on monolayer cell cultures. This same trend was observed for MCTS treated with CDDP with and without 30 minutes of hyperthermia. The  $IC_{50}$  value, the concentration of CDDP that results in 50% cell death, was compared to CDDP alone with the combined treatment. A decrease in the  $IC_{50}$  value from 54 to 34  $\mu$ M was observed upon application of hyperthermia with CDDP on A549 MCTS. Live/dead images obtained in parallel with this experiment confirm qualitatively that a sharp decrease in viability was observed at about 40  $\mu$ M CDDP. However, this study was completed as a single trial ( $n \geq 5$ ) and should be repeated to assess consistency of the treatment.



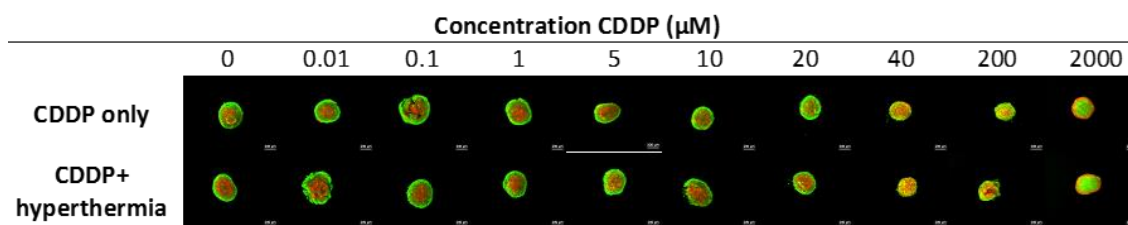
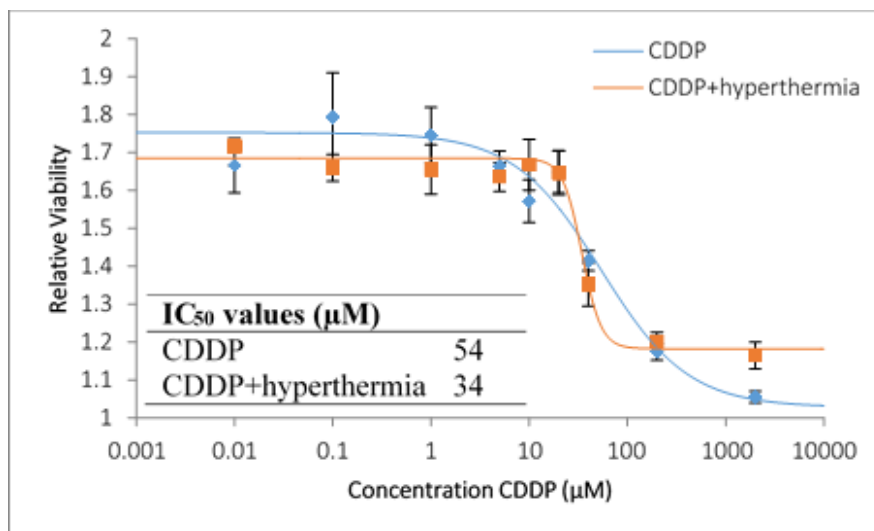


Figure A.7 Relative viabilities of MCTS treated with varying concentrations of CDDP for 72 hours with and without hyperthermia for 30 minutes at 43 °C immediately following CDDP exposure. Error bars represent standard error ( $n \geq 5$ ). Corresponding live/dead images and IC<sub>50</sub> values are included.

### A.3.3 Radiation combined with hyperthermia on MCTS

The third objective of this study was to analyze the effects of radiation combined with hyperthermia treatment on A549 MCTS. Various radiation treatments of 0, 2, 4, and 6 Gy were dosed to MCTS, and following radiation exposure half of the MCTS were treated with 60 minutes of incubator-induced hyperthermia. Normalized viability was determined by the APH assay and live/dead staining 5 and 7 days following treatment. Both 5 and 7 days post treatment, radiation treatment alone effected the relative viability of A549 MCTS however, hyperthermia treatment did not further decrease the relative viability of the MCTS (Figures A.8 and A.11). Additionally, upon analysis of the reported dead fluorescence values, there was a greater increase in dead fluorescence

as radiation treatment increased, but no additional enhancement was observed by hyperthermia treatment (Figures A.9 and A.12).

Analyzing MCTS viability as well as the relative dead fluorescence, there was no difference between the control and hyperthermia treatment alone. This is consistent with previous studies suggesting that hyperthermia is not powerful enough by itself to effectively treat cancer. Traditional monolayer studies suggest that hyperthermia combined with radiation does often result in a synergistic effect (Horsman and Murata 2002) however, this was not observed when treating MCTS. Radiation was combined with hyperthermia to treat MCTS because MCTS work to bridge the gap between traditional monolayer cell culture and *in vivo* animal studies. Most traditional monolayer cell culture used with hyperthermia in literature administer a single treatment of hyperthermia. Since the MCTS are more representative of *in vivo* studies, the protocols may need to be altered to better represent treatments which would be administered *in vivo*, such as fractionated radiation. By fractionating the radiation dosage and exposing the MCTS to cyclic hyperthermia treatments, a synergistic therapy may result however, significant optimization needs to occur.

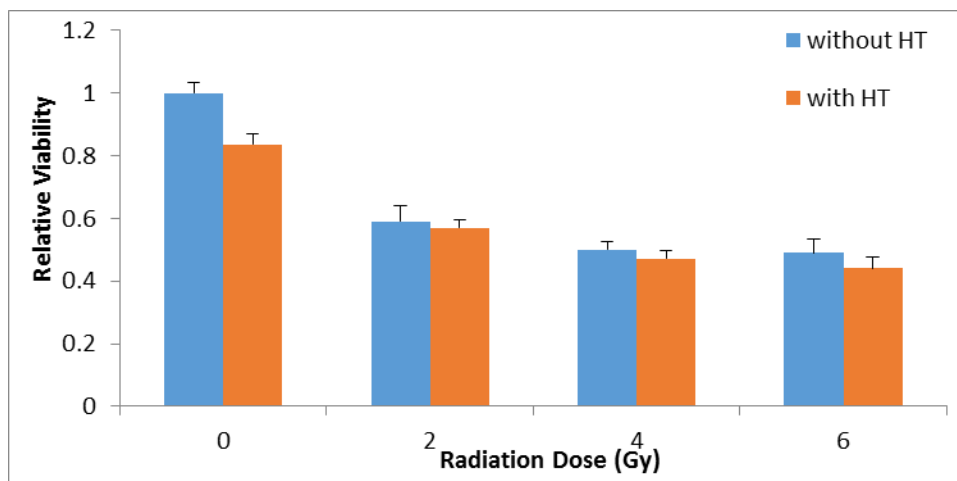


Figure A.8 Relative viability of A549 lung carcinoma 5 days after radiation treatment (0, 2, 4, 6 Gy) with and without 60 minutes incubator induced hyperthermia, measured using APH assay. Error bars represent standard error (n=9).

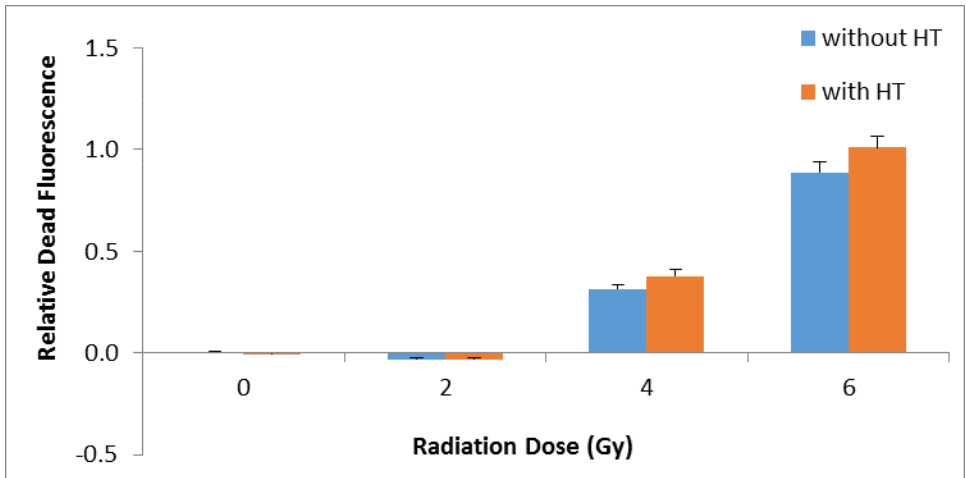


Figure A.9 Relative dead fluorescence of A549 lung carcinoma MCTS 5 days after radiation treatment (0, 2, 4, 6 Gy) with and without 60 minutes incubator induced hyperthermia. Error bars represent standard error (n=6).

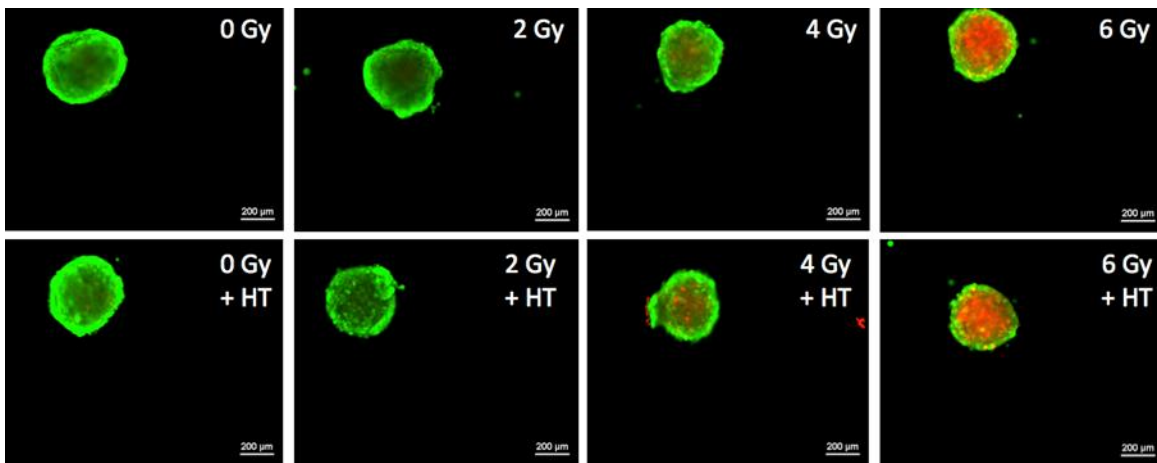


Figure A.10 Live/Dead images of A549 MCTS 5 days following radiation treatment with and without hyperthermia exposure.

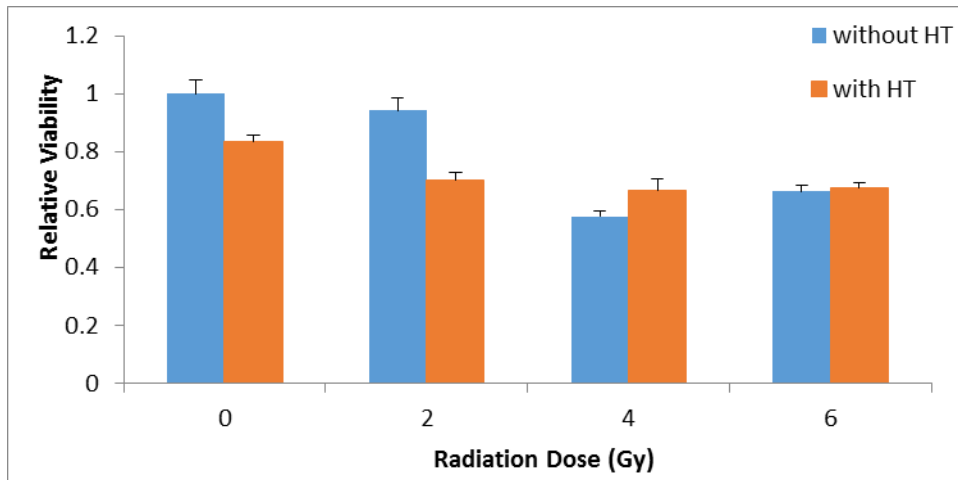


Figure A.11 Relative viability of A549 lung carcinoma 7 days after radiation treatment (0, 2, 4, 6 Gy) with and without 60 minutes incubator induced hyperthermia, measured using APH assay. Error bars represent standard error (n=9).

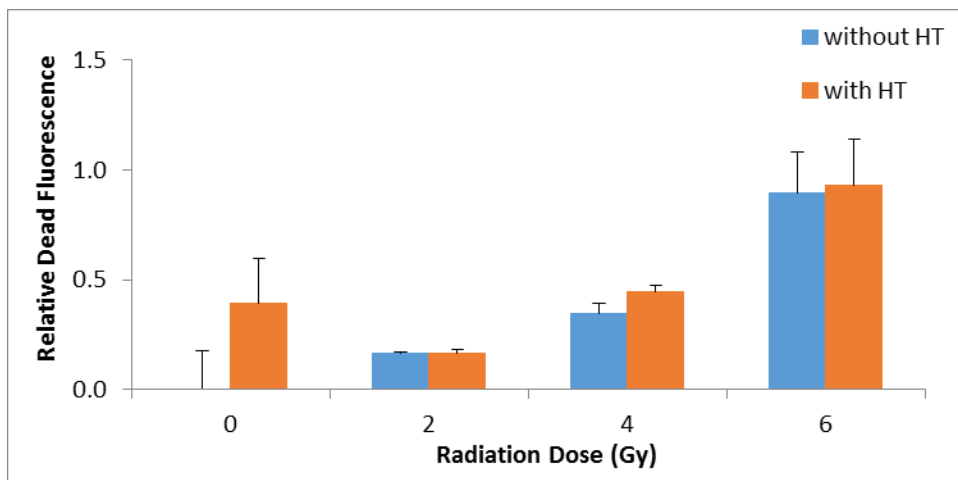


Figure A.12 Relative dead fluorescence of A549 lung carcinoma MCTS 7 days after radiation treatment (0, 2, 4, 6 Gy) with and without 60 minutes incubator induced hyperthermia. Error bars represent standard error (n=6).

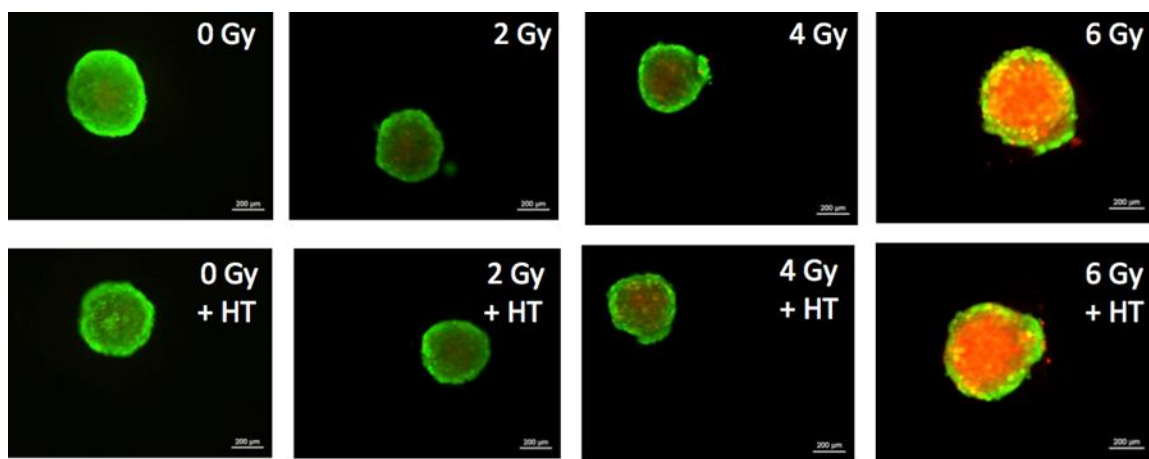


Figure A.13 Live/Dead images of A549 MCTS 7 days following radiation treatment with and without hyperthermia exposure.

#### A.4 Conclusions

Cancer therapy research using MCTS poses significant challenges due to difficulty in analyzing the MCTS post treatment. However, there are significant benefits to utilizing MCTS for analysis prior to expensive *in vivo* studies as MCTS more accurately represent physiological conditions compared to monolayer cell cultures. In this work, three assays were analyzed to determine the most consistent and accurate analysis method of MCTS viability. The APH assay appeared to be more consistent and accurate at determining the relative viability of MCTS compared to the resazurin assay. Although the live/dead assay was not studied as extensively as the APH and resazurin assays, it was determined that due to the associated costs, time sensitivity, and labor intensity, the live/dead assay is not suitable for use in high throughput studies but rather provides images as a verification of results obtained by other assays. Although several previous studies involving MCTS perform a viability assay after dissociation of spheroids, this option is impractical for high throughput due the level of associated labor. Additionally, the dissociation process provides significant opportunity for inconsistency in working volumes and may cause damage or loss of cells.

After determining the appropriate viability assay, two proof of concept studies were completed to analyze the effects of hyperthermia combined with chemotherapy or radiation on A549 lung carcinoma MCTS. When cisplatin was combined with 30 minutes of incubator-induced hyperthermia, the  $IC_{50}$  value decreased, suggesting that the combined treatment was more effective than the CDDP alone. When radiation was combined with 60 minutes of incubator hyperthermia on MCTS, there was no enhancement of radiation therapy. This could be due to a variety of reasons including the cell line, hyperthermia time and temperature, delay between radiation and hyperthermia treatment, order of the treatments, etc. Previous work has indicated the variability in treatment efficacy by combining hyperthermia and radiation and this study further confirms these results. Future work with MCTS and hyperthermia should address magnetically mediated hyperthermia in combination with a chemotherapeutic. MCTS would allow for evaluation of nanoparticle uptake and penetration into the spheroid as well as analysis of the effects of magnetically mediated hyperthermia on an *in vitro* three-dimensional model.

## References

- Abakumov, M., N. V. Nukolova, M. Sokolsky-Papkov, S. A. Shein, T. O. Sandalova, H. M. Vishwasrao, N. F. Grinenko, I. L. Gubsky, A. M. Abakumov, A. V. Kabanov and V. P. Chekhonin (2015). "VEGF-targeted magnetic nanoparticles for MRI visualization of brain tumor." Nanomedicine-Nanotechnology Biology and Medicine **11**(4): 825-833.
- ACS (2013). Cancer Facts and Figures, American Cancer Society.
- Agemy, L., K. N. Sugahara, V. R. Kotamraju, K. Gujraty, O. M. Girard, Y. Kono, R. F. Mattrey, J.-H. Park, M. J. Sailor, A. I. Jimenez, C. Cativiela, D. Zanuy, F. J. Sayago, C. Aleman, R. Nussinov and E. Ruoslahti (2010). "Nanoparticle-induced vascular blockade in human prostate cancer." Blood **116**(15): 2847-2856.
- Ahamed, M., H. A. Alhadlaq, J. Alam, M. Khan, D. Ali and S. Alarafi (2013). "Iron Oxide Nanoparticle-induced Oxidative Stress and Genotoxicity in Human Skin Epithelial and Lung Epithelial Cell Lines." Current Pharmaceutical Design **19**(37): 6681-6690.
- Ahamed, M., H. A. Alhadlaq, M. A. M. Khan and M. J. Akhtar (2013). "Selective killing of cancer cells by iron oxide nanoparticles mediated through reactive oxygen species via p53 pathway." Journal of Nanoparticle Research **15**(1).
- Alarifi, S., D. Ali, S. Alkahtani and M. S. Alhader (2014). "Iron Oxide Nanoparticles Induce Oxidative Stress, DNA Damage, and Caspase Activation in the Human Breast Cancer Cell Line." Biological Trace Element Research **159**(1-3): 416-424.
- Alvarez-Berrios, M. P., A. Castillo, J. Mendez, O. Soto, C. Rinaldi and M. Torres-Lugo (2013). "Hyperthermic potentiation of cisplatin by magnetic nanoparticle heaters is correlated with an increase in cell membrane fluidity." International Journal of Nanomedicine **8**: 1003-1013.
- Alvarez-Berrios, M. P., A. Castillo, J. Mendez, O. Soto, C. Rinaldi and M. Torres-Lugo (2013). "Hyperthermic potentiation of cisplatin by magnetic nanoparticle heaters is correlated with an increase in cell membrane fluidity." International Journal of Nanomedicine **8**: 1003-1013.
- Alvarez-Berrios, M. P., A. Castillo, F. Merida, J. Mendez, C. Rinaldi and M. Torres-Lugo (2015). "Enhanced proteotoxic stress: one of the contributors for hyperthermic potentiation of the proteasome inhibitor bortezomib using magnetic nanoparticles." Biomaterials Science **3**(2): 391-400.
- Alvarez-Berrios, M. P., A. Castillo, C. Rinaldi and M. Torres-Lugo (2014). "Magnetic fluid hyperthermia enhances cytotoxicity of bortezomib in sensitive and resistant cancer cell lines." International Journal of Nanomedicine **9**: 145-153.
- Amin, M. L., J. Y. Joo, D. K. Yi and S. S. A. An (2015). "Surface modification and local orientations of surface molecules in nanotherapeutics." Journal of Controlled Release **207**: 131-142.
- Amstad, E., J. Kohlbrecher, E. Mueller, T. Schweizer, M. Textor and E. Reimhult (2011). "Triggered Release from Liposomes through Magnetic Actuation of Iron Oxide Nanoparticle Containing Membranes." Nano Letters **11**(4): 1664-1670.

Amstad, E., M. Textor and E. Reimhult (2011). "Stabilization and functionalization of iron oxide nanoparticles for biomedical applications." Nanoscale **3**(7): 2819-2843.

Andrade, A. L., D. M. Souza, M. C. Pereira, J. D. Fabris and R. Z. Domingues (2010). "pH EFFECT ON THE SYNTHESIS OF MAGNETITE NANOPARTICLES BY THE CHEMICAL REDUCTION-PRECIPIATION METHOD." Quimica Nova **33**(3): 524-527.

Aranda, A., L. Sequedo, L. Tolosa, G. Quintas, E. Burello, J. V. Castell and L. Gombau (2013). "Dichloro-dihydro-fluorescein diacetate (DCFH-DA) assay: A quantitative method for oxidative stress assessment of nanoparticle-treated cells." Toxicology in Vitro **27**(2): 954-963.

Arbain, R., M. Othman and S. Palaniandy (2011). "Preparation of iron oxide nanoparticles by mechanical milling." Minerals Engineering **24**(1): 1-9.

Atkinson, W. J., I. A. Brezovich and D. P. Chakraborty (1984). "USABLE FREQUENCIES IN HYPERTHERMIA WITH THERMAL SEEDS." Ieee Transactions on Biomedical Engineering **31**(1): 70-75.

Auerbach, M. (2008). "Ferumoxytol as a New, Safer, Easier-to-Administer Intravenous Iron: Yes or No?" American Journal of Kidney Diseases **52**(5): 826-829.

Auffan, M., W. Achouak, J. Rose, M.-A. Roncato, C. Chaneac, D. T. Waite, A. Masion, J. C. Woicik, M. R. Wiesner and J.-Y. Bottero (2008). "Relation between the redox state of iron-based nanoparticles and their cytotoxicity toward Escherichia coli." Environmental Science & Technology **42**(17): 6730-6735.

Austin, L. A., B. Kang, C. W. Yen and M. A. El-Sayed (2011). "Nuclear Targeted Silver Nanospheres Perturb the Cancer Cell Cycle Differently than Those of Nanogold." Bioconjugate Chemistry **22**(11): 2324-2331.

Ayala, V., A. P. Herrera, M. Latorre-Esteves, M. Torres-Lugo and C. Rinaldi (2013). "Effect of surface charge on the colloidal stability and in vitro uptake of carboxymethyl dextran-coated iron oxide nanoparticles." Journal of Nanoparticle Research **15**(8).

Babincova, M., V. Altanerova, C. Altaner, C. Bergemann and P. Babinec (2008). "In vitro analysis of cisplatin functionalized magnetic nanoparticles in combined cancer chemotherapy and electromagnetic hyperthermia." Ieee Transactions on Nanobioscience **7**(1): 15-19.

Bae, K. H., M. Park, M. J. Do, N. Lee, J. H. Ryu, G. W. Kim, C. Kim, T. G. Park and T. Hyeon (2012). "Chitosan Oligosaccharide-Stabilized Ferrimagnetic Iron Oxide Nanocubes for Magnetically Modulated Cancer Hyperthermia." Acs Nano **6**(6): 5266-5273.

Bahrami, B., M. Mohammadnia-Afrouzi, P. Bakhshaei, Y. Yazdani, G. Ghalamfarsa, M. Yousefi, S. Sadreddini, F. Jadidi-Niaragh and M. Hojjat-Farsangi (2015). "Folate-conjugated nanoparticles as a potent therapeutic approach in targeted cancer therapy." Tumor Biology **36**(8): 5727-5742.

Balasubramanian, S., A. R. Girija, Y. Nagaoka, S. Iwai, M. Suzuki, V. Kizhikkilott, Y. Yoshida, T. Maekawa and S. D. Nair (2014). "Curcumin and 5-Fluorouracil-loaded, folate- and transferrin-decorated polymeric magnetic nanoformulation: a synergistic cancer therapeutic approach, accelerated by magnetic hyperthermia." International Journal of Nanomedicine **9**.



Barbaro, D., L. Di Bari, V. Gandin, C. Evangelisti, G. Vitulli, E. Schiavi, C. Marzano, A. M. Ferretti and P. Salvadori (2015). "Glucose-Coated Superparamagnetic Iron Oxide Nanoparticles Prepared by Metal Vapour Synthesis Are Electively Internalized in a Pancreatic Adenocarcinoma Cell Line Expressing GLUT1 Transporter." Plos One **10**(4).

Bautista, M. C., O. Bomati-Miguel, M. D. Morales, C. J. Serna and S. Veintemillas-Verdaguer (2005). "Surface characterisation of dextran-coated iron oxide nanoparticles prepared by laser pyrolysis and coprecipitation." Journal of Magnetism and Magnetic Materials **293**(1): 20-27.

Bee, A., R. Massart and S. Neveu (1995). "SYNTHESIS OF VERY FINE MAGHEMITE PARTICLES." Journal of Magnetism and Magnetic Materials **149**(1-2): 6-9.

Berry, C. C. (2009). "Progress in functionalization of magnetic nanoparticles for applications in biomedicine." Journal of Physics D-Applied Physics **42**(22): 9.

Berry, C. C. and A. S. G. Curtis (2003). "Functionalisation of magnetic nanoparticles for applications in biomedicine." Journal of Physics D-Applied Physics **36**(13): R198-R206.

Bertrand, N., J. Wu, X. Xu, N. Kamaly and O. C. Farokhzad (2014). "Cancer nanotechnology: The impact of passive and active targeting in the era of modern cancer biology." Advanced Drug Delivery Reviews **66**: 2-25.

Bloemen, M., C. Denis, M. Peeters, L. De Meester, A. Gils, N. Geukens and T. Verbiest (2015). "Antibody-modified iron oxide nanoparticles for efficient magnetic isolation and flow cytometric determination of L-pneumophila." Microchimica Acta **182**(7-8): 1439-1446.

Bolhassani, A. (2011). "Potential efficacy of cell-penetrating peptides for nucleic acid and drug delivery in cancer." Biochimica Et Biophysica Acta-Reviews on Cancer **1816**(2): 232-246.

Bonini, M., D. Berti and P. Baglioni (2013). "Nanostructures for magnetically triggered release of drugs and biomolecules." Current Opinion in Colloid & Interface Science **18**(5): 459-467.

Bouras, A., M. Kaluzova and C. G. Hadjipanayis (2015). "Radiosensitivity enhancement of radioresistant glioblastoma by epidermal growth factor receptor antibody-conjugated iron-oxide nanoparticles." Journal of Neuro-Oncology **124**(1): 13-22.

Brazel, C. S. (2009). "Magnetothermally-responsive Nanomaterials: Combining Magnetic Nanostructures and Thermally-Sensitive Polymers for Triggered Drug Release." Pharmaceutical Research **26**(3): 644-656.

Brunk, U. T., J. Neuzil and J. W. Eaton (2001). "Lysosomal involvement in apoptosis." Redox Report **6**(2): 91-97.

Brusentsov, N. A., T. N. Brusentsova, E. Y. Filinova, N. Y. Jurchenko, D. A. Kupriyanov, Y. A. Pirogov, A. I. Dubina, M. N. Shumskikh, L. I. Shumakov, E. N. Anashkina, A. A. Shevelev and A. A. Uchevatkin (2007). "Magnetohydrodynamic thermochemotherapy and MRI of mouse tumors." Journal of Magnetism and Magnetic Materials **311**(1): 176-180.

Butour, J.-L., P. Alvinerie, J.-P. Souchard, P. Colson, C. Houssier and N. P. Johnson (1991). "Effect of the amine non-leaving group on the structure and stability of DNA complexes with cis-[Pt(R-NH<sub>2</sub>)<sub>2</sub>(NO<sub>3</sub>)<sub>2</sub>]." European Journal of Biochemistry **202**(3): 975-980.

Buyukhatipoglu, K. and A. M. Clyne (2010). "Controlled flame synthesis of alpha Fe<sub>2</sub>O<sub>3</sub> and Fe<sub>3</sub>O<sub>4</sub> nanoparticles: effect of flame configuration, flame temperature, and additive loading." Journal of Nanoparticle Research **12**(4): 1495-1508.

Cavalli, S., D. Carbajo, M. Acosta, S. Lope-Piedrafita, A. P. Candiota, C. Arus, M. Royo and F. Albericio (2012). "Efficient gamma-amino-proline-derived cell penetrating peptide-superparamagnetic iron oxide nanoparticle conjugates via aniline-catalyzed oxime chemistry as bimodal imaging nanoagents." Chemical Communications **48**(43): 5322-5324.

Chacko, B. K., P. A. Kramer, S. Ravi, G. A. Benavides, T. Mitchell, B. P. Dranka, D. Ferrick, A. K. Singal, S. W. Ballinger, S. M. Bailey, R. W. Hardy, J. Zhang, D. Zhi and V. M. Darley-USmar (2014). "The Bioenergetic Health Index: a new concept in mitochondrial translational research." Clinical Science **127**(5-6): 367-373.

Charras, G. T., M. Coughlin, T. J. Mitchison and L. Mahadevan (2008). "Life and times of a cellular bleb." Biophysical Journal **94**(5): 1836-1853.

Chen, G. J., Y. Z. Su, C. Hsu, Y. L. Lo, S. J. Huang, J. H. Ke, Y. C. Kuo and L. F. Wang (2014). "Angiopep-pluronic F127-conjugated superparamagnetic iron oxide nanoparticles as nanotheranostic agents for BBB targeting." Journal of Materials Chemistry B **2**(34): 5666-5675.

Chen, Q.-Y., G.-P. Tao, Y.-Q. Liu and X. Yang (2012). "Synthesis, characterization, cell imaging and anti-tumor activity of multifunctional nanoparticles." Spectrochimica Acta Part a-Molecular and Biomolecular Spectroscopy **96**: 284-288.

Chen, W. H., X. W. Zheng, S. L. Li, W. Z. Zhang, X. Wen, L. D. Yue and J. L. Wang (2015). "One-pot synthesis of FePt/CNTs nanocomposites for efficient cellular imaging and cancer therapy." Journal of Nanoparticle Research **17**(11): 444-444.

Choi, W. I., J. H. Lee, J. Y. Kim, S. U. Heo, Y. Y. Jeong, Y. H. Kim and G. Tae (2015). "Targeted antitumor efficacy and imaging via multifunctional nano-carrier conjugated with anti-HER2 trastuzumab." Nanomedicine-Nanotechnology Biology and Medicine **11**(2): 359-368.

Chou, L. Y. T., K. Ming and W. C. W. Chan (2011). "Strategies for the intracellular delivery of nanoparticles." Chemical Society Reviews **40**(1): 233-245.

Chu, X., J. Yu and Y.-L. Hou (2015). "Surface modification of magnetic nanoparticles in biomedicine." Chinese Physics B **24**(1).

Cleal, K., L. He, P. D. Watson and A. T. Jones (2013). "Endocytosis, Intracellular Traffic and Fate of Cell Penetrating Peptide Based Conjugates and Nanoparticles." Current Pharmaceutical Design **19**(16): 2878-2894.

Cochran, D. B., P. P. Wattamwar, R. Wydra, J. Z. Hilt, K. W. Anderson, R. E. Eitel and T. D. Dziubla (2013). "Suppressing iron oxide nanoparticle toxicity by vascular targeted antioxidant polymer nanoparticles." Biomaterials **34**(37): 9615-9622.

Cohn, C. A., S. R. Simon and M. A. A. Schoonen (2008). "Comparison of fluorescence-based techniques for the quantification of particle-induced hydroxyl radicals." Particle and Fibre Toxicology **5**.

Connord, V., P. Clerc, N. Hallali, D. E. H. Diab, D. Fourmy, V. Gigoux and J. Carrey (2015). "Real-Time Analysis of Magnetic Hyperthermia Experiments on Living Cells under a Confocal Microscope." Small **11**(20): 2437-2445.

Corchero, J. and A. Villaverde (2009). "Biomedical applications of distally controlled magnetic nanoparticles." Trends in Biotechnology **27**(8): 468-476.

Creixell, M., A. C. Bohorquez, M. Torres-Lugo and C. Rinaldi (2011). "EGFR-Targeted Magnetic Nanoparticle Heaters Kill Cancer Cells without a Perceptible Temperature Rise." Acs Nano **5**(9): 7124-7129.

Daou, T. J., J. M. Greneche, G. Pourroy, S. Buathong, A. Derory, C. Ulhaq-Bouillet, B. Donnio, D. Guillon and S. Begin-Colin (2008). "Coupling agent effect on magnetic properties of functionalized magnetite-based nanoparticles." Chemistry of Materials **20**(18): 5869-5875.

de la Fuente, J. M. and C. C. Berry (2005). "Tat peptide as an efficient molecule to translocate gold nanoparticles into the cell nucleus." Bioconjugate Chemistry **16**(5): 1176-1180.

Delaviz, N., P. Gill, A. Ajami and M. Aarabi (2015). "Aptamer-conjugated magnetic nanoparticles for the efficient removal of HCV particles from human plasma samples." Rsc Advances **5**(97): 79433-79439.

Deng, S., W. Zhang, B. Zhang, R. Hong, Q. Chen, J. Dong, Y. Chen, Z. Chen and Y. Wu (2015). "Radiolabeled cyclic arginine-glycine-aspartic (RGD)-conjugated iron oxide nanoparticles as single-photon emission computed tomography (SPECT) and magnetic resonance imaging (MRI) dual-modality agents for imaging of breast cancer." Journal of Nanoparticle Research **17**(1).

Dennis, C. L., A. J. Jackson, J. A. Borchers, P. J. Hoopes, R. Strawbridge, A. R. Foreman, J. v. Lierop, C. Grüttner and R. Ivkov (2009). "Nearly complete regression of tumors via collective behavior of magnetic nanoparticles in hyperthermia." Nanotechnology **20**(39): 395103.

Di Corato, R., A. Espinosa, L. Lartigue, M. Tharaud, S. Chat, T. Pellegrino, C. Ménager, F. Gazeau and C. Wilhelm (2014). "Magnetic hyperthermia efficiency in the cellular environment for different nanoparticle designs." Biomaterials **35**(24): 6400-6411.

Dolores, R., S. Raquel and G. L. Adianez (2015). "Sonochemical synthesis of iron oxide nanoparticles loaded with folate and cisplatin: Effect of ultrasonic frequency." Ultrasonics Sonochemistry **23**: 391-398.

Domenech, M., I. Marrero-Berrios, M. Torres-Lugo and C. Rinaldi (2013). "Lysosomal Membrane Permeabilization by Targeted Magnetic Nanoparticles in Alternating Magnetic Fields." Acs Nano **7**(6): 5091-5101.

Du, B., S. P. Han, H. Y. Li, F. F. Zhao, X. J. Su, X. H. Cao and Z. Z. Zhang (2015). "Multi-functional liposomes showing radiofrequency-triggered release and magnetic resonance imaging for tumor multi-mechanism therapy." Nanoscale **7**(12): 5411-5426.

Duguet, E., S. Vasseur, S. Mornet and J. M. Devoisselle (2006). "Magnetic nanoparticles and their applications in medicine." Nanomedicine **1**(2): 157-168.

- Easo, S. L. and P. V. Mohanan (2013). "Dextran stabilized iron oxide nanoparticles: Synthesis, characterization and in vitro studies." Carbohydrate Polymers **92**(1): 726-732.
- Emerit, J., C. Beaumont and F. Trivin (2001). "Iron metabolism, free radicals, and oxidative injury." Biomedicine & Pharmacotherapy **55**(6): 333-339.
- Farkhani, S. M., A. Valizadeh, H. Karami, S. Mohammadi, N. Sohrabi and F. Badrzadeh (2014). "Cell penetrating peptides: Efficient vectors for delivery of nanoparticles, nanocarriers, therapeutic and diagnostic molecules." Peptides **57**: 78-94.
- Feest, T. G. (1976). "LOW-MOLECULAR WEIGHT DEXTRAN - A CONTINUING CAUSE OF ACUTE RENAL-FAILURE." British Medical Journal **2**(6047): 1300-1300.
- Fortin, J. P., C. Wilhelm, J. Servais, C. Menager, J. C. Bacri and F. Gazeau (2007). "Size-sorted anionic iron oxide nanomagnets as colloidal mediators for magnetic hyperthermia." Journal of the American Chemical Society **129**(9): 2628-2635.
- Fox, M. E., F. C. Szoka and J. M. J. Frechet (2009). "Soluble Polymer Carriers for the Treatment of Cancer: The Importance of Molecular Architecture." Accounts of Chemical Research **42**(8): 1141-1151.
- Friedrich, J., R. Ebner and L. A. Kunz-Schughart (2007). "Experimental anti-tumor therapy in 3-D: Spheroids - old hat or new challenge?" International Journal of Radiation Biology **83**(11-12): 849-871.
- Friedrich, J., W. Eder, J. Castaneda, M. Doss, E. Huber, R. Ebner and L. A. Kunz-Schughart (2007). "A reliable tool to determine cell viability in complex 3-D culture: The acid phosphatase assay." Journal of Biomolecular Screening **12**(7): 925-937.
- Frimpong, R. A., J. Dou, M. Pechan and J. Z. Hilt (2010). "Enhancing remote controlled heating characteristics in hydrophilic magnetite nanoparticles via facile co-precipitation." Journal of Magnetism and Magnetic Materials **322**(3): 326-331.
- Frimpong, R. A. and J. Z. Hilt (2010). "Magnetic nanoparticles in biomedicine: synthesis, functionalization and applications." Nanomedicine **5**(9): 1401-1414.
- Gao, F. P., Z. X. Yan, J. Zhou, Y. Y. Cai and J. T. Tang (2012). "Methotrexate-conjugated magnetic nanoparticles for thermochemotherapy and magnetic resonance imaging of tumor." Journal of Nanoparticle Research **14**(10).
- Gautier, J., E. Allard-Vannier, E. Munnier, M. Soucé and I. Chourpa "Recent advances in theranostic nanocarriers of doxorubicin based on iron oxide and gold nanoparticles." Journal of Controlled Release **169**(1-2): 48-61.
- Genet, S. C., Y. Fujii, J. Maeda, M. Kaneko, M. D. Genet, K. Miyagawa and T. A. Kato (2013). "Hyperthermia inhibits homologous recombination repair and sensitizes cells to ionizing radiation in a time- and temperature-dependent manner." J Cell Physiol **228**(7): 1473-1481.
- Glickson, J. D., S. Lund-Katz, R. Zhou, H. Choi, I. W. Chen, H. Li, I. Corbin, A. V. Popov, W. G. Cao, L. P. Song, C. Z. Qi, D. Marotta, D. S. Nelson, J. Chen, B. Chance and G. Zheng (2009). LIPOPROTEIN NANOPLATFORM FOR TARGETED DELIVERY OF DIAGNOSTIC AND

THERAPEUTIC AGENTS. Oxygen Transport to Tissue Xxx. P. Liss, P. Hansell, D. F. Bruley and D. K. Harrison. New York, Springer. **645**: 227-239.

Gordon, R. T., J. R. Hines and D. Gordon (1979). "INTRACELLULAR HYPERTHERMIA - BIOPHYSICAL APPROACH TO CANCER-TREATMENT VIA INTRACELLULAR TEMPERATURE AND BIOPHYSICAL ALTERATIONS." Medical Hypotheses **5**(1): 83-102.

Goya, G. F., V. Grazu and M. R. Ibarra (2008). "Magnetic nanoparticles for cancer therapy." Current Nanoscience **4**(1): 1-16.

Gruettner, C., K. Mueller, J. Teller and F. Westphal (2013). "Synthesis and functionalisation of magnetic nanoparticles for hyperthermia applications." International Journal of Hyperthermia **29**(8): 777-789.

Gruettner, C., K. Mueller, J. Teller, F. Westphal, A. Foreman and R. Ivkov (2007). "Synthesis and antibody conjugation of magnetic nanoparticles with improved specific power absorption rates for alternating magnetic field cancer therapy." Journal of Magnetism and Magnetic Materials **311**(1): 181-186.

Guicciardi, M. E., M. Leist and G. J. Gores (2004). "Lysosomes in cell death." Oncogene **23**(16): 2881-2890.

Gupta, A. K. and M. Gupta (2005). "Synthesis and surface engineering of iron oxide nanoparticles for biomedical applications." Biomaterials **26**: 3995-4021.

Gupta, A. K. and M. Gupta (2005). "Synthesis and surface engineering of iron oxide nanoparticles for biomedical applications." Biomaterials **26**(18): 3995-4021.

Gupta, A. K., R. R. Naregalkar, V. D. Vaidya and M. Gupta (2007). "Recent advances on surface engineering of magnetic iron oxide nanoparticles and their biomedical applications." Nanomedicine **2**: 23-39.

Hajshafiei, P., S. Fatahian and K. Shahanipoor (2014). "In Vivo Toxicity Assessment of Bovine Serum Albumin and Dimercaptosuccinic Acid Coated Fe<sub>3</sub>O<sub>4</sub> Nanoparticles." Iranian Journal of Biotechnology **12**(2).

Halamikova, A., D. Vrana, J. Kasparikova and V. Brabec (2007). "Biochemical studies of the thermal effects on DNA modifications by the antitumor cisplatin and their repair." ChemBiochem **8**(16): 2008-2015.

Hauser, A. K., R. Mathias, K. W. Anderson and J. Z. Hilt (2015). "The effects of synthesis method on the physical and chemical properties of dextran coated iron oxide nanoparticles." Materials Chemistry and Physics **160**: 177-186.

Hauser, A. K., R. J. Wydra, R. Bhandari, P. G. Rychahou, B. M. Evers, K. W. Anderson, T. D. Dziubla and J. Z. Hilt "Corrigendum to "The role of ROS generation from magnetic nanoparticles in an alternating magnetic field on cytotoxicity" [Acta Biomater. 25 (2015) 284–290]." Acta Biomaterialia.

Herea, D. D., H. Chiriac, N. Lupu, M. Grigoras, G. Stoian, B. A. Stoica and T. Petreus (2015). "Study on iron oxide nanoparticles coated with glucose-derived polymers for biomedical applications." Applied Surface Science **352**: 117-125.

Hergt, R., R. Hiergeist, I. Hilger, W. A. Kaiser, Y. Lapatnikov, S. Margel and U. Richter (2004). "Maghemite nanoparticles with very high AC-losses for application in RF-magnetic hyperthermia." Journal of Magnetism and Magnetic Materials **270**(3): 345-357.

Hervault, A. and N. n. T. K. Thanh (2014). "Magnetic nanoparticle-based therapeutic agents for thermo-chemotherapy treatment of cancer." Nanoscale **6**(20): 11553-11573.

Hervouet, E., H. Simonnet and C. Godinot (2007). "Mitochondria and reactive oxygen species in renal cancer." Biochimie **89**(9): 1080-1088.

Hettinga, J. V. E., W. Lemstra, E. G. E. Devries, A. W. T. Konings and H. H. Kampinga (1995). "SENSITIZATION TO CISPLATIN ACTION BY STEP-DOWN HEATING IN CDDP-SENSITIVE AND CDDP-RESISTANT CELLS." International Journal of Cancer **61**(5): 722-726.

Hettinga, J. V. E., W. Lemstra, C. Meijer, W. A. Dam, D. R. A. Uges, A. W. T. Konings, E. G. E. DeVries and H. H. Kampinga (1997). "Mechanism of hyperthermic potentiation of cisplatin action in cisplatin-sensitive and -resistant tumour cells." British Journal of Cancer **75**(12): 1735-1743.

Hetzel, F. W. and J. A. Dunn (1984). "Hyperthermia and radiation in cancer therapy: a review." Radiat. Phys. Chem. **24**(3/4): 337-345.

Hildebrandt, B., P. Wust, O. Ahlers, A. Dieing, G. Sreenivasa, T. Kerner, R. Felix and H. Riess (2002). "The cellular and molecular basis of hyperthermia." Critical Reviews in Oncology Hematology **43**(1): 33-56.

Hill, B. G., G. A. Benavides, J. R. Lancaster, Jr., S. Ballinger, L. Dell'Italia, J. Zhang and V. M. Darley-Usmar (2012). "Integration of cellular bioenergetics with mitochondrial quality control and autophagy." Biological Chemistry **393**(12): 1485-1512.

Ho, D., X. L. Sun and S. H. Sun (2011). "Monodisperse Magnetic Nanoparticles for Theranostic Applications." Accounts of Chemical Research **44**(10): 875-882.

Hola, K., Z. Markova, G. Zoppellaro, J. Tucek and R. Zboril (2015). "Tailored functionalization of iron oxide nanoparticles for MRI, drug delivery, magnetic separation and immobilization of biosubstances." Biotechnology Advances **33**(6): 1162-1176.

Horsman, M. R. and R. Murata (2002). "Combination of vascular targeting agents with thermal or radiation therapy." International Journal of Radiation Oncology Biology Physics **54**(5): 1518-1523.

Horsman, M. R. and J. Overgaard (2007). "Hyperthermia: a potent enhancer of radiotherapy." Clinical Oncology **19**(6): 418-426.

Hu, R., S. Ma, H. Li, X. Ke, G. Wang, D. Wei and W. Wang (2011). "Effect of magnetic fluid hyperthermia on lung cancer nodules in a murine model." Oncology Letters **2**(6): 1161-1164.

- Hu, R. L., S. L. Ma, H. Li, X. F. Ke, G. Q. Wang, D. S. Wei and W. Wang (2011). "Effect of magnetic fluid hyperthermia on lung cancer nodules in a murine model." Oncology Letters **2**(6): 1161-1164.
- Hu, Y., L. D. Li and L. Guo (2015). "The sandwich-type aptasensor based on gold nanoparticles/DNA/magnetic beads for detection of cancer biomarker protein AGR2." Sensors and Actuators B-Chemical **209**: 846-852.
- Huang, G., H. B. Chen, Y. Dong, X. Q. Luo, H. J. Yu, Z. Moore, E. A. Bey, D. A. Boothman and J. M. Gao (2013). "Superparamagnetic Iron Oxide Nanoparticles: Amplifying ROS Stress to Improve Anticancer Drug Efficacy." Theranostics **3**(2): 116-126.
- Huang, H., S. Delikanli, H. Zeng, D. M. Ferkey and A. Pralle (2010). "Remote control of ion channels and neurons through magnetic-field heating of nanoparticles." Nature Nanotechnology **5**(8): 602-606.
- Huang, J. Y., M. H. Chen, W. T. Kuo, Y. J. Sun and F. H. Lin (2015). "The characterization and evaluation of cisplatin-loaded magnetite-hydroxyapatite nanop articles (mHAp/CDDP) as dual treatment of hyperthermia and chemotherapy for lung cancer therapy." Ceramics International **41**(2): 2399-2410.
- Hurwitz, M. D., J. L. Hansen, S. Prokopios-Davos, J. Manola, Q. A. Wang, B. A. Bornstein, K. Hynynen and I. D. Kaplan (2011). "Hyperthermia Combined With Radiation for the Treatment of Locally Advanced Prostate Cancer Long-Term Results From Dana-Farber Cancer Institute Study 94-153." Cancer **117**(3): 510-516.
- Hutmacher, D. W., R. E. Horch, D. Loessner, S. Rizzi, S. Sieh, J. Reichert, C., J. A. Clements, J. P. Beier, A. Arkudus, O. Bleiziffer and U. Kneser (2009). "Translating tissue engineering technology platforms into cancer research." Journal of Cellular and Molecular Medicine **13**(8A): 1417-1427.
- Ikhani, H., M. Sarparast, A. Noori, S. Z. Bathaie and M. F. Mousavi (2015). "Electrochemical aptamer/antibody based sandwich immunosensor for the detection of EGFR, a cancer biomarker, using gold nanoparticles as a signaling probe." Biosensors & Bioelectronics **74**: 491-497.
- Imren, D., M. Gumusderelioglu and A. Guner (2006). "Synthesis and characterization of dextran hydrogels prepared with chlor- and nitrogen-containing crosslinkers." Journal of Applied Polymer Science **102**(5): 4213-4221.
- Issels, R. D. (2008). "Hyperthermia adds to chemotherapy." European Journal of Cancer **44**(17): 2546-2554.
- Itoh, Y., Y. Yamada, Y. Kazaoka, T. Ishiguchi and N. Honda (2010). "Combination of chemotherapy and mild hyperthermia enhances the anti-tumor effects of cisplatin and adriamycin in human bladder cancer T24 cells in vitro." Experimental and Therapeutic Medicine **1**(2): 319-323.
- Ivascu, A. and M. Kubbies (2006). "Rapid generation of single-tumor spheroids for high-throughput cell function and toxicity analysis." Journal of Biomolecular Screening **11**(8): 922-932.

Ivkov, R., S. J. DeNardo, W. Daum, A. R. Foreman, R. C. Goldstein, V. S. Nemkov and G. L. DeNardo (2005). "Application of high amplitude alternating magnetic fields for heat induction of nanoparticles localized in cancer." Clinical Cancer Research **11**(19): 7093S-7103S.

Jaattela, M. (2004). "Multiple cell death pathways as regulators of tumour initiation and progression." Oncogene **23**(16): 2746-2756.

Jacobin-Valat, M.-J., J. Laroche-Traineau, M. Lariviere, S. Mornet, S. Sanchez, M. Biran, C. Lebaron, J. Boudon, S. Lacomme, M. Cerutti and G. Clofent-Sanchez (2015). "Nanoparticles functionalised with an anti-platelet human antibody for in vivo detection of atherosclerotic plaque by magnetic resonance imaging." Nanomedicine-Nanotechnology Biology and Medicine **11**(4): 927-937.

Jafari, A., M. Salouti, S. F. Shayesteh, Z. Heidari, A. B. Rajabi, K. Boustani and A. Nahardani (2015). "Synthesis and characterization of Bombesin-superparamagnetic iron oxide nanoparticles as a targeted contrast agent for imaging of breast cancer using MRI." Nanotechnology **26**(7): 11.

Jafari, S., S. M. Dizaj and K. Adibkia (2015). "Cell-penetrating peptides and their analogues as novel nanocarriers for drug delivery." Bioimpacts **5**(2): 103-111.

Janot, R. and D. Guerard (2002). "One-step synthesis of maghemite nanometric powders by ball-milling." Journal of Alloys and Compounds **333**(1-2): 302-307.

Jarzyna, P. A., L. H. Deddens, B. H. Kann, S. Ramachandran, C. Calcagno, W. Chen, A. Gianella, R. M. Dijkhuizen, A. W. Griffioen, Z. A. Fayad and W. J. M. Mulder (2012). "Tumor Angiogenesis Phenotyping by Nanoparticle-facilitated Magnetic Resonance and Near-infrared Fluorescence Molecular Imaging." Neoplasia **14**(10): 964-973.

Jhaveri, A., P. Deshpande and V. Torchilin (2014). "Stimuli-sensitive nanopreparations for combination cancer therapy." Journal of Controlled Release **190**(0): 352-370.

Jiang, S., K. Y. Win, S. H. Liu, C. P. Teng, Y. G. Zheng and M. Y. Han (2013). "Surface-functionalized nanoparticles for biosensing and imaging-guided therapeutics." Nanoscale **5**(8): 3127-3148.

Jin, R., B. Lin, D. Li and H. Ai (2014). "Superparamagnetic iron oxide nanoparticles for MR imaging and therapy: design considerations and clinical applications." Current Opinion in Pharmacology **18**: 18-27.

Johannsen, M., U. Gneueckow, B. Thiesen, K. Taymoorian, C. H. Cho, N. Waldofner, R. Scholz, A. Jordan, S. A. Loening and P. Wust (2007). "Thermotherapy of prostate cancer using magnetic nanoparticles: Feasibility, imaging, and three-dimensional temperature distribution." European Urology **52**(6): 1653-1662.

Johannsen, M., U. Gneueckow, K. Taymoorian, B. Thiesen, N. Waldofner, R. Scholz, K. Jung, A. Jordan, P. Wust and S. A. Loening (2007). "Morbidity and quality of life during thermotherapy using magnetic nanoparticles in locally recurrent prostate cancer: Results of a prospective phase I trial." International Journal of Hyperthermia **23**(3): 315-323.



- Johannsen, M., A. Jordan, R. Scholz, M. Koch, M. Lein, S. Deger, J. Roigas, K. Jung and S. Loening (2004). "Evaluation of magnetic fluid hyperthermia in a standard rat model of prostate cancer." Journal of Endourology **18**(5): 495-500.
- Johannsen, M., B. Thiesen, U. Gneveckow, K. Taymoorian, N. Waldofner, R. Scholz, S. Deger, K. Jung, S. A. Loening and A. Jordan (2006). "Thermotherapy using magnetic nanoparticles combined with external radiation in an orthotopic rat model of prostate cancer." Prostate **66**(1): 97-104.
- Johannsen, M., B. Thiesen, A. Jordan, K. Taymoorian, U. Gneveckow, N. Waldofner, R. Scholz, M. Koch, M. Lein, K. Jung and S. A. Loening (2005). "Magnetic fluid hyperthermia (MFH) reduces prostate cancer growth in the orthotopic dunning R3327 rat model." Prostate **64**(3): 283-292.
- Johansson, A.-C., H. Appelqvist, C. Nilsson, K. Kagedal, K. Roberg and K. Ollinger (2010). "Regulation of apoptosis-associated lysosomal membrane permeabilization." Apoptosis **15**(5): 527-540.
- Jordan, A., R. Scholz, K. Maier-Hauff, F. K. H. van Landeghem, N. Waldoefner, U. Teichgraeber, J. Pinkernelle, H. Bruhn, F. Neumann, B. Thiesen, A. von Deimling and R. Felix (2006). "The effect of thermotherapy using magnetic nanoparticles on rat malignant glioma." Journal of Neuro-Oncology **78**(1): 7-14.
- Jordan, A., R. Scholz, P. Wust, H. Schirra, T. Schiestel, H. Schmidt and R. Felix (1999). "Endocytosis of dextran and silan-coated magnetite nanoparticles and the effect of intracellular hyperthermia on human mammary carcinoma cells in vitro." Journal of Magnetism and Magnetic Materials **194**(1-3): 185-196.
- Josephson, L., C. H. Tung, A. Moore and R. Weissleder (1999). "High-efficiency intracellular magnetic labeling with novel superparamagnetic-tat peptide conjugates." Bioconjugate Chemistry **10**(2): 186-191.
- Kallumadil, M., M. Tada, T. Nakagawa, M. Abe, P. Southern and Q. A. Pankhurst (2009). "Suitability of commercial colloids for magnetic hyperthermia." Journal of Magnetism and Magnetic Materials **321**(10): 1509-1513.
- Kallumadil, M., M. Tada, T. Nakagawa, M. Abe, P. Southern and Q. A. Pankhurst (2009). "Suitability of commercial colloids for magnetic hyperthermia (vol 321, pg 1509, 2009)." Journal of Magnetism and Magnetic Materials **321**(21): 3650-3651.
- Kaluzova, M., A. Bouras, R. Machaidze and C. G. Hadjipanayis (2015). "Targeted therapy of glioblastoma stem-like cells and tumor non-stem cells using cetuximab-conjugated iron-oxide nanoparticles." Oncotarget **6**(11): 8788-8806.
- Kam, W. W.-Y. and R. B. Banati (2013). "Effects of ionizing radiation on mitochondria." Free Radical Biology and Medicine **65**: 607-619.
- Kanazaki, K., K. Sano, A. Makino, Y. Shimizu, F. Yamauchi, S. Ogawa, N. Ding, T. Yano, T. Temma, M. Ono and H. Saji (2015). "Development of anti-HER2 fragment antibody conjugated to iron oxide nanoparticles for in vivo HER2-targeted photoacoustic tumor imaging." Nanomedicine : nanotechnology, biology, and medicine **11**(8): 2051-2060.

Kang, Y. S., S. Risbud, J. F. Rabolt and P. Stroeve (1996). "Synthesis and characterization of nanometer-size Fe<sub>3</sub>O<sub>4</sub> and gamma-Fe<sub>2</sub>O<sub>3</sub> particles." Chemistry of Materials **8**(9): 2209-&.

Karamipour, S., M. S. Sadjadi and N. Farhadyar (2015). "Fabrication and spectroscopic studies of folic acid-conjugated Fe<sub>3</sub>O<sub>4</sub>@Au core-shell for targeted drug delivery application." Spectrochimica Acta Part a-Molecular and Biomolecular Spectroscopy **148**: 146-155.

Kehrer, J. P. (2000). "The Haber-Weiss reaction and mechanisms of toxicity." Toxicology **149**(1): 43-50.

Kettering, M., J. Winter, M. Zeisberger, S. Bremer-Streck, H. Oehring, C. Bergemann, C. Alexiou, R. Hergt, K. J. Halbhuber, W. A. Kaiser and I. Hilger (2007). "Magnetic nanoparticles as bimodal tools in magnetically induced labelling and magnetic heating of tumour cells: an in vitro study." Nanotechnology **18**(17).

Khan, M. I., A. Mohammad, G. Patil, S. A. H. Naqvi, L. K. S. Chauhan and I. Ahmad (2012). "Induction of ROS, mitochondrial damage and autophagy in lung epithelial cancer cells by iron oxide nanoparticles." Biomaterials **33**(5): 1477-1488.

Khoei, S., B. Goliaei, A. Neshasteh-Riz and A. Deizadji (2004). "The role of heat shock protein 70 in the thermoresistance of prostate cancer cell line spheroids." Febs Letters **561**(1-3): 144-148.

Kievit, F. M., Z. R. Stephen, O. Veiseh, H. Arami, T. Wang, V. P. Lai, J. O. Park, R. G. Ellenbogen, M. L. Disis and M. Zhang (2012). "Targeting of Primary Breast Cancers and Metastases in a Transgenic Mouse Model Using Rationally Designed Multifunctional SPIONs." Acs Nano **6**(3): 2591-2601.

Kim, Y. S., N. H. A. Raston and M. B. Gu (2016). "Aptamer-based nanobiosensors." Biosensors & Bioelectronics **76**: 2-19.

Kirkegaard, T. and M. Jaattela (2009). "Lysosomal involvement in cell death and cancer." Biochimica Et Biophysica Acta-Molecular Cell Research **1793**(4): 746-754.

Klein, S., A. Sommer, L. V. R. Distel, J. L. Hazemann, W. Kroner, W. Neuhuber, P. Muller, O. Proux and C. Kryschi (2014). "Superparamagnetic Iron Oxide Nanoparticles as Novel X-ray Enhancer for Low-Dose Radiation Therapy." Journal of Physical Chemistry B **118**(23): 6159-6166.

Klein, S., A. Sommer, L. V. R. Distel, W. Neuhuber and C. Kryschi (2012). "Superparamagnetic iron oxide nanoparticles as radiosensitizer via enhanced reactive oxygen species formation." Biochemical and Biophysical Research Communications **425**(2): 393-397.

Kodama, R. H. (1999). "Magnetic nanoparticles." Journal of Magnetism and Magnetic Materials **200**(1-3): 359-372.

Koenczoel, M., A. Weiss, E. Stangenberg, R. Gminski, M. Garcia-Kaeufer, R. Giere, I. Merfort and V. Mersch-Sundermann (2013). "Cell-Cycle Changes and Oxidative Stress Response to Magnetite in A549 Human Lung Cells." Chemical Research in Toxicology **26**(5): 693-702.

Kolosnjaj-Tabi, J., R. Di Corato, L. Lartigue, I. Marangon, P. Guardia, A. K. A. Silva, N. Luciani, O. Clement, P. Flaud, J. V. Singh, P. Decuzzi, T. Pellegrino, C. Wilhelm and F. Gazeau (2014).

"Heat-Generating Iron Oxide Nanocubes: Subtle "Destructurators" of the Tumoral Microenvironment." Acs Nano **8**(5): 4268-4283.

Koren, E. and V. P. Torchilin (2012). "Cell-penetrating peptides: breaking through to the other side." Trends in Molecular Medicine **18**(7): 385-393.

Kornhuber, J., A. W. Henkel, T. W. Groemer, S. Staedtler, O. Welzel, P. Tripal, A. Rotter, S. Bleich and S. Trapp (2010). "Lipophilic Cationic Drugs Increase the Permeability of Lysosomal Membranes in a Cell Culture System." Journal of Cellular Physiology **224**(1): 152-164.

Kozissnik, B., A. C. Bohorquez, J. Dobson and C. Rinaldi (2013). "Magnetic fluid hyperthermia: Advances, challenges, and opportunity." International Journal of Hyperthermia **29**(8): 706-714.

Krpetic, Z., P. Nativo, V. See, I. A. Prior, M. Brust and M. Volk (2010). "Inflicting Controlled Nonthermal Damage to Subcellular Structures by Laser-Activated Gold Nanoparticles." Nano Letters **10**(11): 4549-4554.

Kruse, A. M., S. A. Meenach, K. W. Anderson and J. Z. Hilt (2014). "Synthesis and characterization of CREKA-conjugated iron oxide nanoparticles for hyperthermia applications." Acta Biomaterialia **10**(6): 2622-2629.

Kumar, C. and F. Mohammad (2011). "Magnetic nanomaterials for hyperthermia-based therapy and controlled drug delivery." Advanced Drug Delivery Reviews **63**(9): 789-808.

Kumar, C. S. S. R. and F. Mohammad (2011). "Magnetic nanomaterials for hyperthermia-based therapy and controlled drug delivery." Advanced Drug Delivery Reviews **63**: 789-808.

Kumar, M., Z. Medarova, P. Pantazopoulos, G. P. Dai and A. Moore (2010). "Novel Membrane-Permeable Contrast Agent for Brain Tumor Detection by MRI." Magnetic Resonance in Medicine **63**(3): 617-624.

Kumar, M., M. Yigit, G. P. Dai, A. Moore and Z. Medarova (2010). "Image-Guided Breast Tumor Therapy Using a Small Interfering RNA Nanodrug." Cancer Research **70**(19): 7553-7561.

Kut, C., Y. Zhang, M. Hedayati, H. Zhou, C. Cornejo, D. Bordelon, J. Mihalic, M. Wabler, E. Burghardt, C. Gruettner, A. Geyh, C. Brayton, T. L. Dewese and R. Ivkov (2012). "Preliminary study of injury from heating systemically delivered, nontargeted dextran-superparamagnetic iron oxide nanoparticles in mice." Nanomedicine **7**(11): 1697-1711.

Lartigue, L., P. Hugounenq, D. Alloyeau, S. P. Clarke, M. Levy, J.-C. Bacri, R. Bazzi, D. F. Brougham, C. Wilhelm and F. Gazeau (2012). "Cooperative Organization in Iron Oxide Multi-Core Nanoparticles Potentiates Their Efficiency as Heating Mediators and MRI Contrast Agents." Acs Nano **6**(12): 10935-10949.

Laurent, S., S. Dutz, U. O. Hafeli and M. Mahmoudi (2011). "Magnetic fluid hyperthermia: Focus on superparamagnetic iron oxide nanoparticles." Advances in Colloid and Interface Science **166**(1-2): 8-23.

Laurent, S., S. Dutz, U. O. Hafeli and M. Mahmoudi (2011). "Magnetic fluid hyperthermia: Focus on superparamagnetic iron oxide nanoparticles." Advances in Colloid and Interface Science **166**: 8-23.

- Laurent, S., S. Dutz, U. O. Hafeli and M. Mahmoudi (2011). "Magnetic fluid hyperthermia: Focus on superparamagnetic iron oxide nanoparticles." Advances in Colloid and Interface Science **166**(1-2): 8-23.
- Le, B., M. Shinkai, T. Kitade, H. Honda, J. Yoshida, T. Wakabayashi and T. Kobayashi (2001). "Preparation of tumor-specific magnetoliposomes and their application for hyperthermia." Journal of Chemical Engineering of Japan **34**(1): 66-72.
- Lee, J.-H., J.-t. Jang, J.-s. Choi, S. H. Moon, S.-h. Noh, J.-w. Kim, J.-G. Kim, I.-S. Kim, K. I. Park and J. Cheon (2011). "Exchange-coupled magnetic nanoparticles for efficient heat induction." Nature Nanotechnology **6**(7): 418-422.
- Lee, J. S., H. L. Rodriguez-Luccioni, J. Mendez, A. K. Sood, G. Lopez-Berestein, C. Rinaldi and M. Torres-Lugo (2011). "Hyperthermia Induced by Magnetic Nanoparticles Improves the Effectiveness of the Anticancer Drug cis-Diamminedichloroplatinum." Journal of Nanoscience and Nanotechnology **11**(5): 4153-4157.
- Lee, Y., J. Lee, C. J. Bae, J. G. Park, H. J. Noh, J. H. Park and T. Hyeon (2005). "Large-scale synthesis of uniform and crystalline magnetite nanoparticles using reverse micelles as nanoreactors under reflux conditions." Advanced Functional Materials **15**(3): 503-509.
- Lee, Y. T., K. Woo and K. S. Choi (2008). "Preparation of water-dispersible and biocompatible iron oxide nanoparticles for MRI agent." Ieee Transactions on Nanotechnology **7**(2): 111-114.
- Lewin, M., N. Carlesso, C. H. Tung, X. W. Tang, D. Cory, D. T. Scadden and R. Weissleder (2000). "Tat peptide-derivatized magnetic nanoparticles allow in vivo tracking and recovery of progenitor cells." Nature Biotechnology **18**(4): 410-414.
- Lewinski, N., V. Colvin and R. Drezek (2008). "Cytotoxicity of nanoparticles." Small **4**(1): 26-49.
- Li, H., K. Yan, Y. L. Shang, L. Shrestha, R. F. Liao, F. Liu, P. H. Li, H. B. Xu, Z. S. Xu and P. K. Chu (2015). "Folate-bovine serum albumin functionalized polymeric micelles loaded with superparamagnetic iron oxide nanoparticles for tumor targeting and magnetic resonance imaging." Acta Biomaterialia **15**: 117-126.
- Li, T., H. E. Gendelman, G. Zhang, P. Puligujja, J. M. McMillan, T. K. Bronich, B. Edagwa, X. M. Liu and M. D. Boska (2015). "Magnetic resonance imaging of folic acid-coated magnetite nanoparticles reflects tissue biodistribution of long-acting antiretroviral therapy." International Journal of Nanomedicine **10**: 3779-3790.
- Li, T. J., C. C. Huang, P. W. Ruan, K. Y. Chuang, K. J. Huang, D. B. Shieh and C. S. Yeh (2013). "In vivo anti-cancer efficacy of magnetite nanocrystal-based system using locoregional hyperthermia combined with 5-fluorouracil chemotherapy." Biomaterials **34**(32): 7873-7883.
- Li, Y. H., G. Y. Huang, X. H. Zhang, B. Q. Li, Y. M. Chen, T. L. Lu, T. J. Lu and F. Xu (2013). "Magnetic Hydrogels and Their Potential Biomedical Applications." Advanced Functional Materials **23**(6): 660-672.
- Li, Y. J., M. Dong, F. M. Kong and J. P. Zhou (2015). "Folate-decorated anticancer drug and magnetic nanoparticles encapsulated polymeric carrier for liver cancer therapeutics." International Journal of Pharmaceutics **489**(1-2): 83-90.

- Li, Z., K. Dong, S. Huang, E. Ju, Z. Liu, M. Yin, J. Ren and X. Qu (2014). "A Smart Nanoassembly for Multistage Targeted Drug Delivery and Magnetic Resonance Imaging." Advanced Functional Materials **24**(23): 3612-3620.
- Li, Z. F., T. Yang, C. M. Lin, Q. S. Li, S. F. Liu, F. Z. Xu, H. Y. Wang and X. J. Cui (2015). "Sonochemical Synthesis of Hydrophilic Drug Loaded Multifunctional Bovine Serum Albumin Nanocapsules." Acs Applied Materials & Interfaces **7**(34): 19390-19397.
- Lin, M. M., Y. J. Kang, Y. Sohn and D. K. Kim (2015). "Dual targeting strategy of magnetic nanoparticle-loaded and RGD peptide-activated stimuli-sensitive polymeric micelles for delivery of paclitaxel." Journal of Nanoparticle Research **17**(6).
- Lin, R.-Y., K. Dayananda, T.-J. Chen, C.-Y. Chen, G.-C. Liu, K.-L. Lin and Y.-M. Wang (2012). "Targeted RGD nanoparticles for highly sensitive in vivo integrin receptor imaging." Contrast Media & Molecular Imaging **7**(1): 7-18.
- Linder, S. T., H. Erdal, M. Berndtsson and M. Shoshan (2005). "Induction of lysosomal membrane permeabilization by compounds that activate p53-independent apoptosis." Proceedings of the American Association for Cancer Research Annual Meeting **46**: 1171-1171.
- Liu, T. Y., S. H. Hu, D. M. Liu, S. Y. Chen and I. W. Chen (2009). "Biomedical nanoparticle carriers with combined thermal and magnetic responses." Nano Today **4**(1): 52-65.
- Low, P. S., W. A. Henne and D. D. Doorneweerd (2008). "Discovery and development of folic-acid-based receptor targeting for Imaging and therapy of cancer and inflammatory diseases." Accounts of Chemical Research **41**(1): 120-129.
- Luo, C., Y. Li, L. Yang, X. Wang, J. Long and J. Liu (2015). "Superparamagnetic iron oxide nanoparticles exacerbate the risks of reactive oxygen species-mediated external stresses." Archives of Toxicology **89**(3): 357-369.
- Luo, Y., J. Yang, Y. Yan, J. Li, M. Shen, G. Zhang, S. Mignani and X. Shi (2015). "RGD-functionalized ultrasmall iron oxide nanoparticles for targeted T1-weighted MR imaging of gliomas." Nanoscale **7**(34): 14538-14546.
- Ly, J. D., D. R. Grubb and A. Lawen (2003). "The mitochondrial membrane potential ( $\Delta\psi$ ) in apoptosis; an update." Apoptosis **8**(2): 115-128.
- Ma, D.-X., N.-Q. Shi and X.-R. Qi (2011). "Distinct transduction modes of arginine-rich cell-penetrating peptides for cargo delivery into tumor cells." International Journal of Pharmaceutics **419**(1-2): 200-208.
- Ma, Z. Y., Y. P. Liu, L. Y. Bai, J. An, L. Zhang, Y. Xuan, X. S. Zhang and Y. D. Zhao (2015). "Folic acid-targeted magnetic Tb-doped CeF<sub>3</sub> fluorescent nanoparticles as bimodal probes for cellular fluorescence and magnetic resonance imaging." Dalton Transactions **44**(37): 16304-16312.
- Maharramov, A. M., M. A. Ramazanov, A. I. Ahadova, M. Kloor, J. Kopitz, M. v. K. Doeberitz, A. L. Shabanov, Q. M. Eyvazova, Z. A. Agamaliyev, F. V. Hajiyeva, S. B. Veliyeva and U. A. Hasanova (2014). "PREPARATION OF 2-DEOXY-D-GLUCOSE COATED SPIO NANOPARTICLES AND CHARACTERIZATION OF THEIR PHYSICAL, CHEMICAL, AND

BIOLOGICAL PROPERTIES." Digest Journal of Nanomaterials and Biostructures **9**(4): 1461-1469.

Mahmoudi, M., A. Simchi, A. S. Milani and P. Stroeve (2009). "Cell toxicity of superparamagnetic iron oxide nanoparticles." Journal of Colloid and Interface Science **336**(2): 510-518.

Maier-Hauff, K., R. Rothe, R. Scholz, U. Gneveckow, P. Wust, B. Thiesen, A. Feussner, A. von Deimling, N. Waldoefner, R. Felix and A. Jordan (2007). "Intracranial thermotherapy using magnetic nanoparticles combined with external beam radiotherapy: Results of a feasibility study on patients with glioblastoma multiforme." Journal of Neuro-Oncology **81**(1): 53-60.

Maier-Hauff, K., F. Ulrich, D. Nestler, H. Niehoff, P. Wust, B. Thiesen, H. Orawa, V. Budach and A. Jordan (2011). "Efficacy and safety of intratumoral thermotherapy using magnetic iron-oxide nanoparticles combined with external beam radiotherapy on patients with recurrent glioblastoma multiforme." Journal of Neuro-Oncology **103**(2): 317-324.

Mansoori, G. A., K. S. Brandenburg and A. Shakeri-Zadeh (2010). "A comparative study of two folate-conjugated gold nanoparticles for cancer nanotechnology applications." Cancers **2**(4): 1911-1928.

Massart, R. (1981). "PREPARATION OF AQUEOUS MAGNETIC LIQUIDS IN ALKALINE AND ACIDIC MEDIA." Ieee Transactions on Magnetics **17**(2): 1247-1248.

Mattix, B., T. R. Olsen, Y. Gu, M. Casco, A. Herbst, D. T. Simionescu, R. P. Visconti, K. G. Kornev and F. Alexis (2014). "Biological magnetic cellular spheroids as building blocks for tissue engineering." Acta Biomaterialia **10**(2): 623-629.

McCarthy, J. R. and R. Weissleder (2008). "Multifunctional magnetic nanoparticles for targeted imaging and therapy." Advanced Drug Delivery Reviews **60**(11): 1241-1251.

McCormack, P. L. (2012). "Ferumoxytol In Iron Deficiency Anaemia in Adults With Chronic Kidney Disease." Drugs **72**(15): 2013-2022.

Medarova, Z., L. Rashkovetsky, P. Pantazopoulos and A. Moore (2009). "Multiparametric Monitoring of Tumor Response to Chemotherapy by Noninvasive Imaging." Cancer Research **69**(3): 1182-1189.

Melemenidis, S., A. Jefferson, N. Ruparelia, A. M. Akhtar, J. Xie, D. Allen, A. Hamilton, J. R. Larkin, F. Perez-Balderas, S. C. Smart, R. J. Muschel, X. Chen, N. R. Sibson and R. P. Choudhury (2015). "Molecular Magnetic Resonance Imaging of Angiogenesis In Vivo using Polyvalent Cyclic RGD-Iron Oxide Microparticle Conjugates." Theranostics **5**(5): 515-529.

Meng, H. M., L. M. Lu, X. H. Zhao, Z. Chen, Z. L. Zhao, C. Yang, X. B. Zhang and W. H. Tan (2015). "Multiple Functional Nanoprobe for Contrast-Enhanced Bimodal Cellular Imaging and Targeted Therapy." Analytical Chemistry **87**(8): 4448-4454.

Menichetti, L., L. Manzoni, L. Paduano, A. Flori, C. Kusmic, D. De Marchi, S. Casciaro, F. Conversano, M. Lombardi, V. Positano and D. Arosio (2013). "Iron Oxide-Gold Core-Shell Nanoparticles as Multimodal Imaging Contrast Agent." Ieee Sensors Journal **13**(6): 2341-2347.

- Meyn, R. E., P. M. Corry, S. E. Fletcher and M. Demetriades (1980). "THERMAL ENHANCEMENT OF DNA DAMAGE IN MAMMALIAN-CELLS TREATED WITH CIS-DIAMMINEDICHLOROPLATINUM(II)." Cancer Research **40**(4): 1136-1139.
- Minchinton, A. I. and I. F. Tannock (2006). "Drug penetration in solid tumours." Nature Reviews Cancer **6**(8): 583-592.
- Montenegro, J. M., V. Grazu, A. Sukhanova, S. Agarwal, J. M. de la Fuente, I. Nabiev, A. Greiner and W. J. Parak (2013). "Controlled antibody/(bio-) conjugation of inorganic nanoparticles for targeted delivery." Advanced Drug Delivery Reviews **65**(5): 677-688.
- Mornet, S., S. Vasseur, F. Grasset and E. Duguet (2004). "Magnetic nanoparticle design for medical diagnosis and therapy." Journal of Materials Chemistry **14**(14): 2161-2175.
- Moroz, P., S. K. Jones and B. N. Gray (2002). "Magnetically mediated hyperthermia: current status and future directions." International Journal of Hyperthermia **18**(4): 267-284.
- Mu, Q., F. M. Kievit, R. J. Kant, G. Lin, M. Jeon and M. Zhang (2015). "Anti-HER2/neu peptide-conjugated iron oxide nanoparticles for targeted delivery of paclitaxel to breast cancer cells." Nanoscale **7**(43): 18010-18014.
- Mueller-Klieser, W., P. Vaupel, S. Walenta, F. Kallinowski and W. Paschen (1987). "IDENTIFICATION OF HETEROGENEOUS SUBSTRATE DISTRIBUTIONS IN TUMORS AND TUMOR SPHEROIDS USING BIOLUMINESCENCE." Pfluegers Archiv European Journal of Physiology **408**(SUPPL. 1): R84-R84.
- Murbe, J., A. Rechtenbach and J. Topfer (2008). "Synthesis and physical characterization of magnetite nanoparticles for biomedical applications." Materials Chemistry and Physics **110**(2-3): 426-433.
- Murthy, S. K. (2007). "Nanoparticles in modern medicine: State of the art and future challenges." International Journal of Nanomedicine **2**(2): 129-141.
- Mustafa, T., Y. Zhang, F. Watanabe, A. Karmakar, M. P. Asar, R. Little, M. K. Hudson, Y. Xu and A. S. Biris (2013). "Iron oxide nanoparticle-based radio-frequency thermotherapy for human breast adenocarcinoma cancer cells." Biomaterials Science **1**(8): 870-880.
- Nair, B. G., T. Fukuda, T. Mizuki, T. Hanajiri and T. Maekawa (2012). "Intracellular trafficking of superparamagnetic iron oxide nanoparticles conjugated with TAT peptide: 3-dimensional electron tomography analysis." Biochemical and Biophysical Research Communications **421**(4): 763-767.
- Neshasteh-Riz, A., R. Rahdani and A. Mostaar (2014). "Evaluation of The Combined Effects of Hyperthermia, Cobalt-60 Gamma Rays and IUdR on Cultured Glioblastoma Spheroid Cells and Dosimetry Using TLD-100." Cell Journal **16**(3): 335-342.
- Nirmalanandhan, V. S., A. Duren, P. Hendricks, G. Vielhauer and G. S. Sittampalam (2010). "Activity of Anticancer Agents in a Three-Dimensional Cell Culture Model." Assay and Drug Development Technologies **8**(5): 581-590.

Ogawara, K., M. Yoshida, K. Higaki, T. Kimura, K. Shiraishi, M. Nishikawa, Y. Takakura and M. Hashida (1999). "Hepatic uptake of polystyrene microspheres in rats: Effect of particle size on intrahepatic distribution." Journal of Controlled Release **59**(1): 15-22.

Ohno, S., Z. H. Siddik, Y. Kido, L. A. Zwielling and J. M. C. Bull (1994). "THERMAL ENHANCEMENT OF DRUG UPTAKE AND DNA-ADDUCTS AS A POSSIBLE MECHANISM FOR THE EFFECT OF SEQUENCING HYPERTHERMIA ON CISPLATIN-INDUCED CYTOTOXICITY IN L1210 CELLS." Cancer Chemotherapy and Pharmacology **34**(4): 302-306.

Osaka, T., T. Nakanishi, S. Shanmugam, S. Takahama and H. Zhang (2009). "Effect of surface charge of magnetite nanoparticles on their internalization into breast cancer and umbilical vein endothelial cells." Colloids and Surfaces B-Biointerfaces **71**(2): 325-330.

Overgaard, J. and O. S. Nielsen (1980). "The role of tissue environmental factors on the kinetics and morphology of tumor cells exposed to hyperthermia." Annals of the New York Academy of Sciences **335**: 254-280.

Oyelere, A. K., P. C. Chen, X. Huang, I. H. El-Sayed and M. A. El-Sayed (2007). "Peptide-conjugated gold nanorods for nuclear targeting." Bioconjugate Chemistry **18**(5): 1490-1497.

Palmacci, S. and L. Josephson (1993). Synthesis of polysaccharide covered superparamagnetic oxide colloids. United States, Advanced Magnetics, Inc.

Pan, L. M., Q. J. He, J. N. Liu, Y. Chen, M. Ma, L. L. Zhang and J. L. Shi (2012). "Nuclear-Targeted Drug Delivery of TAT Peptide-Conjugated Monodisperse Mesoporous Silica Nanoparticles." Journal of the American Chemical Society **134**(13): 5722-5725.

Pankhurst, Q. A., J. Connolly, S. K. Jones and J. Dobson (2003). "Applications of magnetic nanoparticles in biomedicine." Journal of Physics D-Applied Physics **36**(13): R167-R181.

Pankhurst, Q. A., N. T. K. Thanh, S. K. Jones and J. Dobson (2009). "Progress in applications of magnetic nanoparticles in biomedicine." Journal of Physics D-Applied Physics **42**(22).

Pankhurst, Q. A., N. T. K. Thanh, S. K. Jones and J. Dobson (2009). "Progress in applications of magnetic nanoparticles in biomedicine." Journal of Physics D-Applied Physics **42**(22): 15.

Pardoe, H., W. Chua-anusorn, T. G. St Pierre and J. Dobson (2001). "Structural and magnetic properties of nanoscale iron oxide particles synthesized in the presence of dextran or polyvinyl alcohol." Journal of Magnetism and Magnetic Materials **225**(1-2): 41-46.

Park, E.-J., H. N. Umh, D.-H. Choi, M. H. Cho, W. Choi, S.-W. Kim, Y. Kim and J.-H. Kim (2014). "Magnetite- and maghemite-induced different toxicity in murine alveolar macrophage cells." Archives of Toxicology **88**(8): 1607-1618.

Park, J.-H., G. Von Malzahn, L. Zhang, M. P. Schwartz, E. Ruoslahti, S. N. Bhatia and M. J. Sailor (2008). "Magnetic iron oxide nanoworms for tumor targeting and imaging." Advanced Materials **20**: 1630-1635.



- Park, J., K. J. An, Y. S. Hwang, J. G. Park, H. J. Noh, J. Y. Kim, J. H. Park, N. M. Hwang and T. Hyeon (2004). "Ultra-large-scale syntheses of monodisperse nanocrystals." Nature Materials **3**(12): 891-895.
- Park, J. Y., H. Y. Jeong, M. I. Kim and T. J. Park (2015). "Colorimetric Detection System for Salmonella typhimurium Based on Peroxidase-Like Activity of Magnetic Nanoparticles with DNA Aptamers." Journal of Nanomaterials: 9.
- Parker, N., M. J. Turk, E. Westrick, J. D. Lewis, P. S. Low and C. P. Leamon (2005). "Folate receptor expression in carcinomas and normal tissues determined by a quantitative radioligand binding assay." Analytical Biochemistry **338**(2): 284-293.
- Passemard, S., D. Staedler, L. Ucnova, G. S. Schneiter, P. Kong, L. Bonacina, L. Juillerat-Jeanneret and S. Gerber-Lemaire (2013). "Convenient synthesis of heterobifunctional poly(ethylene glycol) suitable for the functionalization of iron oxide nanoparticles for biomedical applications." Bioorganic & Medicinal Chemistry Letters **23**(17): 5006-5010.
- Petryk, A. A., A. J. Giustini, R. E. Gottesman, P. A. Kaufman and P. J. Hoopes (2013). "Magnetic nanoparticle hyperthermia enhancement of cisplatin chemotherapy cancer treatment." International Journal of Hyperthermia **29**(8): 845-851.
- Petters, C., F. Bulcke, K. Thiel, U. Bickmeyer and R. Dringen (2014). "Uptake of Fluorescent Iron Oxide Nanoparticles by Oligodendroglial OLN-93 Cells." Neurochemical Research **39**(2): 372-383.
- Phillips, M. A., M. L. Gran and N. A. Peppas (2010). "Targeted nanodelivery of drugs and diagnostics." Nano Today **5**(2): 143-159.
- Pierrat, S., I. Zins, A. Breivogel and C. Soennichsen (2007). "Self-assembly of small gold colloids with functionalized gold nanorods." Nano Letters **7**(2): 259-263.
- Plouffe, B. D., S. K. Murthy and L. H. Lewis (2015). "Fundamentals and application of magnetic particles in cell isolation and enrichment: a review." Reports on Progress in Physics **78**(1).
- Polo-Corrales, L. and C. Rinaldi (2012). "Monitoring iron oxide nanoparticle surface temperature in an alternating magnetic field using thermoresponsive fluorescent polymers." Journal of Applied Physics **111**(7).
- Qiao, R. R., C. H. Yang and M. Y. Gao (2009). "Superparamagnetic iron oxide nanoparticles: from preparations to in vivo MRI applications." Journal of Materials Chemistry **19**(35): 6274-6293.
- Rabin, Y. (2002). "Is intracellular hyperthermia superior to extracellular hyperthermia in the thermal sense?" International Journal of Hyperthermia **18**(3): 194-202.
- Rao, K. S., M. K. Reddy, J. L. Horning and V. Labhsetwar (2008). "TAT-conjugated nanoparticles for the CNS delivery of anti-HIV drugs." Biomaterials **29**(33): 4429-4438.
- Razjouyan, J., H. Zolata, O. Khayat, F. Nowshiravan, N. Shadanpour and M. Mohammadnia (2015). "Synthesis and evaluation of radiolabeled, folic acid-PEG conjugated, amino silane coated magnetic nanoparticles in tumor bearing Balb/C mice." Nukleonika **60**(3): 497-502.

Reimer, P. and T. Balzer (2003). "Ferucarbotran (Resovist): a new clinically approved RES-specific contrast agent for contrast-enhanced MRI of the liver: properties, clinical development, and applications." European Radiology **13**(6): 1266-1276.

Rejinold, N. S., R. Jayakumar and Y.-C. Kim (2015). "Radio frequency responsive nanobiomaterials for cancer therapy." Journal of Controlled Release **204**(0): 85-97.

Ridi, F., M. Bonini and P. Baglioni (2014). "Magneto-responsive nanocomposites: Preparation and integration of magnetic nanoparticles into films, capsules, and gels." Advances in Colloid and Interface Science **207**: 3-13.

Rivet, C. J., Y. Yuan, R. J. Gilbert and D.-A. Borca-Tasciuc (2014). "Effect of magnetic nanoparticle heating on cortical neuron viability." International Journal of Hyperthermia **30**(2): 79-85.

Rodriguez-Luccioni, H. L., M. Latorre-Esteves, J. Mendez-Vega, O. Soto, A. R. Rodriguez, C. Rinaldi and M. Torres-Lugo (2011). "Enhanced reduction in cell viability by hyperthermia induced by magnetic nanoparticles." International Journal of Nanomedicine **6**: 373-380.

Rosen, J. E., L. Chan, D.-B. Shieh and F. X. Gu (2012). "Iron oxide nanoparticles for targeted cancer imaging and diagnostics." Nanomedicine-Nanotechnology Biology and Medicine **8**(3): 275-290.

Roy, K., R. K. Kanwar and J. R. Kanwar (2015). "LNA aptamer based multi-modal, Fe<sub>3</sub>O<sub>4</sub>-saturated lactoferrin (Fe<sub>3</sub>O<sub>4</sub>-bLf) nanocarriers for triple positive (EpCAM, CD133, CD44) colon tumor targeting and NIR, MRI and CT imaging." Biomaterials **71**: 84-99.

Ruoslahti, E., S. N. Bhatia and M. J. Sailor (2010). "Targeting of drugs and nanoparticles to tumors." JCB: Review **188**(6): 759-768.

Sadhasivam, S., S. Savitha, C. J. Wu, F. H. Lin and L. Stobinski (2015). "Carbon encapsulated iron oxide nanoparticles surface engineered with polyethylene glycol-folic acid to induce selective hyperthermia in folate over expressed cancer cells." International Journal of Pharmaceutics **480**(1-2): 8-14.

Sanchez, C., D. E. H. Diab, V. Connord, P. Clerc, E. Meunier, B. Pipy, B. Payre, R. P. Tan, M. Gougeon, J. Carrey, V. Gigoux and D. Fourmy (2014). "Targeting a G-Protein-Coupled Receptor Overexpressed in Endocrine Tumors by Magnetic Nanoparticles To Induce Cell Death." Acs Nano **8**(2): 1350-1363.

Sapareto, S. A., G. P. Raaphorst and W. C. Dewey (1979). "CELL KILLING AND THE SEQUENCING OF HYPERTHERMIA AND RADIATION." International Journal of Radiation Oncology Biology Physics **5**(3): 343-347.

Saraswathy, A., S. S. Nazeer, M. Jeevan, N. Nimi, S. Arumugam, V. S. Hari Krishnan, P. R. H. Varma and R. S. Jayasree (2014). "Citrate coated iron oxide nanoparticles with enhanced relaxivity for in vivo magnetic resonance imaging of liver fibrosis." Colloids and Surfaces B-Biointerfaces **117**: 216-224.

- Saraswathy, A., S. S. Nazeer, N. Nimi, S. Arumugam, S. J. Shenoy and R. S. Jayasree (2014). "Synthesis and characterization of dextran stabilized superparamagnetic iron oxide nanoparticles for in vivo MR imaging of liver fibrosis." Carbohydrate Polymers **101**: 760-768.
- Satarkar, N. S., D. Biswal and J. Z. Hilt (2010). "Hydrogel nanocomposites: a review of applications as remote controlled biomaterials." Soft Matter **6**(11): 2364-2371.
- Sawdon, A., E. Weydemeyer and C.-A. Peng (2014). "Antitumor Therapy Using Nanomaterial-Mediated Thermolysis." Journal of Biomedical Nanotechnology **10**(9): 1894-1917.
- Schleich, N., F. Danhier and V. Preat (2015). "Iron oxide-loaded nanotheranostics: Major obstacles to in vivo studies and clinical translation." Journal of Controlled Release **198**: 35-54.
- Schleich, N., C. Po, D. Jacobs, B. Ucakar, B. Gallez, F. Danhier and V. Preat (2014). "Comparison of active, passive and magnetic targeting to tumors of multifunctional paclitaxel/SPIO-loaded nanoparticles for tumor imaging and therapy." Journal of Controlled Release **194**: 82-91.
- Senavirathna, L. K., R. Fernando, D. Maples, Y. Zheng, J. C. Polf and A. Ranjan (2013). "Tumor Spheroids as an In Vitro Model for Determining the Therapeutic Response to Proton Beam Radiotherapy and Thermally Sensitive Nanocarriers." Theranostics **3**(9): 687-691.
- Shan, X. H., H. Hu, F. Xiong, N. Gu, X. D. Geng, W. Zhu, J. Lin and Y. F. Wang (2012). "Targeting Glut1-overexpressing MDA-MB-231 cells with 2-deoxy-d-glucose modified SPIOs." European Journal of Radiology **81**(1): 95-99.
- Shanehsazzadeh, S., C. Gruettner, A. Lahooti, M. Mahmoudi, B. J. Allen, M. Ghavami, F. J. Daha and M. A. Oghabian (2015). "Monoclonal antibody conjugated magnetic nanoparticles could target MUC-1-positive cells in vitro but not in vivo." Contrast Media & Molecular Imaging **10**(3): 225-236.
- Sharapova, V. A., M. A. Uimin, A. A. Mysik and A. E. Ermakov (2010). "Heat Release in Magnetic Nanoparticles in AC Magnetic Fields." Physics of Metals and Metallography **110**(1): 5-12.
- Shinkai, M., M. Yanase, M. Suzuki, H. Honda, T. Wakabayashi, J. Yoshida and T. Kobayashi (1999). "Intracellular hyperthermia for cancer using magnetite cationic liposomes." Journal of Magnetism and Magnetic Materials **194**(1-3): 176-184.
- Shubayev, V. I., T. R. Pisanic and S. H. Jin (2009). "Magnetic nanoparticles for theragnostics." Advanced Drug Delivery Reviews **61**(6): 467-477.
- Simberg, D., T. Duza, J. H. Park, M. Essler, J. Pilch, L. Zhang, A. M. Derfus, M. Yang, R. M. Hoffman, S. N. Bhatia, M. J. Sailor and E. Ruoslahti (2007). "Biomimetic amplification of nanoparticle homing to tumors." Proceedings of the National Academy of Sciences **104**(3): 932-936.
- Singh, A. and S. K. Sahoo (2014). "Magnetic nanoparticles: a novel platform for cancer theragnostics." Drug Discovery Today **19**(4): 474-481.
- Singh, D., J. M. McMillan, A. V. Kabanov, M. Sokolsky-Papkov and H. E. Gendelman (2014). "Bench-to bedside translation of magnetic nanoparticles." Nanomedicine **9**(4): 501-516.

Socaci, C., L. Magerusan, R. Turcu and J. Liebscher (2015). "Developing novel strategies for the functionalization of core-shell magnetic nanoparticles with folic acid derivatives." Materials Chemistry and Physics **162**: 131-139.

Song, Y., Z. Huang, J. Xu, D. Ren, Y. Wang, X. Zheng, Y. Shen, L. Wang, H. Gao, J. Hou, Z. Pang, J. Qian and J. Ge (2014). "Multimodal SPION-CREKA peptide based agents for molecular imaging of microthrombus in a rat myocardial ischemia-reperfusion model." Biomaterials **35**(9): 2961-2970.

Soni, S., H. Tyagi, R. A. Taylor and A. Kumar (2014). "Investigation on nanoparticle distribution for thermal ablation of a tumour subjected to nanoparticle assisted thermal therapy." Journal of Thermal Biology **43**: 70-80.

Sreeja, V. and P. A. Joy (2011). "Effect of inter-particle interactions on the magnetic properties of magnetite nanoparticles after coating with dextran." International Journal of Nanotechnology **8**(10-12): 907-915.

Stephen Palmacci, L. J. (1993). Synthesis of polysaccharide covered superparamagnetic oxide colloids. A. Magnetics. United States. **5,262,176**.

Stephen, Z. R., F. M. Kievit, O. Veiseh, P. A. Chiarelli, C. Fang, K. Wang, S. J. Hatzinger, R. G. Ellenbogen, J. R. Silber and M. Q. Zhang (2014). "Redox-Responsive Magnetic Nanoparticle for Targeted Convection-Enhanced Delivery of O-6-Benzylguanine to Brain Tumors." Acs Nano **8**(10): 10383-10395.

Sun, C., K. Du, C. Fang, N. Bhattarai, O. Veiseh, F. Kievit, Z. Stephen, D. Lee, R. G. Ellenbogen, B. Ratner and M. Zhang (2010). "PEG-Mediated Synthesis of Highly Dispersive Multifunctional Superparamagnetic Nanoparticles: Their Physicochemical Properties and Function In Vivo." Acs Nano **4**(4): 2402-2410.

Sun, D., J. Lu, Y. Zhong, Y. Yu, Y. Wang, B. Zhang and Z. Chen (2016). "Sensitive electrochemical aptamer cytosensor for highly specific detection of cancer cells based on the hybrid nanoelectrocatalysts and enzyme for signal amplification." Biosensors & Bioelectronics **75**: 301-307.

Sun, S. H., H. Zeng, D. B. Robinson, S. Raoux, P. M. Rice, S. X. Wang and G. X. Li (2004). "Monodisperse MFe<sub>2</sub>O<sub>4</sub> (M = Fe, Co, Mn) nanoparticles." Journal of the American Chemical Society **126**(1): 273-279.

Suto, M., Y. Hirota, H. Mamiya, A. Fujita, R. Kasuya, K. Tohji and B. Jeyadevan (2009). "Heat dissipation mechanism of magnetite nanoparticles in magnetic fluid hyperthermia." Journal of Magnetism and Magnetic Materials **321**(10): 1493-1496.

Suzuki, M., M. Shinkai, H. Honda and T. Kobayashi (2003). "Anticancer effect and immune induction by hyperthermia of malignant melanoma using magnetite cationic liposomes." Melanoma Research **13**(2): 129-135.

Takahashi, I., Y. Emi, S. Hasuda, Y. Kakeji, Y. Maehara and K. Sugimachi (2002). "Clinical application of hyperthermia combined with anticancer drugs for the treatment of solid tumors." Surgery **131**(1): S78-S84.

Tarn, D., C. E. Ashley, M. Xue, E. C. Carnes, J. I. Zink and C. J. Brinker (2013). "Mesoporous Silica Nanoparticle Nanocarriers: Biofunctionality and Biocompatibility." Accounts of Chemical Research **46**(3): 792-801.

Tartaj, P., M. D. Morales, S. Veintemillas-Verdaguer, T. Gonzalez-Carreno and C. J. Serna (2003). "The preparation of magnetic nanoparticles for applications in biomedicine." Journal of Physics D-Applied Physics **36**(13): R182-R197.

Tassa, C., S. Y. Shaw and R. Weissleder (2011). "Dextran-Coated Iron Oxide Nanoparticles: A Versatile Platform for Targeted Molecular Imaging, Molecular Diagnostic, and Therapy." Accounts of Chemical Research **44**(10): 842-852.

Terman, A., T. Kurz, B. Gustafsson and U. T. Brunk (2006). "Lysosomal labilization." Iubmb Life **58**(9): 531-539.

Thevenot, J., H. Oliveira, O. Sandre and S. Lecommandoux (2013). "Magnetic responsive polymer composite materials." Chemical Society Reviews **42**(17): 7099-7116.

Thorek, D. L. J. and A. Tsourkas (2008). "Size, charge and concentration dependent uptake of iron oxide particles by non-phagocytic cells." Biomaterials **29**(26): 3583-3590.

Toraya-Brown, S., M. R. Sheen, P. Zhang, L. Chen, J. R. Baird, E. Demidenko, M. J. Turk, P. J. Hoopes, J. R. Conejo-Garcia and S. Fiering (2014). "Local hyperthermia treatment of tumors induces CD8(+) T cell-mediated resistance against distal and secondary tumors." Nanomedicine-Nanotechnology Biology and Medicine **10**(6): 1273-1285.

Torchilin, V. P. (2008). "Tat peptide-mediated intracellular delivery of pharmaceutical nanocarriers." Advanced Drug Delivery Reviews **60**(4-5): 548-558.

Trachootham, D., Y. Zhou, H. Zhang, Y. Demizu, Z. Chen, H. Pelicano, P. J. Chiao, G. Achanta, R. B. Arlinghaus, J. Liu and P. Huang (2006). "Selective killing of oncogenically transformed cells through a ROS-mediated mechanism by beta-phenylethyl isothiocyanate." Cancer Cell **10**(3): 241-252.

Tse, B. W. C., G. J. Cowin, C. Soekmadji, L. Jovanovic, R. S. Vasireddy, M. T. Ling, A. Khatri, T. Q. Liu, B. Thierry and P. J. Russell (2015). "PSMA-targeting iron oxide magnetic nanoparticles enhance MRI of preclinical prostate cancer." Nanomedicine **10**(3): 375-386.

Tucek, J., R. Zboril and D. Petridis (2006). "Maghemite nanoparticles by view of Mossbauer spectroscopy." Journal of Nanoscience and Nanotechnology **6**(4): 926-947.

Tudisco, C., M. T. Cambria, F. Sinatra, F. Bertani, A. Alba, A. E. Giuffrida, S. Saccone, E. Fantechi, C. Innocenti, C. Sangregorio, E. Dalcanale and G. G. Condorelli (2015). "Multifunctional magnetic nanoparticles for enhanced intracellular drug transport." Journal of Materials Chemistry B **3**(20): 4134-4145.

Turcheniuk, K., A. V. Tarasevych, V. P. Kukhar, R. Boukherroub and S. Szunerits (2013). "Recent advances in surface chemistry strategies for the fabrication of functional iron oxide based magnetic nanoparticles." Nanoscale **5**(22): 10729-10752.

- Urano, M., M. Kuroda and Y. Nishimura (1999). "For the clinical application of thermochemotherapy given at mild temperatures." International Journal of Hyperthermia **15**(2): 79-107.
- Vaupel, P., F. Kallinowski and P. Okunieff (1989). "BLOOD-FLOW, OXYGEN AND NUTRIENT SUPPLY, AND METABOLIC MICROENVIRONMENT OF HUMAN-TUMORS - A REVIEW." Cancer Research **49**(23): 6449-6465.
- Vayssieres, L., C. Chanecac, E. Tronc and J. P. Jolivet (1998). "Size tailoring of magnetite particles formed by aqueous precipitation: An example of thermodynamic stability of nanometric oxide particles." Journal of Colloid and Interface Science **205**(2): 205-212.
- Veiseh, O., J. W. Gunn and M. Q. Zhang (2010). "Design and fabrication of magnetic nanoparticles for targeted drug delivery and imaging." Advanced Drug Delivery Reviews **62**(3): 284-304.
- Veiseh, O., F. M. Kievit, C. Fang, N. Mu, S. Jana, M. C. Leung, H. Mok, R. G. Ellenbogen, J. O. Park and M. Zhang (2010). "Chlorotoxin bound magnetic nanovector tailored for cancer cell targeting, imaging, and siRNA delivery." Biomaterials **31**(31): 8032-8042.
- Vertrees, R. A., G. C. Das, V. L. Popov, A. M. Coscio, T. J. Goodwin, R. Logrono, J. B. Zwischenberger and P. J. Boor (2005). "Synergistic Interaction of Hyperthermia and Gemcitabine in Lung Cancer." Cancer Biology & Therapy **4**(10): 1144-1153.
- Villanueva, A., M. Canete, A. G. Roca, M. Calero, S. Veintemillas-Verdaguer, C. J. Serna, M. del Puerto Morales and R. Miranda (2009). "The influence of surface functionalization on the enhanced internalization of magnetic nanoparticles in cancer cells." Nanotechnology **20**(11).
- Vives, E., P. Brodin and B. Lebleu (1997). "A truncated HIV-1 Tat protein basic domain rapidly translocates through the plasma membrane and accumulates in the cell nucleus." Journal of Biological Chemistry **272**(25): 16010-16017.
- Voinov, M. A., J. O. S. Pagan, E. Morrison, T. I. Smirnova and A. I. Smirnov (2011). "Surface-Mediated Production of Hydroxyl Radicals as a Mechanism of Iron Oxide Nanoparticle Biototoxicity." Journal of the American Chemical Society **133**(1): 35-41.
- Walther, W. and U. Stein (2009). "Heat-responsive gene expression for gene therapy." Advanced Drug Delivery Reviews **61**(7-8): 641-649.
- Wang, C., J. Qian, K. Wang, X. Yang, Q. Liu, N. Hao, C. Wang, X. Dong and X. Huang (2016). "Colorimetric aptasensing of ochratoxin A using Au@Fe<sub>3</sub>O<sub>4</sub> nanoparticles as signal indicator and magnetic separator." Biosensors & bioelectronics **77**: 1183-1191.
- Wang, C., L. Qiao, Q. Zhang, H. Yan and K. Liu (2012). "Enhanced cell uptake of superparamagnetic iron oxide nanoparticles through direct chemisorption of FITC-Tat-PEG(600)-b-poly(glycerol monoacrylate)." International Journal of Pharmaceutics **430**(1-2): 372-380.
- Wang, G. H., D. R. Xu, Q. Chai, X. L. Tan, Y. Zhang, N. Gu and J. T. Tang (2014). "Magnetic fluid hyperthermia inhibits the growth of breast carcinoma and downregulates vascular endothelial growth factor expression." Oncology Letters **7**(5): 1370-1374.

Wang, J. and J. Yi (2008). "Cancer cell killing via ROS To increase or decrease, that is the question." Cancer Biology & Therapy **7**(12): 1875-1884.

Wang, L. F., J. Dong, W. W. Ouyang, X. W. Wang and J. T. Tang (2012). "Anticancer effect and feasibility study of hyperthermia treatment of pancreatic cancer using magnetic nanoparticles." Oncology Reports **27**(3): 719-726.

Wang, Q. B., J. F. Li, S. An, Y. Chen, C. Jiang and X. L. Wang (2015). "Magnetic resonance-guided regional gene delivery strategy using a tumor stroma-permeable nanocarrier for pancreatic cancer." International Journal of Nanomedicine **10**: 4479-4490.

Wei, Y., G. Yin, C. Ma, Z. Huang, X. Chen, X. Liao, Y. Yao and H. Yin (2013). "Synthesis and cellular compatibility of biomineralized Fe<sub>3</sub>O<sub>4</sub> nanoparticles in tumor cells targeting peptides." Colloids and Surfaces B-Biointerfaces **107**: 180-188.

Weissleder, R., D. D. Stark, B. L. Engelstad, B. R. Bacon, C. C. Compton, D. L. White, P. Jacobs and J. Lewis (1989). "SUPERPARAMAGNETIC IRON-OXIDE - PHARMACOKINETICS AND TOXICITY." American Journal of Roentgenology **152**(1): 167-173.

Wu, W., Z. H. Wu, T. Yu, C. Z. Jiang and W. S. Kim (2015). "Recent progress on magnetic iron oxide nanoparticles: synthesis, surface functional strategies and biomedical applications." Science and Technology of Advanced Materials **16**(2): 43.

Wust, P., B. Hildebrandt, G. Sreenivasa, B. Rau, J. Gellermann, H. Riess, R. Felix and P. M. Schlag (2002). "Hyperthermia in combined treatment of cancer." Lancet Oncology **3**(8): 487-497.

Wydra, R. J., A. M. Kruse, Y. Bae, K. W. Anderson and J. Z. Hilt (2013). "Synthesis and characterization of PEG-iron oxide core-shell composite nanoparticles for thermal therapy." Materials Science & Engineering C-Materials for Biological Applications **33**(8): 4660-4666.

Wydra, R. J., A. M. Kruse, Y. Bae, K. W. Anderson and J. Z. Hilt (2013). "Synthesis and characterization of PEG-iron oxide core-shell composite nanoparticles for thermal therapy." Materials Science and Engineering: C **33**(8): 4660-4666.

Wydra, R. J., C. E. Oliver, K. W. Anderson, T. D. Dziubla and J. Z. Hilt (2015). "Accelerated generation of free radicals by iron oxide nanoparticles in the presence of an alternating magnetic field." Rsc Advances **5**(24): 18888-18893.

Wydra, R. J., P. G. Rychahou, B. M. Evers, K. W. Anderson, T. D. Dziubla and J. Z. Hilt (2015). "The role of ROS generation from magnetic nanoparticles in an alternating magnetic field on cytotoxicity." Acta Biomaterialia **25**: 284-290.

Xi, Z. J., R. R. Huang, Z. Y. Li, N. Y. He, T. Wang, E. B. Su and Y. Deng (2015). "Selection of HBsAg-Specific DNA Aptamers Based on Carboxylated Magnetic Nanoparticles and Their Application in the Rapid and Simple Detection of Hepatitis B Virus Infection." Acs Applied Materials & Interfaces **7**(21): 11215-11223.

Xie, J., K. Chen, J. Huang, S. Lee, J. Wang, J. Gao, X. Li and X. Chen (2010). "PET/NIRF/MRI triple functional iron oxide nanoparticles." Biomaterials **31**(11): 3016-3022.

Xie, J., G. Liu, H. S. Eden, H. Ai and X. Chen (2011). "Surface-Engineered Magnetic Nanoparticle Platforms for Cancer Imaging and Therapy." Accounts of Chemical Research **44**(10): 883-892.

Xie, W. and X. Zang (2016). "Immobilized lipase on core-shell structured Fe<sub>3</sub>O<sub>4</sub>-MCM-41 nanocomposites as a magnetically recyclable biocatalyst for interesterification of soybean oil and lard." Food Chemistry **194**: 1283-1292.

Xiong, F., Z. Y. Zhu, C. Xiong, X. Q. Hua, X. H. Shan, Y. Zhang and N. Gu (2012). "Preparation, Characterization of 2-Deoxy-D-Glucose Functionalized Dimercaptosuccinic Acid-Coated Maghemite Nanoparticles for Targeting Tumor Cells." Pharmaceutical Research **29**(4): 1087-1097.

Xu, C., J. Xie, N. Kohler, E. G. Walsh, Y. E. Chin and S. Sun (2008). "Monodisperse magnetite nanoparticles coupled with nuclear localization signal peptide for cell-nucleus targeting." Chemistry-an Asian Journal **3**(3): 548-552.

Xu, X. Q., H. Shen, Xu, Jr., J. Xu, X. J. Li and X. M. Xiong (2005). "Core-shell structure and magnetic properties of magnetite magnetic fluids stabilized with dextran." Applied Surface Science **252**(2): 494-500.

Xu, Y., A. Karmakar, W. E. Heberlein, T. Mustafa, A. R. Biris and A. S. Biris (2012). "Multifunctional Magnetic Nanoparticles for Synergistic Enhancement of Cancer Treatment by Combinatorial Radio Frequency Thermolysis and Drug Delivery." Advanced Healthcare Materials **1**(4): 493-501.

Xu, Y., A. Karmakar, D. Y. Wang, M. W. Mahmood, F. Watanabe, Y. B. Zhang, A. Fejleh, P. Fejleh, Z. R. Li, G. Kannarpady, S. Ali, A. R. Biris and A. S. Biris (2010). "Multifunctional Fe<sub>3</sub>O<sub>4</sub> Cored Magnetic-Quantum Dot Fluorescent Nanocomposites for RF Nanohyperthermia of Cancer Cells." Journal of Physical Chemistry C **114**(11): 5020-5026.

Xue, S., C. Zhang, Y. Yang, L. Zhang, D. Cheng, J. Zhang, H. Shi and Y. Zhang (2015). "<sup>99m</sup>Tc-Labeled Iron Oxide Nanoparticles for Dual-Contrast (T-1/T-2) Magnetic Resonance and Dual-Modality Imaging of Tumor Angiogenesis." Journal of Biomedical Nanotechnology **11**(6): 1027-1037.

Yamamori, T., H. Yasui, M. Yamazumi, Y. Wada, Y. Nakamura, H. Nakamura and O. Inanami (2012). "Ionizing radiation induces mitochondrial reactive oxygen species production accompanied by upregulation of mitochondrial electron transport chain function and mitochondrial content under control of the cell cycle checkpoint." Free Radical Biology and Medicine **53**(2): 260-270.

Yamauchi, H., T. Asao, S. Yazawa, W. Kigure, H. Morita, T. Kobayashi, T. Kato, R. Yajima, Y. Tabe, S. Yamaki, T. Fukasawa, T. Fujii, S. Tsutsumi and H. Kuwano (2011). "Cell to Cell Interaction in Clusters Enhances Thermosensitivity in HT29 Human Colon Cancer Cells." Hepato-Gastroenterology **58**(112): 1958-1962.

Yanase, M., M. Shinkai, H. Honda, T. Wakabayashi, J. Yoshida and T. Kobayashi (1998). "Antitumor immunity induction by intracellular hyperthermia using magnetite cationic liposomes." Japanese Journal of Cancer Research **89**(7): 775-782.

Yang, C., M. Neshatian, M. van Prooijen and D. B. Chithrani (2014). "Cancer Nanotechnology: Enhanced Therapeutic Response Using Peptide-Modified Gold Nanoparticles." Journal of Nanoscience and Nanotechnology **14**(7): 4813-4819.



Yang, H., Y. Zhuang, Y. Sun, A. Dai, X. Shi, D. Wu, F. Li, H. Hu and S. Yang (2011). "Targeted dual-contrast T-1- and T-2-weighted magnetic resonance imaging of tumors using multifunctional gadolinium-labeled superparamagnetic iron oxide nanoparticles." Biomaterials **32**(20): 4584-4593.

Yin, C., B. B. Hong, Z. C. Gong, H. Zhao, W. B. Hu, X. M. Lu, J. Li, X. Li, Z. Yang, Q. L. Fan, Y. Y. Yao and W. Huang (2015). "Fluorescent oligo(p-phenyleneethynylene) contained amphiphiles-encapsulated magnetic nanoparticles for targeted magnetic resonance and two-photon optical imaging in vitro and in vivo." Nanoscale **7**(19): 8907-8919.

Yin, P. T., B. P. Shah and K.-B. Lee (2014). "Combined Magnetic Nanoparticle-based MicroRNA and Hyperthermia Therapy to Enhance Apoptosis in Brain Cancer Cells." Small **10**(20): 4106-4112.

Yoffe, S., T. Leshuk, P. Everett and F. Gu (2013). "Superparamagnetic Iron Oxide Nanoparticles (SPIONs): Synthesis and Surface Modification Techniques for use with MRI and Other Biomedical Applications." Current Pharmaceutical Design **19**(3): 493-509.

Yoo, D., H. Jeong, S. H. Noh, J. H. Lee and J. Cheon (2013). "Magnetically Triggered Dual Functional Nanoparticles for Resistance-Free Apoptotic Hyperthermia." Angewandte Chemie-International Edition **52**(49): 13047-13051.

Zaloga, J., C. Janko, J. Nowak, J. Matuszak, S. Knaup, D. Eberbeck, R. Tietze, H. Unterweger, R. P. Friedrich, S. Duerr, R. Heimke-Brinck, E. Baum, I. Cicha, F. Doerje, S. Odenbach, S. Lyer, G. Lee and C. Alexiou (2014). "Development of a lauric acid/albumin hybrid iron oxide nanoparticle system with improved biocompatibility." International Journal of Nanomedicine **9**: 4847-4866.

Zhang, C., M. Jugold, E. C. Woenne, T. Lammers, B. Morgenstern, M. M. Mueller, H. Zentgraf, M. Bock, M. Eisenhut, W. Semmler and F. Keissling (2007). "Specific targeting of tumor angiogenesis by RGD-conjugated ultrasmall superparamagnetic iron oxide particles using a clinical 1.5-T magnetic resonance scanner." Cancer Research **67**(4): 1555-1562.

Zhang, E., M. F. Kircher, M. Koch, L. Eliasson, S. N. Goldberg and E. Renstrom (2014). "Dynamic Magnetic Fields Remote-Control Apoptosis via Nanoparticle Rotation." Acs Nano **8**(4): 3192-3201.

Zhang, H., X. Ma, Y. Liu, N. Duan, S. Wu, Z. Wang and B. Xu (2015). "Gold nanoparticles enhanced SERS aptasensor for the simultaneous detection of Salmonella typhimurium and Staphylococcus aureus." Biosensors & Bioelectronics **74**: 872-877.

Zhao, M., F. Antunes, J. W. Eaton and U. T. Brunk (2003). "Lysosomal enzymes promote mitochondrial oxidant production, cytochrome c release and apoptosis." European Journal of Biochemistry **270**(18): 3778-3786.

Zhao, Z., D. Huang, Z. Yin, X. Chi, X. Wang and J. Gao (2012). "Magnetite nanoparticles as smart carriers to manipulate the cytotoxicity of anticancer drugs: magnetic control and pH-responsive release." Journal of Materials Chemistry **22**(31): 15717-15725.

Zwischenberger, J. B., R. A. Vertrees, E. A. Bedell, C. K. McQuitty, J. M. Chernin and L. C. Woodson (2004). "Percutaneous Venovenous Perfusion-Induced Systemic Hyperthermia for Lung Cancer: A Phase I Safety Study." Annals of Thoracic Surgery **77**: 1916-1925.

## Vita

### PERSONAL INFORMATION

Place of Birth: Louisville, Kentucky, United States of America

### EDUCATION

University of Kentucky, Lexington, KY, May 2012

BS. Chemical Engineering

### RESEARCH EXPERIENCE

NSF Graduate Research Fellow

September 2013-present

University of Kentucky, Lexington, KY

Advisors: Dr. Kimberly W. Anderson and Dr. J. Zach Hilt

NIH Cancer and Nanotechnology Trainee

September 2013 – September 2015

University of Kentucky, Lexington, KY

Advisors: Dr. Kimberly W. Anderson and Dr. J. Zach Hilt

NSF Integrative Graduate Education and Research Traineeship (IGERT) Fellow

May 2012 - August 2013

University of Kentucky, Lexington, KY

Advisors: Dr. Kimberly W. Anderson and Dr. J. Zach Hilt

NSF Research Experience for Undergraduates (REU), Research Assistant

May 2010 - May 2012

University of Kentucky, Lexington, KY

Advisors: Dr. Kimberly W. Anderson and Dr. J. Zach Hilt

Research Intern

May 2011 - August 2011

Alltech, Inc., Nicholasville, KY

Advisor: Dr. Stefan Kwiatkowski

### AWARDS/HONORS

Dean's Award for Outstanding PhD Student 2016

NSF Graduate Research Fellowship Program 2013 - 2016

Philanthropic Educational Organization (P.E.O.) Scholar Award 2014 - 2015

Student Travel Allowance Research (STAR) Award - Society for Biomaterials 2014

NIH Cancer and Nanotechnology Training Center Fellowship 2013 - 2016

NSF IGERT Graduate Fellowship 2012 - 2013

Dr. Jennifer S. and Mr. Jeffery N. Quinn Graduate Fellowship 2012 - 2015

Daniel R. Reedy Quality Achievement Fellowship 2012 - 2015

Maurice A. Clay Leadership Award 2012

Omega Chi Epsilon Outstanding Senior 2012

UK AIChE Outstanding Junior 2011

Oswald Research Award  
UK AIChE Outstanding Sophomore

2011  
2010

## PUBLICATIONS

Anastasia K. Hauser, Mihail I. Mitov, Emily F. Daley, Kimberly W. Anderson, J. Zach Hilt. *Targeted iron oxide nanoparticles for the enhancement of radiation therapy*. Biomaterials (in review).

Anastasia K. Hauser, Kimberly W. Anderson, J. Zach Hilt. *Peptide conjugated magnetic nanoparticles for magnetically mediated energy delivery to lung cancer cells*. Nanomedicine (in revision).

Anastasia K. Hauser, Robert J. Wydra, Rohit Bhandari, Piotr G. Rychahou, B. Mark Evers, Kimberly W. Anderson, Thomas D. Dziubla, and J. Zach Hilt. Corrigendum to *The Role of ROS Generation from Magnetic Nanoparticles in an Alternating Magnetic Field on Cytotoxicity*. Acta Biomaterialia 2015; 25:284-290

Anastasia K. Hauser, Robert J. Wydra, Nathanael A. Stocke, Kimberly W. Anderson, J. Zach Hilt. *Magnetic Nanoparticles and Nanocomposites for Remote Controlled Therapies*. America's Special Issue of the Journal of Controlled Release 2015; 219: 76-94

Anastasia K. Hauser, Ronita Mathias, Kimberly W. Anderson, J. Zach Hilt. *Effects of nanoparticle synthesis on the physical and chemical properties of dextran coated iron oxide nanoparticles*. Materials Chemistry and Physics 2015; 160:177-186.

Anastasia M. Kruse, Samantha A. Meenach, Kimberly W. Anderson, J. Zach Hilt. *Synthesis and Characterization of CREKA-conjugated Iron Oxide Nanoparticles for the Treatment of Cancer via Hyperthermia*. Acta Biomaterialia 2014; 10:2622-2629

Robert J. Wydra, Anastasia M. Kruse, Younsoo Bae, Kimberly W. Anderson, J. Zach Hilt. *Synthesis and Characterization of PEG-Iron Oxide Core-shell Composite Nanoparticles for Thermal Therapy Applications*. Materials Science and Engineering C: Materials for Biological Applications 2013; 33:4660-4666

## PRESENTATIONS

Anastasia K. Hauser, Emily F. Daley, J. Zach Hilt, Kimberly W. Anderson. *Radiation enhancement via ROS generation catalyzed by peptide-conjugated iron oxide nanoparticles*. American Institute of Chemical Engineers National Meeting, Salt Lake City, UT, November 12, 2015

Anastasia K. Hauser, Emily F. Daley, J. Zach Hilt, Kimberly W. Anderson. *Radiation enhancement via ROS generation catalyzed by iron oxide nanoparticles*. MACE Spring Symposium (Award Presentation), Lexington, KY, May 29th, 2015.

Anastasia K. Hauser, Samantha A. Meenach, J. Zach Hilt, Kimberly W. Anderson. *Development and Characterization of CREKA-Conjugated Iron Oxide Nanoparticles for Hyperthermia in Combination with Chemotherapy*. American Institute of Chemical Engineers National Meeting, Atlanta, GA, November 19, 2014

Anastasia K. Hauser, Samantha A. Meenach, J. Zach Hilt, Kimberly W. Anderson. *Development and Characterization of CREKA-Conjugated Iron Oxide Nanoparticles for Hyperthermia in Combination with Chemotherapy*. American Institute of Chemical Engineers National Meeting, Atlanta, GA, November 18, 2014

\*Awarded 2<sup>nd</sup> place in the Nanoscale Science and Engineering Graduate Student Award Session

Anastasia K. Hauser, J. Zach Hilt, Kimberly W. Anderson. *Development of CREKA-conjugated Iron Oxide Nanoparticles for the Treatment of Cancer via Hyperthermia*. UK Biomaterials Day, Lexington, KY, September 27, 2014

Anastasia M. Kruse, Samantha A. Meenach, J. Zach Hilt, Kimberly W. Anderson. *Synthesis and Characterization of CREKA-conjugated Iron Oxide Nanoparticles for the Treatment of Cancer via Hyperthermia*. AIChE National Conference, San Francisco, CA, November 8, 2013

Anastasia M. Kruse, Robert J. Wydra, J. Zach Hilt, Kimberly W. Anderson. *Biocompatibility Analysis and Cancer Therapy Application of Core-Shell Composite Magnetic Nanoparticles*. 2011 AIChE Southern Region Student Meeting, Atlanta, GA, April 1-3, 2011.

#### **Posters**

Anastasia K. Hauser, Emily F. Daley, J. Zach Hilt, Kimberly W. Anderson. *Radiation enhancement via ROS generation catalyzed by iron oxide nanoparticles*. Markey Cancer Research Day, Lexington, KY, May 28, 2015

Anastasia K. Hauser, J. Zach Hilt, Kimberly W. Anderson. *Development of CREKA-conjugated iron oxide nanoparticles for hyperthermia treatment of cancer*. Society for Biomaterials Annual Meeting, Charlotte, NC, April 16, 2015

Anastasia K. Hauser, J. Zach Hilt, Kimberly W. Anderson. *The effects of synthesis method on the physical and chemical properties of dextran coated iron oxide nanoparticles*. American Institute of Chemical Engineers National Meeting, Atlanta, GA, November 18, 2014

Anastasia K. Hauser, J. Zach Hilt, Kimberly W. Anderson. *Development of CREKA-conjugated iron oxide nanoparticles for hyperthermia treatment of cancer*. Kentucky Innovation and Entrepreneurship Conference, Louisville, KY, September 5, 2014

\*Awarded 2<sup>nd</sup> place

Anastasia M. Kruse, J. Zach Hilt, Kimberly W. Anderson. *Development of CREKA-conjugated Iron Oxide Nanoparticles for Hyperthermia Applications*. Markey Cancer Day, University of Kentucky, May 22, 2014

Anastasia M. Kruse, J. Zach Hilt, Kimberly W. Anderson. *Development of CREKA-conjugated Iron Oxide Nanoparticles for Hyperthermia Applications*. Graduate Student Poster Session, University of Kentucky, May 9, 2014

\*Awarded 1<sup>st</sup> place

Anastasia M. Kruse, Samantha A. Meenach, J. Zach Hilt, Kimberly W. Anderson. *Synthesis and Characterization of CREKA-conjugated Iron Oxide Nanoparticles for the Treatment of Cancer via Hyperthermia*. Society for Biomaterials, Denver, CO, April 16-19, 2011

Anastasia M. Kruse, Samantha A. Meenach, J. Zach Hilt, Kimberly W. Anderson. *Synthesis and Characterization of CREKA-conjugated Iron Oxide Nanoparticles for the Treatment of Cancer via Hyperthermia*, Graduate Student Poster Session, University of Kentucky, September 13, 2013

Anastasia M. Kruse, Samantha A. Meenach, J. Zach Hilt, Kimberly W. Anderson. *Synthesis and characterization of peptide-conjugated dextran coated iron oxide for hyperthermia applications*. 2013 Markey Cancer Day, Lexington, KY, April 15, 2013.

Anastasia M. Kruse, Samantha A. Meenach, J. Zach Hilt, Kimberly W. Anderson. *Synthesis and characterization of peptide-conjugated dextran coated iron oxide for hyperthermia applications*. 2012 Biomaterials Day, Lexington, KY, September 22, 2012.

Anastasia M. Kruse, Robert J. Wydra, J. Zach Hilt, Kimberly W. Anderson. *Biocompatibility Analysis and Cancer Therapy Application of Core-Shell Composite Magnetic Nanoparticles*. 2011 AIChE Student Meeting, Minneapolis, MN, October 14-17, 2011.

Anastasia M. Kruse, Robert J. Wydra, J. Zach Hilt, Kimberly W. Anderson. *Biocompatibility Analysis and Cancer Therapy Application of Core-Shell Composite Magnetic Nanoparticles*. 2010 AIChE Student Meeting, Salt Lake City, UT, November 5-8, 2010.

\*Awarded 2nd Place in the Food, Pharmaceutical, and Biotechnology Division